The Telecommunications and Data Acquisition Progress Report 42-60

September and October 1980

N. A. Renzetti
Editor

December 15, 1980

National Aeronautics and
Space Administration

Jet Propulsion Laboratory
California Institute of Technology
Pasadena, California

The Telecommunications and Data Acquisition Progress Report 42-60

September and October 1980

N. A. Renzetti
Editor

December 15, 1980

National Aeronautics and
Space Administration

Jet Propulsion Laboratory
California Institute of Technology
Pasadena, California

The research described in this publication was carried out by the Jet Propulsion Laboratory, California Institute of Technology, under NASA Contract No. NAS7-100.

Preface

This publication was formerly entitled *The Deep Space Network Progress Report*. Although the practice of reporting progress in the development and operations of the Deep Space Network continues, the report has been expanded to include developments in Earth-based radio technology as applied to other research programs. These programs are:

(1) Geodynamics: For several years, the laboratory has been developing radio interferometry at microwave frequencies for application to geodetic measurements. This branch of telecommunications technology is now being applied to the study of geodynamics.

(2) Astrophysics: The deep space stations, individually and in pairs as an interferometer, have been used by radio astronomers for astrophysics research by direct observations of radio sources.

(3) An activity closely related to radio astronomy's use of the deep space stations is NASA's continuing program of radio search for extraterrestrial intelligence in the microwave region of the electromagnetic spectrum.

Each succeeding issue of this report will present material in some, but not all, of the following categories:

Radio Astronomy
Search for Extraterrestrial Intelligence
Radio Interferometry at Microwave Frequencies

- Geodetic Techniques Development
- Spacecraft Navigation
- Orbiting Very Long Baseline Interferometry

Deep Space Network

- Description
- Program Planning
- Planetary and Interplanetary Mission Support
- Advanced Systems
- Network and Facility Engineering and Implementation
- Operations
- Spacecraft Radio Science
- Planetary Radar
- Energy

In each issue, there will be a report on the current configuration of one of the seven DSN systems (Tracking, Telemetry, Command, Monitor and Control, Test Support, Radio Science, and Very Long Baseline Interferometry).

The work described in this report series is either performed or managed by the Telecommunications and Data Acquisition organization of JPL.

This Page Intentionally Left Blank

Contents

RADIO ASTRONOMY

RADIO INTERFEROMETRY AT MICROWAVE FREQUENCIES

GEODETIC TECHNIQUES DEVELOPMENT

ORION

THE DEEP SPACE NETWORK

PROGRAM PLANNING

PLANETARY AND INTERPLANETARY MISSION SUPPORT

Interplanetary Flight Projects

ADVANCED SYSTEMS

Tracking and Ground-Based Navigation

Communications

Station Control and System Technology

NETWORK AND FACILITY ENGINEERING AND IMPLEMENTATION

Network

Ground Communications

Deep Space Stations

OPERATIONS

Deep Space Stations

Radio Astronomy

R. M. Taylor
Deep Space Network Operations Section

R. N. Manchester
Division of Radiophysics, CSIRO, Sydney, Australia

This article reports on the activities of the Deep Space Network in support of Radio and Radar Astronomy operations during July and August 1980. A brief update on the OSS-sponsored Planetary Radio Astronomy experiment is provided. Also included are two updates, one each from Spain and Australia, on current Host Country activities.

I. Introduction

Deep Space Network (DSN) 26-, 34- and 64-meter-antenna stations are utilized in support of experiments in three categories: NASA Office of Space Science (OSS), Radio Astronomy Experiment Selection (RAES), and Host Country.

II. Radio Astronomy Operations

A. NASA OSS Category

During this period support has increased for the series of ALSEP/Quasar VLBI observations to 56 hours of station time. Support for Pulsar Rotation Constancy observations has continued at prior levels at the Goldstone and Madrid 26-meter antenna stations. Similarly, the Planetary Radio Astronomy experiment has enjoyed a consistent level of support. The following is a brief summary of the status of this activity.

Planetary Radio Astronomy (OSS196-41-73)

1. **Observational objectives.** These objectives are twofold: first, to study the variations in synchrotron emissions from Jupiter's radiation belts and, second, to make precision measurements, over a long period, of atmospheric stability in the outer planets.

2. **Observed results.**

(a) Synchrotron variations change on time scales of days or months or years.

(b) Data must cover 11 years for solar wind and long-term orbital parameters.

(c) In collaboration with Professor E. Gerard of Nancay Observatory, France, a concentrated 6-hour-per-day observation effort (at the Madrid 26-meter station) for three months at 21 cm in early 1979 produced good Jovian short term variation data from which publication of the results is eagerly awaited.

(d) Radio astronomy can make high precision, consistent measurements year after year and, thus, is very useful for studying atmospheric stability and seeking correlation between atmospheric changes and other natural variations such as solar flux. These studies involve the

outer planets and require long-term observations in order to detect large-scale time changes.

3. **Implications.**

(a) It is interesting to try to determine the correlation, if any, of the synchrotron variations with solar parameters, orbital parameters, solar wind parameters and other natural phenomena.

(b) What mechanism causes this type (source function) of variations?

(c) How deep in planetary atmospheres can we detect climatic changes? Certainly to 10 atmospheres in the outer planets. Long-term observations are required, over several years. For example, the equatorial-to-pole temperature variation of 30 to 35 percent in the planet Uranus changes in a 22-year cycle. Can we detect climatic changes in the troposphere?

4. **Future interest.** In the Jupiter Patrol experiment the future looks toward millimeter or submillimeter observations but useful work could be done between 20 and 24 GHz in the molecular line area with a 64-meter single telescope. K-band interferometry looks like an exciting, realizable prospect in the near future. The question of why choose the DSN when the Very Large Array is available is answered by the Southern Hemisphere view not seen by the Very Large Array. It would be exciting to record the waterline spectra of planetary objects, including comets, in the Southern Hemisphere.

5. **Deep Space Network contribution.** The DSN provides facilities which have a long-term base, consistently high quality, stable instrumentation with continuity and instrument traceability and well-calibrated antennas. Planetary Radio Astronomy provides the DSN with a calibration base and a list of radio sources. The remaining problem with the facilities is that of blind pointing accuracy, a problem which is being resolved at this time.

B. RAES Category

1. **RA 175.** On June 13 and 14 and again on July 1 and 3, 1980, for a total of 51 hours, the Goldstone 26-meter station supported VLBI observations of the source SS 433 (1909+04). These observations represent continuing efforts in support of the experimental objective of resolving this bizarre galatic object to determine its angular radio structure and, if possible, its origin. These activities will continue in a similar fashion at regular intervals until the end of the year.

2. **RA 137 Quasar Patrol.** Dual polarization Very Long Baseline Interferometry (VLBI) observations were made on July 31 and August 1 at the Goldstone and Madrid 64-meter antenna stations of the source 3C454.3. Other telescopes supporting this experiment were Onsala, Sweden (26-meter), Haystack, Massachusetts (26-meter), Owens Valley, California (40-meter), Fort Davis, Texas (26-meter), Green Bank, West Virginia (40-meter).

The experimental objective was to observe the source in dual polarization, that is, right circular polarization and left circular polarization, as part of a scheme to construct a radio map of the region surrounding the quasar. Recordings were made using the Mark II VLBI Data Recording System. One of the principal investigators, Dr. William Cotton, of NRAO was in attendance during the experiment at the Goldstone 64-meter antenna station. Due to the failure of one of the S-band masers at Goldstone, it was not possible to record dual polarization simultaneously, so a time sharing technique was adopted, observing primarily in left circular polarization.

At this time, data reduction and analysis is in progress and the published results are anticipated in the near future.

C. Host Country

The primary host country activity in Spain is the Instituto Geografico Nacional Interferometric Survey (IGNIS) project. The objectives of this activity are:

(1) To conduct VLBI measurements of the relative position vectors between the 34- and 64-meter-antenna stations at Robledo de Chavela, the 26-meter-antenna station at Cebreros and comparison with other geodetic techniques.

(2) In cooperation with other agencies involved in geodetic VLBI to exchange information on the following:

  (a) Scale and orientation of the European Geodetic Net.

  (b) UT1 and polar motion.

  (c) Lithospheric plate motion.

(3) Software development for post correlation data processing.

From time to time, when scheduled, observations are performed using the bandwidth switching technique in order to obtain the synthesized delay and fringe rate observables. Early results, reduced and analyzed in an IBM 370/158 computer with JPL-generated software, show the following baseline components and length of the Cebreros 26-meter to Robledo 64-meter baseline vectors in a right-handed coordinate system

with the Z-axis directed to the Continental International Origin and the X-axis along the Greenwich Meridian:

$$Bx = -2392.192 \pm 0.028 \text{ m}$$

$$By = -10015.228 \pm 0.011 \text{ m}$$

$$Bz = 1797.116 \pm 0.019 \text{ m}$$

$$\text{Total length} = 10452.607 \pm 0.013 \text{ m}$$

In order to compare these results with those of classical methods, several previous surveys performed during the last 10 years in this zone were reanalyzed. The analysis indicated that the compatibility between the different surveys is not assured due to various reoccupation problems of the common points and the existing uncertainty regarding the altitude of the geoid over the ellipsoid in this zone. Nevertheless, the difference between the VLBI and the classical results is 18 centimeters.

Planning for the future includes the following objectives:

(1) Perform a new survey by tridimensional methods (laser, vertical deflection, etc.) for comparison purposes.

(2) Make VLBI measurements of the relative position vectors between the three antennas.

(3) Participate in European and transcontinental projects related to geodetic and geophysical applications of VLBI.

The only host country activity being supported in Australia during this period has been the pulsar observations being conducted for the Commonwealth Scientific and Industrial Research Organization (CSIRO) in Australia. The observations are conducted almost exclusively at the 26-meter-antenna facility at Honeysuckle Creek. The following is a brief summary of the status of this activity prepared and submitted by R. N. Manchester of the Division of Radiophysics of CSIRO, Sydney, Australia.

III. Pulsar Observations Using DSN Facilities in Australia

Since May 1975 a program of pulsar radio science observations has been carried out using the 26-meter-antenna station at Tidbinbilla, and more recently the similar facility at Honeysuckle Creek. The objective of this program is to determine accurate positions and pulsational periods for a set of southern pulsars and to monitor variations in the observed period. To achieve this objective a regular series of observations of pulse arrival times is required with an antenna and receiver system which has stable characteristics over long time intervals (several years) and high sensitivity at a radio frequency in the L- or S-bands. An accurate time reference is also required. Since the Deep Space Network provides an S-band system with these characteristics it is ideal for this program.

Pulsars were first discovered in late 1967 by Antony Hewish and Jocelyn Bell of the Mullard Radio Astronomy Observatory, Cambridge, England, using a large 80-MHz array designed to study interplanetary scintillations of compact radio sources. Several time-varying sources not attributable to scintillation were detected. After further investigation it was realized that the emission from these sources was unlike that from any other natural celestial radio source and consisted of a series of regularly spaced pulses. The pulse interval was typically about 1 s. Publication of this result triggered a large effort at many radio observatories to understand these sources and to detect new examples. The searches have been very successful, with over 300 pulsars now known.

In 1968 the Molonglo radio telescope in Australia detected a relatively strong pulsar near the center of the Vela supernova remnant, which had the very short period of 89 ms. At about the same time a pulsar was detected by Green Bank, West Virginia, near the center of the Crab nebula (a well-known supernova remnant whose birth was observed by the Chinese in A.D. 1054), which had an even shorter period of 33 ms. The detection of these two pulsars and the subsequent observation that the pulsation period was increasing at a slow but regular rate established that pulsars are born in supernova events and consist of rapidly rotating neutron stars. By some means not yet fully understood the neutron star emits a narrow beam of intense radiation and we observe a pulse each revolution of the star as the beam sweeps across the earth. A neutron star, which is one of the possible end points of the evolution of normal stars, is an extremely compact star with a mass about equal to that of our sun but a radius of only 10 km or so. Only a star as compact as this could survive rotation at speeds up to 30 revolutions per second (1800 rpm!).

In general, pulsar periods are very stable and predictable. Typical rates of change are less than one part per billion per day and many are predictable to better than one part in 10^{12}. However, some pulsars are subject to unpredictable changes in period. In the Vela pulsar these changes are more dramatic than for any other known pulsar. On four occasions since its discovery the Vela pulsar period suddenly decreased by about 200 ns (two parts in a million) and then, after some perturbations, resumed its normal rate of increase of about 11 ns per day. These period jumps are thought to be caused by a change in the moment of inertia of the neutron star and correspond to a shrinking of the stellar radius by about 1 cm. Observations

limit the time taken for the change to less than a week or so, but theoretical models suggest that it occurs within minutes. Since observations began at Tidbinbilla, two of these jumps have been observed, one in October 1975 and the other in July 1978. Figure 1 shows these two discontinuities in the otherwise regular increase of period.

Closer examination of the data shows that the rate of period increase is greater after the jump than before by about 1 percent and that this excess rate decays away on a time scale of a few years. In fact, the Tidbinbilla observations show that decay after the 1976 jump was still occurring at the time of the 1978 jump. This increase in period derivative followed by an approximately exponential decay suggested a model in which the neutron star consists of two main parts, a solid outer crust (probably a lattice of iron atoms) and an inner superfluid consisting largely of neutrons. Figure 2 shows the result of fitting this model to the Tidbinbilla and Honeysuckle Creek data. The parameters for the two jumps obtained from this fit are important constraints on the model. In particular, there are important differences in the post-jump recovery for the two events which cannot be accounted for in the simple version of the model.

Figure 2 shows that, while the model provides a close fit to the observed variations, the fit is not perfect. On top of the other variations the period appears to wander in random fashion. These fluctuations are very small (about one part in a billion per year) and quite unpredictable, but nevertheless they are significant and are present to a greater or lesser extent in all pulsars. Several of the pulsars monitored at Tidbinbilla and Honeysuckle Creek show relatively strong period fluctuations. Analysis of these results is giving further information on the interior structure of neutron stars.

Besides the Vela pulsar the only other large period discontinuity observed was also detected at Tidbinbilla. In November 1977 it was discovered that the period of the pulsar PSR 1641-45 had decreased by about 90 ns or two parts in 10^7. The post-jump recovery seems to be well fitted by the exponential decay model in this case also. Two similar events have been observed in the Crab pulsar, but both were much smaller, about one part in 10^8.

The Vela events occur on average approximately once every three years, so we are about due for another one. Regular observations of this and the other pulsars are continuing at Tidbinbilla and Honeysuckle Creek with the cooperation of the Director of the Canberra Deep Space Communications Complex and the staffs of the stations. Along with similar programs at Goldstone and Madrid operated by G. S. Downs (JPL) these observations form the only long-term monitoring of pulsar periods and their variations currently being undertaken. The Deep Space Network is therefore fulfilling a unique and valuable role for radio science which we hope will continue and expand in the future.

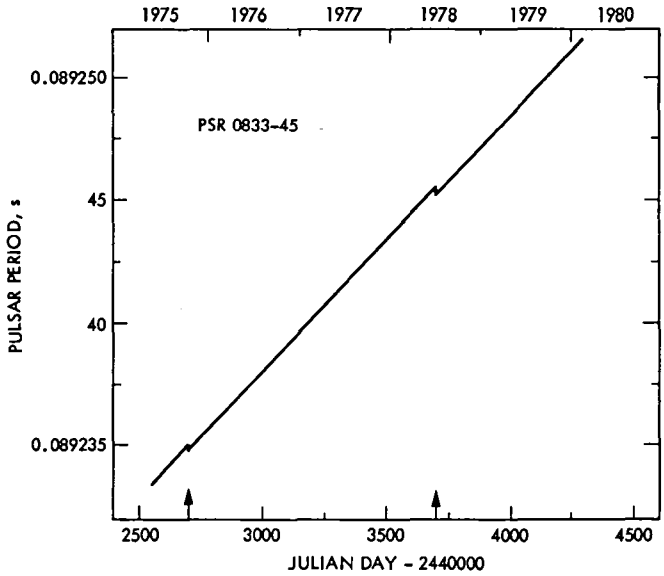

Fig. 1. Observed variations in the intrinsic period (i.e., after correction for doppler shifts resulting from the Earth's motion) of the Vela pulsar, PSR 0833-45, over the five-year interval, 1975–1980. The two period jumps are indicated by the arrows on the lower axis

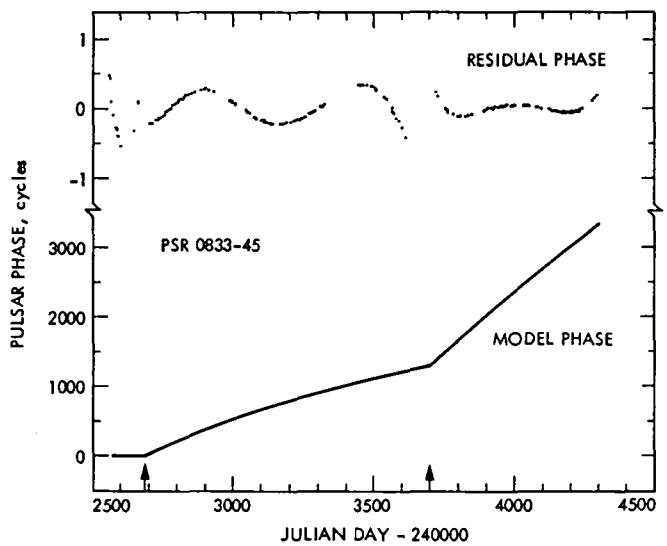

Fig. 2. Results of a fit of an exponential post-jump decay model to two period discontinuities observed in the Vela pulsar, PSR 0833-45. The lower part of the figure shows the model contribution to the observed pulse phase; the upper part of the figure shows the phase residuals after the fit. The two period discontinuities, indicated by arrows on the lower axis, each result in a discontinuous change in the gradient of the model phase.

ORION Mobile Unit Design

D. L. Brunn and S. C. Wu
Tracking Systems and Applications Section

E. H. Thom
TDA Engineering Office

F. D. McLaughlin and B. M. Sweetser
DSN Engineering Section

An overview of the design of the ORION mobile system is presented. System capability and performance characteristics are outlined. Functional requirements and key performance parameters are stated for each of the nine subsystems. A master design and implementation schedule is given.

I. Introduction

The ORION (Operational Radio Interferometry Observing Network) mobile system is being implemented in support of the NASA Crustal Dynamics Project (Ref. 1). Its purpose is to provide a means for measurement of lengths and orientation of vectors between sites located in areas of geophysical interest. This is accomplished by using Very Long Baseline Interferometry (VLBI) techniques operating at microwave frequencies using extragalactic radio sources (quasars).

With the recent emergence of the theory of plate tectonics (Ref. 2) and its potential for modeling motions on the Earth's surface, the need for precision geodetic measurements over long distances has increased. Experimental confirmation of the theory requires centimeter-level precisions over distances of 100-5000 km. This level of precision is also needed for earthquake research since it is believed that small motions of the Earth's crust may be precursors to episodic events (Ref. 3). Conventional surveying techniques are neither accurate enough nor economically feasible over distances in excess of 50 km, particularly if the terrain is mountainous or extends over large bodies of water. Therefore, there is a need for improved techniques capable of such measurements.

VLBI technology has progressed over the past decade to the point where centimeter-level accuracies are possible over the desired distances. Principal contributors to this advancement have been the advent of highly accurate atomic clocks, development of a suitable radio source catalog, development of a phase calibration system, and refined data processing techniques. A typical mobile VLBI system is shown in Fig. 1.

The extragalactic radio sources emit energy in the microwave frequency spectrum which is detectable by a suitably designed receiving system. In addition, the sources are located at such large distances that they exhibit no proper motion and

therefore serve as a highly stable inertial reference frame. The signals are received simultaneously at each end of the baseline, converted to baseband and recorded on magnetic tape. The tapes are forwarded to a central processing facility where the signals are cross-correlated and the difference in time of arrival is determined. This information, coupled with source-position knowledge and calibration of error sources, permits accurate determination of the baseline length and orientation.

Project ARIES (Astronomical Radio Interferometric Earth Surveying) has provided the Research and Development needed to demonstrate the feasibility of mobile system interferometry as applied to geodetic measurement (Ref. 4). Based on these results and analysis (Ref. 5) it was determined that an operational system could be implemented. This article gives an overview of the design of the mobile system which has been developed within the past year.

II. Requirements

The technical performance requirement for the ORION system is as follows: The three-dimensional baseline measurement precision shall be $\leqslant 5$ cm (1σ) for baseline lengths up to 5000 km. Length-only measurements shall be accurate to <2 cm.

The requirements are to be interpreted as the measurement repeatability or precision and not absolute accuracy. This level of performance must be achieved when operating with a co-site having a minimum antenna diameter of 9 meters, efficiency $\geqslant 0.50$ at X-band and system temperature $\leqslant 40$ K.

Given these requirements the next step is to determine the magnitude of each error contributor and to develop a design which will meet the requirements. Normally one of the criteria for an optimized system design is to have a balanced error budget; however, for the ORION system this turns out not to be a main consideration. The reason for this is that calibrations of several of the error sources are not under control of the mobile unit design.

The error sources associated with geodetic VLBI measurements are as follows:

(1) Signal-to-noise ratio (SNR).

(2) Instrumental delay calibration.

(3) Troposphere (wet and dry).

(4) Ionosphere.

(5) Antenna location.

(6) Clock stability.

(7) Source position.

(8) Polar motion.

(9) UT1.

The magnitude of error contributors (1) through (6) may be controlled either by choice of design parameters or by calibrations. Items (7) through (9) are calibrations not under control of the design. Reference 5 provides a detailed analysis of the interrelationship of these various error sources and Figs. 2 and 3 with accompanying Table 1 display the errors in bar chart form. It may be seen that a reasonably balanced error budget is achieved for a 300-km baseline and that the project requirements are met. For a 5000-km baseline the errors not under control of the design are dominant, resulting in a larger than desired measurement precision. As improvements are made in calibrations of the source positions and Earth platform parameters, the desired measurement precision will be possible without change in the mobile unit design.

A single quantity affecting the observation accuracy which involves the key design parameters is the signal-to-noise ratio. The relationship of these quantities is given in the Appendix.

In addition to measurement precision a number of other requirements must be met to achieve an operational design capable of worldwide performance. These are summarized as follows:

(1) The system must be economical to operate. Cost per continental U.S. site visit shall not exceed $5K.

(2) Mean time between failures shall be greater than 600 hours.

(3) The mobile unit shall be air transportable via C-130 and shall not require special permits for U.S. road transportation.

(4) No more than two persons shall be required to transport, assemble, operate and disassemble the mobile unit.

(5) The mobile unit shall be capable of sustained operations for periods up to one week without reprovisioning.

(6) Calibrations and observing sequences shall be fully automated, with the exception of tape changes.

There are a number of other requirements; however, these are the main drivers for the design. (The reader is referred to JPL internal document 1700-2, "ORION Mobile Station Functional Requirements," for further details).

The succeeding sections of this article describe the work completed, leading to a design which will meet the requirements.

III. Typical Operating Scenario

To acquaint the reader with the manner in which the mobile system can be utilized, a typical operating scenario involving one unit will be described. This is but one of several possible operating modes. It is assumed that the mobile configuration consists of two vans. One is called the electronics van, which contains the majority of the electronic equipment, the operations area and the crew amenities area. The other van is the antenna transporter, which consists of the antenna, antenna pedestal and servos, and the remaining electronics equipment. Other assumptions are a crew of two working a standard 40 hour work week, a 6-hour observing sequence and a site located 300 km from the departure point.

Monday – Prepare vehicles for transport.

Complete checklist

Drive to site or accommodation located nearby.

Tuesday – Establish communications with control center.

Position antenna transporter.

Erect antenna and interconnect vans.

Measure antenna position relative to geodetic marker.

Perform equipment readiness and calibration procedures.

Conduct observations.

Secure equipment.

Wednesday – Prepare equipment for transport.

Drive to next site or return to base.

Thursday – Repeat of Tuesday if at new site.

Friday – Repeat of Wednesday.

There are numerous details not included in this description; however, the main point is that, if desired, the unit can support a two-site-per-week schedule, using a two-person crew. Many other possibilities exist such as increasing the crew size to permit 24-hour observation schedules. This would only require a third vehicle to transport the crew or, if the site is remotely located, a recreational vehicle could be provided.

In developing the functional design, close attention has been given to the operational aspects. These have included ease of operations, maintainability and reliability with the philosophy that optimization of these parameters will best meet the project requirements of cost effectiveness over a 10-year life cycle.

IV. Tradeoff Studies

One of the studies performed early in the project (August 1979) was to determine the effects and sensitivities of antenna size and system temperature for both the fixed and mobile stations on the implementation and life cycle costs. Other variables included record time per observation, number of channels recorded, setup and teardown times for various antenna sizes. Some values were assumed to be fixed such as a minimum SNR per channel of 7 and source strength of 2 jansky.

Estimates of cost were made for both the implementation and operational costs, with the goal of minimizing the overall cost per site visit.

Certain assumptions were made such as:

(1) Thirty-two observations per site visit were required for delay measurement precision.

(2) An adequate star catalog would exist in 1982 to allow operation at any time.

(3) Barstow was used as the center point for tape shipping costs.

(4) One or more of the following base stations would be used:

Station	Antenna diam., m	System temp., K
DSS 13	26	30
OVRO	39 6	160
HRAS	26	160
Mojave	12.2	30

(5) Data (tape) handling costs were estimated as follows:

Correlator cost, $50/hr, two tape pairs/hr.	$25.00
Tapes, X2, @ $100 X 0.1 wearout factor	20.00
Clean, erase, certify tapes $2.5 X 2	5.00
Ship, round trip, Pasadena to Barstow	2.50
Total processing cost per tape pair	$52.50

The operating scenario included time to drive 160 km between sites; stop for fuel, tape shipment and pickup; setup and calibration time, operating time and teardown time.

Based on the above assumption, the study showed two things: (1) the better the base station the lower the per site cost, and (2) the shorter the setup and teardown times, the lower the per-site cost. A series of curves were developed to also show the optimum antenna size for each base station. Primarily, this showed that 4 to 5 m was optimum using a 130 K system temperature for the mobile station.

The design of the ORION mobile station requires a 5-m-diameter antenna and a 110-K system temperature. It is expected that a system temperature of 110 K at X-band can be achieved with current FET technology.

To calibrate for the ionospheric effects, ORION will also include an S-band link. The analysis by Wu (Ref. 6) indicates that the requirements on the S-band link are not very stringent. A system temperature in the range of 160-200 K at S-band would be appropriate. The analysis also indicates that precise data volume allocation between S- and X-band observations is not critical; an S/X data ratio between 1:2 and 1:4 is appropriate with a 160 K S-band receiver. Such a configuration, in conjunction with a typical 26-m base station on a 300-km baseline and recording 600 seconds per observation yields a 3-D baseline error due to SNR of 0.62 cm. When this is RSSed with all the other contributions to the overall error, it is somewhat insignificant. Reducing the record time by a factor of 4 would double the SNR error but would increase the overall 3-D baseline error only by 0.2 cm. In other words, data processing costs would reduce proportionately from $1680 per site visit to $420 by allowing the vector accuracy to degrade from 3.6 to 3.8 cm. This could be reduced even more by varying the record time for sources stronger than 2 jansky. Assuming ORION measures two sites per week for 10 years with an 80 percent utilization factor, this would amount to a $1,050,000 saving in data processing costs alone.

If the observation period per site could also be correspondingly reduced, then more sites could be visited per year, thereby reducing the cost per site even more. The above saving does not apply when a 9-m antenna is used as a base station. To maintain an SNR above 7, the 600-sec record time cannot be greatly reduced.

V. Electronics Design

The electronic equipment is required to perform the following functions:

(1) Receive and down-convert microwave energy at S and X-bands.

(2) Provide a highly stable clock.

(3) Produce an adequate signal-to-noise ratio (SNR).

(4) Provide an automated means to acquire, time tag and record the data.

(5) Produce a permanent record of equipment performance and generate real-time displays.

(6) Calibrate transmission media effects and record meteorological data.

(7) Furnish communications links to the control center.

To accomplish these functions the system design was divided into nine subsystems:

(1) Microwave (MWS).

(2) Receiver (RS).

(3) Data Acquisition (DAS).

(4) Frequency and Timing (FTS).

(5) Phase Calibrator (PCS).

(6) Monitor and Control (MCS).

(7) Water Vapor Radiometer (WVR).

(8) Antenna (AS).

(9) Facilities (FS).

The last two subsystems will be described in Sections VI and VII. The interrelationships of these subsystems are shown in block diagram form in Fig. 4.

A. Microwave Subsystem

The Microwave Subsystem consists of the S- and X-band antenna feeds, low-noise amplifiers (LNA) and cooling assembly. It performs the following functions:

(1) Receives the amplified S- and X-band signals from the antenna subsystem.

(2) Provides coupling for the S- and X-band phase calibration tones.

(3) Provides performance monitoring information to the Monitor and Control Subsystem.

The S-band operating frequency range is 2220-2320 MHz with a half-power bandwidth of 100 MHz. X-band operating frequency range is 8200-8600 with a half-power bandwidth of 400 MHz. Antenna efficiencies are $\geqslant$0.40 and $\geqslant$0.50 at S- and X-band respectively, and the polarization is right circular. System temperatures are $\leqslant$160 K and $\leqslant$110 K for S- and X-band. A preliminary vendor survey indicates these performance parameters can be achieved using commercially available equipment. The microwave equipment will be located on

the antenna assembly in protective enclosures. Monitor and control will be provided via an RS-232C interface.

B. Receiver Subsystem

The Receiver Subsystem performs the following functions:

(1) Receives S-band signals from the Microwave Subsystem and downconverts to an intermediate frequency of 300 MHz with a half-power bandwidth of 100 MHz.

(2) Receives X-band signals from the Microwave Subsystem and downconverts to an intermediate frequency of 300 MHz with a half-power bandwidth of 400 MHz.

(3) Generates appropriate mixing frequencies using a reference signal supplied by the Frequency and Timing Subsystem (FTS).

(4) Provides performance status signals to the Monitor and Control Subsystem via an RS-232C interface.

(5) Supplies dc power to the Phase Calibration Subsystem.

Input signals will be supplied from the LNAs via coaxial cables within a range of -70 to -40 dBm. Reference frequency input will be 100 MHz at 13 dBm. The receiver will be located on the antenna transporter within a suitable enclosure. Monitor and control will be provided via a RS-232 interface.

C. Data Acquisition Subsystem

The Data Acquisition Subsystem (DAS) is a general-purpose digital recording device for sample data rates ranging from 0.25 to 8 MHz. The subsystem is the operational version of the Crustal Dynamics Project MK-III VLBI Data System. Primary inputs to the DAS are the S- and X-band IF signals and information for the ancillary data record provided by the Monitor and Control Subsystem. A detailed description of the MK-III Data System may be found in Ref. 7.

The DAS performs the following functions:

(1) Accepts the S- and X-band intermediate frequencies from the Receiver Subsystem.

(2) Provides 14 selectable center frequencies within the microwave bandpass.

(3) Downconverts energy on either side of the selected frequencies to 14 pairs of video bands.

(4) Provides video bandwidth selection for each pair of video bands.

(5) Formats and time tags the data.

(6) Provides real-time and non-real-time recording performance monitoring and diagnostics.

(7) Provides for remote control operation of the subsystem.

(8) Supplies computer and computer interface for the Monitor and Control Subsystem.

(9) Reproduces data for digital tone extraction and post-real-time processing or reduction.

(10) Provides redundant recorders.

(11) Determines total power within microwave bandpass.

The performance parameters of the DAS are:

Input Characteristics

(1) Input IF Frequencies:

S-band IF, 300-MHz center frequency

S-band bandwidth ±50 MHz (-3 dB)

X-band IF, 300-MHz center frequency

X-band bandwidth, ±200 MHz (-3 dB)

(2) IF Input Levels: -10 dBm to -42 dBm

(3) FTS Reference Frequency: 5 MHz 13 ±3 dBm

(4) Monitor and Control interface: RS-232

(5) Power Requirements: 105-130 Vac, 10, 48-63 Hz, 1650 W average, 1900 W peak

Output Characteristics

(1) Selectable channel bandwidth in five steps each by a factor of two: 0.12 – 2.0 MHz.

(2) Selectable section on input spectrum to be output by any pair of channels: selectable in 10-kHz steps.

(3) Peak-to-peak gain ripple over 80 percent of the sample bandwidth of any channel: $\leqslant 0.5$ dB.

(4) Image rejection over 80 percent of sample bandwidth of any channel: $\geqslant 23$ dB.

(5) Deviation from gain linearity over output range -37 dBm to +3 dBm: $\leqslant 1\%$.

(6) Gain variation due to temperature change to be predictable within < 0.5 dB (1σ).

(7) Peak-to-peak phase ripple (deviation from linearity) in the frequency domain at 73°F: $< 10°$.

(8) Phase delay as a function of frequency to be predictable over allowable temperature and humidity range with uncertainty of 2° (1σ).

(9) Records:

Tape width, 1 in.

Number of tracks, 28

Longitudinal density, 33 kb/in./track at 135 ips

Recording code, NRZM in MI-III format

Control, local or remote via RS232C interface

(10) Monitor and Control interface: RS-232

Operating modes of the DAS are the following:

(1) Wideband – 28 tracks recorded in one pass, upper sideband outputs to first 14 tracks and lower sideband outputs to the remaining 14.

(2) Continuum – 14 tracks recorded per pass, only seven converters used.

(3) Multiline – 4 tracks recorded in each pass.

(4) Spectral – 1 track recorded per pass (Mark II compatible mode).

D. Frequency and Timing Subsystem

The Frequency and Timing Subsystem (FTS) provides one or more highly precise phase-coherent reference frequencies. It also provides accurate time information to the Data Acquisition Subsystem. Major assemblies include the Frequency Standard, Frequency and Timing Distribution Assembly, Time Sync Receiver and Time Sync Antennas.

The FTS performs the following main functions:

(1) Provides highly stable frequency reference.

(2) Distributes reference frequencies.

(3) Provides means to establish accurate epoch time.

(4) Distributes timing pulses.

(5) Monitors subsystem performance.

A hydrogen maser will be used for the timing standard. Frequency stability requirements are $< 1 \times 10^{-14}$ for time periods > 60 sec up to 86,400 sec. The standard is required to reach this stability four hours after arrival on site, which necessitates operating the unit and maintaining temperature control while in-transit. Time offset calibration will be accomplished using a global positioning receiver. The subsystem will supply 1 pps and 5 MHz signals to the DAS, Monitor and Control Subsystem, and Phase Calibration Subsystem.

E. Monitor and Control Subsystem

The Monitor and Control Subsystem (MCS) performs the following main functions:

(1) Provides the central control point for the station.

(2) Provides schedule input via floppy disk.

(3) Prepares the ancillary data record.

(4) Provides operator input-output via CRT terminal.

(5) Generates antenna pointing commands.

(6) Performs station calibration and malfunction diagnosis.

(7) Monitors weather conditions.

(8) Monitors subsystem performance.

(9) Provides operational communications.

The function of providing the central operating point for the station included control of all subsystem operating modes and display of all subsystem status and alarm messages. The ancillary data record consists of meteorological data, water vapor radiometry data, phase calibration data, end-to-end system performance verification data, and other data as appropriate for delivery to the user with the VLBI data from the Data Acquisition Subsystem. Generation of antenna pointing commands includes commands for conducting the calibration and observation sequence.

Station calibration includes determination of antenna axis intersection location based on site survey data and all periodic subsystem performance verification test. Malfunction diagnosis includes special operational sequences conducted after an abnormal condition is detected during an operational sequence or station calibration. Weather monitoring includes temperature, pressure, humidity, and wind speed. All of these except wind speed are for inclusion in the ancillary data record. Rapid communication includes those transceivers and antennas necessary to provide 90% reliable communications to the point from which the experiment is being coordinated. It specifically excludes the equipment for nonoperational communication between the antenna and electronics transporter prime movers (which are included in the Facilities Subsystem).

The MCS utilizes the DAS HP-1000 to perform its functions. Subsystem interfaces are via RS-232C. Operator interface will be via keyboard and CRT, with hard disk supplied for program storage. Floppy disk will be used for storage of the ancillary data record. Routine status displays will be provided with detailed subsystem performance available upon request.

Meteorological data will be measured using one of several commercially available instrument packages. The data will be a part of the ancillary data record.

Communications will be via a combination of land line radio-telephone and HF transceivers for continental U.S. operations. Foreign country operations may require tailoring the communications capability to meet requirements.

F. Phase Calibration Subsystem

The Phase Calibration Subsystem (PCS) will provide calibration tones at S- and X-band which permit monitoring of the respective radio source signal paths. The tones will be digitally sampled and recorded simultaneously with the signals and will be detected and displayed in real-time by a digital tone extractor.

The PCS performs the following functions:

(1) Generates phase-stable signals at S- and X-band which are coherent with the FTS references.

(2) Couples the signals at the proper level into the S- and X-band low noise amplifiers.

(3) Detects and displays the calibration signal phase and amplitude for the purpose of real-time monitoring.

(4) Monitors electrical length of the frequency reference cable to the antenna transporter.

(5) Monitors subsystem performance and reports to MCS via RS232C interface.

The phase calibrator generates a phase-stable comb pattern at S- and X-band which is injected at a point preceding the low-noise amplifiers. Spacing between tones is adjustable to permit presence of several tones within the video passband.

G. Water Vapor Radiometer Subsystem

Figure 5 illustrates the Water Vapor Radiometer Subsystem (WVR) functions and interfaces. The WVR performs the following main functions:

(1) Determines water vapor apparent brightness temperature.

(2) Monitors water vapor radiometer performance.

The radiometer will be located on the backside of the main antenna with an opening provided to allow viewing along the line-of-sight of the main beam. This eliminates the need for a separate antenna pedestal and its attendant electronics and pointing software. Operating frequencies will be 20.7 and 31.4 GHz with a halfpower bandwidth of 7 degrees and a beam efficiency of >97 percent. Integration time will be variable and selectable from 0.1 to 10 sec. An absolute accuracy of 2.0 K (rms) is required.

VI. Antenna Transporter Design

A. Requirements

The more salient features of the functional requirements driving the design of the antenna/transporter are as follows:

(1) No more than two people are required for any phase of the ORION mobile station operation. This includes setup of the antenna.

(2) No more than four hours shall be required to prepare the station for operation after arrival at a prepared site. Therefore, approximately two hours is the maximum time allotted to positioning, assembly and alignment of the antenna.

(3) The vehicles must be transportable by C-130 aircraft. While on the highways, they must stay within the standard envelope of 13.5 ft high by 8 ft wide.

(4) The location of the axis intersection of the antenna must be known within 0.5 cm of an established monument.

(5) Five meter antenna with system efficiency of $\geqslant 50\%$ at 8.6 GHz and $\geqslant 40\%$ at 2.3 GHz.

B. Error Budget

An error budget was prepared to allocate dish distortion losses and pointing error losses and to proportion the phase center location allowance among the various components and error contributing factors. Estimates received from the Microwave Subsystem were that an RF efficiency, excluding central blockage and quadripod blockage, would be approximately 0.72. Assuming a 5 percent area blockage for subreflector and quadripod, the balance of the required 50 percent overall efficiency allotted to dish distortion and point error is:

$$\frac{0.50 \text{ (target overall)}}{0.72 \text{ (RF)} \times (1 - 0.05)^2 \text{ (central and quad blockage)}} = 0.77$$

Figure 6 shows the relationship of allowable pointing error to the rms dish distortion for the 77 percent at 8.6 GHz. Thus, as indicated in Fig. 6, with a likely rms dish distortion of 1.2 mm (including manufacturing, gravity and wind distortions), the allowable error for pointing is approximately 0.083 degrees.

Table 2 shows the estimated contribution for the various sources of error.

With regard to the 0.5-cm antenna location with respect to a local monument, the plan is to construct a locator arm which is connected to the antenna pedestal and is positioned to be in contact with the established monument (by means of a spherical seat or similar connection).

The arm, Fig. 7, will be provided with angular encoders to measure the azimuth and elevation angle of the device and a linear transducer to measure the arm extension. Thus, the vector relationship between the reference point on the antenna pedestal and the monument may be determined and monitored.

An additional feature shown in Fig. 7 is the north-seeking gyro. This may or may not be located as shown on the locator arm but will be provided to enable setup and determination of true north quickly. There is no guarantee that a clear sky will enable us to initially align the antenna to the sun as is done with ARIES antenna.

The rectangular coordinates of the phase center with respect to the monument (Fig. 8) are X_T, Y_T, Z_T. The actual phase center components will also depend on the errors from six transducers, namely,

ϵ_X level about x axis

ϵ_Y level about y axis

ϵ_L length of locating arm

ϵ_A arm azimuth angle

ϵ_E arm elevation angle

ϵ_G gyroscope north-seeking compass

The actual phase center components will also include displacements caused by:

(1) Deflection of structure from wind.

(2) Deflection of ground at trailer supports.

(3) Thermal deflection of structure from ambient temperature change.

(4) Thermal deflection of structure from differential temperature between sun and shade sides.

The measured phase center coordinates including level errors are:

$$x_T = -c\epsilon_y + \ell \cos(\Theta_E - \epsilon_Y \cos\Theta_A + \epsilon_x \sin\Theta_A)\cos(\Theta_A - \epsilon_y \sin\Theta_E \sin\Theta_A - \epsilon_x \sin\Theta_E \cos\Theta_A)$$

$$y_T = c\epsilon_x + \ell \cos(\Theta_E - \epsilon_y \cos\Theta_A + \epsilon_x \sin\Theta_A)\sin(\Theta_A - \epsilon_y \sin\Theta_E \sin\Theta_A - \epsilon_x \sin\Theta_E \cos\Theta_A)$$

$$z_T = c + \ell \sin(\Theta_E - \epsilon_y \cos\Theta_A + \epsilon_x \sin\Theta_A)$$

The measured phase center coordinates including errors on azimuth, elevation, and length encoders of locating arm are:

$$x_T = (\ell \pm \epsilon_\ell)\cos(\Theta_E \pm \epsilon_E)\cos(\Theta_A \pm \epsilon_A)$$

$$y_T = (\ell \pm \epsilon_\ell)\cos(\Theta_E \pm \epsilon_E)\sin(\Theta_A \pm \epsilon_A)$$

$$z_T = C + (\ell \pm \epsilon_\ell)\sin(\Theta_E \pm \epsilon_E)$$

The errors x_T, y_T, z_T are obtained by subtracting their nominal values from the above measured values.

Representative values are obtained by taking $\Theta_A = 0$, $\Theta_E = 45°$, $\ell = 2000$ mm, C = 4800 mm, phase center locked at zenith.

Table 3 summarizes the error budget for the encoder accuracies as shown on Fig. 7 and the representative values listed above.

C. Antenna-Transporter Description

It became clear early on in the project that if the goal of low cost was to be achieved, an extensive R&D effort for antenna development could not be entered into. Thus, commercially available components are to be used to the maximum extent possible.

Figures 9 and 10 show the proposed general arrangement of the antenna transporter. The trailer ① is approximately 40 ft in overall length, has sides ② which fold down mechanically to provide working platforms, and a cover ③ which is retractable by rolling forward on a drum ④. The trailer provides support for a commercially available pedestal ⑤, which is erected into the vertical position and lowered for the transporting mode by means of hydraulic cylinders ⑥.

The reflector is 5 meters in diameter, f/d of 0.34, and is a fiberglass layup in five pieces. The center piece ⑦ is permanently mounted to a yoke structure ⑧. The quadripod ⑨ and feed ⑩, along with the center piece of the dish, remains permanently attached to the yoke-pedestal assembly; thus, there is no need for time-consuming alignments at each setup.

The remaining dish quadrants (11) are assembled in halves on erection aids which are positioned near the pedestal at setup (Fig. 11). The already upright (and pointed to zenith) pedestal, yoke and center dish assembly is moved to zero degree elevation, engaging fasteners permanently moulded into the reflector. A turn of an allen-head wrench connects the dish halves by means of the aforementioned fasteners, which are over-center, clamping devices. The assembly is then plunged 180 degrees in elevation and the other dish half is similarly connected.

The assembled, erected antenna is shown in Fig. 12. The appropriate leveling outriggers (13) are provided on the pedestal. The locator arm (14) is shown mounted at the aft end of the pedestal for ease of removal for protection during shipping.

VII. Facilities Design

A. Scope

The facilities portion of the ORION project has been defined to include the electronic van and all support utilities.

B. Environmental Requirements

The first step in the design of the facilities was to establish the environmental requirements, which were determined to be that the mobile station must be able to operate under worldwide conditions. To develop environmental specifications for these conditions, the MIL-STD-210B "Climatic Conditions for Military Equipment" was used as a guide. From this starting point the following environmental requirements (Table 4) were developed for the project.

1. General. The mobile station electronics van shown in Fig. 13 will house the major electronics equipment, including the maser, and will also provide living quarters and amenities for the two station operators. Figure 13 shows the layout of the van interior. The van will be 33 feet in length and eight feet in width, with a clear height of eight feet. On the road it will have a height of under 13 feet 6 inches. Upon removal of the wheels and suspension system, it will be transportable on a C-130 aircraft. To minimize road shock to the electronic equipment, an air ride suspension system will be utilized. The construction details of the van will conform to standard commercial practice in the industry.

2. Electronics area. The primary concern in planning the layouts of the van electronics area was to provide for efficient and convenient operation. For maintenance purposes full access to the rear of the equipment is provided without moving the racks so that all equipment can be rigidly and permanently anchored. Due to temperature sensitivity, the maser is installed in an area separate from the operations area.

Storage space has been provided for 48 tape reels, which is adequate for one operational cycle. The reels are to be stored in sealed cans to prevent degradation due to high humidity. Space for storage of electronic spares is also provided within the van, and other spares can be stored in containers and placed in racks under the van.

3. Living quarters. The living quarters are separated from the operations area and provide suitable amenities to support the operators. These include shower, toilet facilities, microwave oven, refrigerator, bunks, storage space for personal effects, and space for consumables for a period of one week.

4. Heating/ventilation/air conditioning (HVAC). The entire electronic van will be air-conditioned, and it is planned to provide three air-conditioning zones: the living quarters, the electronic operations area, and the maser area. The trailer shell is designed to provide a well-insulated thermal barrier between the outside environment and the three air-conditioning zones.

These zones provide successive layers of environmental isolation for the critical maser area, which will be heavily insulated and will be controlled to ±0.1°C. The electronic operational area serves as an air lock to the maser zone. The operational area will be temperature-controlled to ±2.8°C, with minimum humidity control to maintain a range of 20 to 80 percent. The living quarters, in turn, serve as an air lock for the operational zone. This zone may experience high humidity loads due to the presence of people and their activities (i.e., showers and cooking). Exhaust fans will be used to minimize the humidity in this area. The living quarters will also be controlled to ±2.8°C. Finally, a small air lock is provided to shield the trailer interior from outside temperature, wind, dust and moisture.

The heating, ventilating, and air conditioning (HVAC) system utilizes two compressors. A small precision unit cools the maser compartment and is capable of operating on batteries while the van is being moved. The larger unit air-conditions both the operations area and the living quarters, utilizing two air-handlers. In case of failure of one air-handler, the air flow can be dampered to assure air flow to the operations area. The HVAC equipment will provide the interface between the monitor and control systems to indicate the operational status of all equipment. No air conditioning is required on the antenna trailer.

5. Fire protection. Ion-type smoke detectors and a Holon fire suppression system will be installed.

6. **Power.** Two 480-volt, 3-phase, 60-hertz diesel-driven generators will be provided to supply the stations' power requirements. Each unit will be capable of supplying the full station load to provide 100 percent redundancy. AC/DC power supplies will provide power to the electronic equipment. In addition, a battery bank will be provided to operate the maser and its air-conditioning system for a 24-hour period. The battery bank will have the capability of being charged from 50-cycle and 400-cycle sources, the latter being available during air transport. In addition, it will be possible to operate the entire station from a 60-cycle exterior source. The possible use of a 50-cycle source is presently being studied.

The starting of the diesel generators at low temperatures will be achieved either through the use of a small auxiliary engine-driven generator or utilizing compressed air if the battery requirements prove excessive.

All power equipment will interface with the Monitor and Control Subsystem to provide operational status of all the equipment.

7. **Lighting.** Interior lighting will utilize fluorescent fixtures; exterior area lighting will consist of incandescent fixtures permanently mounted on the van and the antenna trailer.

VIII. Schedules

The master schedule is shown in Fig. 14. The system design and subsystem functional designs will be completed by October 1980. Antenna transporter fabrication will commence in October 1980 with completion scheduled for June 1981. Facilities procurement is not scheduled until FY 82 due to funding limitations. However, electronics subsystems will be processed and integrated in FY 80 and FY 82. System test and operations training will begin in August 1982 and the first ORION mobile unit will be transferred to operations in October 1982. All succeeding mobile units will be fabricated by a system contractor beginning in FY 83.

Table 1. Estimated measurement accuracies

Parameter	Estimated accuracy
Baseline center latitude	ϕ = 35 deg
Baseline orientation	Arbitrary
Antenna diameters	9 m, 5 m
System temperatures	
S-band	40 K, 160 K
X-band	40 K, 110 K
Antenna efficiencies	
S-band	0.5, 0.4
X-band	0.5, 0.5
Source strength	2 jansky
Integration time per observation	600 s
Channel bandwidths	7 X 2 MHz per sideband per S- or X-band
Span bandwidths	
S-band	100 MHz
X-band	400 MHz
Clock stability	$\Delta f/f$ = 10-14 ($t > 100$ s)
Zenith dry troposphere, wet troposphere	0.5 cm, each site (systematic)
Bias	Immaterial
Systematic	$0.5/\sqrt{2}$ cm, zenith, each site
Random	$0.5/\sqrt{2}$ cm, zenith, each site
Ionosphere	Calibrated by S/X observations
Polar motion	30 cm
UT1	0.6 ms
Source position	0.01 arcseconds
Antenna location	0.5 cm at mobile site only
Instrumental delay	0.2 cm, each site
Number of observations	32
Number of solved for parameters	16 (baseline components and clock parameters)

Table 2. Pointing error budget

Alidade pedestal	0.065 deg
Encoders	
Servo	
Orthogonality of axes	
Compliance under 30 mph wind	
Antenna angular changes	
Bending deflection of structure from wind	0.0078
Bending deflection of structure from temp.	0.033
Trailer support shift from 30 mph wind	0.0176
Trailer level instrument	0.0166
Gravity direction	0.0166
Latitude	0.004
Longitude	0.004
North seeking gyro compass	0.025
Total error, RSS	0.083

Table 3. Phase center location error budget

Error source	x	y	z	x	y	z
Levels	$3386\,\epsilon_y$	$3800\,\epsilon_x$	$1414\,\epsilon_y$	0.985	1.105	0.411
Arm encoders	$1414\,\epsilon_E + 0.7\,\epsilon_l$	$1414\,\epsilon_A$	$1414\,\epsilon_E + 0.7\,\epsilon_l$	0.447	0.411	0.447
Gyro compass		$1414\,\epsilon_G$			0.617	
Trailer feet wind loading		1.91			1.91	
Structure wind loading		0.498			0.498	
Structure temp., $\Delta T = 52°C$			3.43			3.43
Structure temp., $\Delta T = 5.5°C$	1.72	1.72		1.72	1.72	
RSS vector sum = 4.99 mm				2.032	2.937	3.483

Table 4. Mobile station environmental specifications

External conditions	Operating	Nonoperating
High temperature	45°C	53°C
Low temperature	-29°C	-45°C
Wind speed	48 km/h	64 km/h while in transit; 193 km/h in stowed condition
Humidity		
with high temperature	Maximum 100% relative Humidity (RH) minimum 3% RH, 46°C	100%, 24°C (24 h)
with low temperature	100% RH, -29°C	100%, -45°C
Rainfall	N/A	2.54 cm/h
Ice accretion	N/A	7.5 cm glaze (specific gravity 0.9)
Snow load	N/A	97.6 kg/m
Hail	N/A	2.54 cm with antenna covered
Altitude		
Maximum	3048 m	15,240 m
Minimum	Sea level	Sea level
Sand and dust	0.15 GMS/M, 150	Raised level 1.0 GMS/M, 75-1000
Lightning and static charge	Provide ground	Provide ground
Fungus	MIL-V-173 c	MIL-V-173C
Salt spray	Coastal conditions	Coastal conditions
Shock and vibration	Air ride suspension and vibration isolators	Air ride suspension not applicable during air transport

Internal conditions	Operating	Withstanding
High temperature	27°C	66°C
Low temperature	16°C	-45°C
Temperature range	+1.1°C	93°C
Humidity	20% to 80% RH	Exterior conditions
Fungus	MIL-V-173C	MIL-V-173C
Hydrogen maser	26 ±0.1°C (For t > 16 m)	22-26 ±1°C

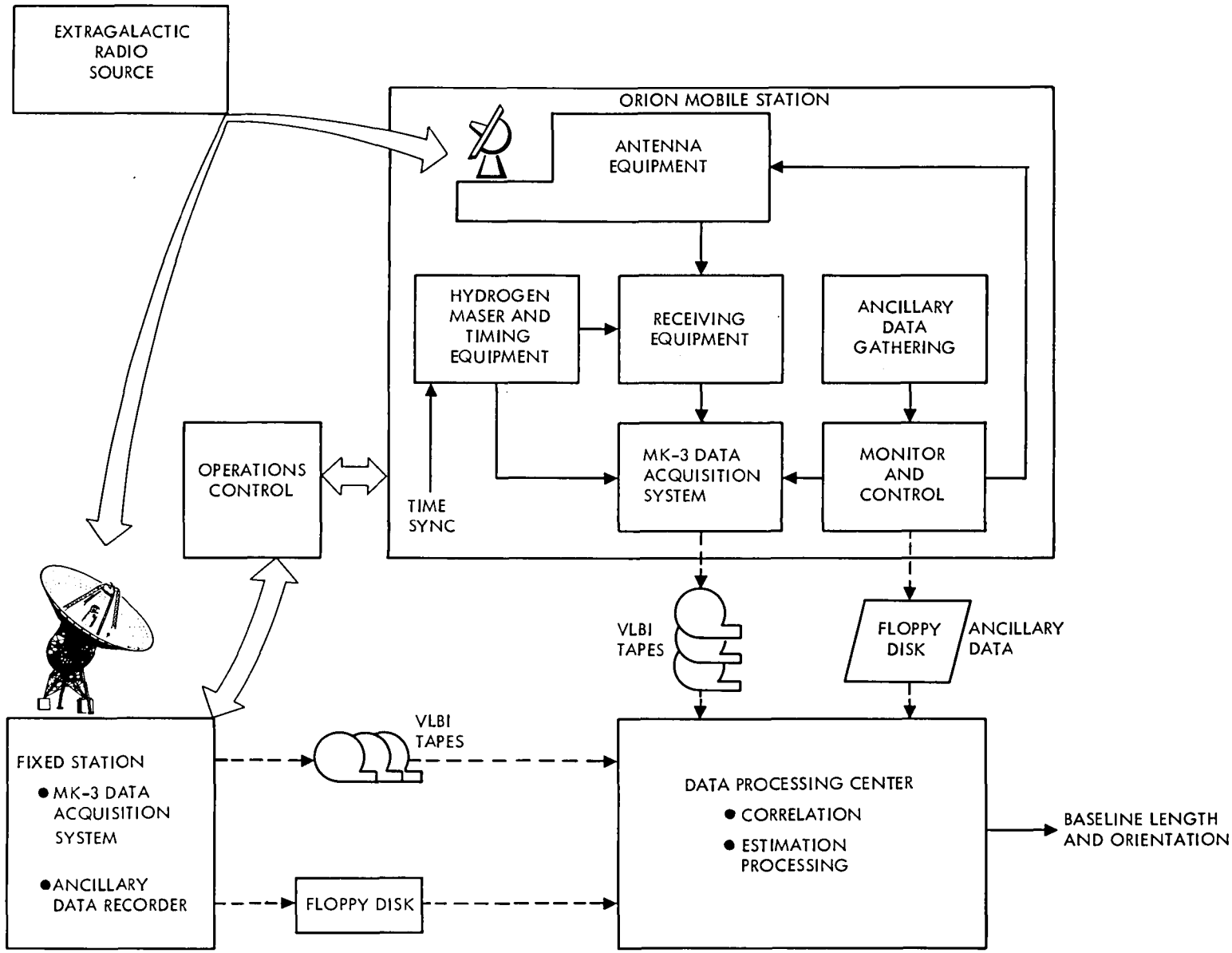

Fig. 1. ORION system, simplified block diagram

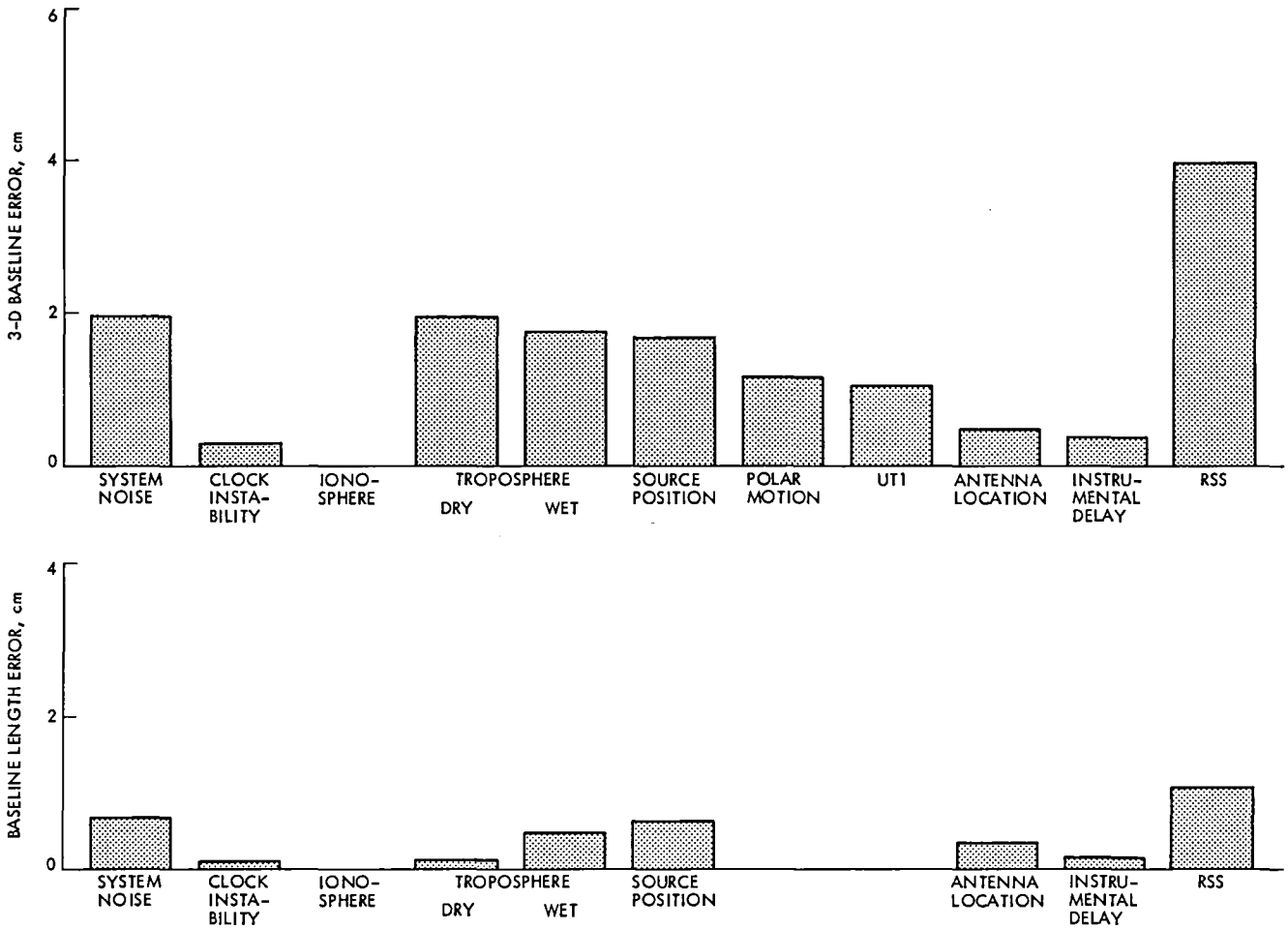

Fig. 2. Baseline vector and length estimation errors (300 km baseline)

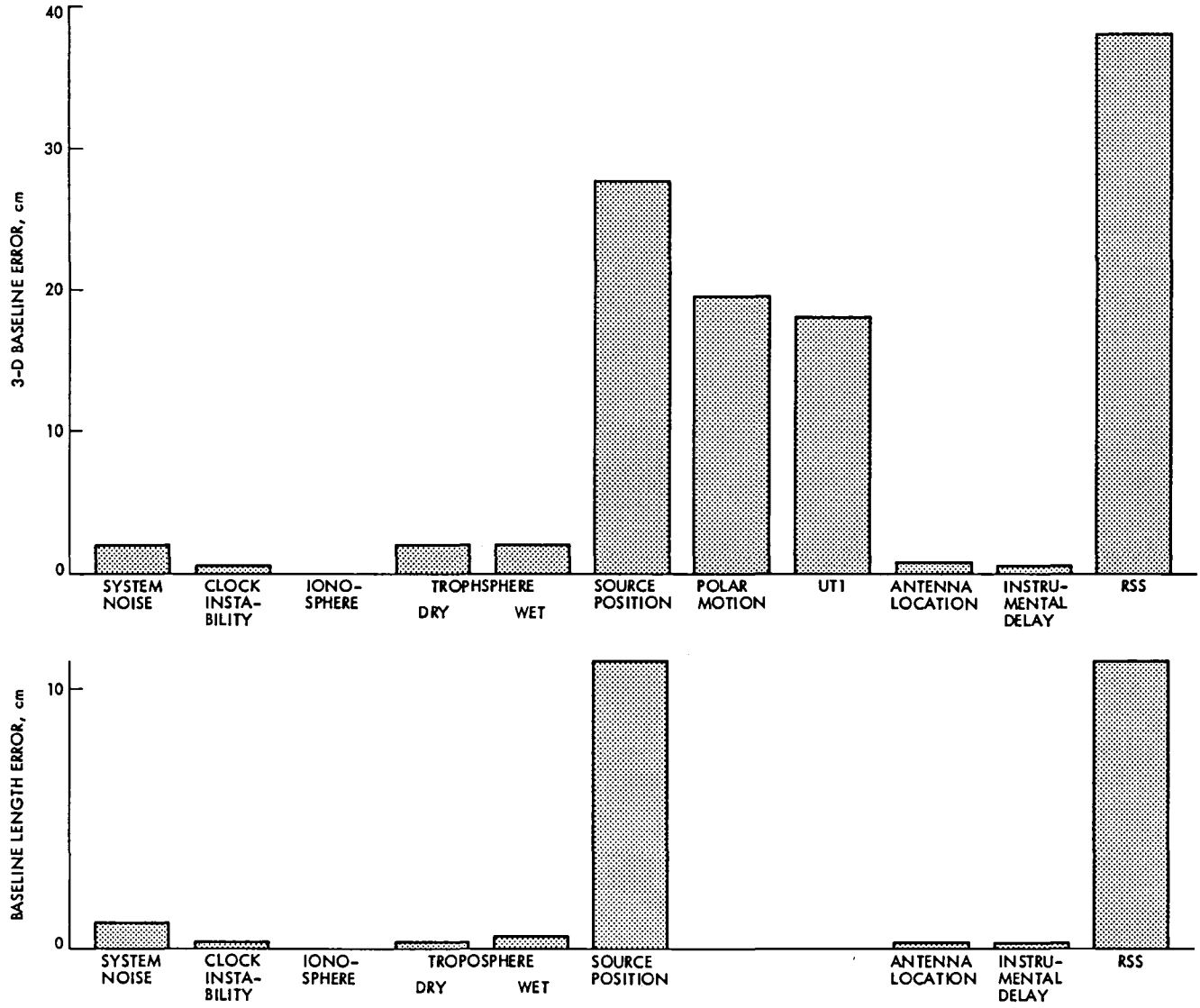

Fig. 3. Baseline vector and length estimation errors (5000 km baseline)

This Page Intentionally Left Blank

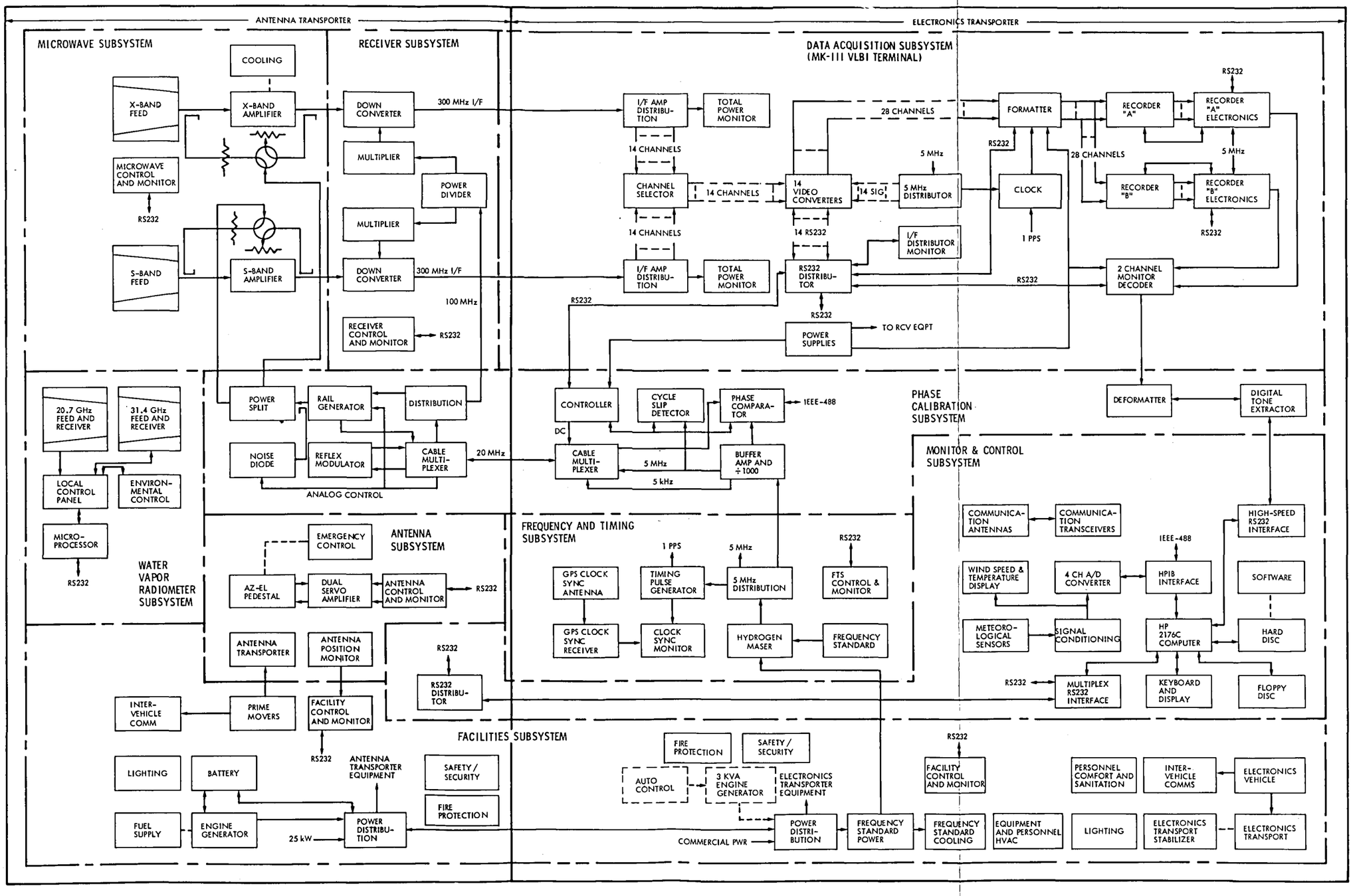

Fig. 4. Mobile station block diagram

This Page Intentionally Left Blank

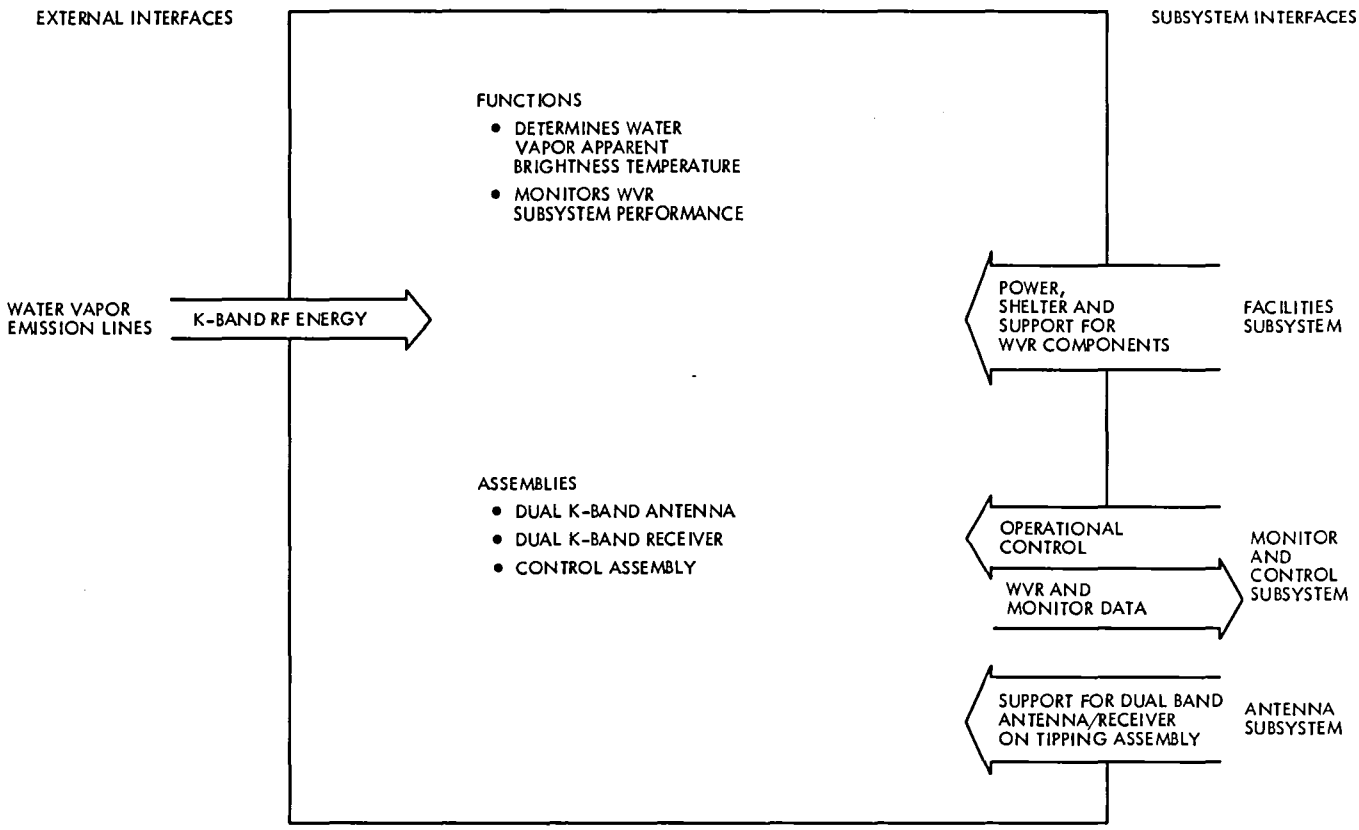

Fig. 5. Water vapor radiometer subsystem, function and interfaces

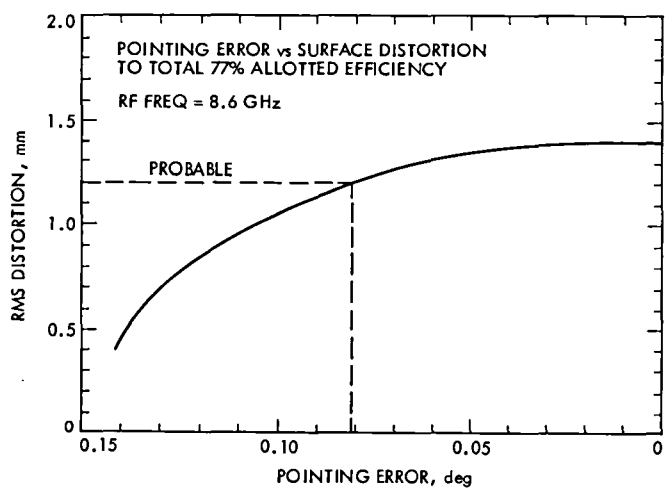

Fig. 6. Pointing error/surface distortion

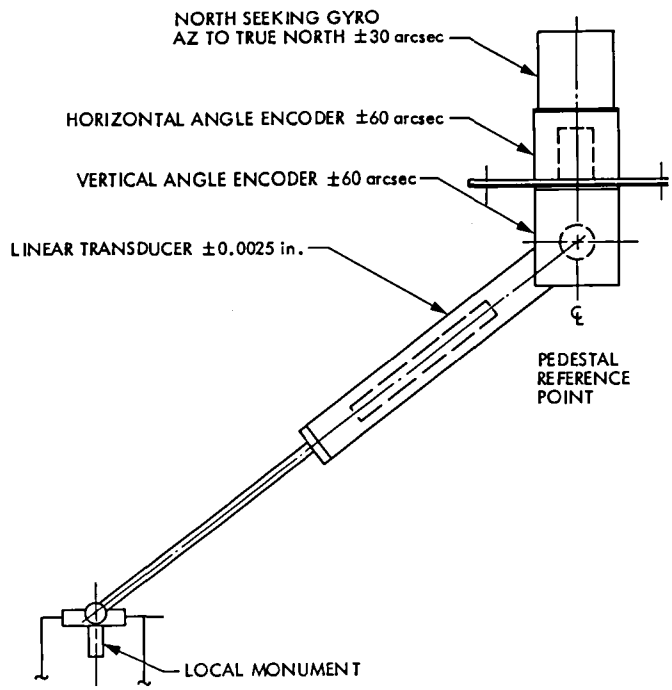

Fig. 7. Antenna transporter locator arm

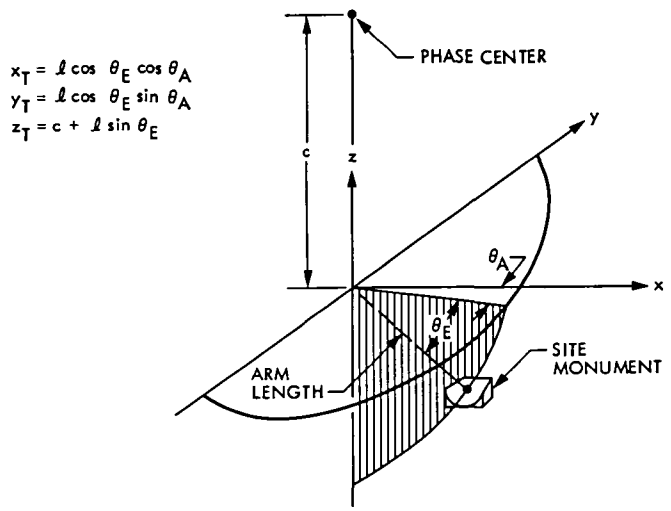

Fig. 8. Phase center/monument coordinates

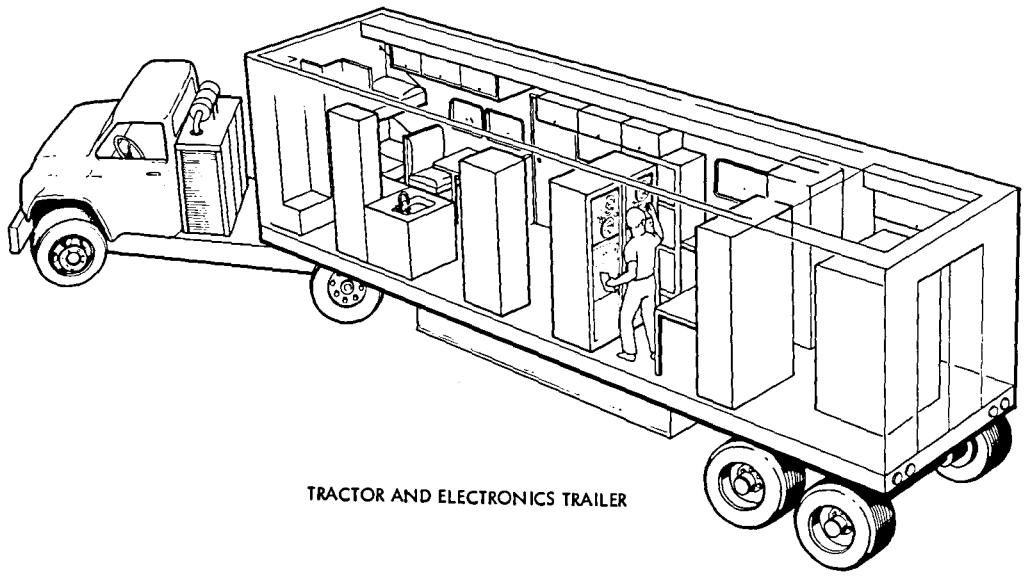

TRACTOR AND ELECTRONICS TRAILER

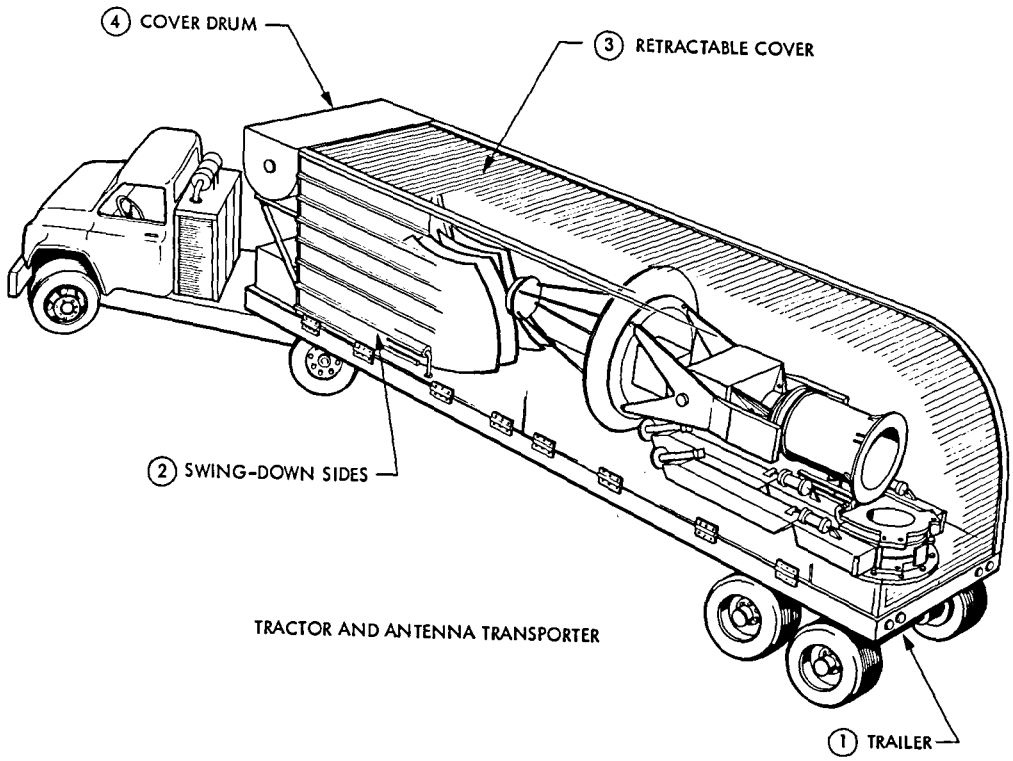

TRACTOR AND ANTENNA TRANSPORTER

Fig. 9. General arrangement, antenna/facilities subsystem

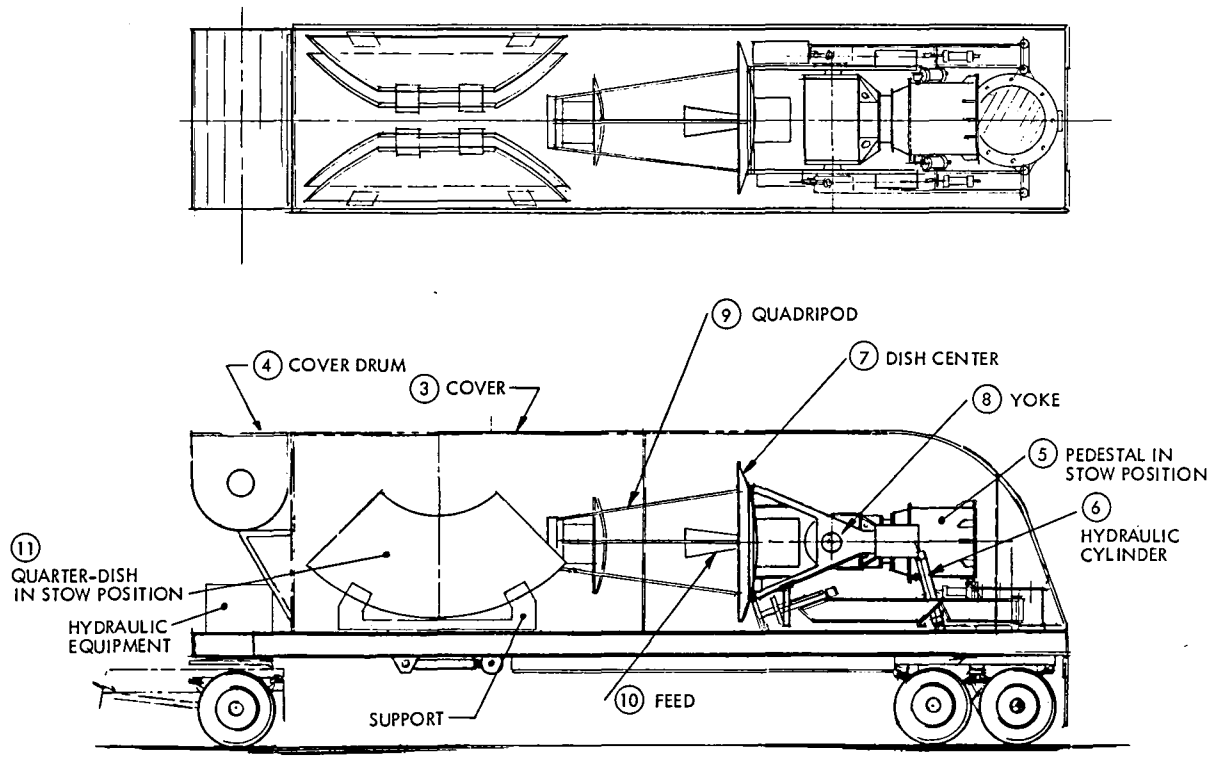

Fig. 10. Antenna transporter

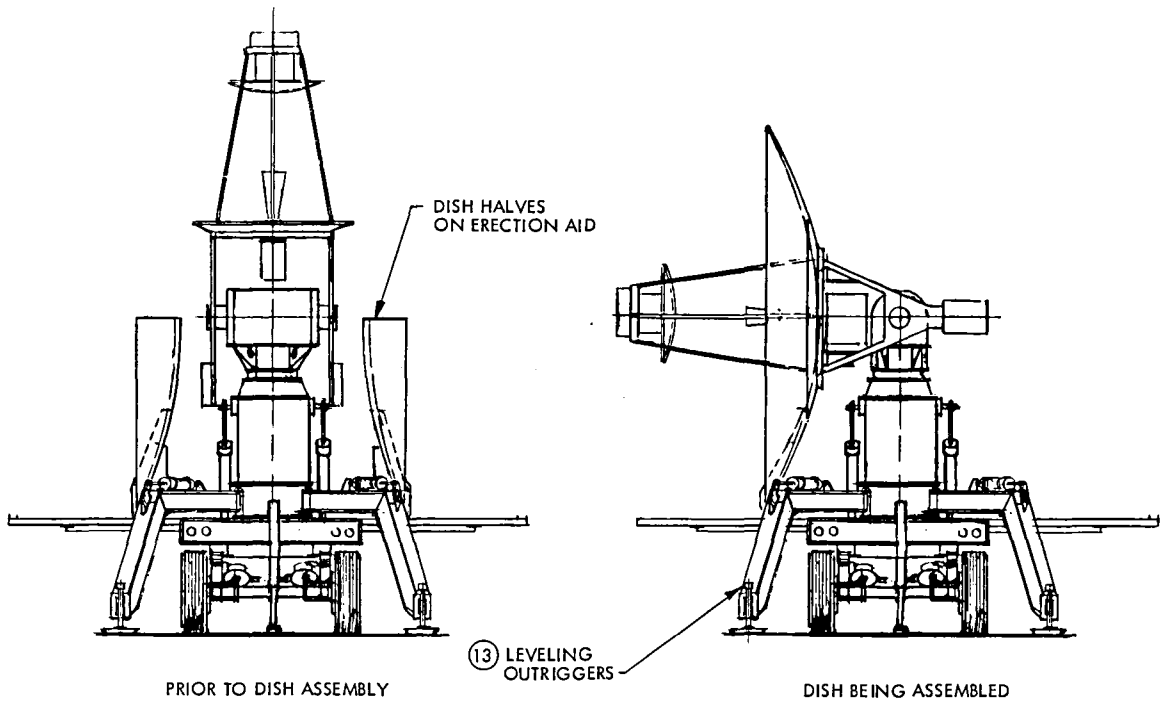

Fig. 11. Antenna transporter

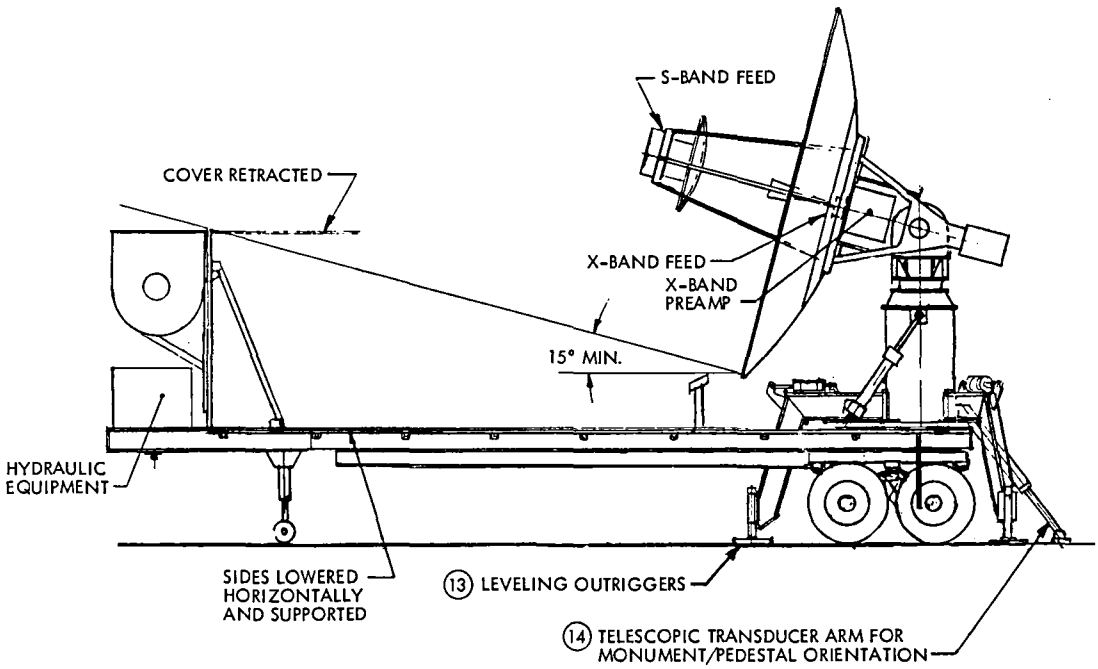

Fig. 12. Antenna transporter, operating mode

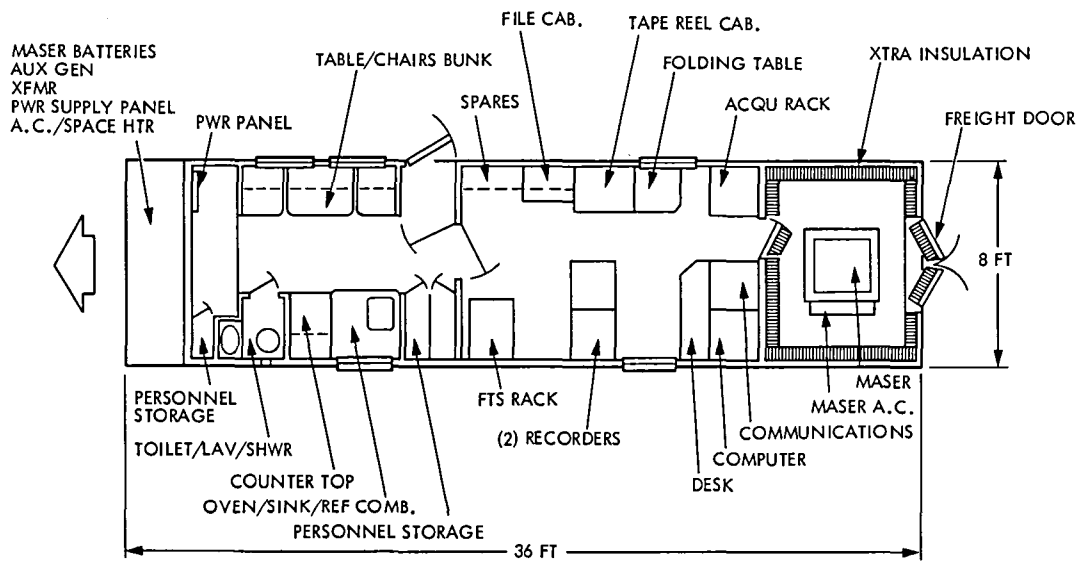

Fig. 13. ORION mobile station, electronics trailer

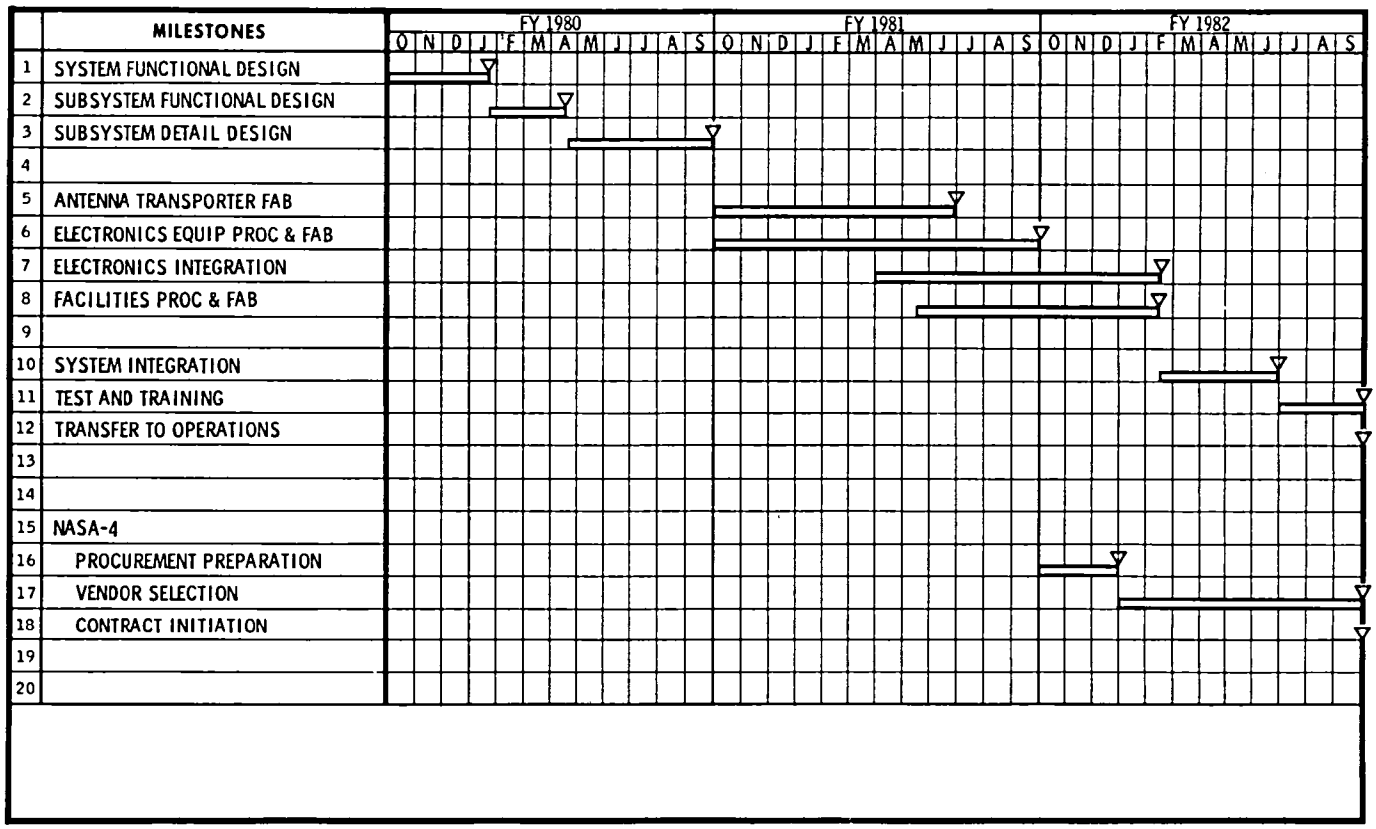

Fig. 14. ORION master schedule

Appendix
Signal-to-Noise Ratio

The signal-to-noise ratio (SNR) is defined as the ratio of the correlated fringe amplitude to RMS noise. For the case of two-level digitization, as used in the MK-III data acquisition system, the SNR at peak amplitude in a given channel is given by:

$$SNR_P = A \frac{1}{\sqrt{2}} \frac{2}{\pi} \gamma_v \sqrt{\frac{T_{A,1}\, T_{A,2} 2BT}{T_{S,1}\, T_{S,2}}} \qquad (1)$$

where

A = 0.8 (this conservatively accounts for unknown losses due to imperfect filter responses, unequal bandpass centering, etc.)

$1/\sqrt{2}$ = this factor accounts for heterodyning of the fringe phase in the correlator (lobe rotator)

$2/\pi$ = this factor accounts for loss due to two-level digitizing

γ_v = fraction of the correlated flux density out of the total source flux density

$T_{A,1}, T_{A,2}$ = antenna temperatures, K

$T_{S,1}, T_{S,2}$ = system noise temperatures, K

B = channel bandwidth, Hz

T = integration period, sec

Equation (1) is the SNR for a single correlation function at the delay lag near the correlation peak. In actual practice, energy from all lags within the main correlation lobe and nearby sidelobes is utilized, resulting in a $\sqrt{2}$ increase in a signal level. The antenna temperature is given by:

$$T_A = \frac{10^{-26} S}{2k} \left(\frac{\pi}{4} D^2\right) e \quad \text{(K)} \qquad (2)$$

where

S = total source flux density, jansky

k = Boltzman's constant (1.38×10^{-23} joule/deg)

e = antenna efficiency

D = antenna diameter, m

The factor of 2 in the denominator accounts for the fact that only single polarization of the power is received. With the inclusion of the factor and Eq. (2), we obtain an expression for the SNR per channel:

$$SNR_{ch} \doteq 2.05 \times 10^{-4} (\gamma_v S) D_1 D_2 \sqrt{\frac{e_1\, e_2\, BT}{T_{S,1}\, T_{S,2}}} \qquad (3)$$

The SNR/channel defined above is not to be confused with system SNR. With coherent addition of channels the system SNR available for detection is approximately equal to the above expression times N_{ch}, which is the number of channels coherently combined. However, for the ORION system, it is not the detection threshold that sets the lower limit on SNR, but the maximum allowed system-noise error in bandwidth synthesis (BWS) delay. If SNR_{ch} is approximately the same for all channels, the system-noise error in BWS delay is given by:

$$\sigma_\tau \approx \frac{1}{2\pi\, SNR_{ch} * \sqrt{\sum_k (f_k - \bar{f})^2}} \qquad (4)$$

where f_k represents the channel frequencies and f is the average of those frequencies.

The SNR lower limit arising from this expression can be approximately computed on the basis of the following assumptions. It is to be emphasized that the assumed quantities are not design goals but are set equal to "boundary values" in order to allow computation of a lower limit on SNR. First, assume that the maximum system-noise error in baseline length will not be allowed to exceed 20 percent of the total error budget of 2 cm. Second, for channel placement, assume the extreme configuration of seven channels at each edge of the 400-MHz passband at X-band. Under these assumptions, the minimum allowed channel SNR will be seven. If one places an even tighter requirement on system-noise error or assumes less extreme channel placement, the lower limit on channel SNR will be even greater. Thus, the ORION system will require channel SNR's of seven or greater. At this level, system SNR will be far greater than the detection threshold and detection will present no limitations.

The reader is referred to Ref. 5 for a detailed analysis of the SNR and other error sources involved in the ORION design. Also, Ref. 8 is an excellent bibliography of articles relating to VLBI.

References

1. "Execution Phase, Product Plan for Crustal Dynamics," Goddard Space Flight Center, Greenbelt, Md., May 1980.

2. Hurley, P. M., "The Confirmation of Continental Drift," *Scientific American,* April 1968, pp. 56-57.

3. Anderson, D. L., and Whitcomb, J. H., "Time-Dependent Seismology," *J. Geophys. Res.*, 80, 1975, pp. 1497-1503.

4. Niell, A. E., et al., "Comparison of a Radiointerferometric Differential Baseline Measurement with Conventional Geodesy." *Techtonophysics*, 52, 1979, pp. 49-58.

5. Wu, S. C., "Error Estimation for ORION Baseline Vector Determination," in *TDA Progress Report 42-57*, Jet Propulsion Laboratory, Pasadena, Calif., June 1980.

6. Wu, S. C., "ORION S-Band Data Acquisition for S-X Calibration," in *TDA Progress Report 42-59*, Jet Propulsion Laboratory, Pasadena, Calif., October 1980, pp. 33-36.

7. "MK-III VLBI System Documentation," Haystack Radio Observatory, Mass., May 20, 1980.

8. "An Extensive Bibliography on Long Baseline Interferometry," in *DSN Progress Report 42-46*, Jet Propulsion Laboratory, Pasadena, Calif., Aug. 15, 1978.

Life-Cycle Cost Analysis Task Summary

M. McKenzie
Telecommunications Science and Engineering Division

The DSN life-cycle cost (LCC) analysis methodology has been completed. This article summarizes the LCC analysis methodology goals and objectives, the issues covered by the methodology, and its expected use and long-range implications.

I. Introduction

Development and implementation of the DSN life-cycle cost (LCC) analysis methodology has been completed. Policy, standards, guidelines, and procedures for performing LCC analysis are stated in Ref. 1, while background information and general guidance are supplied by the TDA document noted in Ref. 2.

The following is a summary of methodology goals and objectives, topics covered in the above documents, and expected use and implications of the methodology.

II. Methodology Goals and Objectives

Motivation for an LCC analysis methodology arose from the following conditions:

(1) The level of requirements levied on the DSN, relative to the budget, was greater than in the past.

(2) The probable cost of systems over their full lifetimes was often not available at the time of major planning decisions.

(3) NASA Office of Space Tracking and Data Systems needed stronger and stronger justification of budget items to obtain concurrence within NASA and the rest of the government.

(4) The cost of some items such as energy were increasing at a rate greater than the general inflation rate, and there was no mechanism by which to consider these relationships during the design phase.

(5) A technique, called LCC analysis, was developed by industry and the government that was capable of deriving the estimated cost of systems over their full lifetimes.

Thus, development of a DSN LCC analysis methodology was proposed. The goals of implementing and supporting the methodology were to minimize total future costs of existing and proposed DSN systems while still supplying required services, and to factor life-cycle cost predictions into decisions regarding the services provided.

The attending objectives were therefore as follows:

(1) To supply the methodology and motivation by which planning and design decisions:

  (a) become sensitive to estimated life-cycle costs.

  (b) consider cost relationships between components of a system.

(2) To provide a quantitative life-cycle cost analysis tool to help managers and engineers in planning and design decisions.

(3) To improve budgeting capabilities for the DSN as a whole.

III. Subjects Addressed

To meet the above goals and objectives, the two aforementioned documents (Refs. 1 and 2) were produced. Major topics covered in the documents are listed below:

(1) Definition of "life-cycle cost" and other terms.

(2) Criteria prescribing when an LCC analysis must be performed.

(3) Conditions under which an LCC calculation would be useful, though it is not required.

(4) Activities, roles, and responsibilities.

(5) Information needed before the analysis begins.

(6) Planning the LCC analysis.

(7) Gathering cost estimates.

(8) Calculation of the estimated life-cycle cost.

(9) Interpretation of the LCC.

(10) Reporting results.

(11) Examples.

IV. Use and Implications

The two LCC documents, together with the training package available from TDA Engineering, enables managers and engineers to perform and use LCC analysis. Consideration is also being given to follow-on tasks that might further enhance the effectiveness of LCC analysis within the DSN. Among these tasks are the following:

(1) Evaluation of the methodology in practice.

(2) Augmentation of existing cost data bases.

(3) Compilation of existing cost models and cost estimation techniques.

(4) Additional cost model development.

There are long-range implications of using life-cycle cost analysis to support planning in the DSN. Performance of cost trade-offs will become standard. The objective of minimum life-cycle cost will impact capabilities, specifications, and designs selected, and thus, the overall cost effectiveness of the DSN will continue to improve. Lastly, formal information exchange and feedback between implementing and operating organizations, as well as between levels of implementation, will increase.

References

1. *Life-Cycle Cost Analysis*, TDA Standard Practice 810-23. Jet Propulsion Laboratory, Pasadena, Calif., Sept. 15, 1980 (JPL internal document).

2. *DSN Life-Cycle Cost Analysis Handbook*, TDA Document 890-119. Jet Propulsion Laboratory, Pasadena, Calif., Oct. 1, 1980 (JPL internal document).

Voyager Mission Support (I)

N. Fanelli and H. E. Nance
Control Center Operations Section

This article is a continuation of the Deep Space Network report on Tracking and Data Acquisition for Project Voyager, covering the period from May through July 1980.

I. Introduction

Both Voyager 1 and 2 continue in the Jupiter-Saturn Cruise Phase of the mission. Voyager 1 is scheduled to begin the Observation Phase on 22 August 1980 for the Saturn Encounter.

II. DSN Support

During the reporting period, the DSN continued to support routine and special activities with both spacecraft. Concurrently, implementation was being completed at the stations for the capabilities that would be required for the Saturn Encounter. Two of these capabilities, Real-Time Combining and Radio Science, are major additions to the stations and are described in detail.

III. Real-Time Combining and Antenna Arraying

During the Saturn Near Encounter Phase of the mission, an antenna arraying and data combining configuration at each DSN 64/34-m complex will be used to enhance the 29.8 or 44.8 kbps telemetry data. The real-time combined telemetry signal-to-noise ratio (SNR) improvement is dependent upon the SNR difference between the two supporting stations. Telemetry shall use the X-band TWTA at high power. The data rate strategy shall be based on the maximum data rate availability as shown in Fig. 1 at the 95 percent, 90 percent, and 80 percent confidence levels. The contrasting 64-m coverage for the same confidence ranges are shown in Fig. 2. The strategy specifically is based on the 90 percent confidence level for real-time data and the double digital tape recorder (DTR) playback of critical data and on the 95 percent confidence level for single DTR playback of noncritical data or for the real-time transmission of OPNAV frames. For the above strategy, the maximum number of hours available each day for the 44.8, 29.9, 19.2 and 7.2 kbps data rates are listed in Table 1.

The antenna arraying (real-time combining baseband signals) to be used for the Saturn Encounter is an upgrade of the previous subsystems. On 21 September 1974, the Goldstone stations were arrayed to improve the telemetry data received during the Mariner 73 Mercury Encounter. The current effort began in FY 78 with the objective of developing a permanent Real-Time Combiner (RTC) installation for the 64/34-m network. A prototype unit became available in November 1978 and was successfully used for the Voyager 2 Jupiter Encounter and for the Pioneer 11 Saturn Encounter. This prototype was the basis for the system presently installed at the three Deep Space Communication Complexes (DSCC). (See Ref. 1 for more detail.)

Figure 3 shows the RTC block diagram. Inputs to the RTC are from the telemetry receivers of the two supporting stations. The inputs are baseband data consisting of telemetry subcarrier plus data. In the RTC, the two signals are combined (added). Since the noise power is random in nature, the increase in signal power is greater than the noise power and results in an increase in SNR.

The baseband signals enter the RTC through low-pass filters. The signals then pass through AGC circuitry, which maintains equal amplitudes for both signals and sets the level for input to the Analog-to-Digital (A-to-D) converters. The A-to-D 10 MHz variable phase input clock is used to quantify the analog inputs into ten million samples per second. The phase variations of the input clocks, as controlled by the Central Processing Unit (CPU), act as a push-pull circuit so that if the phase of the 64-m signal input clock is advanced, and the 34-m signal input clock phase is delayed by an equal amount. The signals are then fed to the First-In-First-Out (FIFO) memory. The same input clock used by A to D is used to strobe the data into the FIFO. The FIFO inputs are strobed by the output clock, which is coherent to the input clock, but whose phase is fixed. The two signals are phase locked through use of the In-Phase and Quadrature Correlator (IP and Q Corr).

The 64-m signal IP and Q Corr has inputs from the 64-m FIFO and the 34-m FIFO. The correlation of the two signals is the average of their product. The IP correlator allows the CPU to adjust total phase tracking loop gain for optimum performance.

The Q correlator produces a count proportional to relative signal delay. This information is fed to the CPU, which creates an error signal used to correct the push-pull input clock phase. The signals are then routed to the Digital-to-Analog (D-to-A) converters, which are synchronized by the output clock, and then through low-pass filters to the summing amplifier (Σ amp). The input resistor values of the summing amplifier are selected so that the 34-m signal is six-tenths as great as the 64-m signal. The signals are, therefore, in phase and correctly proportioned for real-time combining. The CPU is interfaced via the Star Switch Controller to the Data System Terminal Assembly (DST) for control input and receipt of error messages. The 34-m TP and Q Corr is redundant and not used. These correlators may be hand switched in cases of anomalous operation.

Several improvements have been made to the antenna array subsystem, which were not available during Jupiter Encounter. Receiver lock and Automatic Gain Control (AGC) indications from the 34-m DSSs are now provided to the 64-m DSSs. These indications provide the 64-m DSSs with partial status of the 34-m station, and in the event of a problem, the 64-m DSS would be informed in real-time via these indicators.

The Block IV receiver telemetry detectors have been modified to reduce degradation, thus providing four possible paths for the 64-m output to the RTC. A procedural means of measuring the RF path delay has been formulated. The time required for RTC Pre-Track Preparation (PTP) has been reduced by deletion of some precal items and the streamlining of others. Operational equipment provides additional control statements and options. For example, the new RTC is able to be restarted without being reinitialized and parameters can be changed without reinitialization.

The RTC installation was completed at the Goldstone DSCC in mid-May 1980. Antenna arraying and RTC training and operational evaluation was started on 19 May. This training-evaluation consisted of a series of periods, during which both DSS 12 and 14 were scheduled simultaneously to track either Voyager 1 or 2.

The test activity allowed the station personnel to operate the RTC as they desired for the greater part of the scheduled period, but required them to maintain a standard configuration for a specified period of time. Under this concept, the noncombined telemetry data was transmitted to the project to meet the DSN commitment. The combined telemetry string was displayed via the monitor stream so that the advisors at JPL could monitor the station activity. During the standard configuration period, the symbol SNR was recorded for both the 64-m telemetry string and the 34-m telemetry string, and at both 29.8 and 44.8 kbps. This recorded data was the basis for operational evaluation.

It was generally found that the RTC operated within the specifications. However, some problems were experienced with the FIFO boards since some components were prone to fail. Likewise, it was found that the condition of the entire telemetry string, including all components, greatly influences the combiner performance. In order to measure the combiner performance, it is necessary to know the performance of the telemetry string to ±0.1 dB. This requires each component to be calibrated and within specs to ±0.1 dB. The SNR spread between the 34-m and 64-m stations was found to be greater than anticipated and part of the discrepancy is probably due to the telemetry string performance.

Eight array-RTC periods were conducted with DSS 12/14 prior to completion of the RTC installation at the overseas complexes. On 23 and 24 June, the first arraying period was scheduled for both DSS 42/43 and DSS 61/63. The same training-evaluation philosophy was observed during the subsequent tracking periods for these stations. The same findings

and evaluation were made of the data from these DSCC as were made of the Goldstone complex. Variances were observed in the SNR spread between the stations and, in some cases, the spread was so great as to invalidate any combiner gain. Likewise, telemetry strings had problems in being locked up to the data, indicating marginal operation of some components.

The final conclusion from this testing is that a carefully calibrated, tuned, and stable telemetry string and RTC is a prerequisite to successful encounter operation. Training passes will continue to be scheduled to allow the stations to be properly prepared for critical encounter operation with this configuration.

IV. Radio Science

Radio Science is defined as the acquisition and extraction of information from spacecraft transmitted signals, which have been directly affected by passage through:

(1) Planetary neutral atmospheres

(2) Planetary ionospheres

(3) Planetary magnetospheres

(4) Solar corona (plasma)

(5) Gravitation (relativity)

(6) Planetary rings (particles)

and indirectly affected by forces acting upon the spacecraft:

(1) Gravity waves

(2) Gravitational fields

(3) Planetary atmospheric winds

(4) Solar radiation

The experimentation to be carried out during each Saturn Encounter by Voyager that requires the DSN Radio Science capability are:

(1) Voyager 1

(a) Solar Corona

(b) General Relativity Time Delay Measurement

(c) Saturn System Celestial Mechanics

(d) Titan Occultation

(e) Rhea Mass Determination

(f) Saturn Occultation

(g) Saturn Ring Occultation

(h) Saturn Ring Scatter

(2) Voyager 2

(a) Saturn System Celestial Mechanics

(b) Saturn Occultation

(c) Saturn Ring Scatter

It is anticipated that the activities listed for Voyager 2 will expand as the results of the Voyager 1 Encounter are evaluated and as the Voyager 2 Encounter approaches.

A brief description of the DSN support requirement for each of these experiments follows.

A. Saturn System Celestial Mechanics

This experiment will require one-way (or TWNC) and two-way (or three-way) tracking in order to optimize data-taking for the various Celestial Mechanics investigations. Ground events will include normal tracking and ranging with selected doppler sample rates. Doppler and range data will be delivered to the project on tracking IDRs.

B. Rhea Mass Determination

The DSN will acquire two-way tracking data near Rhea encounter to determine the mass of Rhea to within ±5 percent. A ten sample-per-second doppler rate will also be required. Data will be delivered on tracking IDRs.

C. Radio Occultation of the Solar Corona

This experiment will require alternating periods of S-X differential ranging (two-way) and scintillation (one-way or TWNC) for Sun-Earth Probe (SEP) angles of less than 15 degrees. The DSN will provide open- and closed-loop dual frequency one-way doppler and ODA data during TWNC-ON periods. Closed-loop dual frequency ranging will be required during TWNC-OFF periods. Tracking IDRs will provide doppler and range data, with ODA data being delivered on ODA DODRs.

D. General Relativity Time Delay Measurement

The acquisition of ranging data for 15 hours before and after minimum SEP angle will be required. This will enable the measurement of the General-Relativistic Time Delay induced in the communication link by the sun's gravity field. The DSN will provide continuous ranging during the period of interest. Data will be delivered on tracking IDRs.

E. Titan Radio Occultation

The requirements here are to perform ingress and egress measurements at fixed high-gain antenna (HGA) offset angles with respect to Earth. The ingress is optimized for ionosphere and upper atmosphere studies, and the egress will be for measurements as deep as several atmospheres. The DSN will provide closed-loop doppler data at ten samples per second, open-loop medium-band recording, and use of special frequency predicts. Tracking IDRs will provide doppler data to project and the open-loop data will be delivered on ODA DODRs.

F. Saturn Radio Occultation

A limb-tracking maneuver will continuously be performed throughout Earth occultation except for a 20-minute period where maneuvering will cease in order to accommodate the ultraviolet spectrometer sun-occultation exit. The DSN will support with one sample-per-second closed-loop doppler data, open-loop narrow bandwidth recording, and special frequency predicts. Also, a station transfer from DSS 43 to DSS 63 will occur during occultation. Doppler data will be supplied to project via IDRs, and the open-loop data via ODA DODRs.

G. Radio Occultation of Saturn's Rings

This experiment will occur with the High-Gain Antenna (HGA) pointed at Earth from Saturn Earth Occultation Exit (EOE) through "F" ring EOE. The DSN will provide one sample-per-second closed-loop doppler data, open-loop medium bandwidth recording, and special frequency predicts. Doppler data will be supplied via tracking IDRs, and open-loop data will be delivered via medium bandwidth computer compatible tapes produced at CTA 21 from DRA recordings.

H. Radio Scattering by Saturn's Rings

This experiment will be accomplished by obtaining radio scattering data by tracking an area of the "A" ring with the HGA for approximately 100 minutes after "F" ring EOE and for approximately 30 minutes during Earth occultation. Again, the DSN will provide one-per-second closed-loop doppler data, open-loop medium bandwidth recording, and also special frequency predicts. Doppler data will be supplied to project via tracking IDRs, and open-loop data will be via medium bandwidth computer-compatible tapes from CTA 21.

The key characteristics of the DSN Radio Science System to be used to support these experiments are:

(1) Acquires left and right circularly polarized spacecraft signals at S- and X-band frequencies.

(2) Digitizes and bandwidth-reduces up to four open-loop receiver channels simultaneously by means of an automatically controlled programmed oscillator.

(3) Digitizes and records wide bandwidth open-loop receiver output.

(4) Generates programmed oscillator frequency predictions that incorporate effects due to planetary atmospheres.

(5) Performs real-time system performance monitoring and provides system performance data in real-time to the project.

(6) Transmits quick look radio science data from Deep Space Stations (DSS) to Network Operations Control Center (NOCC) via High-Speed Data Line (HSDL).

(7) Performs non-real-time bandwidth reduction of wide bandwidth radio science data.

(8) Provides radio science data to the project via computer-compatible magnetic tape.

The following paragraphs describe these capabilities.

1. Wide bandwidth recording and subsequent non-real-time bandwidth reduction. Spacecraft signals are acquired by the wide bandwidth (2 MHz) multi-mission open-loop receiver (MMR). These signals are digitized and recorded on a high-rate, high-precision digital recorder (the Digital Recording Assembly, or DRA). The DRA recordings are shipped via Network Information Control (NIC) to CTA 21, where the (radio science) data bandwidth is processed and reduced by the NWK Radio Science Subsystem (WRS). The digitized, bandwidth-reduced data are supplied to the project on computer compatible magnetic tape.

2. Real-time bandwidth reduction (narrow bandwidth). Real-time bandwidth reduction (narrow bandwidth) is initiated when a spacecraft state vector is supplied to the "POEAS" software program. The output of the POEAS program is a Polynomial Coefficient Tape (PCT), which includes the frequency-independent, planetary atmosphere-refracted spacecraft observables. The PCT is input to the Network Control (NC) Tracking Subsystem software program "PREDIK." The output of PREDIK consists of radio science formatted downlink frequency predictions, which are transmitted to the appropriate 64-m DSS via high-speed data line. The predictions are received by the Occultation Data Assembly (ODA) of the DSS Radio Science Subsystem (DRS). The ODA processes the predictions and provides them to the Programmed Oscillator Control Assembly (POCA). The POCA drives a Programmed Oscillator (PO), the output of which is

multiplied up to S-band and X-band frequencies in a two-channel open-loop receiver (either the Block III OLR at DSS 43, or the new narrow bandwidth MMR at DSS 14 and 63) and mixed with the two (S- and X-band) spacecraft downlinks. The open-loop receiver filters the baseband product(s) of the mixing, and provides the filtered signals to the ODA. The baseband signals are digitized and recorded on magnetic tape along with the counted output of the PO. During actual operations, the ODA-recorded signals are validated (singly) via usage of the Signal Spectrum Indicator (SSI). After data acquisition is complete, the ODA formats the data for WBDL transmission to the GCF Data Records Subsystem (GDR). The real-time bandwidth-reduced data are supplied on computer-compatible tape to the appropriate flight project.

3. Real-time bandwidth reduction (medium bandwidth). Generation of radio science predictions and subsequent handling by the ODA, POCA, and PO are the same as described in the preceding paragraphs. In this case, however, four spacecraft signals (permutations of LCP and RCP, and S- and X-band) are acquired by the four-channel medium bandwidth MMR, and mixed with appropriate PO frequencies. The mixed product(s) are filtered and provided to the DRS. Within the DRS, the signals are digitized and recorded on the DRA. During data acquisition, the recorded signals are verified (singly) by the SSI. Subsequent to data acquisition, the DRA-recorded data and the various PO data recorded on computer-compatible tape by the ODA are shipped to the NWK Radio Science Subsystem (WRS). The DRA-recorded data are processed and rewritten on computer-compatible tape by the WRS and provided to the project.

4. Real-time system performance validation. Digital spectrum (radio science) data from the Spectral Signal Indicator (SSI) are provided to the Occultation Data Assembly (ODA), where they are formatted for WBDL transmission to the NOCC. The digital spectrum data are routed to the NC Radio Science Subsystem (NRS), which processes the data to form a replica of the original (SSI) spectral display. The NC Display Subsystem (NDS) displays the spectra in the Network Operations Control Area (NOCA) and, additionally, provides the displays to the appropriate project area(s) for viewing by radio science experimenters. Additionally, the NRS provides displays of the DRS status and configuration.

a. Predicts. The open-loop receiver POCA predicts will be generated at JPL and transmitted to the Occultation Data Assembly (ODA), where the predicts will be stored on disk and used to drive the S/X-band open-loop receiver POCA. Time of Earth occultation may vary by several seconds with no predict bias changes required, but if the timing error is too large, time or frequency deltas will be provided.

b. Open-loop recording.

(1) The DODR recording will begin prior to the start of occultation. It is necessary to collect baseline data prior to and after occultation. The Project SOE will provide the time to turn on the ODA recording, and will also provide the turn off time. Approximately four hours of recording are anticipated. The ODA narrow band or medium band will be prime for occultation, dependent upon special requirements.

(2) ODA narrow band open-loop backup recording will be provided by the medium band or wide-band (150/300 kHz) Open-Loop Receiver (OLR) and its Digital Recorder Assembly (DRA) (see Fig. 4).

(3) Voyager will not make use of the HSDL to get open-loop ODA data to JPL, except for preliminary quick-look data, because the number of station hours to replay data via HSDL is prohibitive. The prime method of getting data to JPL is to ship the open-loop DODRs to JPL.

(4) DODR recording for Voyager will use six DODR tapes per hour, five DODRs per hour for the narrow band MMR/ODA subsystem, and approximately one DODR per hour for the medium band or wide band OLR/DRA subsystem.

(5) New or once used digital tape, at least 2300 feet in length for ODA and 9,200 feet in length for DRA, must be used for recording open loop data, to insure optimum data return.

c. Spectral Signal Indicator. Station personnel will use the Spectral Signal Indicator (SSI) to verify that occultation data are actually being recorded onto the DODR. The SSI will provide recording status for the narrow band, medium band, and wide band recording subsystems. The narrow and medium bands are used for the prime data and will require more monitoring by the DSS operator than the wide band subsystems. The DSS will report signal status to the NOC at least every 15 minutes, more often if requested, if the signal disappears or is marginal.

Testing of the Radio Science System, particularly the recording of open-loop receiver data, is relatively easy as compared to real-time combining because any spacecraft X-band data can be used. The stations have been making such recordings for training and testing purposes. In addition, two ORTs have been conducted. The first ORT was a preliminary training exercise since much of the equipment had not been installed at the stations. ORT-2 was likewise considered unsuccessful because the SSI, PPM, backup Multi-Mission Receiver

(MMR) at DSS 63 and MDA OP-E software were not available (not installed or not functioning) for test support.

Mission Configuration Tests (MCTs) were conducted by the DSN as the new equipment was installed. A successful ORT was conducted with DSS 43 on 24 July 1980; however, the DSS 63 portion was canceled due to X-band Maser problems at the station. ORT-3 is scheduled to be conducted concurrently with the Near Encounter Test to be conducted in August 1980.

Reference

1. Simon, N. K., and Hoynes, C., "Preliminary Telemetry Operations Experience With the Real-Time Combiner: 1 November 1978 to 1 November 1979," in *The Deep Space Network Progress Report 42-55*, pp. 90-96, Jet Propulsion Laboratory, Pasadena, Calif., February 15, 1980.

Table 1. Maximum number of hours per day of telecom capability, 64/34-m array, during VGR-1 NE

44.8 kbps 90%	29.9 kbps 95%	29.9 kbps 90%	19.2 kbps 90%	7.2 kbps 90%
15.1	18.1	22.1	23.6	24

7.2 kbps @ 90% - GS-2 (rec), GS-4 (rec), IM-2 (rec), GS-3, OC-1
19.2 kbps @ 90% - IM-12, plus all of the above
29.9 kbps @ 90% - IM-9, IM-11, plus all of the above
29.9 kbps @ 95% - PB-3, plus all of the above
44.8 kbps @ 90% - IM-7, PB-2, plus all of the above

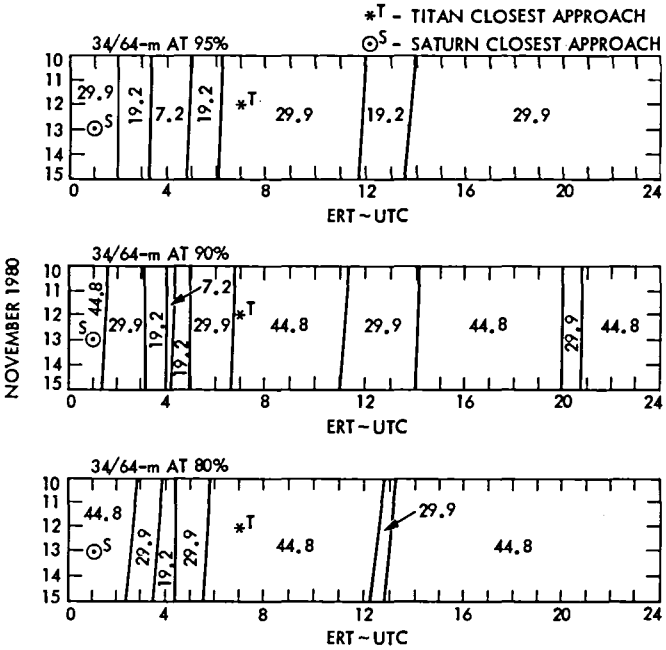

Fig. 1. VGR-1 NE 34/64-m telecom performance maximum kbps envelope

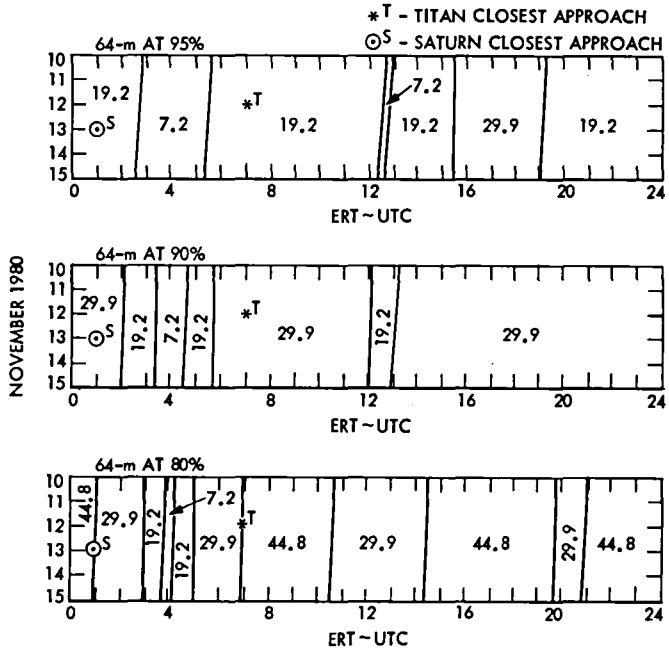

Fig. 2. VGR-1 NE 64-m telecom performance maximum kbps envelope

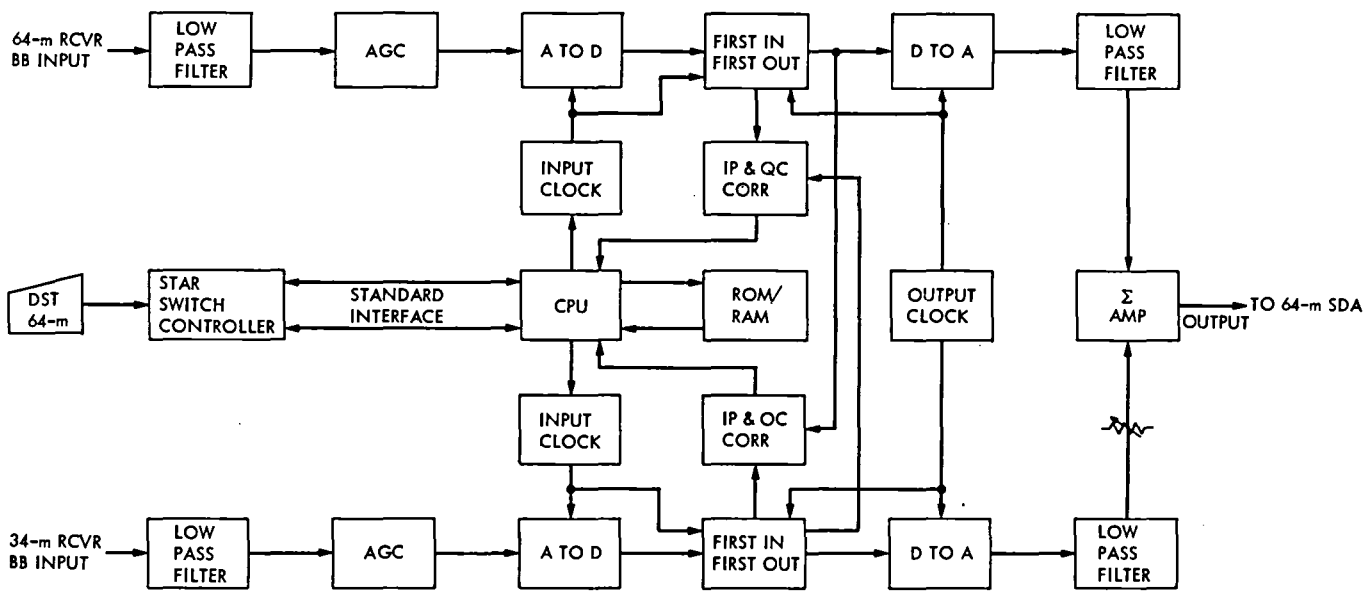

Fig. 3. Real-time combiner configuration

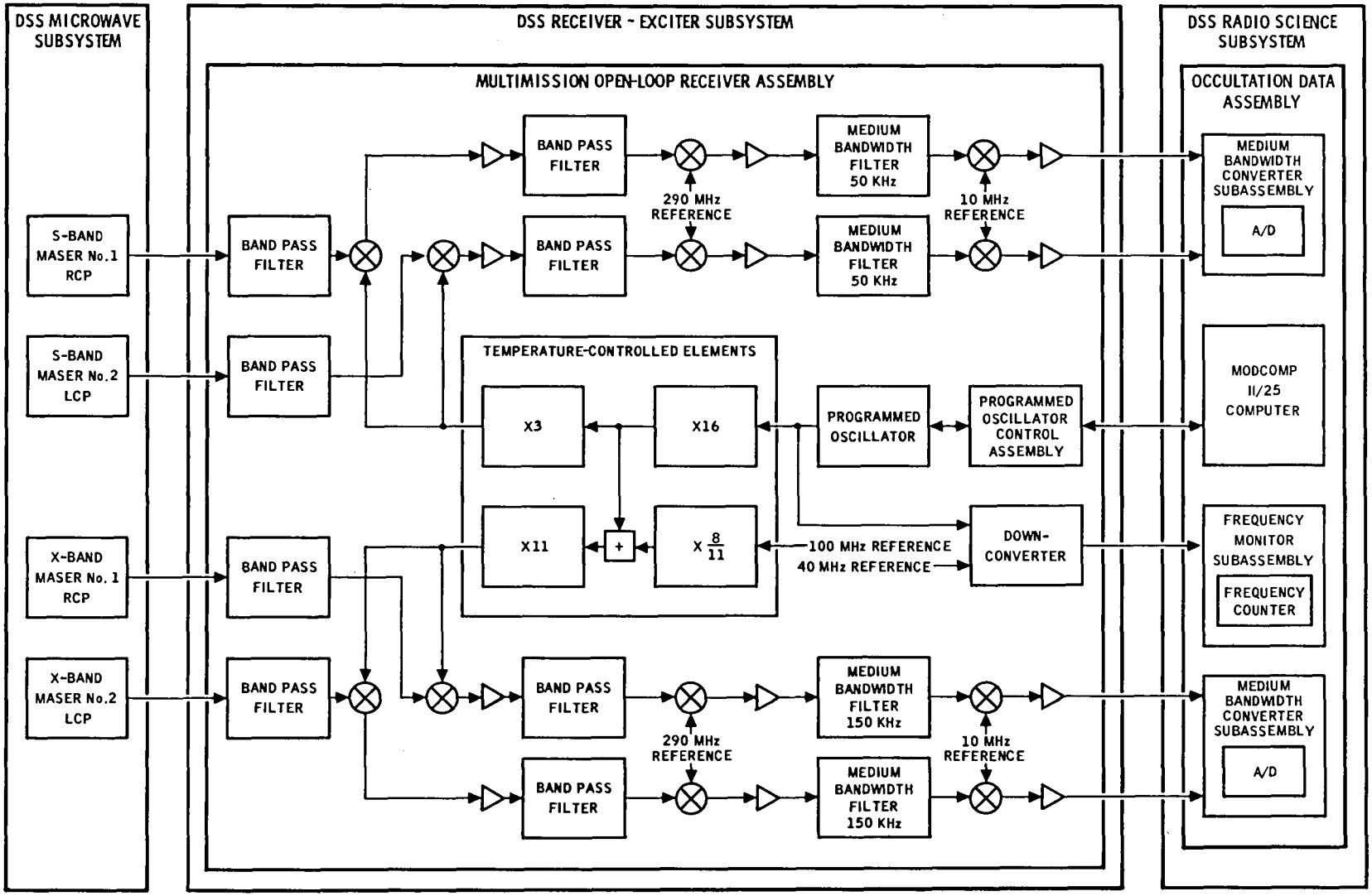

Fig. 4. Voyager open-loop receiver configuration

Voyager Mission Support (II)

N. Fanelli and H. E. Nance
Deep Space Network Operations Section

This is a continuation of the Deep Space Network report on Tracking and Data Acquisition for Voyager Project. This article covers the period August through October 1980.

I. Introduction

Voyager 1 has entered the Encounter Phase of the mission, while Voyager 2 continues in the Jupiter-Saturn Cruise Phase.

The Saturn Encounter activities are divided into five phases based on the field of view of the narrow-angle camera in relation to the distance to the planet. The five phases are Observatory, Far Encounter 1, Far Encounter 2, Near Encounter, and Post Encounter.

The Observatory Phase for Voyager 1 started on 22 August and ended on 24 October, when the Far Encounter 1 (FE1) Phase started. The FE1 Phase will not be concluded until 2 November 1980.

II. DSN Support

A. Near Encounter Test

Starting in July 1980, the Voyager Mission Support Team, including all support facilities, entered the Test and Training period for the forthcoming encounter. The DSN performed the required System Performance Tests and Operational Verification Tests necessary to check out and train operations personnel on the new capabilities as implemented. This training activity was culminated in a Near Encounter Test on 19 and 20 August 1980. The Near Encounter Test (NET) was a simulation of the 18-hour period of closest approach to Saturn. During this test both the 34-meter and 64-meter Deep Space Stations were configured and supported the Project in the same manner as will be required during the actual closest approach. During the NET, a Radio Science Operational Readiness Test (ORT No. 3) was conducted with DSSs 43 and 63. The period tested corresponds to the one required to support the closest approach and occultation periods.

Although the support provided by the Deep Space Network was considered satisfactory overall, several areas were identified for which additional attention was required. It was found that generally the arrayed antenna performance was lower than expected. Problems causing this were suspected to be telemetry string degradation due to improper calibration, an adverse weather condition affecting the X-band data, and variations between the 34-meter and 64-meter station symbol signal-to-noise ratio. Special emphasis was given to improving the array performance for the movie phase that was included in the observatory phase.

Problems were likewise encountered during the ORT. Occultation Data Assembly halts were experienced, which caused some data loss. Appropriate calibration on the antenna at DSS 63 could not be performed one time due to an

unusually heavy rain storm during the pretrack preparation period. Although the Spectral Signal Indicator (SSI) and Precision Signal Power Monitor (PPM) data was generally good, problems were experienced in displaying the data at JPL. These were determined to be procedural problems that had not been fully resolved due to the newness of the capability. Additional voice communication had been provided for the radio science support, which was improperly configured and caused operational confusion.

Other minor operational problems, procedural and equipment failures, were experienced that provided insight into the events that could occur during the actual closest approach. The test results provided a valuable insight into the areas for improvement and correction. Actions have been taken to accomplish this and internal testing has validated the measures taken.

B. Observatory Phase

1. Movie phase – solar conjunction. A time-lapse movie was compiled from photographs taken during the period 12 to 14 September 1980. Photographs were taken every 4.8 minutes during four Saturn rotations. The photographs were transmitted in either real-time or during a playback period over DSS 14. To obtain the telemetry data, including the photographs, the 34-meter and 64-meter networks were arrayed for the entire support period. Overlapping this movie activity was the solar conjunction (3 September to 6 October) when the Sun was between the Earth and spacecraft. The smaller the angle of the Sun-Earth Probe, the more hampering of the radio communications was experienced. However, the condition did allow study of the Sun as the radio signals passed through the corona. Although the "noise" was evident in some photographs, the movie requirement was met. Likewise, the solar conjunction data were collected from both Voyager 1 and Voyager 2 to complete the experiment data requirements.

2. Target maneuver. On 5 to 6 August, a target maneuver with Voyager 1 was supported by Deep Space Network. The purpose of the maneuver was to calibrate the imaging and IRIS instruments. The spacecraft was maneuvered to point at the science calibration target and several wide- and narrow-angle images plus IRIS data are recorded. Following the calibration, the scan platform was slewed to a safe position for a turn unwind. The spacecraft then maneuvered to reacquire the Sun and Canopus, and the scan platform slewed back to a neutral position. Recorded calibration data were played back on 7 August. DSSs 12, 61, and 43 were involved in the transmission of the command load, the enable file, tracking until loss of data due to the spacecraft turning, reacquisition of the spacecraft signal on return to Earth point, and receipt of the transmission of the calibration data. The sequence went as scheduled, and the spacecraft was reacquired by DSS 43 as anticipated.

3. Trajectory correction maneuver (TCM-A8). On 10 to 11 October, Voyager 1 was again maneuvered; however, this time it was to accomplish a trajectory correction. The correction was to change the trajectory so that the spacecraft would pass the Saturnian satellite Titan at a closest point of 4600 km from the surface. Without the maneuver, there was the possibility of a collision with Titan.

The spacecraft was rolled 90 degrees and then turned through a yaw of 136.7 degrees to place it in the proper position for the change in velocity vector. A "burn" of 806 seconds was used to produce a velocity delta change of 1.778 meters/second. The spacecraft was then maneuvered back to Earth point.

During this maneuver, the downlink was lost from the spacecraft after the positioning for the "burn," and reacquired after the spacecraft reposition on Earth point. This maneuver was supported by DSSs 61, 12, and 14.

To provide a small margin of additional capability, the stations were instructed to put in the bypass to the antenna film-height detector. Under normal operation when the antenna film-height detector senses a low film height, the antenna is automatically stopped. By placing the bypass "IN," the operator will manually stop the antenna if the film-height detector alarm is activated for 15 seconds or more. By using this option, false alarms are reduced, and unnecessary data loss avoided during critical data periods.

4. Array readiness. After the implementation of the Real-Time Combiner (RTC) at the 64-meter stations, and during the testing of the arraying operation, it was found that there was a variation in the actual gain achieved by a station during a series of passes. A good deal of the variation was due to the calibration of the telemetry string. Precise and consistent calibration was required to produce the desired gain over a series of passes. To assist the stations in this effort, a period of RTC and telemetry string maintenance was scheduled each week for the station to accomplish the required work.

DSSs 12 and 14 started operational support of Voyager 1 with the array configuration on 23 August 1980. The level of proficiency and improved results were evident after a few days of operation. To insure DSSs 42 and 43 and DSSs 61 and 63 crew proficiency, a series of proficiency test passes were

provided during the normal scheduled support of Voyager 1 by these stations. The gain on the arrayed data has been within the desired level for the encounter period. DSSs 42 and 43 and DSSs 61 and 63 began active support of Voyager 1 on 24 October at the start of the Far Encounter Phase.

5. Radio Science Subsystem (RSS) Operational Readiness Test-4 (ORT-4). The fourth RSS ORT-4 was conducted on 2 to 3 October 1980. The ORT was to demonstrate (1) Occultation Data Assembly (ODA) medium band width right circular polarization/left circular polarization (RCP/LCP) S- and X-band and narrow-bandwidth S- and X-band data acquisition, (2) acquisition of radio science wideband width backup data acquisition using the Digital Recorder Assembly (DRA), (3) capability of measuring and recording system temperatures in real-time, and (4) demonstrate SSI performance and utility for occultation data acquisition.

Although the ORT was conditionally successful, there were problems with the SSI equipment and the wideband backup equipment. There were misunderstandings on the calibration procedures for input and/or output levels of equipment.

To resolve these problems and to increase the proficiency in the operation and support of the RSS effort, a series of 14 OVTs were scheduled for DSSs 43 and 63. The results obtained from the OVTs in increased efficiency and effectiveness became more evident with each succeeding test. Procedures for calibration and operation of system and equipment were clarified and standardized as a product of the tests. By the end of October, the RSS problems were mainly resolved and the system operation greatly improved. ORT-5 is now scheduled for 5 to 6 November 1980 for the final validation of the system and operations for support of the closest approach and occultation experiments with Saturn and Titan.

Improvements in Galileo–Mars Navigation Using the Viking Lander

F. B. Winn, M. P. Ananda, F. T. Nicholson, and E. W. Walsh
Navigation Systems Section

When the geocentric angular separation between two spacecraft is but a few degrees, navigational advantages may be achieved by navigating one spacecraft with respect to the other. In this dual-spacecraft navigation technique, radio metric data from the two spacecraft are not treated independently, but differenced to cancel common observable modeling errors.

In the circumstance of the Galileo Spacecraft flyby of Mars, the Mars Viking Lander 1 might provide a radio beacon that could be used to navigate Galileo past Mars. The Viking Lander has been operating on the Martian surface since July 20, 1976, and is expected to continue through 1990. It is intended that the navigational delivery accuracy capability of Galileo at Mars [25 km (1σ)] is going to be met with interferometric angular measurements (VLBI) and range and range-rate measurements. Like VLBI, however, dual-spacecraft differenced range has little sensitivity to transmission media modeling errors, and to tracking-station location errors. Similarly, differenced range provides angular information about the separation between the Mars Viking Lander 1 and the Galileo Spacecraft. In covariance studies, dual-spacecraft differenced range coupled with conventional range and doppler is shown to estimate the Galileo-Mars flyby distance to better than 10 km (1σ), which is favorably comparable to the projected ΔVLBI performance. For the Galileo-Mars flyby, dual-spacecraft differenced range promises to be an excellent backup to VLBI if the Mars Viking Lander remains operational.

I. Introduction

The Galileo mission (Ref. 1) is a highly ambitious scientific project and this will be the first time an artificial satellite will be placed in an orbit around an outer planet. The major objectives of this mission are to maximize the number of flybys of the Galilean satellites and maximize the scientific return about the Jovian neighborhood. This and the constraints due to the shuttle-IUS (Interim Upper Stage) launch capability requires an interplanetary trajectory that includes a Mars flyby, which provides a needed gravity assist. Subsequent to this flyby, a propulsive maneuver is executed that places the spacecraft on a Jupiter-bound trajectory. To minimize the ΔV required for this maneuver, it is desired to pass as close to Mars as possible, consistent with planetary quarantine and spacecraft safety constraints. These constraints have placed the requirement on the navigation system that the delivery accuracy at Mars should be better than 20 to 25 km (1σ).

The conventional radio metric data, two-way doppler and range measurements from the Deep Space Network stations, can provide a heliocentric position accuracy for the Galileo spacecraft to an accuracy of about 35 km (1σ). However, this does not include the uncertainty in the Mars ephemeris. When the projected Mars ephemeris uncertainty of 40 km (1σ) is considered, the spacecraft position uncertainty at the Mars encounter point exceeds 50 km (1σ). Thus, the Galileo Project is planning to augment conventional radio metric two-way doppler and range with VLBI to achieve the required accuracy.

The VLBI method for navigational application has been extensively studied (Refs. 2 and 3); however, the concept is yet to be successfully demonstrated (Ref. 4). The potential application of the wideband VLBI system is discussed by Brown and Hildebrand (Ref. 5). This VLBI technique will be utilized in a differential mode with VLBI data referenced to an extragalactic radio source (EGRS) to difference out various common error sources. This imposes an additional requirement that the Mars ephemeris should be known with reference to an extragalactic radio source frame with an accuracy of better than 20 to 25 km (1σ). There exists an on-going activity, using Viking orbiter data, that is expected to provide the needed accuracy (Newhall, 1980, personal communication).

The Galileo project is also considering the utilization of the onboard optical system to achieve the desired accuracy. The use of optical data at Mars encounter has been successfully demonstrated during the Viking mission. It is not currently decided whether the optical system will be available for approach navigation at the Mars encounter phase.

Although the use of interplanetary beacons in general deep-space navigation has not been adequately investigated, the possible use of the Viking Lander as a beacon in Galileo navigation has been examined in covariance studies. Galileo-Viking, dual DSS range promises to improve conventional radio metric range and doppler orbit determination by a factor of 4. Its performance is favorably comparable to that of VLBI.

II. Radio Metric Measurements

Since the early 1960s, interplanetary navigation has been accomplished with such conventional radio metric measurements as the coherent two-way doppler data and two-way range data (Ref. 7). Measurement accuracies and model accuracies have been improved significantly over the years; however, the new anticipated navigation functions require alternate radio metric techniques to achieve the projected accuracy requirements.

A brief examination of the information content of these radio metric measurements is presented here. By processing one pass of coherent doppler data, the primary orbit parameters (the geocentric range rate, the right ascension, and declination of the spacecraft) can be determined. The accuracy with which these parameters can be determined is given by the following equations:

$$\sigma_{\dot{r}} = \sigma_{\dot{\rho}}$$

$$\sigma_{\alpha} = \frac{1}{\omega r_s \cos\delta}\,\pi\,\sigma_{\dot{\rho}}$$

$$\sigma_{\delta} = \frac{1}{\omega r_s \sin\delta}\,\frac{\pi}{2}\,\sigma_{\dot{\rho}}$$

where r, α, and δ are the geocentric range rate, the right ascension, and declination of the spacecraft respectively, $\dot{\rho}$ is the range rate measurement, ω is the spin rate of the earth, and r_s is the distance off the spin axis of the DSS.

Single-station range data taken over a pass provides the same information as that using doppler; however, the geocentric range information is better known. These, of course, are radial measurements. These measurements are corrupted primarily by transmission media modeling errors, station location errors, instrumentation errors, and unmodeled spacecraft accelerations. It is possible to minimize some of these errors by combining radio metric doppler and range from two stations and from two spacecraft into first and second differences. Errors that are common cancel. For first differenced range and doppler, spacecraft unmodeled accelerations, solar plasma corruptions, and spacecraft oscillator instability cancel, while ionospheric and tropospheric corruptions and station location and clock errors do not cancel. For dual-spacecraft-dual-station, differenced range and range-rate that is doubly differenced data, even the ionospheric, tropospheric, and station errors mostly cancel to yield relatively error-free observables. For doubly differenced range where one spacecraft is tied to the planet, even the planet ephemeris errors cancel to a large degree. The information that doubly differenced range does process is the relative right ascension and declination between two spacecraft.

$$\Delta^2\rho = \Delta Z\,[\cos\delta\,\Delta\delta]$$

$$- \Delta L\,[\sin(\alpha-\theta)\cos\delta\,\Delta\alpha + \cos(\alpha-\theta)\sin\delta\,\Delta\delta]$$

with ΔZ and ΔL being the east-west and north-south projections of the baseline on the plane-of-sky, and $\Delta\alpha$ and $\Delta\delta$ being the separation between the spacecraft and the beacon in right ascension and declination. θ is the local sidereal time.

III. Doubly Differenced Range Measurements

The use of differenced radio metric data from two spacecraft has been previously studied (Refs. 6 and 7). Dual-spacecraft-dual-station doubly differenced range simply carries the process one step further as suggested by Chao (Ref. 7).

Figure 1 shows the various components required to form this measurement. Stations A and B shown in Fig. 1 are separated by intercontinental distance. The two spacecrafts are shown as the Viking Lander (1) and the Galileo Spacecraft (2). Station A transmits a signal to the Lander and one round-trip light time later the range measurement is acquired. Range measurements from the Lander are acquired for about 10 to 15 minutes. Station B then transmits a signal to the Lander and ranging data are acquired a round-trip light time later. Then this procedure is repeated using both stations with Galileo. The doubly differenced range measurement can be formed from the following equation:

$$\Delta^2\rho = \{\rho_{1A}(t_1) - \rho_{1B}(t_2)\} - \{\rho_{2A}(t_3) - \rho_{2B}(t_4)\}$$

where ρ_{ij} $(i = 1, 2; j = A, B)$ are the two-way range measurements, and t_K $(k = 1, 2, 3, 4)$ are the corresponding station acquisition times.

As discussed earlier, each two-way range component of this measurement is susceptible to various error sources with most of the errors thought common to multiple links. Thus, the differencing process is expected to achieve cancellation of most of these errors. A theoretical error budget has been formed to account for those errors that do not completely cancel in the formation of dual spacecraft differenced range (Table 1). The assumptions made in generating this error budget are that the Viking Lander/Galileo separation angle is about 5 degrees, the data are taken near Mars opposition and at about 0.7-AU distance, and two stations observe the Lander for approximately 15 minutes each and then observe the Galileo spacecraft for the same amount of time. Also, the measurements are assumed to be taken at about 25-deg elevation angle. This may not be totally realistic because in general the observations from at least one of the two stations has a low elevation (10 to 15 deg) when the spacecraft is visible from two widely separated stations. However, 90 percent of the error budget stems from the system noise term and not the media errors. A root-sum-square (rss) error of about 2.2 m is obtained for a doubly differenced range measurement, and this is assumed to be random because the error is mostly due to the thermal white noise.

Since the achievable navigation accuracy using the technique described in this article strongly depends on the assumed measurement error, it is important to validate the measurement accuracy using existing spacecraft. Thus, near-simultaneous ranging experiments have been already conducted using the Viking Orbiter 1 and Lander 1, and are being planned using the Voyager 1 and 2 spacecraft.

Before the Orbiter became inoperative in July 1980, there were two opportunities to acquire doubly differenced range: 5 June 1980 (this attempt failed), and 28 June 1980. The 28 June experiment was successful. The difference between the Lander and Orbiter relative range residuals was 3.4 m. Details of this data validation process are contained in the Appendix. To date, this is the only empirical assessment of doubly differenced range rms error. Voyager may provide additional opportunities in the near future.

IV. Galileo-Mars Flyby Navigation

The Galileo mission presents a number of navigational challenges (Ref. 1); one of the more stringent of these relates to the Mars flyby phase of the mission.

Galileo Project plans call for the Galileo Spacecraft to flyby Mars ~200 km (σ_d = 25 km) above the planet's surface (Ref. 1). To achieve this accurate flyby, two new technological advances must be accomplished: one, the Mars ephemeris must be improved to better than 25 km (1σ); and two, a wide-band Very Long Base Interferometry (VLBI) technology must be developed that will permit the Galileo Spacecraft and Mars trajectories to be defined relative to a quasar inertial reference frame. Both efforts are underway and offer a means to reduce the Galileo-Mars relative trajectory errors, and also to obtain observables free from the preponderance of the Deep Space Station (DSS) location effects and transmission media effects.

What is shown here is that doubly differenced range from Viking Lander 1 and the Galileo Spacecraft can, like VLBI, achieve the Project Mars flyby requirement, providing the Lander survives. However, doubly differenced range is (1) essentially independent of planetary ephemeris uncertainty, and (2) is operationally simpler to use than VLBI.

There are 43 opportunities to obtain Viking range during the Galileo Mars approach. Viking has been programmed to transpond range on those 43 occasions (Table 2). This limit in opportunities exists because

(1) Galileo cruise time from Earth to Mars is ~93 days (March 1984 to June 1984).

(2) Lander thermal and power constraints permit only two 13-minute contiguous ranging segments per day.

(3) The Lander is not always in view during overlapping portions of tracking station view periods of Mars.

These joint Viking-Galileo ranging opportunities are shown on Fig. 2 and listed in Table 2. Since the Martian day ($\sim 24^h 37^m 23^s$) and Earth day are of comparable length, for a given hour angle of the Earth the relative geometry between DSS baselines and the Lander changes very slowly. Each baseline, in turn, can view the Lander for nearly eight days continuously.

The DSS identification numbers 14, 43, and 63 represent the Deep Space Network Stations at Goldstone, California; Canberra, Australia; and Madrid, Spain, respectively.

Each baseline's performance is not only time dependent, but is also governed by the alignment of the baseline with respect to the Galileo-Mars direction at encounter (Fig. 3). In essence, first differenced range from a spacecraft provides information as to the direction of that spacecraft with respect to the baseline but only in the direction of the baseline. Orthogonal to the baseline, there is no information. When measurements from two spacecraft are differenced to obtain $\Delta^2\rho$, $\Delta^2\rho$ defines the component of the earth-centered angular separation between the two spacecraft in the baseline direction. Figure 3 shows the baseline orientations relative to the Mars-Galileo direction at encounter. The DSS 43 - DSS 63 baseline, which is approximately 4-deg offset, yields the strongest information concerning the flyby distance, while the DSS 63 - DSS 14 ($\sim$12-deg offset) and the DSS 14 - DSS 43 ($\sim$60-deg offset) baselines provide progressively less information.

V. Covariance Analysis

The covariance analysis performed in this paper assumed a maximum likelihood estimator with gaussian errors on the observations. The assumed observations include two-way coherent doppler data from the Galileo Spacecraft using the three Deep Space Network stations continuously, one Doppler measurement every hour, one range measurement from the Goldstone station every day and the available doubly differenced range measurements as shown in Fig. 2. Since the dynamical state parameters are nonlinear functions of the measurements, the observation equations are linearized and the results obtained are based on a linear estimator. When a standard maximum likelihood estimator is constructed, the computed statistics based on data noise errors do not reflect the effect of model errors in the solution. Thus, the statistics must be adjusted to account for their effects.

The measurement equation can be written in this form:

$$\mathbf{z} = \mathbf{A}\mathbf{x} + \mathbf{C}\mathbf{p} + \mathbf{e}$$

where $\mathbf{z}$ is the vector of measurements, $\mathbf{x}$ the vector of estimated parameters, $\mathbf{p}$ the vector of model parameters whose effects on the estimated parameters are to be investigated, and $\mathbf{e}$ the vector of measurement errors. A weighted least squares estimator of $(\hat{\mathbf{x}})$ can be obtained by

$$(\hat{\mathbf{x}}) = [\mathbf{A}^T\mathbf{P}^{-1}\,\mathbf{A}]^{-1}\,\mathbf{A}^T\mathbf{P}^{-1}\mathbf{z}$$

with the assumption that $\mathbf{p}$ is a random vector of zero mean with covariance $\mathbf{P}_c$, $E(\mathbf{e}) = 0$, $\text{cov}(\mathbf{e}) = \mathbf{P}$ and $E(\mathbf{p}\,\mathbf{e}^T) = 0$ and the covariance of $(\hat{\mathbf{x}})$ is given by

$$\mathbf{P}_x^c = \text{Cov}(\hat{\mathbf{x}}) = \mathbf{P}_x + \mathbf{P}_x\,\mathbf{A}^T\mathbf{P}^{-1}\,\mathbf{C}\mathbf{P}_c\,\mathbf{C}^T\mathbf{P}^{-1}\,\mathbf{A}\mathbf{P}_x$$

where $\mathbf{P}_x = (\mathbf{A}^T\mathbf{P}^{-1}\mathbf{A})^{-1}$ is the noise covariance matrix. The matrix $\mathbf{P}_x^c$ is known as the "consider" covariance matrix and the matrices $\mathbf{A}$ and $\mathbf{C}$ are the partial derivatives of the measurement with respect to the estimated and the consider parameters. Both station locations and Mars ephemeris parameters are treated as "considered" parameters. Only the Galileo trajectory is being estimated. The a priori uncertainties of the parameters are given in Table 3.

In this covariance analysis the doppler data accuracy is assumed to be 1 mm/s with a 60-s averaging time, the range data is weighted with 1-km accuracy. The doubly differenced range measurements are assumed to be accurate to 2 m. Figure 4 presents the results of the covariance analysis. The flyby distance uncertainty is below the 10-km level about 25 days before the encounter.

If $\Delta^2\rho$ is not employed, conventional range and doppler estimates of the Galileo-Mars flyby distance are dominated by the Mars ephemeris uncertainty of 40 km (1σ). If conventional and VLBI data are employed with an improved Mars ephemeris, 25 km (1σ), the uncertainty in the estimates is still dominated by the ephemeris uncertainty and is always greater than 25 km (1σ).

Estimates of the flyby distance based on doubly differenced range have uncertainties often smaller than the ephemeris sigmas or tracking station location standard deviations because of the like influence of these error sources on the individual range measurements that are differenced to develop a doubly differenced range measurement. The ephemeris and station uncertainties cancel. Figure 5 illustrates how the influences of ephemeris and tracking station location uncertainties are less when $\Delta^2\rho$ is included in the covariance. Here only the Galileo state is estimated. The Mars ephemeris and station location are considered in the manner previously discussed. The uncertainty of the estimate of the Mars encounter distance of Galileo due to the Mars ephemeris uncertainty ($\sigma_{d\,|\text{Mars Ephemeris}}$) and due

to station uncertainty ($\sigma_d|_{\text{DSS Locations}}$) rapidly decreases as the tracking data arc of conventional data and $\Delta^2\rho$ become longer. When conventional data only is reduced, sensitivities to these consider parameters do not diminish.

VI. Summary and Conclusion

A newly proposed navigation technique utilizing two-way range data taken nearly simultaneously from two spacecraft has been analyzed and the results clearly show that the relative position of one spacecraft to the other can be determined with an accuracy depending only on the accuracy of the measurement. It is also shown that this technique can be applied during the Mars flyby phase of the Galileo mission. Covariance analyses show that the improvement in flyby navigation accuracy is significant compared to the conventional ground-based radio metric navigation. Since the achievable navigation accuracy strongly depends on the assumed measurement accuracy, experiments were conducted to evaluate the measurement accuracy: A single experiment using Viking Lander and Orbiter was viable for this purpose and the data reductions indicate that the expected accuracy can be attained. Since the Viking Orbiter is no longer operational, future experiments will be conducted using Voyager 1 and 2 spacecraft to increase the confidence level of the measurement accuracy.

This analysis has shown that the use of beacons for interplanetary navigation, specifically for target related navigation, will be of significant value. Thus, the utilization of interplanetary beacons should be a part of the next generation navigation technology development program.

References

1. Rourke, "Navigation of the 1982 Jupiter Orbiterprobe Mission," presented at AAS/AIAA Astrodynamics Specialist Conference, Jackson Hole, Wyoming, Sept. 7-9, 1977.

2. Melbourne, W., and D. Curkendall "Radio Metric Direction Finding: A New Approach to Deep Space Navigation," presented at AAS/AIAA Astrodynamics Specialist Conference, Jackson Hole, Wyoming, Sept. 7-9. 1980.

3. Curkendall, D., "Radio Metric Technology for Deep Space Navigation, A Development Overview," presented at AIAA/AAS Astrodynamics Conference, Palo Alto, California, Aug. 7-9, 1978.

4. Christensen, C. S., et al., "Results of a Demonstration of the Use of ΔVLBI Data for Precise Navigation of Interplanetary Spacecraft," presented at AIAA/AAS Astrodynamics Conference, Danvers, Mass., Aug. 11-13, 1980.

5. Brown, D., and C. Hildebrand, "Wideband ΔVLBI for Deep Space Navigation," presented at IEEE PLANS 80 Conference, Atlantic City, New Jersey, Dec. 1980.

6. Melbourne, W., "Navigation Between the Planets," *Scientific American*, Vol. 234, No. 6, June 1976.

7. Chao, C. C., et al., "Improvements in Navigation Resulting from the Use of Dual Spacecraft Radio Metric Data," presented at the AIAA/AAS Astrodynamics Conference, 76-834, San Diego, California, Aug. 18-20, 1976.

8. Mayo, A. P., et al., "Lander Locations, Mars Physical Ephemeris, and Solar System Parameters: Determination from Viking Lander Tracking Data," *J. Geophys. Res.* Vol. 82, No. 27, 1977.

9. Hildebrand, C., et al., "Viking Satellite Orbit Determination," presented at AIAA 15th Aerospace Sciences meeting, Los Angeles, California, Jan. 24-26, 1977.

10. Komarek, T., and T. Otoshi, "Terminology of Ranging Measurements and DSS Calibrations," *DSN Progress Report 42-36*, Jet Propulsion Laboratory, Pasadena, Calif., Dec. 1976.

11. Chao, C., *New Tropospheric Range Corrections with Seasonal Adjustment*, TR 32-1526, Vol. VI. Jet Propulsion Laboratory, Pasadena, Calif., 1971.

Appendix A
Viking Lander/Orbiter Data Processing

The experiment that was conducted on June 28, 1980 employed the Deep Space Stations at Goldstone, California (DSS 14) and Madrid, Spain (DSS 63). The time sequence of data acquisitions is given in Fig. 6. The Orbiter was first tracked by DSS 63. Two-way coherent doppler and range measurements were obtained. Subsequent to this, DSS 14 was used to acquire the Lander, and range and doppler measurements were generated. After 13 minutes of data acquisition, DSS 14 handed over to DSS 63 tracking of the Lander. Both range and doppler measurements were obtained for about 13 minutes. Subsequent to this, DSS 14 was used to track the Orbiter. This completed the cycle with four independent tracking links.

From tracking the Lander for an extensive period of time, the Lander location with respect to the dynamic center of Mars has been determined very accurately (Ref. 8). The current uncertainty of the Lander location is about 300 m. The Orbiter position can be determined by processing doppler tracking data. With sufficient data, the Orbiter position can be determined with an accuracy better than 10 km. Thus, the Lander relative position of the Orbiter is known to better than 10 km, and doubly differenced range measurement residuals can be generated and the measurement accuracy can be evaluated.

The Orbiter position (state vector) is determined by processing the coherent two-way doppler data. This is accomplished by estimating state parameters (position and velocity components of the Orbiter) only. However, the low-order gravity coefficients are included in the trajectory model equations. The best fit to the orbit of the Orbiter is obtained when continuous tracking data over the whole orbit, except for a couple of hours near the periapsis, are available. When the periapsis data are available, these are often deleted out to desensitize the effects of unmodeled higher degree coefficients of the gravity field. In this experiment, although there were sufficient tracking data, the doppler data were not continuous throughout the orbit. The tracking data (doppler) were available from the Australian station (DSS 43) about one hour after periapsis, for about 2.75 hours. Then there was a gap of about 1.75 hours without any data. After this, the Spain station (DSS 63) provided the data for about 6.5 hours. Then there were no tracking data for about 7.5 hours. Once again DSS 43 provided about three hours of doppler data. Even though the tracking data were not available continuously over the orbit, previous studies (Ref. 9) have shown that the accuracy degradation is relatively small if the available data are distributed over the orbit.

The postfit residuals from the Orbiter data are shown in the Fig. 7. On both sides of the periapsis, the data are taken with a frequency of one measurement every minute. The rest of the data are with a frequency of one measurement every 10 minutes. The data with both sample sizes are weighted accordingly with a data weight of 15 mHz with 1-minute averaging time, in the data reduction process. The standard deviation of the postfit data residuals is less than 10 mHz indicating that the residuals do not contain any orbit related systematic signature.

As discussed previously, the doubly differenced range data are generated by explicitly differencing two differenced range data points from two different sources. In this case, one of the sources is the Viking Orbiter. Thus, it is necessary to examine the residuals of the differenced range points of the Orbiter. This is accomplished simply by generating range residuals of the data from both stations. The range residuals are obtained by passing the raw range measurements through the best fit orbit. The range residuals have to be adjusted for (1) ground station calibration, (2) transponder delay, and (3) the media effects.

A discussion of ground station calibration is given by Komarek and Otoshi (Ref. 10). The calibration for media effects is achieved by adjusting for the troposphere effects using a troposphere table based on pressure and temperature models for the stations as a function of elevation angle (Ref. 11). Ionospheric effects are calibrated either by using Faraday rotation data or multifrequency data from the spacecraft. Faraday rotation data have been used here. There is a modeling error in the Faraday rotation calibration for the ionospheric effects primarily due to the mapping of the Faraday rotation data to the line of sight of the spacecraft. However, this error is significantly less than the estimated accuracy of this new data type.

The range residuals are shown in the Fig. 8. The residuals are expressed in meters. A range bias of 13.5 m is observed between DSSs 63 and 14.

The Lander data is processed in a manner similar to the Orbiter range data, however, the Lander location is known a priori, and the parameters related to the Lander location are given in Table 3. The Lander range residuals are generated by

differencing the computed values of range points based on assumed models from the observed range points. The range residuals, after appropriate calibration is applied, are shown in Fig. 9. It is clear from this figure that there exists a bias of about 10.1 m between DSSs 63 and 14 in the same direction as observed in the case of the Orbiter data. When the doubly differenced range observable is formed, these two biases are also differenced and the resulting bias is about 3.4 m and this represents the measurement accuracy of this data type.

Both Orbiter and Lander range residuals (Figs. 8 and 9) show that the scatter within a single station measurement is considerably small (< 1 m) as predicted by theoretical error budget. This scatter is mostly due to the system noise, depending on the spanned-bandwidth of the ranging code. The range bias between two stations is often introduced by the range calibration error. Errors in both ground station calibration and media calibration can cause the 3.4-m bias. Theoretically, this bias is expected to cancel when two spacecraft data are differenced. However, the cancellation due to media errors is a function of the spatial separation of the two spacecraft and the time separation in the data acquisition. In this experiment, the spatial separation is negligible (< 0.1 deg). However, the data acquisition time separation between the Orbiter and the Lander is over an hour. Thus, a part of the residual bias may stem from temporal changes in media. Cancellation of errors due to ground station calibration is achievable if the same instrumentation configuration is utilized in acquiring both Orbiter and Lander ranging data. In this experiment, although most of the instrumentation used in tracking the Orbiter and the Lander is the same, different receivers were employed. Thus, it is possible that the remaining residual bias in the doubly differenced data is due to the error in the calibration values and this is consistent with the currently expected calibration accuracy. More doubly differenced range data is required to understand its noise characteristics.

Table 1. Doubly differenced range data error budget

Source	Error (1σ), cm
Instrumentation:	
Station clock stability (15 min)	4
Station delay calibration	0
SNR (Thermal noise; (S-band with 2-MHz spanned band width)	200
Waveform distortion	88
Spacecraft delay	28
Media	
Troposphere (25-deg elevation)	20
Ionosphere (25-deg elevation)	6
Solar wind	15
	rss: ~222 cm

Table 2. Viking Lander direct link ranging opportunities for Galileo navigation, 1984

Point	DSS Baseline[a]	Date
1	63-14	22 March 84
2	63-14	23 March 84
3	63-14	24 March 84
4	63-14	25 March 84
5	63-14	26 March 84
6	14-43	29 March 84
7	14-43	30 March 84
8	14-43	31 March 84
9	14-43	1 April 84
10	14-43	2 April 84
11	14-43	3 April 84
12	14-43	5 April 84
13	14-43	6 April 84
14	43-63	14 April 84
15	43-63	15 April 84
16	43-63	16 April 84
17	43-63	17 April 84
18	43-63	18 April 84
19	63-14	25 April 84
20	63-14	26 April 84
21	63-14	27 April 84
22	63-14	29 April 84
23	63-14	30 April 84
24	63-14	1 May 84
25	14-43	4 May 84
26	14-43	6 May 84
27	14-43	7 May 84
28	14-43	8 May 84
29	14-43	9 May 84
30	14-43	10 May 84
31	14-43	11 May 84
32	43-63	17 May 84
33	43-63	18 May 84
34	43-63	20 May 84
35	43-63	21 May 84
36	43-63	22 May 84
37	14-43	23 May 84
38	63-14	27 May 84
39	63-14	29 May 84
40	63-14	30 May 84
41	63-14	31 May 84
42	63-14	1 June 84
43	63-14	2 June 84

[a]DSS 14 (Goldstone, California)
DSS 43 (Woomera, Australia)
DSS 63 (Madrid, Spain)

Table 3. Error analysis parameters

Parameter	A priori σ
Galileo state	$\sigma_x = \sigma_y = \sigma_z = 10^7$ km $\sigma_x = \sigma_y = \sigma_z = 100$ km/s
Mars ephemeris	$\sigma_{radial} = 10$ km, $\sigma_{intrack} = 40$ km $\sigma_{out\ of\ plane} = 70$ km
Station locations	$\sigma_{long} = 3$ m, $\sigma_{r_s} = 1.5$ m $\sigma_{r_z} = 15$ m
Viking Lander locations	$\sigma_x = 10.0$ m $\sigma_x = 40.0$ m $\sigma_z = 300.0$ m
Mars mass	$\sigma = 0.1$ km^3/s^2

r_s = distance off the spin axis

r_z = distance off the earth equator plane

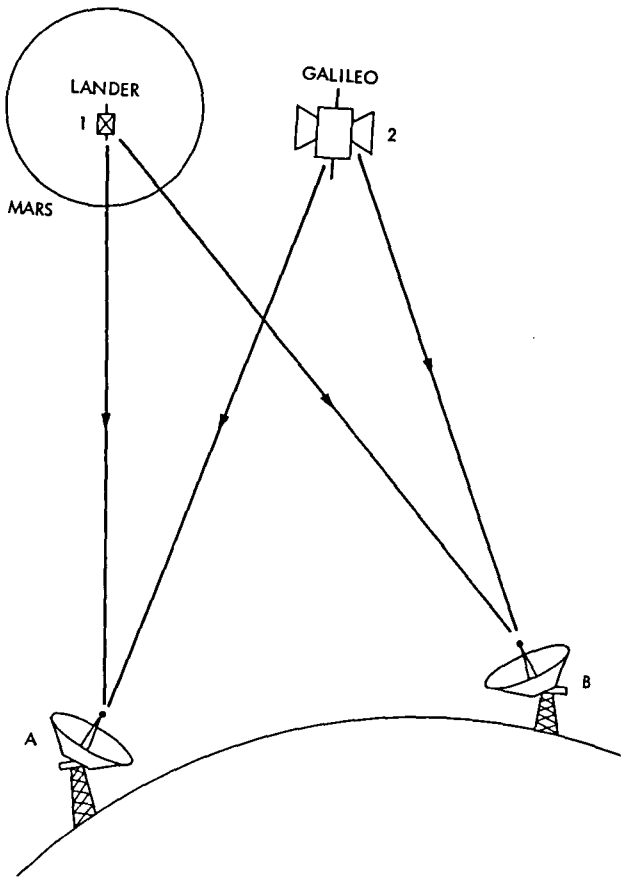

Fig. 1. Doubly differenced range data links

43/63	63/14	14/43	43/63	63/14	14/43	43/63	63/14
-80	-70	-60	-50	-40	-30	-20	-10	E(DAYS)
3/14	3/24	4/3	4/13	4/23	5/3	5/13	5/23	6/2
1984								

Fig. 2. Lander/Galileo viewing opportunities

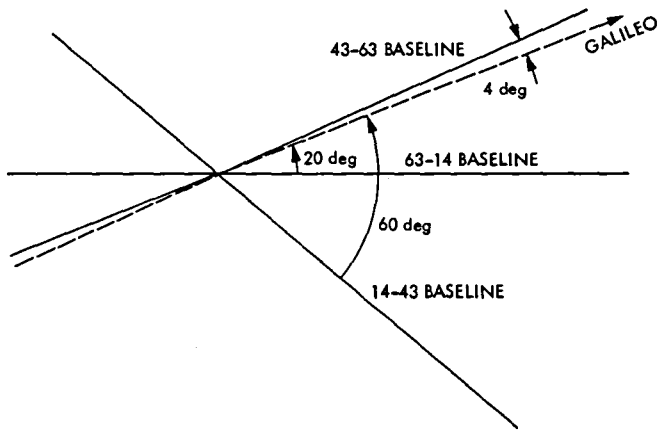

Fig. 3. Deep Space Station baselines projected in the plane normal to the Galileo approach asymptote at the Mars encounter

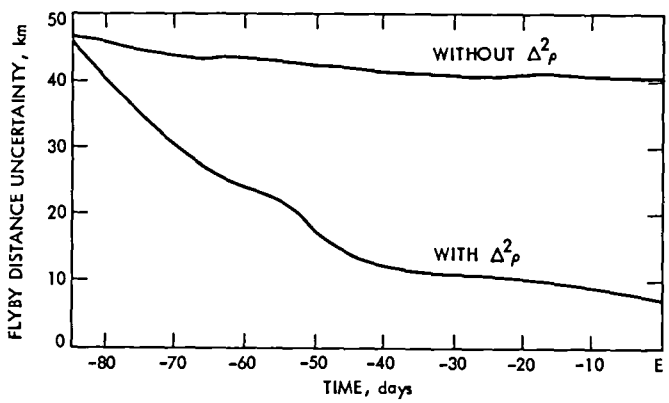

Fig. 4. Covariance analysis results

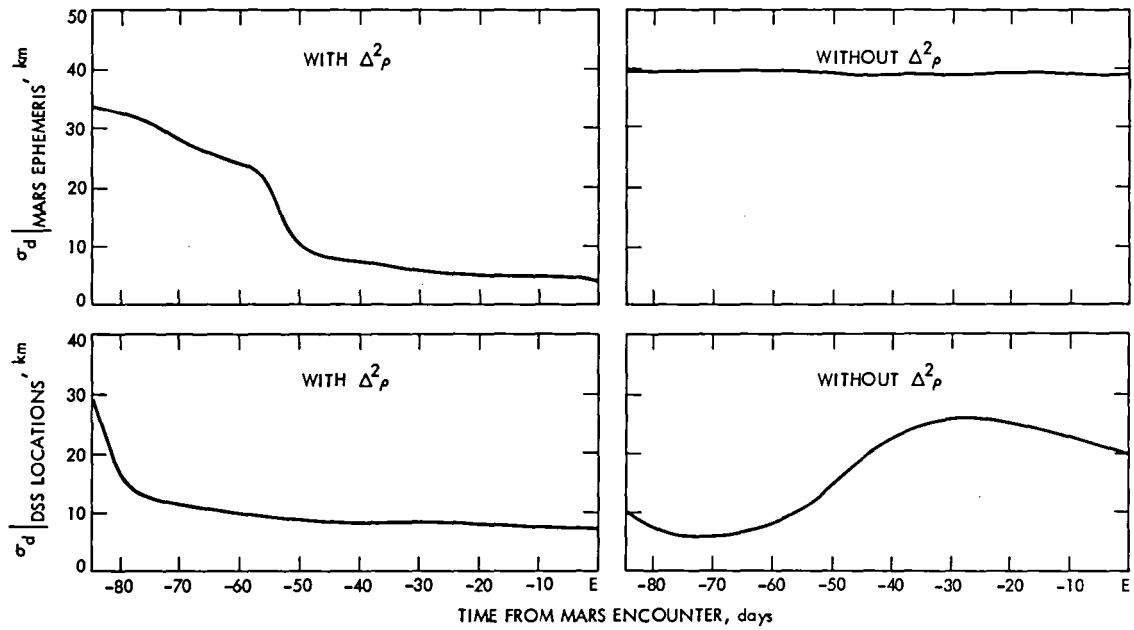

Fig. 5. Reduced sensitivity consider parameters

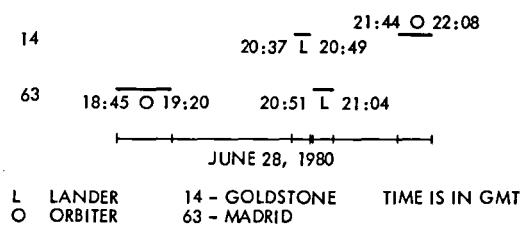

Fig. 6. Lander/Orbiter tracking sequence

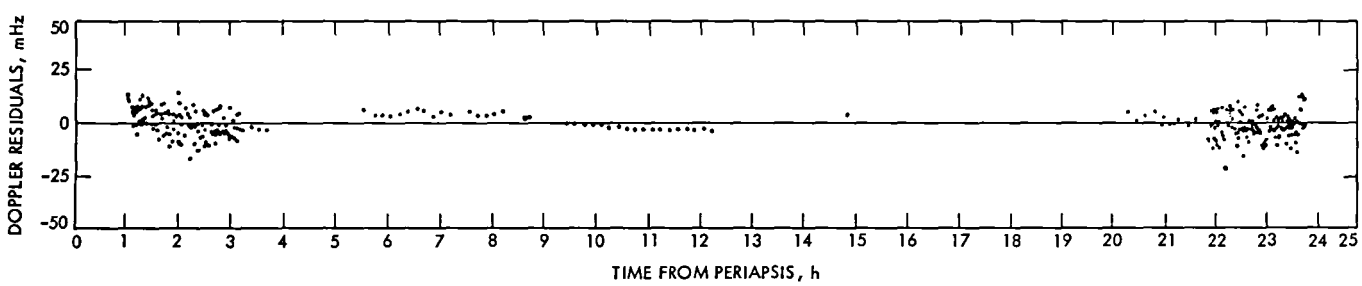

Fig. 7. Orbiter doppler data postfit residuals

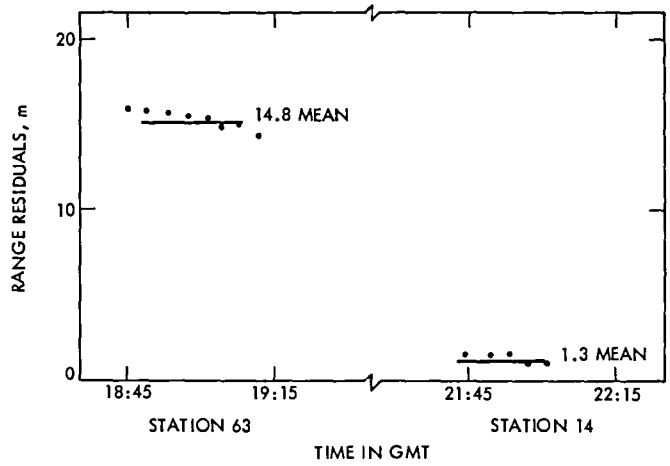

Fig. 8. Orbiter range residuals

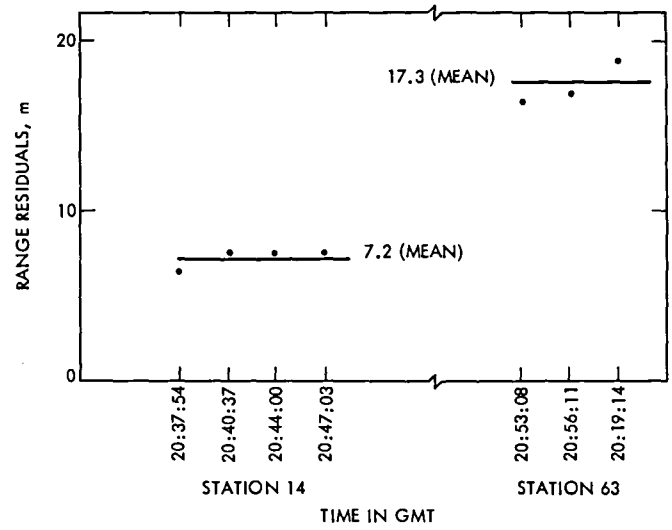

Fig. 9. Lander range residuals

ΔVLBI Spacecraft Tracking System Demonstration Part II: Data Acquisition and Processing

C. S. Christensen and B. Moultrie
Navigation Systems Section

and

P. S. Callahan, F. F. Donivan, and S. C. Wu
Tracking Systems and Application Section

A set of experiments in the use of Differential Very Long Baseline Interferometry (ΔVLBI) for spacecraft navigation have been completed. Data using both Voyager spacecraft and a single quasar were acquired during the Jupiter encounter time period. The data were processed and analyzed to assess the navigation accuracy of ΔVLBI. This article focuses on the data reduction and techniques for assessing data quality and consistency.

I. Introduction

This is the second article in a series describing the DSN development of an improved spacecraft navigation system using Very Long Baseline Interferometry (VLBI) techniques. The first article (Ref. 1) described the goals and design and planning of a demonstration of narrow-band ΔVLBI using data taken near the two Voyager encounters of Jupiter. This article includes a review of the demonstration plan. It discusses the data acquisition for the demonstration and the data processing steps followed. There is an emphasis on the techniques used for assessing data quality and consistency. Consistency of the ΔVLBI passes used in the demonstration is at the 0.5-μradian level rather than the 0.05-μradian level expected. Reasons for the discrepancy are discussed.

II. The Voyager Narrowband ΔVLBI Demonstration

VLBI data is obtained by two widely separated antennas simultaneously receiving and recording a signal from a single radio source. These recorded signals are brought together and correlated to obtain precise differential (between the stations) range (wideband VLBI) or differential range rate (narrow-band VLBI). Delta VLBI (ΔVLBI) involves differencing VLBI data taken from a spacecraft with VLBI data taken from an angularly nearby extragalactic radio source (EGRS). Differencing between sources improves accuracy by near cancellation of common errors sources such as those introduced by station electronics, clocks, transmission media, and station locations.

To obtain an angular measurement from narrow-band ΔVLBI, a "pass" of data nominally four to five hours in length is required. During a pass, data is collected alternately from each source, the EGRS and the spacecraft. Each burst of data from a single source is called a "scan." In this demonstration, each scan was seven minutes long. Passes for this demonstration utilized baselines between the Deep Space Stations (DSS) at Goldstone, California, and either Madrid, Spain, or Canberra, Australia. A more detailed background on ΔVLBI and its expected use in spacecraft navigation is contained in Refs. 1, 2, and 3.

The demonstration involved both Voyager spacecraft and a single EGRS, OJ 287. The EGRS was near the retrograde loop of each spacecraft, hence angularly close to both spacecraft for a period of almost a year (see Fig. 1). Though the spacecraft-EGRS angular separation was far from ideal, reaching 12 deg near the Voyager 1 encounter, it was felt that the advantage of using a single radio source throughout outweighed the disadvantage of the large separation. A wide separation between sources implies that errors due to media (troposphere and charged particles) may not cancel well in the differenced data. More will be said on media calibration and cancellation in Section IV.

The demonstration design is as follows: Narrow-band ΔVLBI passes were taken using Voyager 1 and OJ 287 before and after the encounter of the spacecraft with Jupiter. These data were intended to give an accurate measure of the relation between the EGRS and spacecraft as it moved on its trajectory past Jupiter. This information, along with the accurate knowledge of the Jupiter-relative spacecraft trajectory given by conventional doppler data near the encounter, was intended to give an accurate measurement of the Jupiter-EGRS angle. This angular information and narrow-band ΔVLBI passes taken using Voyager 2 and OJ 287 were to predict the Voyager 2 Jupiter encounter more accurately than conventional doppler data. The Voyager 2 encounter prediction could be verified with the accurate knowledge obtained after encounter from conventional doppler. An accurate encounter prediction would by implication verify the accuracy of the ΔVLBI data used in the demonstration.

III. Data Acquisition

To perform the demonstration, narrow-band VLBI data passes were scheduled during several weeks before and after the Jupiter encounter of each Voyager spacecraft. The passes were scheduled on a noninterference basis with normal Voyager operation. Twenty-five passes were scheduled on Voyager 1 between 27 January (DOY 027) and 5 April (DOY 095) 1979. Thirty-three passes were scheduled on Voyager 2 between 3 April (DOY 093) and 6 August (DOY 218). Of these, 22 passes had data quality sufficient to permit further processing. Figure 2 shows the passes analyzed in relation to the two Jupiter encounters.

The data were taken with VLBI equipment at each DSS. The equipment consists of radio frequency hardware to reduce the incoming S- or X-band signal to a 0- to 2-MHz band. This band is sampled, digitized, and recorded on video tape at a rate of 4 Mbits/s. The signal mixing and sampling are all controlled by each station's frequency standard, usually a hydrogen maser. Both the frequency standard and the instrumentation path delay must be stable to $\Delta f/f \lesssim 2 \times 10^{-14}$ for the measurements to be successful. The tapes were shipped to JPL for processing.

IV. Data Processing

The data processing steps necessary for the reduction of narrow-band ΔVLBI are shown in Fig. 3. Each step in the process will be discussed.

A. Correlation

Each tape contains approximately one hour of 4 Mbits/s data. To proceed with the data reduction, this huge volume of bits (up to 10^{11} per pass) must be reduced to more manageable proportions. This initial reduction is done by processing the tapes on the CIT-JPL Mark II VLBI correlator at Caltech (Ref. 4).

Briefly, the correlator operates by computing the geometric delay and delay rate between the stations, offsetting the bit streams by the proper amount and then multiplying the streams together. The resulting fast fringes are slowed by a phase model that includes the expected delay rate and the local oscillator frequencies. The output of the correlator is one-second (typically) averages of the sine and cosine of the differenced (residual) phase between the cross-correlated signals and the model. The correlator operates at the 4 Mbits/s rate at which the data were recorded so that correlation, once the clock and frequency offsets are determined, requires the same length of time as the observations.

The correlator was developed to work with broad-band white noise signals that fill the 2-MHz channel. However, the spacecraft carrier is a very narrow, and when considered over the 2-MHz channel, a very weak signal. To overcome the latter problem, advantage was taken of the narrowness of the signal by using local-model correlation. The correlator was adapted so that the phase model could be represented by a polynomial. The spacecraft data were then correlated against an effectively noise-free polynomial model of the phase at each station. These phases were differenced later in the data processing to produce interferometric phase like that obtained in the EGRS cross correlation. The use of local-model correlation produced a very narrow effective bandwidth, and thus, a high signal-to-noise ratio (SNR).

The polynomial model used for local-model correlation had to be reasonably accurate. The predicted received frequency had to be accurate to a few hertz and the frequency rate accurate to ~0.1 Hz over a several hour pass. The polynomials were generated using the best spacecraft trajectory available and a current earth platform and troposphere model.

B. Phase Tracking

The correlator output is a magnetic tape that contains the sine and cosine of the residual phase at 1-s (typically) intervals, along with time tags, model phase and delay, and housekeeping information. The data are treated scan by scan. A scan is broken up into 5 to 100 sections for fitting. The sine and cosine values for each section are fit by least squares to a function of the form A exp $i(\omega t + \phi)$, where the initial values for the fit are obtained from a fast Fourier transform and/or the previous section. The value of the argument of the exponential *evaluated at the midtime* is the residual phase for the section, and ω is the residual fringe frequency. Further description of the phase tracking process can be found in Ref. 5.

The two spacecraft data streams (one for each station) can be differenced either before or after phase tracking. After phase tracking, the residual phase for each section is added to the model phase to obtain the total phase.

C. Observable and Partial Calculation

The separate spacecraft and EGRS data streams now form the observable for a standard orbit determination process. Using the best available estimate of the spacecraft ephemeris and the EGRS position, the observables (phase) and partial derivatives of the observables with respect to the parameters to be used in estimation are calculated. The program REGRES, from JPL's Orbit Determination Program set (Ref. 6) was used for this step. The observable phase calculated by REGRES is now subtracted from the total observed phase to obtain a new residual phase, hereinafter called REGRES residuals.

D. Media Calibration

Transmission media (troposphere, ionosphere, and solar wind) are significant error sources in radio tracking. A key feature of ΔVLBI is that the data are expected to be largely self-calibrating due to the differencing of data streams. However, to remove large, easily modelled phase rates that might interfere with phase tracking or phase connection, calibrations are applied to the data. A slab model of the troposphere was used in the correlation for both spacecraft and EGRS. Polynomials representing the line-of-sight phase change through the ionosphere to each source, based on Faraday rotation measurements from geostationary satellites, are subtracted from the REGRES residuals.

E. Phase Connection

Recall that each data stream for the spacecraft and EGRS are segmented into disconnected scans of seven minutes. The information content of narrow-band VLBI is strongly dependent on a continuing time history of phase (Refs. 1 and 2). Hence, each data stream must be connected.

The residual phase output from the phase tracking software has an ambiguity with respect to that in the previous scan of 1 cycle. Hence the REGRES residuals have the same ambiguity. Phase connection consists of deciding upon the number of integer cycles that should be added or subtracted from each scan (after the first) such that the resulting residual phase has a smooth behavior (see Fig. 4). Numerical algorithms designed to determine the residual phase rate in the gap between two consecutive scans are used to aid in phase connection. One such algorithm is described in Ref. 7.

In addition, "connected" phase plots are examined to heuristically correct seemingly incorrect phase connections. Nevertheless, phase connection between two consecutive scans can still be in doubt as indicated in Fig. 4. When this occurs, the question arises as to whether it is better to leave it disconnected or to run the risk of having a misconnected pass. To answer this question a comparison was made between the effects of disconnecting a pass and of misconnecting it.

Figure 5 shows the results of a covariance analysis comparing misconnection and disconnection for a pass taken on the Goldstone/Madrid baseline at the declination and scan length of the demonstration. Both a long pass (4.75 hours, Fig. 5b) and a short pass (2.65 hours, Fig. 5a) are shown. The larger curves show the error in the determination of the spacecraft-EGRS angular separation for a single misconnection of one cycle vs the location in the pass of the misconnection. On the long pass, the error can be as great as the expected data accuracy (0.05 μrad). On the short pass, a single misconnection is disastrous! The error can be as large at 0.2 μrad with an expected error of 0.14 μrad in right ascension and 0.07 μrad in declination.

For a single disconnection during the pass, the one-sigma error resulting from a conservative 3-cm (1σ) Gaussian phase noise is shown. The statistical error is an order of magnitude lower than the misconnection error. Consequently, it is far better to discard a doubtful connection between two scans than make a mistake and misconnect.

Figure 6 shows the angular separation errors due to a conservative 3-cm phase noise as functions of the number of disconnected segments in the pass for the same long and short passes. It is observed that, with 3-cm phase noise, the error in each component will not exceed 0.02 μrad until the pass is disconnected into seven segments for the long pass. This implies that even with every third scan left disconnected, the effects of phase-type noise remain acceptable. For a totally disconnected long pass, the error becomes 0.17 μrad in each

component, clearly unacceptable. The short pass appears to be acceptable for 1, 2, or 3 segments. Without phase connection over such a pass, the expected angular separation errors are 0.38 μrad in right ascension and 0.21 μrad in declination.

F. Differencing

Finally, the data streams, in the form of REGRES residuals and partials, are differenced. Since the differencing is intended to cancel common errors, the data streams are offset in time to maximize the cancellation. Two major error sources are the troposphere and ionosphere. The maximum cancellation of these errors for sources separated in right ascension and declination occurs for a time offset in minutes of

$$\Delta t = 4\Delta\alpha + 2.8\Delta\delta$$

where $\Delta\alpha$ and $\Delta\delta$ are the differences in degrees in right ascension and declination. A time offset of $\Delta t = 4\Delta\alpha$ also minimizes the sensitivity of ΔVLBI to station location errors. A linear phase drift in the instrumentation will be removed by differencing regardless of the time offset. However, nonlinear phase variations such as a clock frequency drift will be enhanced by the time offsetting. (See the error analysis discussion in Ref. 1).

The optimum time offset could not be realized with the demonstration data. To difference a scan of spacecraft data with a scan of EGRS data, an offset must be an odd integer times 7 minutes. The time offsets available are shown in Fig. 2. The available offset nearest the computed offset was considered optimal for that pass.

The differenced phase history is examined visually for discontinuities, usually at several time offsets including the optimal one. If a discontinuity shows up clearly, the individual phases are reexamined and corrected. It should be noted that there is a disconnection in the differenced phase whenever there is a disconnection in phase from either source. Thus, if there is one disconnection in the phase of each source, there will be two in the difference, i.e., three segments – the maximum number for usable data from short passes.

G. Parameter Estimation

The last step in the data processing is that of parameter estimation. The VLBI residuals and partials (possibly along with other data) are now input to an orbit determination filter where selected parameters are estimated.

To assess the consistency of the 22 passes, the EGRS right ascension α and declination δ were estimated for each pass. The spacecraft parameters were held fixed, so that with an accurate spacecraft trajectory, the solutions should cluster within the accuracy of the data. The passes were differenced with varying time offsets. Passes were phase connected with various algorithms; they were disconnected at points where connection seemed in doubt. The scatter of the α, δ solutions remained essentially the same for different data treatments.

Figure 7 shows the scatter of seven Voyager 1 passes and ten Voyager 2 passes resulting from a set of α, δ solutions. Right ascension and declination are shown separately vs time. The shaded region represents a conservative estimate of the uncertainty of the spacecraft trajectory. The "true" spacecraft trajectory would be represented by a straight line within the shaded region. Clearly, the scatter in the solutions are an order of magnitude larger than the expected 0.05 radians. The magnitude of the scatter and lack of a trend indicate that the spacecraft trajectory error is not contributing to the large scatter.

V. Discussion

The results of the Voyager ΔVLBI demonstration have not fulfilled the promise of the original error analysis. There are several reasons why the observed error is nearly a factor of 10 larger than originally predicted. Basically, the reasons are that the passes were shorter and the individual error sources were larger than was anticipated. Figure 6 clearly illustrates the effect of shorter passes by comparing covariance analyses for passes of 21 scans (4.75 hours) and 12 scans (2.65 hours). The predicted error is about a factor of 3 larger for the shorter pass. The shorter pass is typical of the actual observations, while the original error analysis was done for the longer pass.

Two major error sources for ΔVLBI are the transmission media, particularly the ionosphere, and the station instrumentation. Four passes of Voyager 2 data have dual-frequency (S- and X-band) data, which provide a direct measurement of the charged-particle-induced phase change. These measurements were compared to the Faraday polynomial calibrations. Assuming that there are no large instrumental effects in the SX data, the comparisons show 5- to 7-cycle differences over a pass between the actual line of sight phase change and the Faraday polynomial for each source. When the data are differenced between sources, most of this accumulation is removed, but discrepancies of about 1 cycle remain independent of time offsets. Thus, the differenced data calibrated with the Faraday polynomials are likely to contain false signatures of at least 1-cycle accumulation from transmission media. This exceeds the total original error allocation by a factor of 2.

It is thought that the effect of false signatures in the Faraday calibrated differenced data may be even larger in the

Voyager 1 data where one station went through the day-night ionosphere transition during the observations. Because the Faraday polynomials are of relatively low order, they do not capture the rapid recombination of the ionosphere at the day-night transition. During a day-night transition, it is likely that the difference between the polynomial and the line of sight values will be larger than at other times, and the error cancellation between the 10-deg separated sources will be less. One might therefore expect errors of 2 to 3 cycles in the differenced data over a pass.

A second possible source of error in the observations is phase variations in the receiver chain and/or fluctuations in the stations' frequency standards. No direct measurements of the frequency standards are available. Equipment to measure the instrumental phase was available only at the Goldstone station and only for the latter part of the demonstration. Some of these data have been examined, and no large effects are apparent. It is interesting to consider what sort of instrumental errors would affect the data. Because of the data differencing, linear phase drifts have no effect, but linear frequency drifts do. A frequency drift of only 5 parts in 10^{14} could contribute 1 cycle to the accumulated phase in the differenced data. Similarly, a phase wander with an amplitude of 1 cycle and a period of a few hours could cause a 1-cycle error in the differenced data. Both of these effects come about because of the time offsetting, which is done in the data processing to minimize transmission media errors.

Note that both the media and instrumental errors discussed here are accumulated over a pass and thus go directly into the solutions unlike the phase noise used in the covariance analyses shown in Figures 5 and 6. An order of magnitude estimate of the effect of accumulated errors can be obtained from the curve for misconnections in Fig. 5a; it shows that a 1-cycle error gives a solution error of about 0.1 μrad. This is consistent with the above discussion of media errors of 1 to 3 cycles and consistent with the observed scatter of the solutions.

As was pointed out previously, phase connection is both difficult and extremely important. Transmission media and instrumental errors can not only contribute to solution errors in their own right, but can also cause mistakes in phase connection. In this case, rapid local variations in the phase rate are of the most concern. The SX data show that the ionosphere may have small scale irregularities on the order of 1/4 cycle (S-band) in a few minutes. Since the effect is only 3/11 as large at X-band, X-band data are likely to be correctly connected. Thus, S-band data calibrated with SX are likely to be much more reliable than when they are calibrated with Faraday polynomials.

The foregoing discussion makes it clear that the data actually acquired were not in line with the demonstration's original goals. The most significant problem with the actual data is the shortness of the passes. The data errors encountered probably would have allowed solutions at the 0.1-μrad level with passes > 4.5 h in length. On the other hand, it is very likely that the data errors would have been smaller if the source separation had been smaller. Tests will soon begin to investigate data errors as a function of source separation. Therefore, while the demonstration did not meet its goals, it did provide a much clearer understanding of the problems of navigating with ΔVLBI and what sort of system and data acquisition procedures are needed to reach angular accuracies of 0.05 μrad.

References

1. Brunn, D. L., et al., "ΔVLBI Spacecraft Tracking System Demonstration: Part 1. Design and Planning," *DSN Progress Report, 42-45, March and April 1978,* pp. 111-132, Jet Propulsion Laboratory, Pasadena, Calif.

2. Curkendall, D. W., "Radio Metric Technology for Deep Space Navigation: A Development Overview," paper 78-1395 presented at the AIAA/AAS Astrodynamics Conference, Palo Alto, Calif., August 7-9, 1978.

3. Melbourne, W. G., and Curkendall, D. W., "Radio Metric Direction Finding: A New Approach to Deep Space Navigation," paper presented at the AAS/AIAA Astrodynamics Specialist Conference, Jackson Hole, Wyoming, September 7-9, 1977.

4. Thomas, J. B., "Cross Correlation and Fringe Stepping for a Multistation Correlator," Engineering Memo 315-23, March 15, 1977. Jet Propulsion Laboratory, Pasadena, Calif. (JPL internal document.)

5. Thomas, J. B., *An Analysis of Long Baseline Radio Interferometry, Part III*, Technical Report 32-1526, Vol. XVI, pp. 47-64. Jet Propulsion Laboratory, Pasadena, Calif.

6. Ekelund, J. E., "The JPL Orbit Determination Software System," paper 79-111 presented at the AAS/AIAA Astrodynamics Specialist Conference, Provincetown, Mass., June 25-27, 1979.

7. Wu, S. C., "Connection and Validation of Narrow-Band ΔVLBI Phase Observation," *DSN Progress Report 42-52,* pp. 13-20. Jet Propulsion Laboratory, Pasadena, Calif., August 15, 1979.

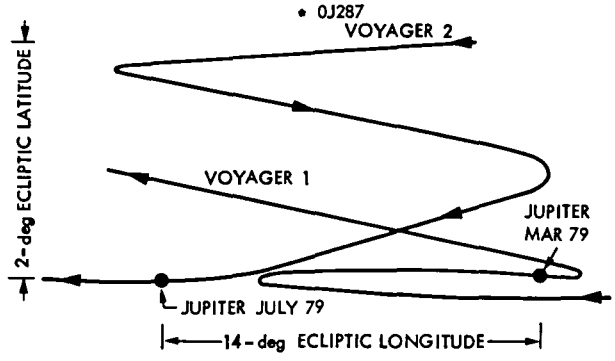

Fig. 1. The Voyager Spacecraft trajectories as seen from Earth

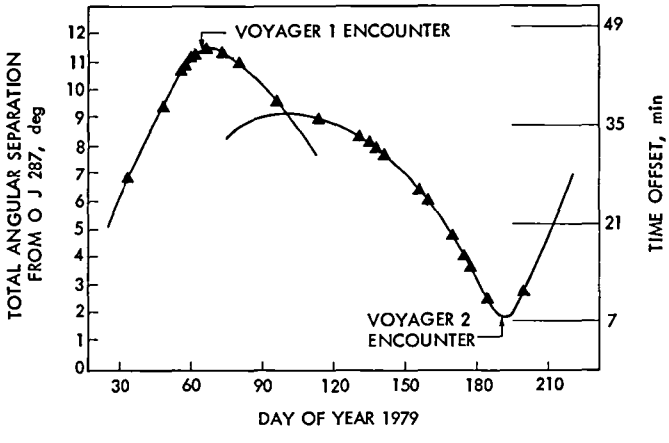

Fig. 2. The Voyager ΔVLBI passes and the Voyager-OJ 287 angular separation

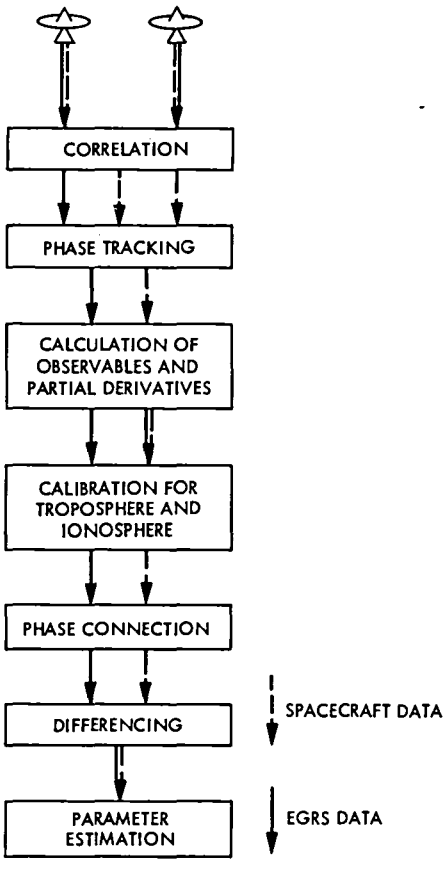

Fig. 3. Narrow-band ΔVLBI data processing steps

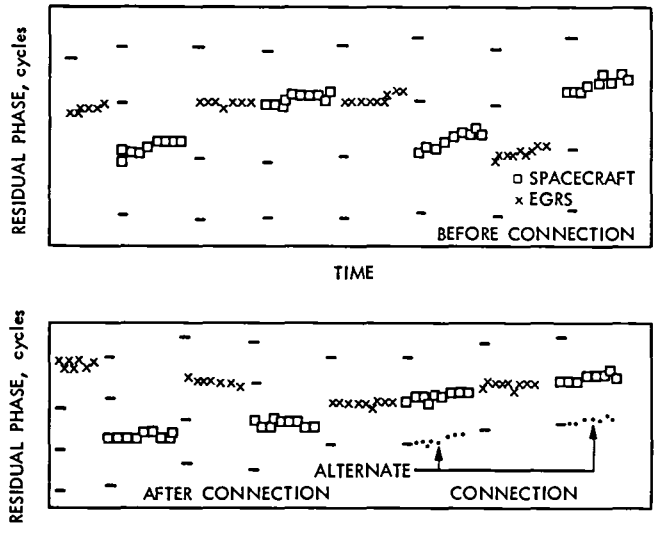

Fig. 4. Alternating scans of Voyager 2 and OJ 287 residual phase. The marks are spaced at 1-cycle increments from the first-phase residual of each scan. Note the alternative phase connection shown

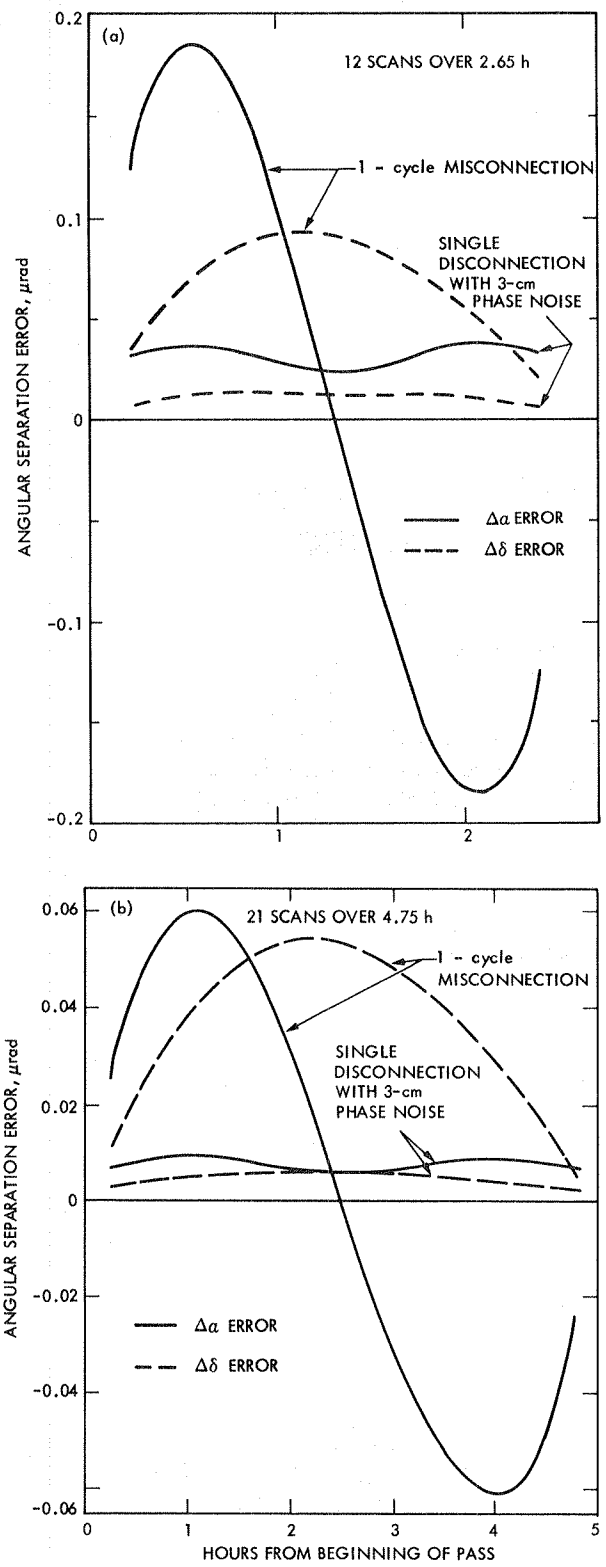

Fig. 5. Comparison of errors due to phase misconnection and disconnection (a) for a short pass (2.65 h), (b) for a long pass (4.75 h). Note the scale difference between (a) and (b)

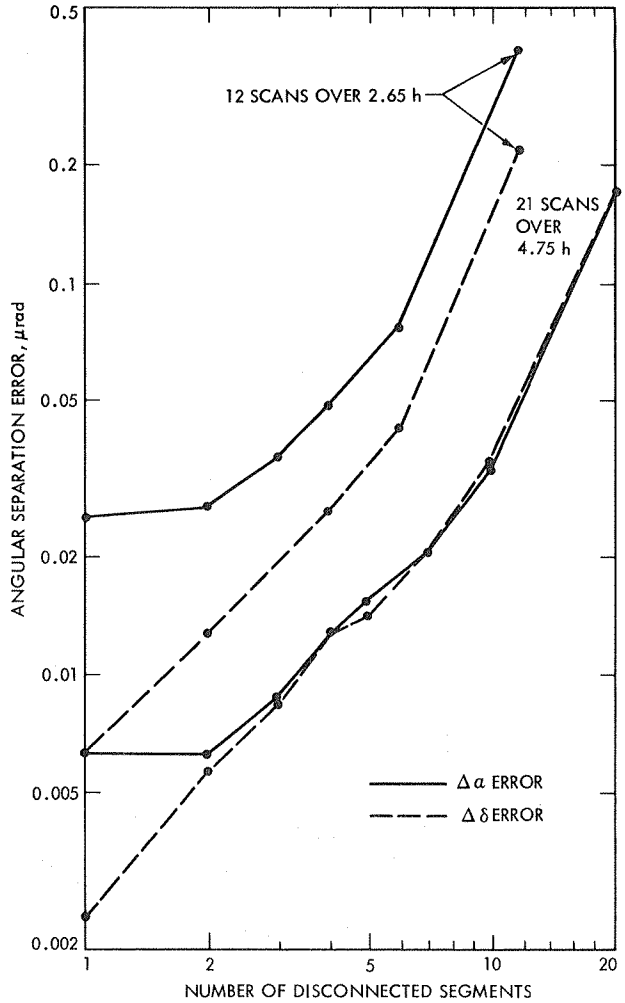

Fig. 6. Effects of phase noise on a multiply disconnected pass

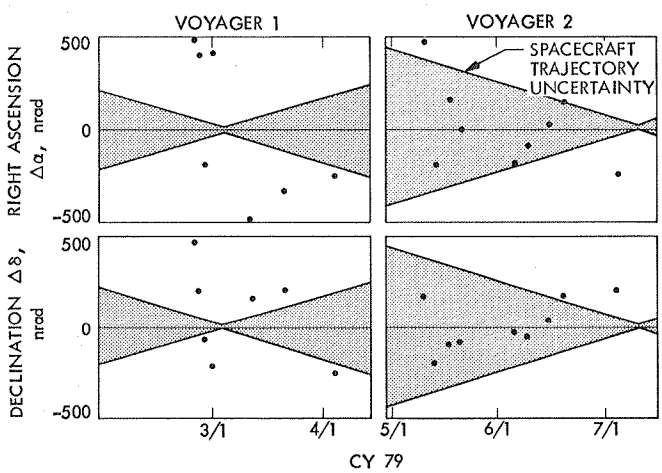

Fig. 7. Scatter plot of right ascension and declination of narrow-band ΔVLBI

Capacity, Cutoff Rate, and Coding for a Direct-Detection Optical Channel

J. L. Massey*
Communications Systems Research Section

It is shown that Pierce's pulse-position modulation scheme with 2^L pulse positions used on a self-noise-limited direct-detection optical communication channel results in a 2^L-ary erasure channel that is equivalent to the parallel combination of L completely-correlated binary erasure channels. The capacity of the full channel is the sum of the capacities of the component channels, but the cutoff rate of the full channel is shown to be much smaller than the sum of the cutoff rates. An interpretation of the cutoff rate is given that suggests a complexity advantage in coding separately on the component channels. It is shown that if short-constraint-length convolutional codes with Viterbi decoders are used on the component channels, then the performance and complexity compare favorably with the Reed-Solomon coding system proposed by McEliece for the full channel. The reasons for this unexpectedly fine performance by the convolutional code system are explored in detail, as are various facets of the channel structure.

I. Introduction

A recent paper by Pierce (Ref. 1) has heightened interest in direct-detection optical communications, particularly for space applications. Pierce considered the situation where the only "noise" limiting communications is that due to the inherent randomness of the optical field at the receiver. He proposed using M-ary pulse position modulation (PPM) together with direct-detection by photon-counting at the receiver. The T second modulation symbol interval is divided into M "slots," in only one of which an optical frequency pulse is transmitted. By virtue of the noiseless assumption, no photons will be detected by the receiver in the $M - 1$ slots where no signal is present. In the single slot where the transmitter was active, the number of photons detected will be a Poisson random variable whose mean we denote by λ. Thus λ is the average number of received photons per modulation symbol interval. With probability

$$\epsilon = e^{-\lambda}, \tag{1}$$

no photons will be detected in the slot where the pulse was transmitted. Thus, Pierce's PPM scheme creates a constant discrete memoryless channel (CDMC) that is just the M-ary erasure channel where ϵ is the erasure probability. For purposes of this paper, we restrict consideration to the case where

$$M = 2^L \tag{2}$$

*Consultant from University of California, Los Angeles. Now at Swiss Federal Technical University, Sternwartstrasse 7, CH-8006 Zurich, Switzerland.

for some positive integer L so that the modulation symbol can be specified by L binary digits.

A simple calculation gives the capacity of Pierce's PPM channel as

$$C = L(1-\epsilon)\ln(2)$$

$$= L(1-e^{-\lambda})\ln(2). \quad \text{(nats)} \tag{3}$$

On a per-photon basis, this capacity is just

$$C = L(1-e^{-\lambda})\ln(2)/\lambda, \quad \text{(nats/photon)} \tag{4}$$

which, as Pierce noted, can be made arbitrarily large by increasing the modulation alphabet size M or, equivalently, by increasing L. Pierce concluded that the problem of communicating efficiently over this self-noise-limited optical channel was thus the coding problem of finding easily implementable schemes to exploit this unlimited capacity.

Although the capacity of the CDMC created by a modulation system is an undeniably interesting characterization of the system's capabilities, it unfortunately gives no information about the complexity of the coding system needed to achieve a desired decoding error probability. This limitation led Wozencraft and Kennedy (Ref. 2) to propose using the cutoff rate, R_0, of the resulting CDMC to characterize the modulation system. They were motivated by the fact that R_0 is the upper limit of code rates for which the average decoding computation per information bit is finite when sequential decoding is employed. Massey (Ref. 3) suggested further reasons for preferring R_0 over C as a single parameter characterization of a modulation system. He noted that, whether block codes or convolutional codes are employed, R_0 specifies both a range of code rates for which reliable decoding is possible and also a measure of the complexity of the coding system that will be required to achieve a desired error probability. Massey suggested that, as a rule of thumb, R_0 is the practical upper limit on code rates for reliable communications, whereas capacity is the theoretical upper limit.

McEliece and Welch (Ref. 4) and McEliece (Ref. 5) have investigated the cutoff rate of the self-noise-limited direct-detection optical channel and reached conclusions startlingly different from those that arise from capacity considerations. In Ref. 5, McEliece showed that, even allowing multiamplitude pulsing and soft-decision demodulation, the modulation system is limited to

$$\mathcal{R}_0 \leq 1, \quad \text{(nats/photon)} \tag{5}$$

where the upper limit is attained by Pierce's PPM scheme in the limit of large M and small λ, a result anticipated in Ref. 4. In (5), we have continued the practice begun in Ref. 4 of employing script letters to denote channel measures on a per-photon basis. Note that $\mathcal{R}_0 = R_0/\lambda$ for Pierce's PPM channel.

The enormous discrepancy between the values of R_0 and C for Pierce's PPM channel renders it an ideal channel for resolving the question of which parameter gives a more meaningful measure of the quality of the modulation system. The evidence thus far has seemed to favor R_0. Note that for a fixed symbol time T, the bandwidth of Pierce's PPM scheme grows linearly with M and hence exponentially with L because of Eq. (2). McEliece, Rodemich and Rubin (Ref. 6) and McEliece (Ref. 7) have shown that this "explosive" increase in bandwidth is unavoidable in the self-noise-limited direct-detection optical channel; they showed that for code rates $\mathcal{R}$ above 1 nat/photon, the required bandwidth and the required peak-to-average signal power must both grow exponentially with $\mathcal{R}$. They conclude that no practical system could ever be built to operate at a rate $\mathcal{R}$ above, say, 10 nats/photon. The same conclusion was reached by Butman, Katz and Lesh (Ref. 8) starting from a much different point, namely with practical constraints on achievable time resolution and specification that the information rate be interestingly large, say 10^4 nats/sec or greater.

Besides the R_0 versus C debate, Pierce's PPM channel impinges on another ongoing controversy, namely assessing the relative merits of block codes and convolutional codes. For Pierce's PPM channel, the evidence thus far has seemed to favor block codes. McEliece (Refs. 7 and 9) has proposed using Reed-Solomon (RS) codes on the optical PPM channel and has shown that code rates up to 2 or 3 nats/photon are feasible. Moreover, the large alphabet over which RS codes are defined makes these codes appear as virtually ideal for this application, as will be seen in Section IIIA.

In this article, we offer additional evidence in favor of R_0 over C as a meaningful characterization of Pierce's PPM channel. But we also offer some rather surprising evidence to support the claim that convolutional codes are superior to block codes even in this application that is almost tailor made to fit the virtues of RS codes.

In Section II, we show that the optical PPM channel can be viewed as the parallel combination of L "completely correlated" binary erasure channels (BEC's), and we investigate both R_0 and C from this perspective. In Section III, we show that the use of short-constraint-length binary convolutional codes with Viterbi decoding on each component BEC yields coding performance and complexity that compare favorably to those

for RS codes, and we isolate the somewhat strange cause of this excellent performance by convolutional codes. Finally, in Section IV, we offer some additional interpretations of our results and raise some further questions of interest.

II. The Optical PPM Channel as Parallel Completely Correlated BEC's

Suppose we number the slots in Pierce's PPM scheme from 0 to $2^L - 1$. For the modulation symbol, $\underset{\sim}{x}$, we can choose the index of the slot containing the optical frequency pulse. Writing $\underset{\sim}{x}$ as the L-place radix-two number

$$\underset{\sim}{x} = [x_1, x_2, \cdots x_L]$$

$$= x_1 2^{L-1} + x_2\, 2^{L-2} + \cdots + x_L\,, \qquad (6)$$

we can view the transmission of a single modulation symbol $\underset{\sim}{x}$ as the transmission of the L binary digits $x_1, x_2, \ldots, x_L$. For example, with $L = 3$, the slots would be numbered from 0 to 7 and $\underset{\sim}{x} = [1, 1, 0]$ would instruct the transmitter to send the optical frequency pulse in slot 6. Notice that so long as even one photon is detected in the slot where the pulse was sent, the demodulator will correctly identify all L binary digits since the pulse position will be known. But when no photons are detected in this slot, the *entire* modulation symbol is "erased" and hence all L binary digits are simultaneously erased. Thus, we can represent the demodulation symbol, $\underset{\sim}{y}$, as

$$\underset{\sim}{y} = [y_1, y_2, \ldots, y_L] \qquad (7)$$

where $\underset{\sim}{y} = \underset{\sim}{x}$ when one or more photons are detected at the receiver, but $\underset{\sim}{y} = [E, E, \ldots, E]$ (where E is the "erasure indicator") when no photons are detected as happens with probability $\epsilon = e^{-\lambda}$.

Notice that with respect to the transmission of a given component x_i of $\underset{\sim}{x}$ and the reception of the corresponding component y_i of $\underset{\sim}{y}$, the PPM channel becomes simply a binary erasure channel (BEC) with the same erasure probability ϵ as for the entire modulation symbol. Thus, *each use of the 2^L-ary optical PPM channel is entirely equivalent to one use in parallel of L BEC's that are completely correlated* in the sense that an erasure either occurs on all L channels or on none.

The capacity of the BEC with erasure probability ϵ is just $(1 - \epsilon)\ln(2)$ nats. The total capacity, $(C)_{TOT}$, of the L parallel BEC's is thus

$$(C)_{TOT} = L\,(1 - \epsilon)\ln(2). \quad \text{(nats)} \qquad (8)$$

Comparing Eq. (8) with Eq. (3), we see that *there is no penalty in capacity if each of the L parallel BEC's is coded independently*, as opposed to coding jointly over the component channels, but neither is there any gain.

The situation for the cutoff rate, R_0, is much more interesting. In general, R_0 for a CDMC is given by the expression

$$R_0 = -\min_{Q} \ln \left\{ \sum_y \left[\sum_x Q(x) \sqrt{P(y|x)} \right]^2 \right\} \text{ (nats)} \qquad (9)$$

where $P(y|x)$ is the probability that the channel output symbol is y given that the input symbol was x, and where Q is a probability distribution over the channel input alphabet (Ref. 3). For the 2^L-ary erasure channel, $Q(x) = 2^{-L}$ for all x is the minimizing distribution in Eq. (9) and gives

$$R_0 = -\ln\left[\epsilon + 2^{-L}(1 - \epsilon)\right] \quad \text{(nats)} \qquad (10)$$

or, on a per-photon basis,

$$\mathcal{R}_0 = -\ln\left[e^{-\lambda} + 2^{-L}(1 - e^{-\lambda})\right]/\lambda\,. \quad \text{(nats/photon)} \qquad (11)$$

From Eq. (11), we see that for any fixed $\lambda > 0$, $\mathcal{R}_0$ increases with L but

$$\lim_{L\to\infty} \mathcal{R}_0 = 1 \text{ (nat/photon)} \qquad (12)$$

in agreement with Eq. (5).

The cutoff rate of the BEC with erasure probability ϵ is $\ln[2/(1 + \epsilon)]$ nats, as can be found by taking $L = 1$ in Eq. (10). The total cutoff rate, $(R_0)_{TOT}$, of the L parallel BEC's is thus

$$(R_0)_{TOT} = L \ln\left[2/(1 + \epsilon)\right], \quad \text{(nats)} \qquad (13)$$

which is much larger than the cutoff rate for the full channel as given by Eq. (10). In fact, from Eq. (10) and Eq. (13) we see that

$$\lim_{L\to\infty} \frac{R_0}{(R_0)_{TOT}} = 0\,. \qquad (14)$$

We will take up the interpretation of this result in Section IV-A, where we will argue that a small value of $R_0/(R_0)_{TOT}$

suggests a complexity advantage in coding over the component channels rather than jointly coding the component channels.

III. Coding for the Optical PPM Channel

A. Joint Coding of the Component Channels

McEliece (Refs. 7 and 9) has proposed using Reed-Solomon (RS) codes on Pierce's 2^L-ary PPM channel in the following manner. Each modulation symbol $\underset{\sim}{x} = [x_1, x_2, \ldots x_L]$ is treated as a digit in the finite field $GF(2^L)$. An (n, k) RS code over this field has block length $n = 2^L - 1$, k information digits for any k such that $1 \leqslant k < n$, and minimum Hamming distance $d = n - k + 1$, which is the maximum possible for a linear code with $n - k$ parity digits. A linear code with $d = n - k + 1$ is called maximum-distance-separable (MDS) to emphasize this optimality (Ref. 10, pp. 70-72). See Ref. 10, pp. 277-308 for further properties of RS codes and for decoding procedures.

The maximum number of erasures guaranteed correctable by a linear code with minimum Hamming distance d is $d - 1$. Thus an (n, k) RS code can correct all patterns of $n - k$ or fewer erasures, but cannot correct all patterns of $n - k + 1$ erasures. All the well-known algebraic decoding procedures for RS codes correctly decode all patterns of $n - k$ or fewer erasures but virtually no patterns of more than $n - k$ erasures. Thus, it is customary to assume that a decoding error occurs whenever $n - k + 1$ or more erasures occur so that the block error probability, P_e, after decoding is

$$P_e = \sum_{s=n-k+1}^{n} \binom{n}{s} \epsilon^s (1 - \epsilon)^{n-s} \tag{15}$$

where ϵ is the symbol erasure probability. Our interest, however, is in the bit error probability, P_b, defined as the average probability of error among the kL binary digits that form the k $GF(2^L)$ information digits in the RS code. When a decoding error is made, it is made with high probability to a nearest-neighbor codeword so that $d = n - k + 1$ symbol errors are made. Because a RS code is cyclic, the error probability in each symbol is the same so that the probability that a particular information symbol is in error, given a decoding error, is very nearly d/n. But on the average very close to half of the binary digits forming an information symbol will be incorrect when that symbol is decoded incorrectly. Hence, to a very good approximation,

$$P_b \approx \frac{1}{2} \frac{n - k + 1}{n} P_e \tag{16}$$

for the RS codes.

McEliece (Refs. 7 and 9) has observed that the best performance (i.e., smallest P_e for a given bandwidth after coding) on Pierce's PPM channel is obtained from the RS codes with dimensionless rate $k/n \approx 1/2$. In particular, he proposed using the (31, 16), (63, 32) and (127, 64) RS codes over $GF(2^5)$, $GF(2^6)$ and $GF(2^7)$, respectively. In Fig. 1, we give plots of P_b versus the code rate

$$\mathcal{R} = \frac{k}{n} \frac{\ln (L)}{\lambda} \quad \text{(nats/photon)}$$

for these three codes. These plots were taken from Ref. 8, where they were given as P_e as calculated by Eq. (15), after conversion to P_b via Eq. (16). Note that the above expression reflects the fact that on the average, λ photons are used to transmit each $GF(2^L)$ encoded symbol. Note also that λ determines the erasure probability ϵ according to Eq. (1).

Figure 1 shows that reliable communications using RS codes is feasible for rates up to about 2 nats/photon. Notice that the coding and modulation together expand the transmitted bandwidth relative to on/off binary signalling by a factor

$$F = \frac{n}{k} \frac{2^L}{L} \approx \frac{2^{L+1}}{L} \tag{17}$$

where the factor $2^L/L$ is due to the PPM modulation which uses 2^L slots to transmit L binary digits, and where the factor $n/k \approx 1/2$ is due to the RS code which uses (very close to) 2 encoded symbols for each information symbol. The bandwidth expansion factor F is indicated on each curve in Fig. 1. The 37-fold expansion for the (127, 64) RS code is perhaps near the practical limit for time resolution at reasonably high data rates; the required 63 erasure-correcting RS decoder is certainly near the practical limit of complexity.

The RS codes, because they are MDS codes, have maximum erasure-correcting power for their length and number of information symbols. Moreover, their symbol alphabet $GF(2^L)$ is ideally matched to the 2^L-ary PPM channel since each erasure by the receiver erases only one code symbol although it erases all L binary components of that symbol. It is doubtful that any block coding scheme can significantly outperform McEliece's RS coding scheme on the PPM channel for a given bandwidth expansion and a given decoder complexity.

B. Separate Coding of the Component Channels

We now consider employing a separate binary coding scheme on each of the L BEC's that constitute the 2^L-ary

optical PPM channel. Note that this is equivalent to interleaving L separate binary encoded streams to form a single binary stream whose digits, taken in blocks of length L, constitute the modulation symbols.

The use of binary block codes with algebraic decoding gives disappointingly poor performance in this separate channel mode of coding for the PPM channel. For instance, the (31, 16) binary BCH code has minimum Hamming distance 7 and is thus 6 erasure correcting. However, the (31, 16) RS code considered above can also be considered to be encoding 16 information bits on each component channel into 31 binary digits, yet is 15 erasure correcting on each component channel. The cross channel constraints imposed by the RS code effectively more than doubles the number of correctable erasures compared to the single channel BCH code. The BCH code performs thus much worse than the RS code when L is chosen for the BCH code to give the same bandwidth expansion as does the RS code, and is not significantly easier to decode. The (24, 12) 7 erasure correcting Golay binary code fares little better than the BCH code, as can also be seen from Fig. 1.

In light of the above, it seems quite surprising that good performance relative to the RS codes can be obtained by separately coding the component BEC's, using short-constraint-length convolutional codes with Viterbi (i.e., maximum-likelihood (ML)) decoding (Ref. 11, pp. 227-252). In Fig. 1, we show the performance of dimensionless rate 1/2 binary convolutional codes with constraint length K (measured in information bits) for $K = 4$, 6 and 8. In each case, the number L of component channels was chosen so that the bandwidth expansion factor

$$F = \frac{2^{L+1}}{L} \tag{18}$$

matched that of one of the RS codes considered above.

We see from Fig. 1 that the binary $K = 4$ convolutional code gives virtually the same performance as the (31, 16) RS code with the same bandwidth expansion factor. The required $2^{K-1} = 8$ state Viterbi decoder appears much easier to implement than the corresponding 15 erasure correcting RS decoder. Similarly, we see from Fig. 1 that the $K = 6$ binary convolutional code is an attractive competitor to the (63, 32) RS code, and that the $K = 8$ binary convolutional code fares well against the (127, 64) RS code.

Inasmuch as they sacrifice the substantial advantage that can be gained by coding across the component channels (which the RS codes exploit with maximum effectiveness), it appears puzzling at first that the short-constraint-length binary convolutional codes perform so well in the separate channel coding mode for the PPM channel. The explanation is that Viterbi decoders, unlike algebraic decoders, degrade gracefully. The free distance d_f of the convolutional code determines that no patterns of $d_f - 1$ or fewer erasures can cause a decoding error but that some patterns of d_f erasures will. However, the Viterbi decoder, because it is a ML decoder, corrects the overwhelming majority of patterns of d_f, $d_f + 1$, and more erasures. This ability to go beyond the minimum distance bound on erasure correction fully compensates for the sacrifice made in coding separately on the component channels.

The convolutional code performance curves in Fig. 1 are actually the Bhattacharyya upper bounds on P_b (Ref. 11, p. 246). According to this bound,

$$P_b \leqslant f(z) \tag{19}$$

where f is a rational function determined by the state-transition structure of the convolutional encoder, and where z is the channel parameter

$$z = \sum_y \sqrt{P(y|0)\,P(y|1)}\,. \tag{20}$$

For the BEC,

$$\begin{aligned} z &= \epsilon \\ &= e^{-\lambda} \end{aligned} \tag{21}$$

where we have made use of Eq. (1).

To obviate explicitly finding f, we employed the following "trick" due to Omura (Ref. 12). For the additive white Gaussian noise (AWGN) channel with binary antipodal signals of energy E and one-sided noise power spectral density N_o, one finds

$$z = e^{-E/N_o}\,. \tag{22}$$

Thus, for the same code, the bound Eq. (19) on P_b will be the same for the BEC as for the AWGN if one chooses

$$\lambda = E/N_o\,. \tag{23}$$

By the artifice of Eq. (23), we converted the bound Eq. (19) on P_b versus E_b/N_o (where $E_b = 2E$ is the energy per

information bit) given in Ref. 12 to the convolutional code performance curves given in Fig. 1.

IV. Interpretations, Remarks, and Questions

A. On the Significance of R_0

As was first shown by Viterbi, the average bit error probability for ML decoding of the ensemble of time-varying convolutional codes of rate R and constraint length N (measured in encoded digits) on a CDMC with cutoff rate R_0 satisfies

$$P_b \leqslant c_R\, e^{-NR_0} \quad \text{if } R < R_0 \tag{24}$$

where c_R is an unimportant factor that depends on R but not on N (Ref. 11, p. 312). Moreover, the error exponent R_0 in Eq. (24) is also the exponent of P_b versus N for the sequence of best codes at each length N when $R \approx R_0$ (Ref. 11, p. 320). This strongly suggests that R_0 should be considered as at least a rough measure of the necessary code constraint length in channel symbols required to achieve a given P_b, in the sense that doubling R_0 will roughly halve the required N.

To validate this interpretation in a fairly trivial instance, consider a CDMC that is the parallel combination of L identical and independent CDMC's. Letting R_0 be the cutoff rate of the full channel and $(R_0)_{TOT}$ be the sum of the cutoff rates of the component channels, one easily verifies from Eq. (9) that

$$R_0 = (R_0)_{TOT} \tag{25}$$

so that R_0 is exactly L times that of each component channel. Thus, by the above interpretation, for a given P_b separate coding on each channel should require a constraint length in channel symbols L times that required for joint coding of the channels. But a channel symbol for the full channel is equivalent to L channel symbols for a component channel. Thus, the required constraint length, measured in symbols for the component channel, is the same whether separate channel or joint channel coding is used. This is hardly surprising since one use of the full channel is, because of the independence of the component channels, entirely equivalent to L uses of one component channel. But this does illustrate that the above interpretation of R_0 is precisely correct in this case.

Next, consider the optical PPM channel viewed as L parallel but completely correlated BEC's. Recall also from Eq. (14) that R_0 for the full channel is generally much smaller than L times that for each channel, i.e., $R_0 \ll (R_0)_{TOT}$. The above interpretation of R_0 then suggests that a much smaller binary digit constraint length on the component channels will suffice to give the same P_b compared to the constraint length *in binary digits* required for cross-channel coding. This suggests a complexity advantage in coding separately for each of the component channels. To illustrate the quantitative validity of R_0 in this context, note that for dimensionless rate 1/2 coding on the 2^L-ary PPM channel, a rate of $\mathcal{R}$ nats/photon corresponds to an average of

$$\lambda = \frac{1}{2} L \ln(2)/\mathcal{R} \tag{26}$$

photons in the transmitted pulse. For example, with $L = 5$ and $\mathcal{R} = 1.0$ nats/photon, Eq. (26) gives $\lambda = 1.73$ photons. From Eq. (1), we find the corresponding erasure probability to be $\epsilon = 0.177$. Then from Eqs. (10) and (13) we find $R_0 = 1.597$ and $(R_0)_{TOT} = 2.652$, respectively. This suggests that the required constraint length in binary digits required for joint coding of the $L = 5$ BEC's will be about $2.652/1.597 = 1.66$ times that required for separate coding of each BEC to obtain the same P_b. To test this conclusion, consider again Fig. 1. Note that for $\mathcal{R} = 1.0$, the $K = 4$ ($L = 5$) convolutional code gives virtually the same P_b as does the (31, 16) RS code. But the RS code has a constraint length of $5(31) = 155$ binary digits. Using the rule of thumb that the effective decoding constraint length of a convolutional code is about twice that of a block code with the same encoding constraint length, we can approximate the equivalent block code constraint length of the convolutional code as about $2K/(1/2) = 16$ binary digits. The ratio $155/16 = 9.7$ of the required constraint lengths is rather larger than the ratio $(R_0)_{TOT}/R_0 = 1.66$, but the discrepancy is probably due more to the difficulty of comparing a convolutional code to a block code than to the coarseness of our interpretation of R_0.

B. On ML Decoding of the RS Codes

We observed in Section III-B that the ML nature of Viterbi decoding, which allows most patterns of more than $d_f - 1$ erasures to be corrected, was the primary reason for the strong performance of binary convolutional codes as compared to the RS block codes on the 2^L-ary optical PPM channel. The question then arises as to whether the performance of the RS codes could not also be greatly enhanced if they were decoded by a ML decoder rather than a distance-limited algebraic decoder. The answer, surprisingly, is no.

Suppose that s erasures occur in the RS code symbols where $s > n - k$. This leaves only $n - s < k$ unerased digits in the block. However, the MDS property of RS codes implies that every set of k code positions is an information set, i.e., that it can be used as the positions containing the k information digits. Thus, there will be at least one erased

position to which we can assign an arbitrary digit in $GF(2^L)$ and still be able to find a codeword that matches it and all the unerased digits. Thus there will be at least 2^L codewords matching all the unerased digits, and even a ML decoder can do no more than guess which of these was the transmitted codeword. It follows that, given that more than $n - k$ erasures have occurred, any decoder for the RS code will err with probability at least $(2^L - 1)/2^L \approx 1$, even though the code can correct all patterns of $n - k$ and fewer erasures. The conclusion is that no RS decoder can degrade gracefully on the optical PPM channel and that a ML decoder is negligibly better than an algebraic decoder on this channel. We caution the reader, however, to note that this conclusion would not hold on many other types of channels where ML decoding would be significantly better than algebraic decoding of RS codes.

C. Correlated Decoding of the Component Channels

When coding separately for each of the L component BEC's of the optical PPM channel, one can either use L separate binary coding systems or time-share one such system that operates at L times the speed required for the separate systems. In either case, the decoding complexity would be reckoned at about L times that of each separate system. We point out now that there is a possibility to reduce substantially the decoding complexity when separate channel coding is used.

Because the L components BEC's of the 2^L-ary optical PPM channel are completely correlated, the decoder for one channel can pass useful information to the other $L - 1$ decoders to simplify their decoding tasks; i.e., the decoders can profitably operate in a "correlated" fashion. To see this more clearly, note that the decoder for a linear (whether block or convolutional) binary code used on the BEC effectively solves the linear equations, determined by the code, that relate the erased digits to the unerased digits. The decoder effectively evaluates each erased digit as a modulo-two sum of certain unerased digits. Thus, after the first decoder has determined which set of unerased digits should be added to find a given erased digit, it can pass this information to the other $L - 1$ decoders. Then, because the erasure patterns on all L BEC's are identical, these other decoders need merely to add (modulo-two) the unerased digits that have been received over their own channels in those positions specified by the first decoder. Such correlated or "cooperative" decoding is clearly possible in principle and would have obvious complexity advantages. However, we have not yet succeeded in finding a general way to implement such correlated decoding when a Viterbi decoder is used, although we have been able to find simple implementations for certain very-short-constraint-length convolutional codes.

D. Correlated Channels

The somewhat curious properties of the optical PPM channel viewed as a parallel combination of completely correlated BEC's suggest that it might be interesting to consider more generally a CDMC that is the parallel combination of identical CDMC's that have some specified dependency. The relationship of R_0 to $(R_0)_{TOT}$ should be especially interesting. It should also be interesting to consider whether correlated decoding to reduce decoding complexity can be performed when each component channel is separately encoded.

E. Background Noise on the Optical PPM Channel

It is clear that the self-noise-limited optical PPM channel model used throughout this paper becomes physically inappropriate when the signalling bandwidth becomes sufficiently large. Account then must be taken of background radiation that can lead to "errors" as well as erasures by the (preferably soft-decision) demodulator. We will not pursue these matters further here except to note that the short-constraint-length convolutional codes with Viterbi decoding can easily be adapted to make use of the soft-decision demodulation information, but the RS block codes cannot. Thus, the convolutional codes should become even more attractive vis-a-vis the RS codes when background noise is sufficiently strong so that it must be taken into account. Convolutional codes with Viterbi decoding seem to make a more robust coding system than do RS codes with algebraic decoding.

References

1. Pierce, J. R., "Optical Channels: Practical Limits with Photon Counting," *IEEE Trans. Comm.*, vol. COM-26, pp. 1819-1821, Dec. 1978.

2. Wozencraft, J. M., and Kennedy, R. S., "Modulation and Demodulation for Probabilistic Coding," *IEEE Trans. Info. Th.*, vol. IT-12, pp. 291-297, July 1966.

3. Massey, J. L., "Coding and Modulation in Digital Communications," in *Proc. Int. Zurich Sem. on Digital Comm.*, Zurich, Switzerland, Mar. 12-15, 1974.

4. McEliece, R. J., and Welch, L. R., "Coding for Optical Channels with Photon Counting," in *The Deep Space Network Progress Report 42-52*, pp. 61-66, Jet Propulsion Laboratory, Pasadena, Calif., Aug. 15, 1979.

5. McEliece, R. J., "The R_0-Parameter for Optical Communication Using Photon Counting, in *The Deep Space Network Progress Report 42-53*, pp. 62-65, Jet Propulsion Laboratory, Pasadena, Calif., Oct. 15, 1979.

6. McEliece, R. J., Rodemich, E. R., and Rubin, A. L., "The Practical Limits of Photon Communication," in *The Deep Space Network Progress Report 42-55*, pp. 63-67, Jet Propulsion Laboratory, Pasadena, Calif., Feb. 15, 1980.

7. McEliece, R. J., "Practical Codes for Photon Communication," submitted to *IEEE-Trans. Info. Th.*, 1980.

8. Butman, S. A., Katz, J., and Lesh, J. R., "Practical Limitations on Noiseless Optical Channel Capacity," in *The Deep Space Network Progress Report 42-55*, pp. 12-14, Jet Propulsion Laboratory, Pasadena, Calif..

9. McEliece, R. J., "Coding for the Photon Channel," in *Proc. Nat. Tel. Conf.*, pp. 23.3.1-23.3.3, 1979.

10. Peterson, W. W., and Weldon, E. J., Jr., *Error-Correcting Codes*, 2nd ed. M.I.T. Press, Cambridge, Mass., 1972.

11. Viterbi, A. J., and Omura, J. K., *Principles of Digital Communication and Coding*, McGraw-Hill, New York, 1979.

12. Heller, J. A., and Jacobs, I. M., "Viterbi Decoding for Satellite and Space Communication, *IEEE Trans. Comm.*, vol. COM-19, pp. 835-848, 1971.

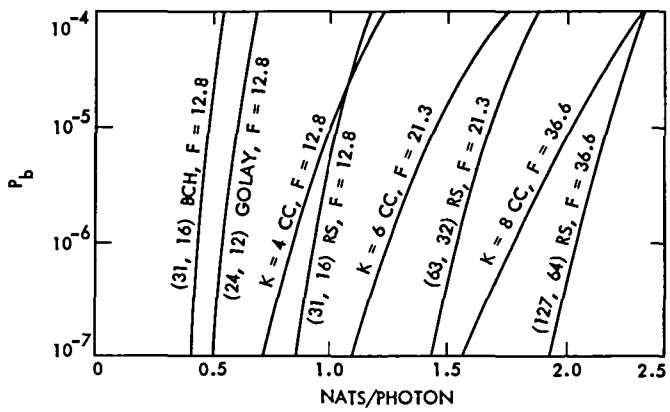

Fig. 1. Bit decoding error probability versus code rate in nats/photon for selected Reed-Solomon (RS) codes, convolutional codes (CC), the (31, 16) BCH code, and the (24, 12) Golay code on the optical PPM channel. F is the bandwidth expansion factor due both to the modulation system and coding scheme

A Prototype DSN X/S-Band Feed: DSS 13 Application Status (Fourth Report)

W. Williams and H. Reilly
Radio Frequency and Microwave Subsystems Section

This article, the fourth in this series, discussing a prototype X/S-band common aperture horn feed for future use at various DSN sites and the Network Consolidation Program, deals with the final design and fabrication of the second-generation feedhorn and combiner. The results of the measurements obtained with the second-generation, full-scale feed configuration are presented.

I. Introduction

The first three articles (Refs. 1, 2, and 3) in this series discussed the development of a first-generation, dual-band (X-S) corrugated feedhorn for DSN applications. The earlier articles presented horn radiation patterns and resultant reflector antenna efficiencies using a half-scale horn model, the design of an X-S combiner permitting injection of both bands into the horn, and finally the measurements on the full-scale, first-generation horn and combiner.

The first horn model tests gave evidence of a small amount of "moding" in the X-band, but still within the specification requirement, and the X-S combiner had just enough S-band frequency bandwidth to satisfy the original narrow S-band requirement of approximately 40 MHz.

A second-generation horn system was begun and evolved where the major requirement was to increase the S-band performance across sufficient range to encompass DSN S-band high-power transmission as well as the DSN receive bands (2.10 to 2.30 GHz). As an adjunct, it was desired to determine the cause of X-band moding and, if possible, to correct it. The technique for broadening the combiner S-band bandwidth was by increasing the combiner radial line height and carefully designing a wideband matching network; the method of correcting X-band moding is discussed in Ref. 3.

II. The Full-Scale, Second-Generation X/S Horn

Early investigations into the causes of X-band moding indicated that the abrupt horn input angular change from cylindrical waveguide to the 34-degree wide-angle horn caused some moding, but probably not as much as noted. Therefore, the final horn version was to be built using a gradual change to the 34-degree flare angle over a 100-mm transition length to partially reduce moding.

A unique concept for this corrugated horn, relative to others that have been used, is the abrupt change in corrugation (groove) depth in the region of the horn where S-band is introduced. Grooves must be between ¼- and ½-wavelength deep to generate the proper corrugated waveguide hybrid mode. When cut the required depth for S-band, they become from 1¼- to 1½-wavelength deep in X-band, and hence will generate the proper X-band boundary conditions and modes.

However, the particular configuration of the combiner design in this program did not allow the full groove depths to be used in the horn input region where only X-band was present and so shallower grooves were used (¼ to ½ wavelength at X-band) at the input. This then necessitated an abrupt change near the combiner S-band input from the ¼-wavelength groove (X-band) to the 1¼ wavelength groove (X-band). This change represents a potential discontinuity in groove impedance for the X-band, dependent upon X-band frequency.

Experiments with sections of the first-generation horn revealed that this impedance discontinuity was the major cause of extraneous moding, (indicated by the level of cross polarization in the 45-degree pattern cut). Therefore, groove depths were cut that gave a groove impedance match near the center of the desired X-band range, and hence symmetrical mismatches at the band edges; e.g., at 7.8 GHz, the two groove depths at the abrupt change were 0.297λ (λ = X-band wavelengths) and 1.297λ, giving a "perfect" match. This resulted in measured -43-dB cross polarization, a good result indeed. At 7.1 GHz, the selected depth results in a 0.271λ input groove and a 1.18λ output groove, a mismatch giving rise to a cross-polarization level of -28 dB; however, this is still acceptable. At 8.45 GHz, the selected (7.8-GHz) depth results in a mismatch from 0.322λ to 1.405λ, and similar (-28-dB) cross-polarization levels.

Therefore, the full-scale, second-generation horn was made with X-band input grooves at 11.43 mm and output grooves at 49.89 mm, giving the ideal match at midband, 7.8 GHz, unfortunately a frequency region of no planned use. Our intentions are to provide 7.1-GHz and 8.4-GHz bands in the second-generation horn.

In the first-generation horn, the grooves were but 3.55-mm wide, the object being to have as many grooves per X-band wavelength as possible. This has always been reasonable in the past because such an assumption was made in theoretically solving for the hybrid mode fields in corrugated waveguide. However, in our second-generation horn (at the suggestion of B. M. Thomas, Ref. 4) the grooves were cut much wider; the only requirement being that they remain less than ½-wavelength wide at the highest intended frequency. This has worked quite well and permitted an easier (higher waveguide) access for the S-band horn input. The second generation horn has grooves of 12.7-mm width with a 3.55-mm wall.

The full-scale, second-generation horn was machined from five billets of aluminum with the smaller X-band input section and the X/S combiner made from separate pieces. The first generation horn exterior photograph given in Ref. 3 is not unlike our later development.

The radiation patterns of the second-generation horn have been measured at many frequencies throughout both the X and S bands. These measurements are made using linear polarizations. At each frequency, an E- and an H-plane pattern were recorded and also a pattern in the 45-degree plane. Also in the 45-degree plane the cross-polarization pattern was recorded, this indicating the lack or presence of unwanted radiating modes. E- and H-plane patterns are presented together on one graph while a second graph shows the 45-degree plane matched and cross polarized.

Figure 1 presents the results at X-band while Fig. 2 presents results at S-band. The E- and H-plane equivalence is very good and the complete lack of sidelobes down to minus 40 dB (and lower) contributes to a uniquely higher forward spillover efficiency than has been available before in X-band. Although the S-band patterns also are devoid of sidelobes, the shape of these patterns results in greater than typical forward spillover. Note the relative steepness on the sides of the X-band patterns compared to the sides of S-band patterns – a result of maintaining a sensible horn aperture size.

III. The Full-Scale, Second-Generation X/S Combiner

The first-generation X/S-band combiner performed its function well; it extracted the S-band receive signal from the horn at low loss, contributing little to system noise performance and its X-band isolation was great enough such that any additional X-band noise contribution was not detectable. However, this unit was, at S-band, of such narrow bandwidth that it could not be used for simultaneous S-band reception and transmission. Broadening the S-band bandwidth of this combiner so that receive/transmit functions could be included was the major objective of the second-generation development.

The first-generation combiner is comprised (see Ref. 2 for photos and a detailed discussion) of a thin radial line, only 8.89-mm wide, surrounding the horn at a horn diameter of about 119.4 mm and used to inject S-band into the horn. Internal to the radial line are a pair of X-band rejection chokes that isolated the X-band successfully so that no additional X-band noise could be detected as coming from the S-band portions. The very narrow radial line was chosen to help assure that no X-band energy could penetrate the combiner. However, this narrow line also tends to make the S-band passband more limited (as determined by the impedance variation with frequency looking into the combiner). The horn entry point (119.4-mm diam.) was selected for a best impedance match at 2.3 GHz and this resulted in a bandwidth of approximately 50 MHz over which input VSWR was less than 1.2:1.

In the second-generation combiner, the radial line section has been increased to 12.7 mm to increase the S-band bandwidth performance to include S-band transmission from 2.1 to 2.3 GHz. The band center is now lower (2.2 GHz) and therefore a new injection horn diameter of 127 mm is used. An increase to four X-band reject radial line chokes is used to maintain the required high X-band isolation. As with the first-generation combiner, tuning irises were required to be inserted into the radial line area to achieve an acceptable performance across the S-band. It was convenient to place these irises as metal blocks inserted into portions of the X-band chokes. A disassembled picture of this combiner is shown in Fig. 3.

The combiner along with its four 12.7-mm input waveguide terminals is not matched to standard S-band waveguide. The additional matching must be done with a transformer-tuner that transforms the 12.7-mm waveguide height to the 54.6-mm height of standard S-band (WR-430) waveguide and at the same time provides the necessary tuning to match the input impedance over the required bandwidth to a VSWR (voltage standing wave ratio) of less than 1.2:1. The graph shown in Fig. 4 represents the VSWR looking into any one of the four combiner input terminals. The requirement on the tuner is to develop a response VSWR of less than 1.2:1 from 2.1 to 2.3 GHz.

The transformer-tuner was designed and is fabricated using a 3-step, 2-section waveguide section to transform from the 12.7-mm height waveguide combiner input (standard 109.2-mm width), down to a narrow height guide of only 3.12 mm, increasing to a section of 39.4-mm height and then to the full 54.6 mm of standard waveguide. At the final step, an inductive iris is inserted into the 39.4-mm size that tunes the total combination across the required band. The VSWR response of the transformer-tuner and combiner is also shown in Fig. 4. Note that there exists a small region above 2.25 GHz where the VSWR exceeds 1.2:1, but this receive-only region is less critical than the lower or transmit end of the band, and fully acceptable.

The tuner-combiner is designed to transmit 20-kW CW power, or 5 kW into each tuner port under circular polarization excitation. Calculations of voltage breakdown in the 3.12-mm height section of waveguide indicate that it has this capability with sufficient safety factor. However, if the transmitter requirement should become 100 kW or more at a later date, there is serious question about the performance of this particular transformer-tuner design.

IV. A Tuner Design for High Power

Another model transformer-tuner was designed for the eventuality of higher power transmission. This unit has but two steps and one section to transform the required impedances. The minimum waveguide height of this unit is 12.3 mm and will withstand a 200-kW transmitter with sufficient safety factor. However, the unit does not meet the 1.2:1 VSWR specification across the entire 2.1- to 2.3-GHz S-band, but only in two narrow bands that include the present DSN transmit (2110- to 2120-MHz) and receive (2290- to 2300-MHz) bands. The VSWR response of the high-power tuner and combiner is also shown in Fig. 4. From Fig. 4, one notes that the two bands remain less than VSWR = 1.2 over roughly equal 35-MHz bandwidths.

V. Calculated Performance for DSS 13 Demonstration Application

Referring to Ref. 2, p. 41, one notes the discussion concerning the DSS 13 subreflector having been designed for S-band. Again, as in the first generation case, the measured horn patterns of Figs. 1 and 2 are used in a scattering program with the DSS 13 subreflector (including the vertex plate and outer flange) to determine the final primary reflector excitation and efficiency for the 26-meter paraboloid at DSS 13.

Two techniques are used to determine these subreflector scattered patterns. In one, the measured *far field* pattern is used to determine current excitations on the subreflector and finally the physical optics scattering. In the other technique, the horn radiation pattern is used to determine its spherical wave coefficients (Ref. 5) and these are then used to determine currents on the subreflector at its unique range from the horn, instead of assuming far field. These techniques agreed to within 0.5 percent, and so the far field approach is used for all calculations herein.

Figure 5 shows the DSS 13 scattered patterns in X-band and S-band. One can observe the effect of the S-band designed vertex plate at X-band with a smaller, perhaps modest, effect at S-band. Although subreflector blockage of radiated power is reduced to essentially zero at X-band, a corresponding X-band loss is noted (relative to S-band) in illumination efficiency and phase efficiency, due to pattern distortions related to the (oversized) vertex plate.

The efficiencies calculated from these scatter patterns are tabulated in Table 1. The 71.3-percent value at X-band is about 5 percent higher than the heretofore standard (22-dB) horn feed used, or about +0.3 dB.

Figure 6 presents the calculated far-field patterns from the 26-meter paraboloid. These patterns neglect the effect of spar blocking and surface tolerance; hence all final measured patterns will have somewhat higher sidelobes.

Using the geometrical shadow from the spars at DSS 13 and an empirically developed radio-frequency factor for spar blockage, a spar blockage efficiency of 0.861 has been determined. Also the surface tolerance (ϵ) at DSS 13 is less than 1.5-mm rms. When applied to the surface tolerance efficiency formula

$$\eta(\text{surface}) = \exp\left(\frac{-\{4\pi\epsilon\}^2}{\lambda}\right)$$

there results the surface tolerance efficiencies

75.4 percent at 8.450 GHz

97.9 percent at 2.295 GHz

The final expected performance at DSS 13 may now be obtained as shown in Table 2. These overall efficiencies neglect all feed internal losses and final feed VSWR.

VI. Conclusions

The X/S second-generation feed system will develop about 3-percent more gain than the standard 22-dB horn in the DSS 13 configuration. Also, since the noise contribution from rear spillover is less, a slight improvement in system noise temperature may be expected. A significant advantage will be seen in the application of this feed in other configurations, particularly the planned Network Consolidation Project. This will be the subject of a later article.

The concluding work on the horn system will take place at the DSN Microwave Test Facility where system noise and power capability will be measured. This will be the subject of a final article.

References

1. Williams, W. F., "A Prototype DSN X-S Band Feed: DSS 13 First Status Application," *DSN Progress Report 42-44, January and February 1978.* Jet Propulsion Laboratory, Pasadena, Calif.

2. Williams, W. F., "A Prototype DSN X-S Band Feed DSS 13 Application Status (Second Report)," *DSN Progress Report 42-47, July and August 1978.* Jet Propulsion Laboratory, Pasadena, Calif.

3. Williams, W., et al., "A Prototype DSN X/S Band Feed: DSS 13 Application Status (Third Report)," *DSN Progress Report 42-52, May and June 1979.* Jet Propulsion Laboratory, Pasadena, Calif.

4. Thomas, B. Mac A., "Design of Corrugated Horns," *IEEE Trans. on Ant. and Prop.*, Vol. AP-26, No. 2, March 1978.

5. Ludwig, Arthur C., "Near-Field Far-Field Transformations Using Spherical Wave Expansions," *IEEE Trans. on Ant. and Prop.*, Vol. AP-19, March 1971, pp. 214-220.

Table 1. Second-generation DSS 13 efficiencies

Efficiency	Frequency = 8.450 GHz	Frequency = 2.290 GHz
Rear spillover	0.997	0.994
Forward spillover	0.979	0.889
Illumination	0.811	0.865
Cross-polarization	0.999	0.999
Phase	0.902	0.925
Blockage (subreflector)	1.0	0.972
Total	0.713	0.686

Table 2. Second-generation DSS 13 final overall efficiency

Efficiency	Frequency = 8.450 GHz	Frequency = 2.295 GHz
RF feed efficiency	0.713	0.686
Surface efficiency	0.754	0.979
Spar blockage	0.861	0.861
Final overall efficiency	0.463	0.578

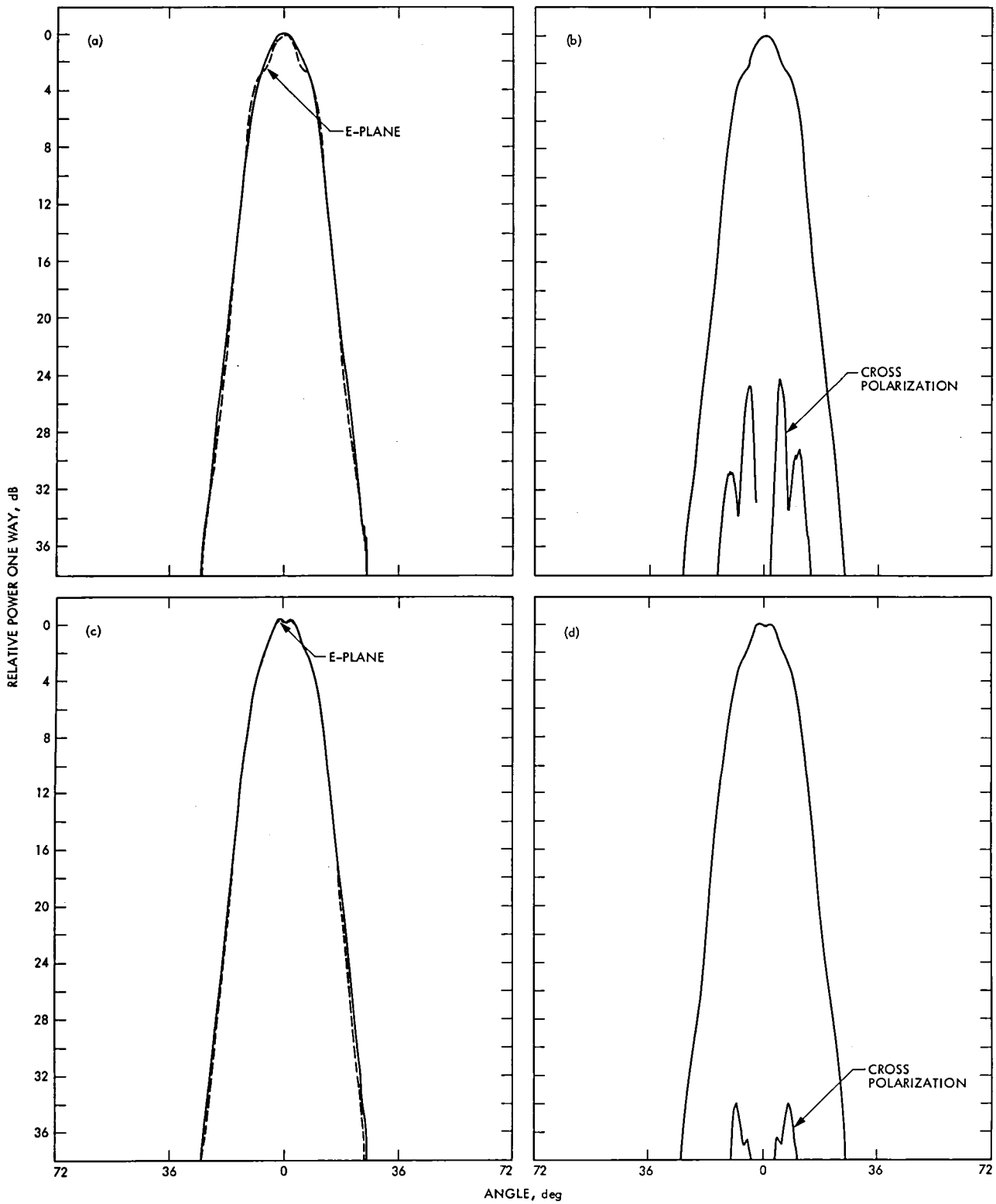

Fig. 1. Radiation patterns of the second-generation feedhorn in X-band: (a) E and H plane patterns at 8.45 GHz; (b) pattern cut at 45 deg to show cross polarization at 8.45 GHz; (c) E and H plane patterns at 7.8 GHz; (d) pattern cut at 45 deg to show cross polarization at 7.8 GHz; (e) E and H plane patterns at 7.1 GHz; (f) pattern cut at 45 deg to show cross polarization at 7.1 GHz

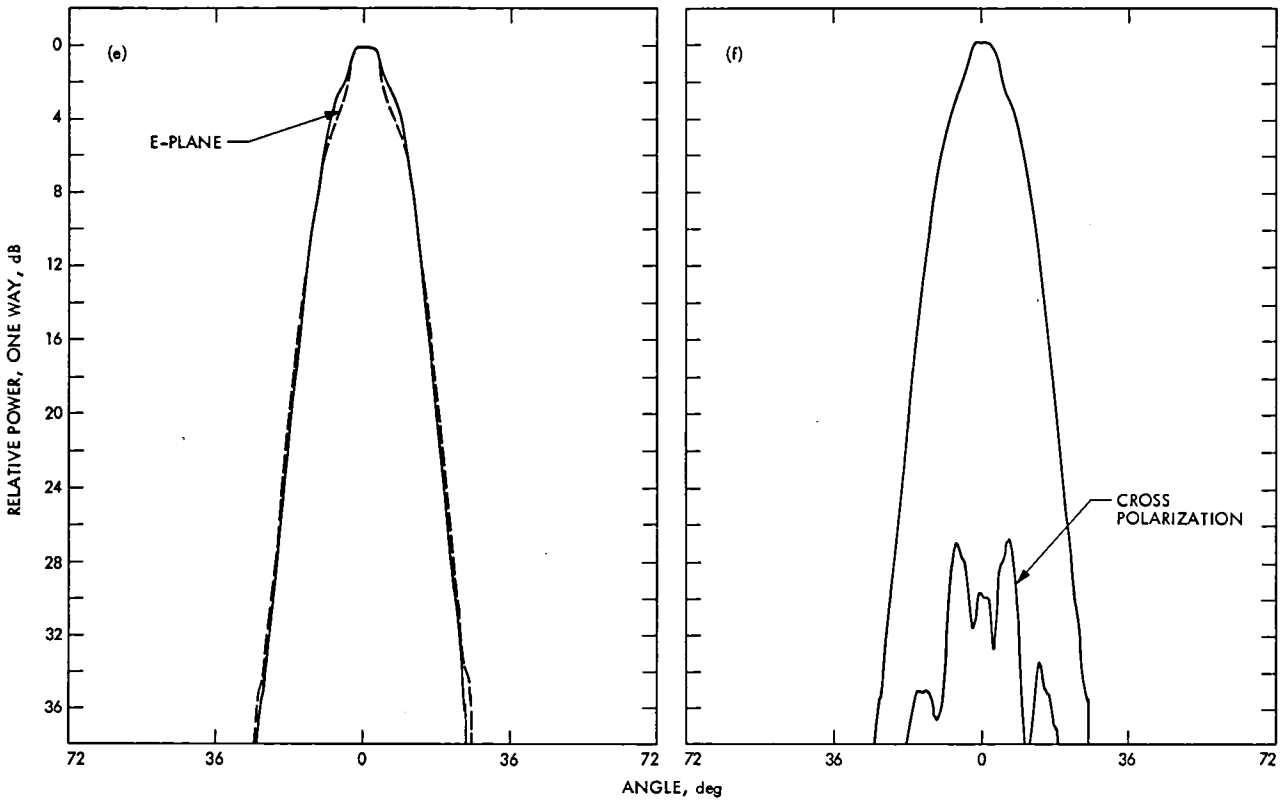
(e)
(f)
E-PLANE
CROSS
POLARIZATION
RELATIVE POWER, ONE WAY, dB
0
4
8
12
16
20
24
28
32
36
72
36
0
36
72
ANGLE, deg

Fig. 1 (contd)

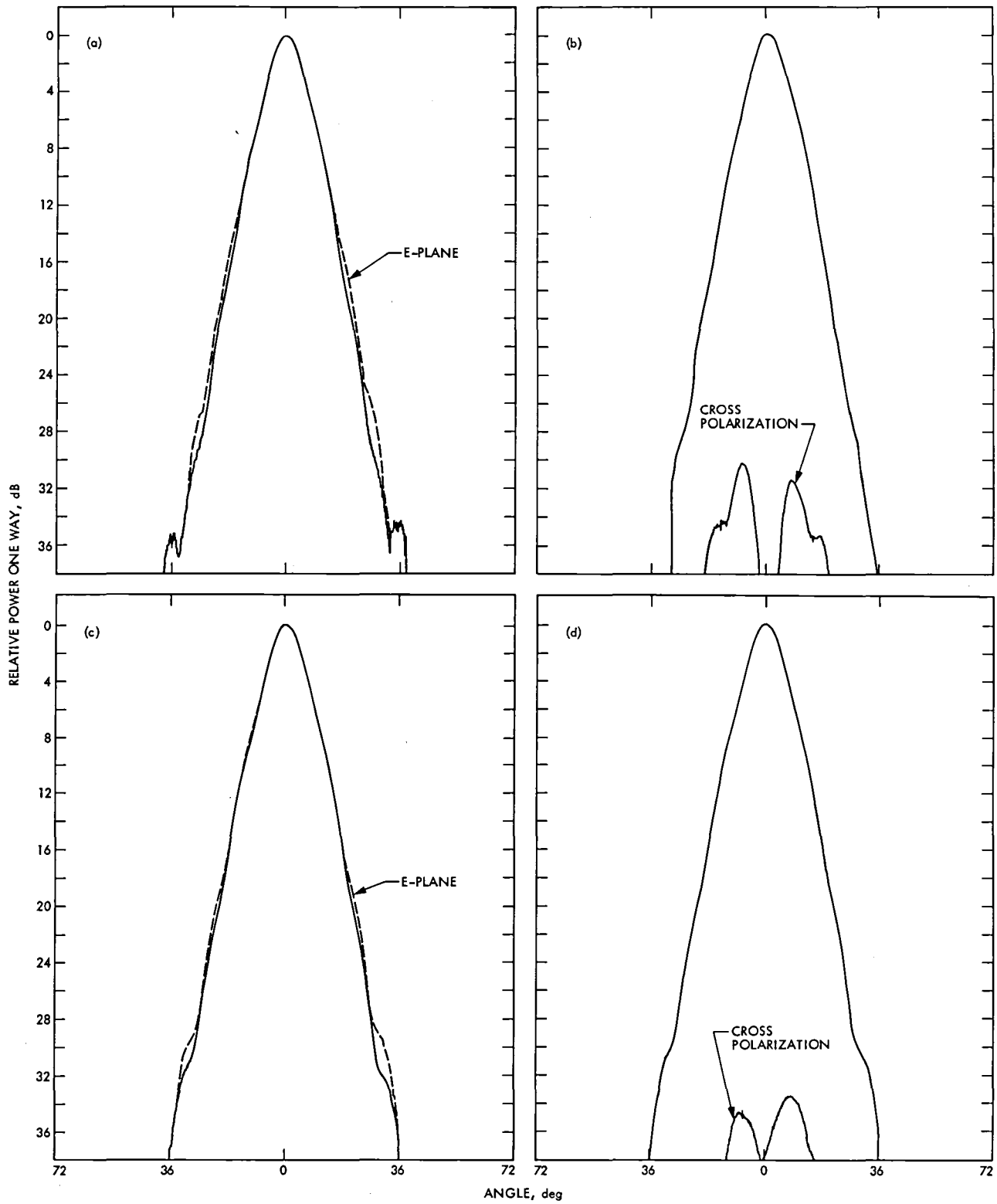

Fig. 2. Radiation patterns of the second-generation feedhorn in S-band: (a) E and H plane patterns at 2.3 GHz; (b) pattern cut at 45 deg to show cross polarization at 2.3 GHz; (c) E and H plane patterns at 2.1 GHz; (d) pattern cut at 45 deg to show cross polarization at 2.1 GHz

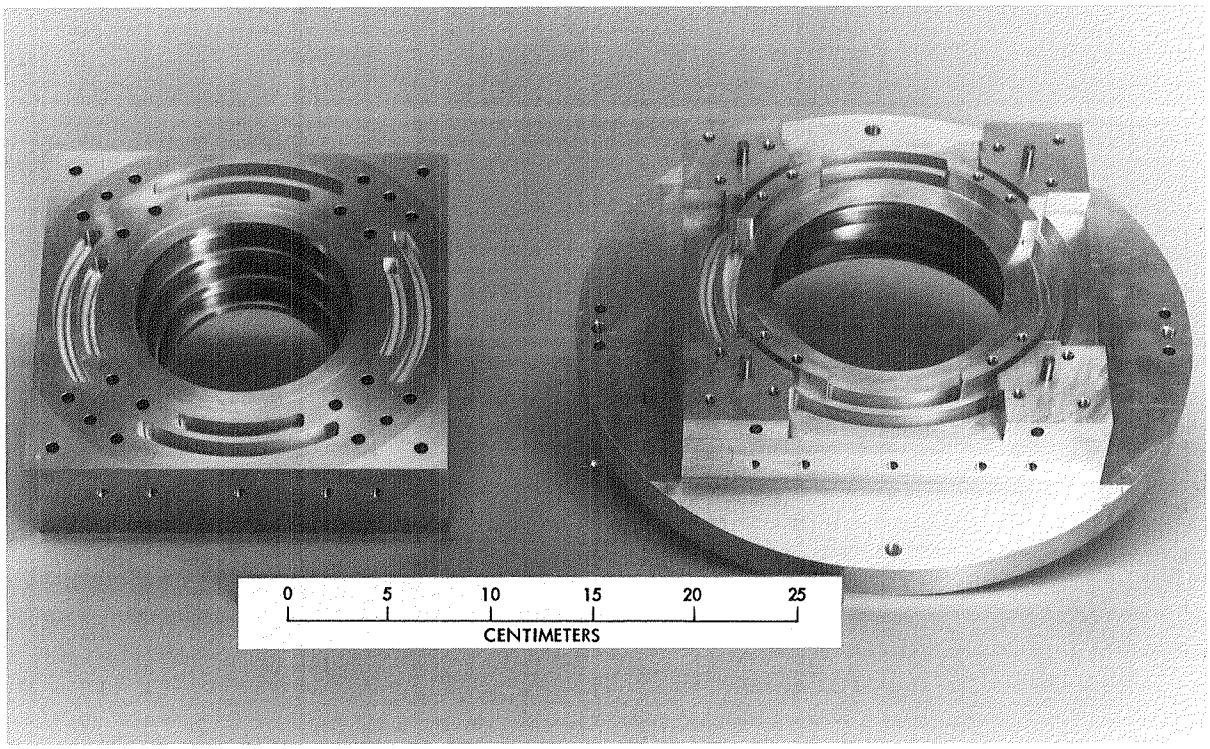

Fig. 3. The Mod II X/S Combiner

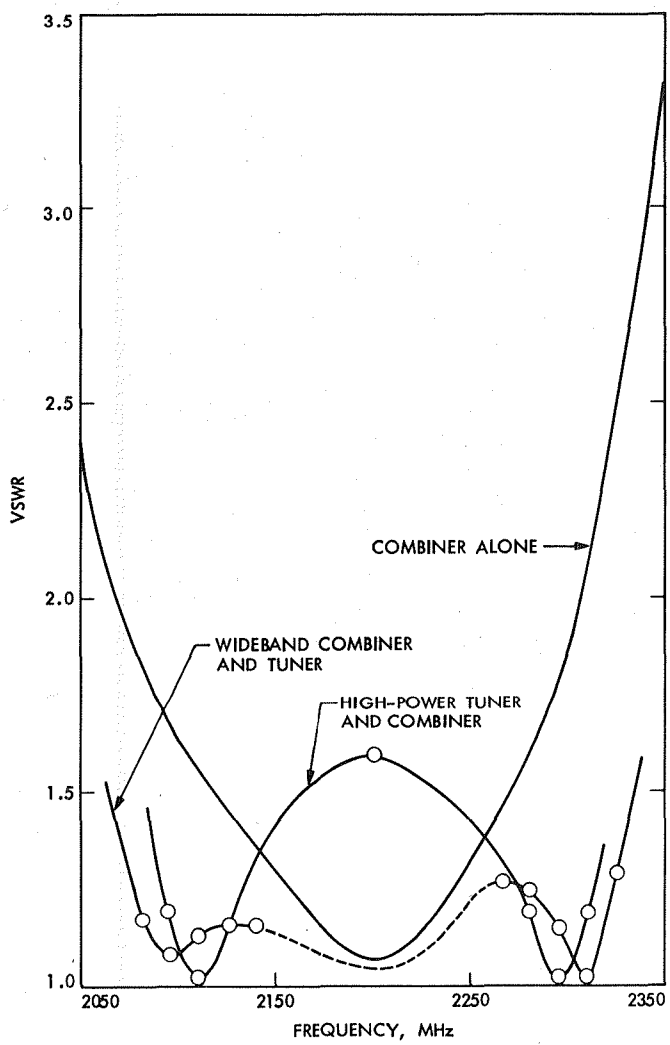

Fig. 4. The VSWR at input to the second-generation combiner and at the tuner input

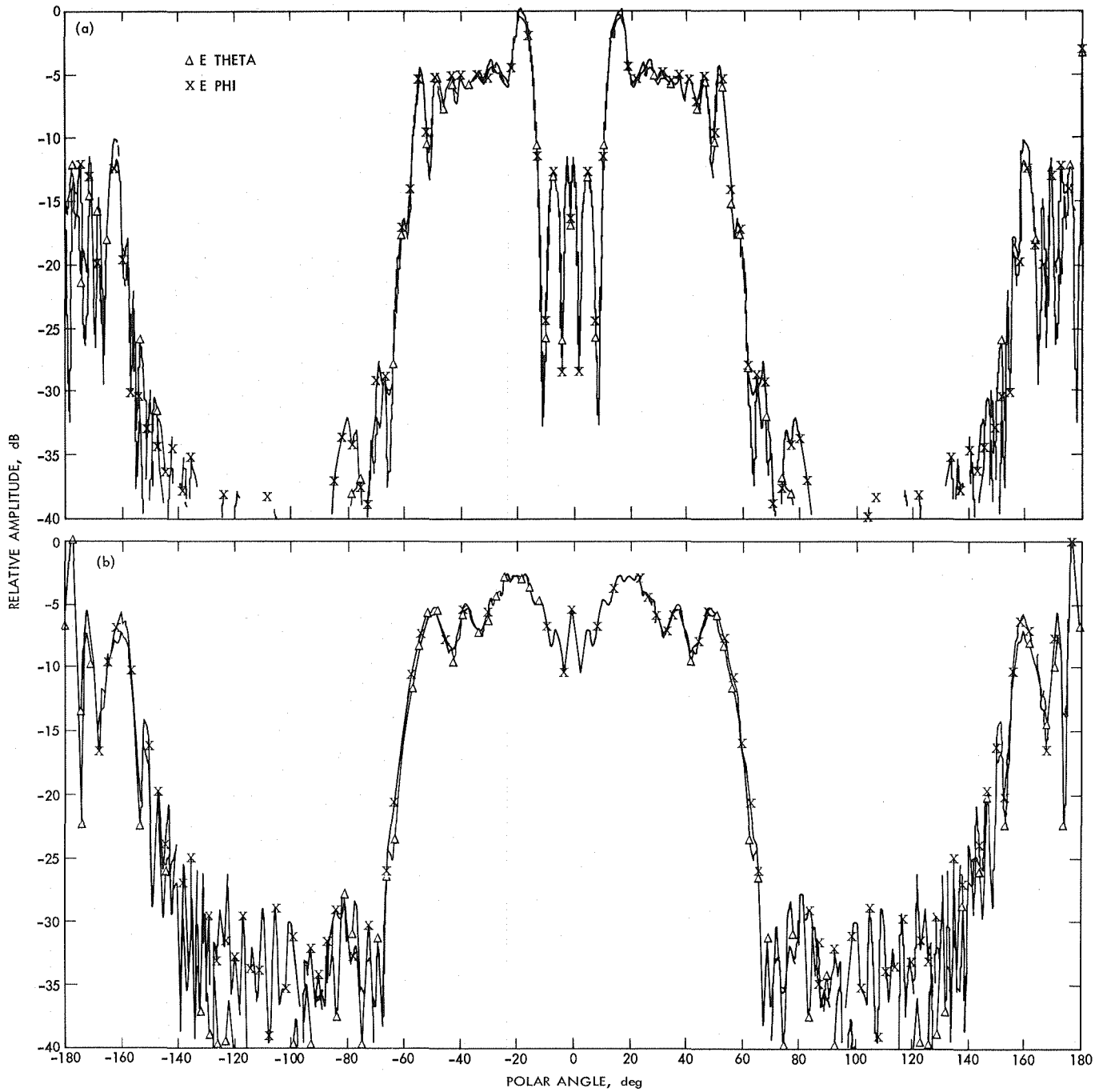

Fig. 5. Subreflector scattering at azimuth angle = 0.00, second-generation horn from the DSS 13 subreflector: (a) at 8.450 GHz; (b) at 2.295 GHz

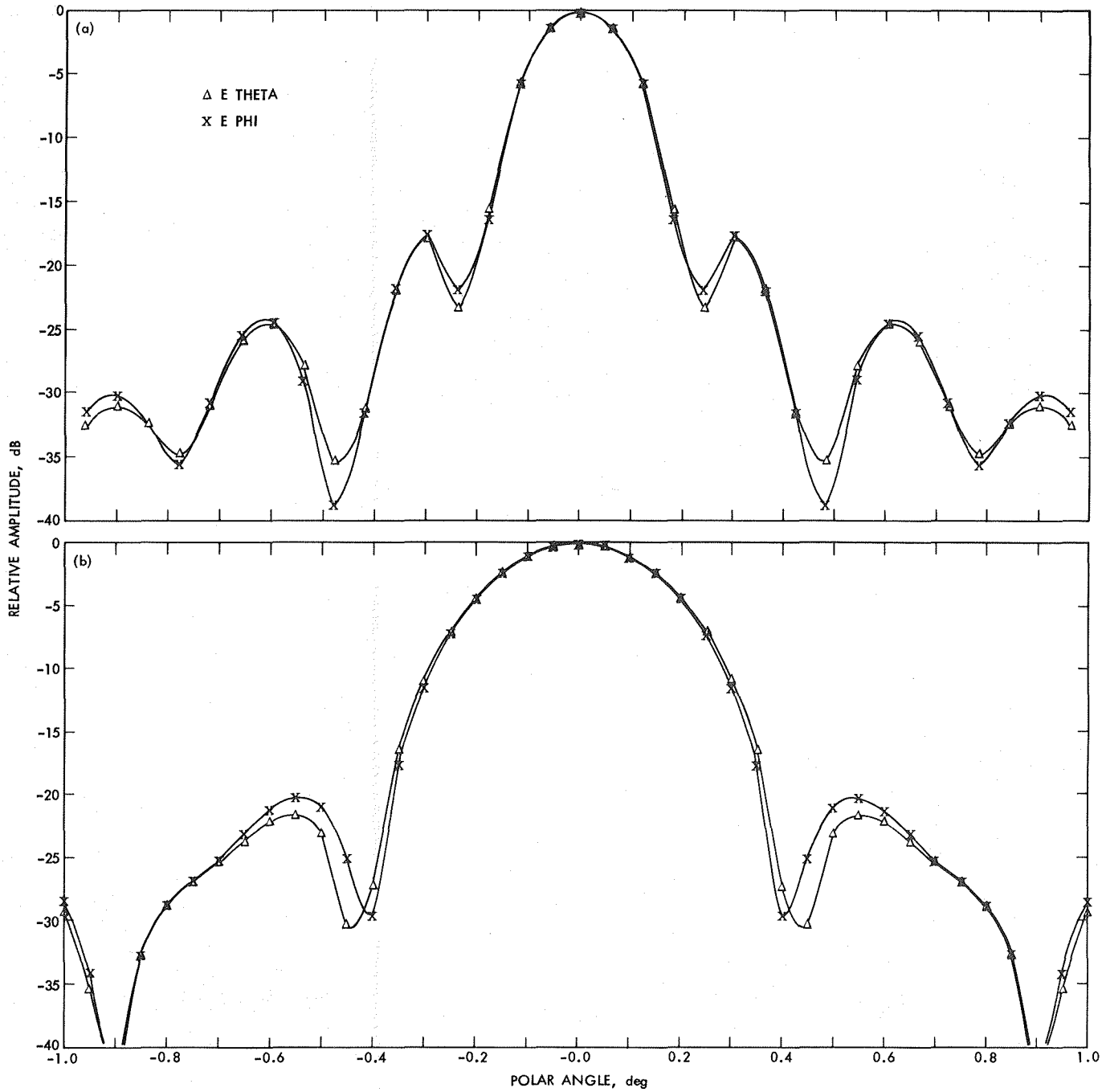

Fig. 6. Secondary patterns at azimuth angle = 0.00 from the Venus paraboloid (DSS 13): (a) at 8.450 GHz; (b) at 2.295 GHz

20-kW X-Band Uplink Transmitter Development

R. B. Kolbly
Radio Frequency and Microwave Subsystems Section

The 20-kW X-band transmitter Power Amplifier and its related control and monitor cabinet are described, along with the circuitry for the monitoring and protection of various transmitter components.

I. Introduction

A future requirement exists for a 20-kW X-band (7145-7235 MHz) uplink transmitter for utilization in the Deep Space Network (DSN). A developmental model is being designed and built for installation at DSS 13, where this transmitter will be evaluated for possible application in the Deep Space Network (Ref. 1). A major portion of any transmitter design is the system for protection, monitor and control of the various subsystems associated with the transmitter, the Power Amplifier (PA) Assembly and its related support equipment which is located in an adjacent rack. Also, the protective interlock logic and transducer conditioning circuits will be described.

II. Power Amplifier Assembly

Figures 1 and 2 show the actual PA Assembly that contains the klystron, focus magnet, filament circuit, and buffer amplifier units. A simplified schematic diagram is shown in Fig. 3. The PA Assembly is designed for maximum RF shielding. All electrical connections through the klystron compartment are filtered, and box joints are metal-to-metal for best shielding integrity. Three of the box sides are removable for ease of klystron removal. The fourth side of the PA Assembly serves as a mounting surface for the output waveguide assembly (consisting of the harmonic filter, arc detector, water load, switch and directional coupler) as well as a heat sink for the buffer amplifier. The cathode cooling air is routed over this plate and out the top of the power amplifier. All coolant connections for the klystron pass through the top of the PA on AN-type flare bulkhead fittings. This top plate is also removable for klystron replacement. The lower section is for the filament transformer, cathode blower, and associated circuits. The filament transformer divides the lower (cathode) compartment into two sections, one of which has all of the high-voltage connections. The other compartment has the filament control circuits and a card cage for interlock and monitor circuits. The filament transformer has both current and potential monitor windings for supplying operating conditions to the PA controller. These ac monitor signals are conditioned in the PA card cage to provide 0 - 5 volt dc analog signal, and the limit conditions are tested by the conditioning circuitry to provide the filament hardware interlocks. The filament circuit is started by a "step-start" circuit, with the final voltage set by an adjustable autotransformer in the filament primary circuit. After 5 minutes, the series resistor is switched out by a time-delay relay, applying full voltage to the klystron filament. After another 5 minutes, a second time delay relay provides a "filament ready" signal to the PA controller.

Protection for the beam operating conditions (beam overvoltage/current, excess body current, etc.) is provided by the power supply, so it is not necessary to provide beam or body current monitors in the PA Assembly. However, a local beam voltage and beam current monitor is provided for local diagnosis. A 50-millivolt shunt and 5000:1 voltage divider are used for these local indicators.

III. Power Amplifier Monitor Control Rack

Figures 4, 5 and 6 illustrate the PA monitor-control rack that is mounted next to the PA in the feedcone. This rack contains the PA controller, magnet power supply, control monitor interface, buffer control chassis and power supplies.

The PA controller is mounted on tilt slides for ease of access to the system interconnect terminal strips. This controller is in a standard industrial chassis with the interface panels mounted on a separate chassis under the controller.

The control monitor interface contains the analog conditioning cards and the summing logic for the protective hardware interlocks. In addition, local indicators for the analog signals and interlock status annunciators are provided to assist in failure diagnosis.

IV. Flowmeter Signal Conditioning Circuit

The 20-kW X-band uplink transmitter will use turbine flowmeters to sense coolant flow in the various parts of the klystron, the magnet and water load. The turbine flowmeter is linear in output, highly accurate, and lends itself to remote readout. In addition, the turbine flowmeter has been used extensively in industrial applications, providing a high confidence in the reliability of these units.

The output signal from a turbine flowmeter is a low-level (approximately 1 to 10 millivolts) sine-wave ac signal ranging from 100 to 2500 Hz. This signal must be converted to a 0 - 5 volt dc signal with a hardware underflow interlock signal. The frequency of the ac signal is proportional to the flow, so a tachometer circuit is required. A commercial linear integrated circuit (National Semiconductor LM2907) is well-suited for this application. The LM2907 has provision for sensing low-flow, so it is only necessary to add an output buffer amplifier and an interlock isolator. Figure 7 is a schematic diagram of this flowmeter conditioning circuit; U1 is the LM2907, with the associated discrete components to set the operating conditions, and U2 is an optical isolator to provide isolation from the interlock circuits and to reduce ground current noise. A light-emitting diode (CR1) provides a local indication of low-flow condition. The simplicity of this circuit allows eight of these circuits to be built on a standard wirewrap card.

V. Protective Logic Circuit

The protective logic circuit presently consists of 16 latched and two unlatched inputs which are logically summed into one output to enable the transmitter to operate. The latched inputs will detect and hold a momentary failure so that operators can determine the cause of transmitter tripoffs (e.g., momentary loss of flow). No provision is made for the bypassing of interlocks. The controller is provided with the status of the latched channels, and this information is also displayed on the control monitor panel.

The protective logic circuit (sometimes referred to as the "summing logic") uses complementary metal-oxide-silicon (CMOS) integrated circuits for high noise immunity and a 15-volt logic true (safe or run condition). The 15-volt level was chosen over the more common 5-volt logic level for noise immunity.

Acknowledgements

The design of the flowmeter signal conditioning circuit was done by John Daeges of Section 333. Al Bhanji designed the protective logic circuitry.

Reference

1. Hartop, R., Johns, C., and Kolbly, R., "X-Band Uplink Ground Systems Development," in *The Deep Space Network Progress Report 42-56*, Jet Propulsion Laboratory, Pasadena, Calif., Apr. 15, 1980, pp. 48-58.

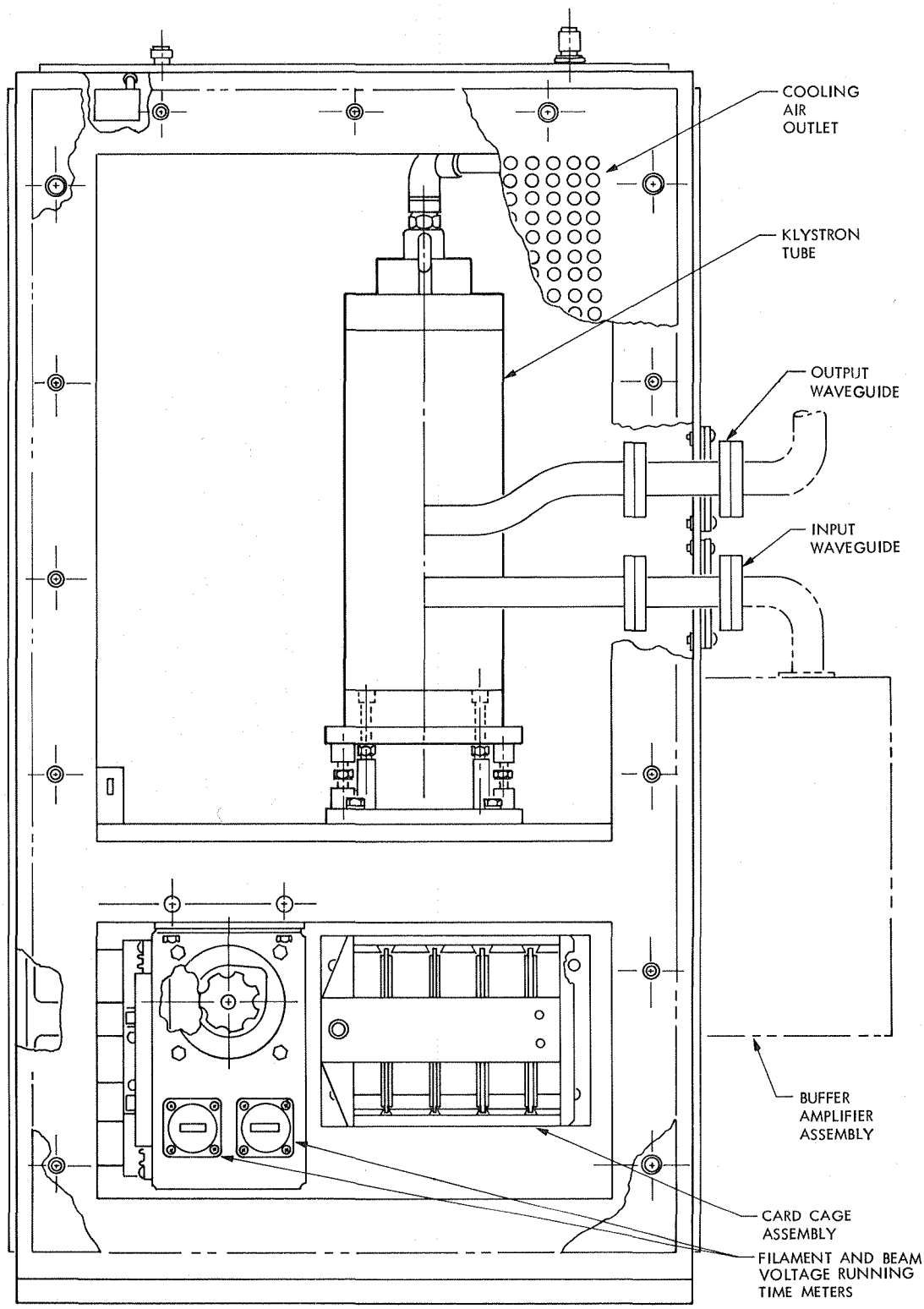

Fig. 1. Power Amplifier Assembly (front)

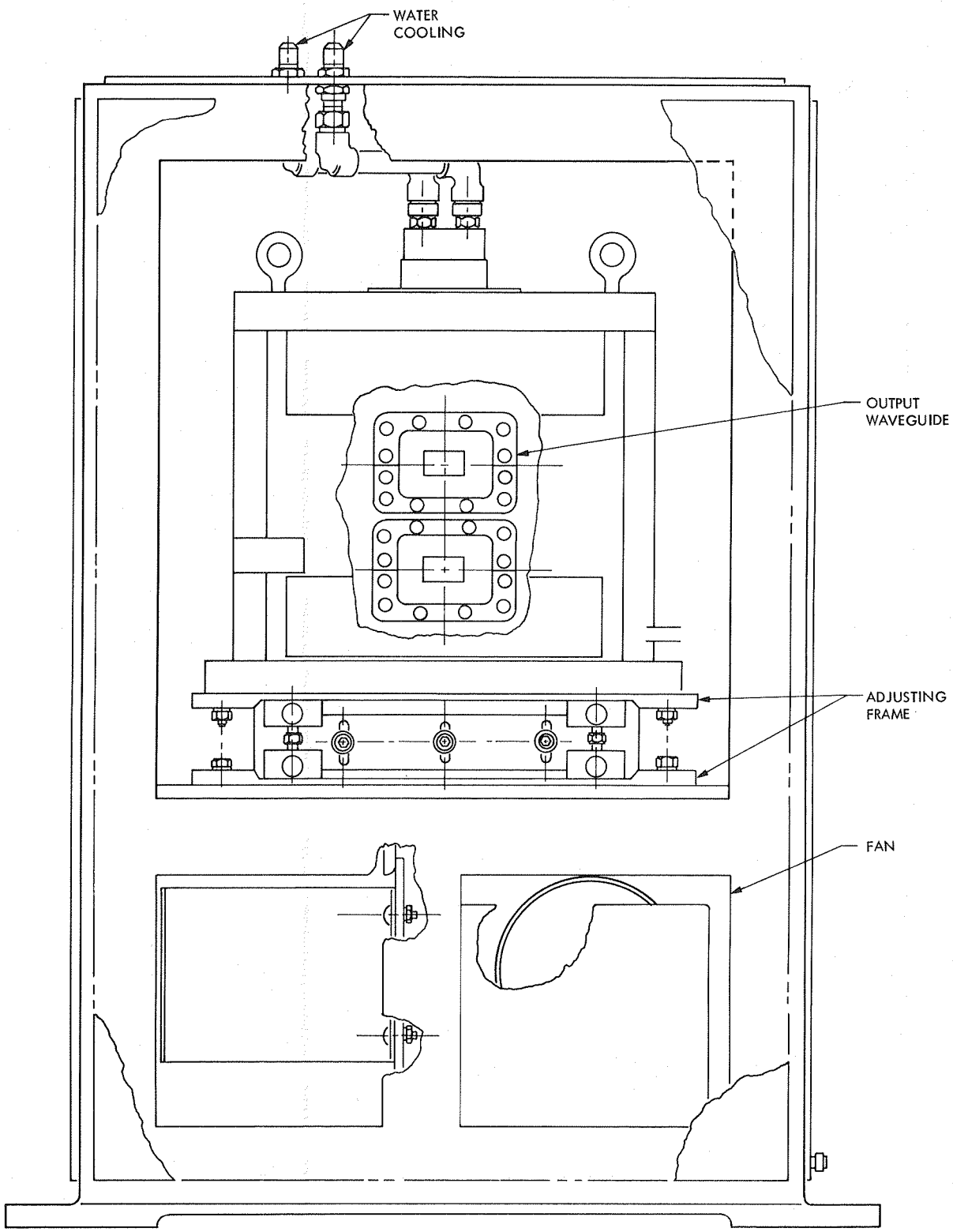

Fig. 2. Power Amplifier Assembly (side)

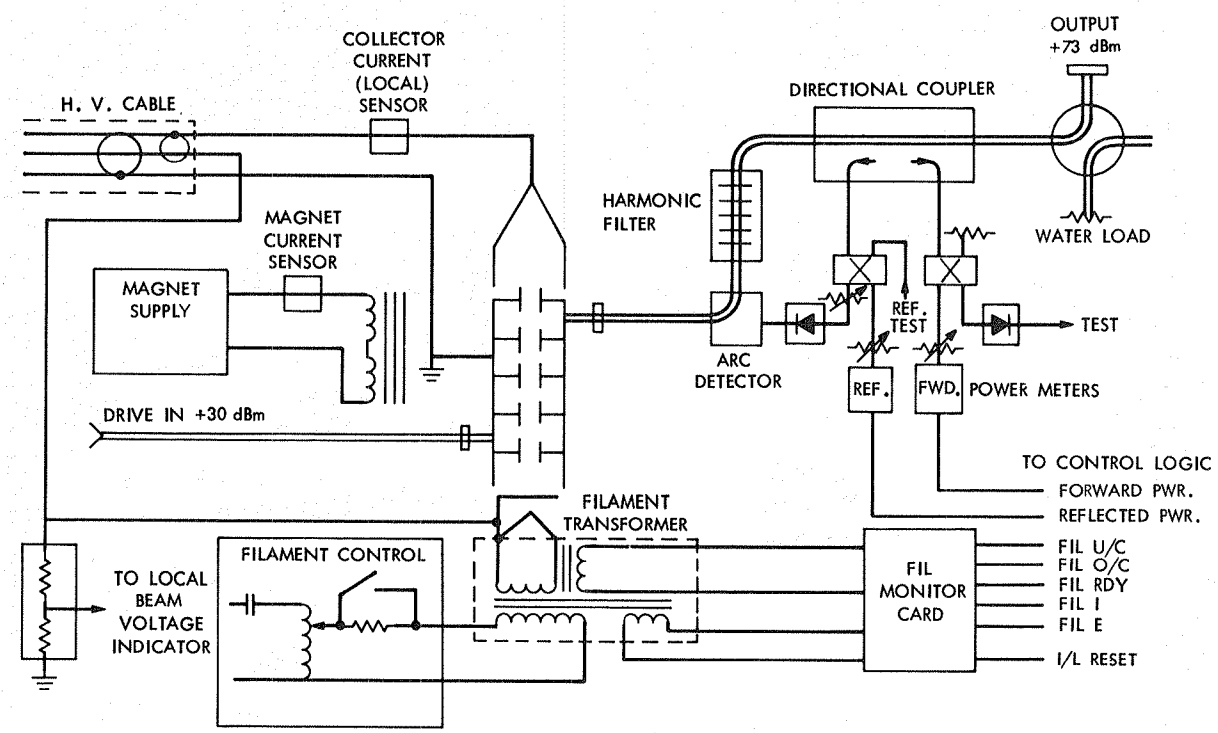

Fig. 3. Power Amplifier Assembly schematic

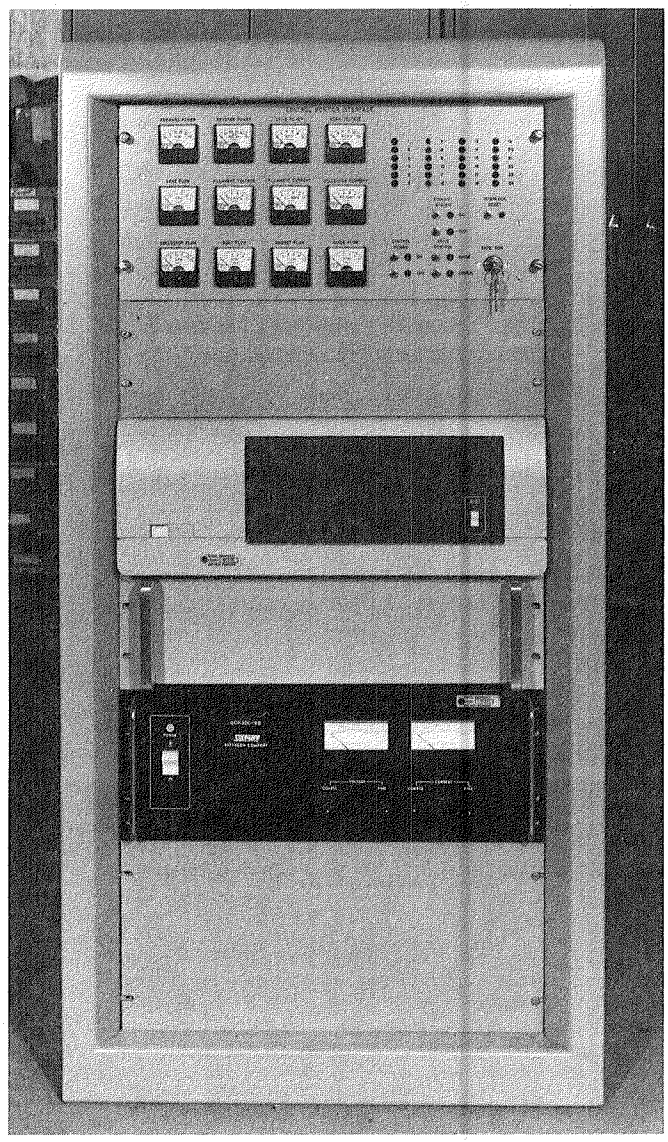

Fig. 4. PA monitor/control rack

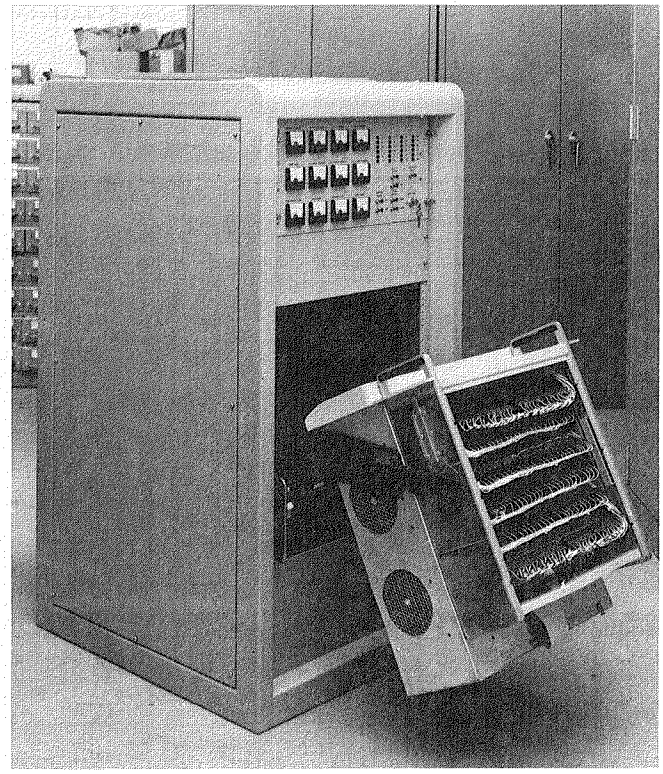

Fig. 5. PA monitor/control rack with controller extended

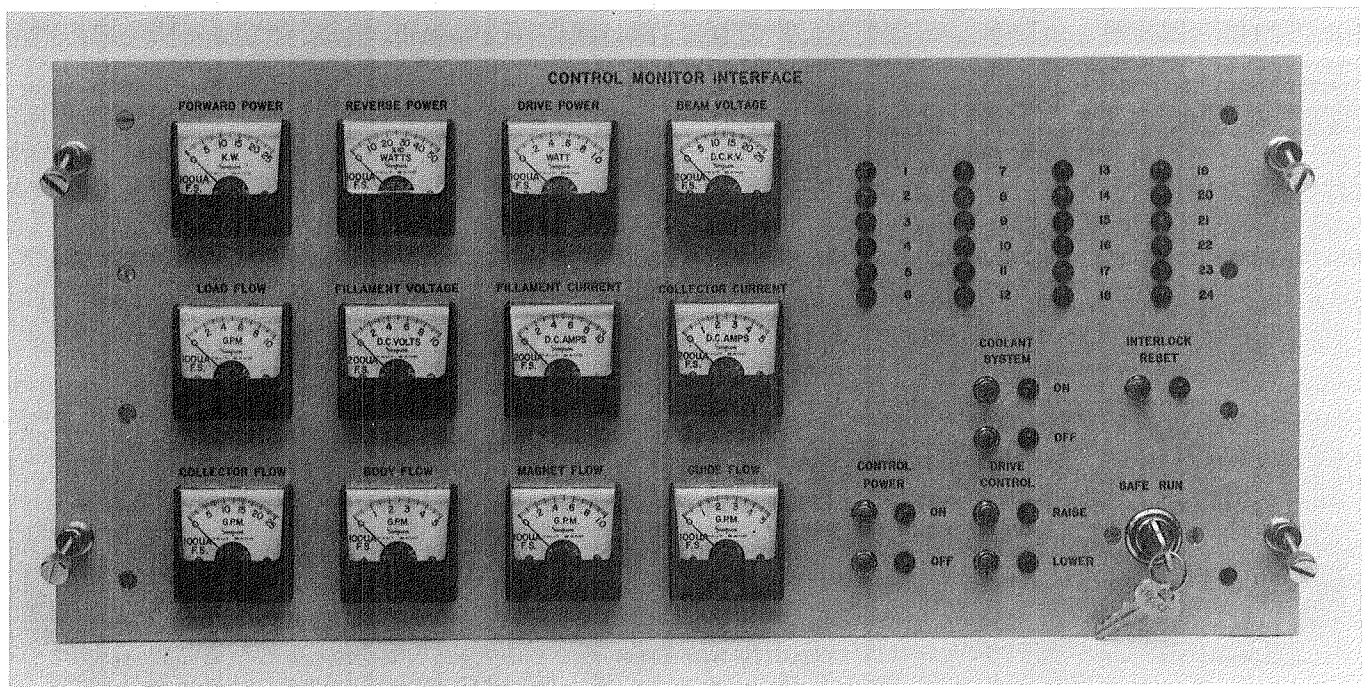

Fig. 6. Monitor/control interface

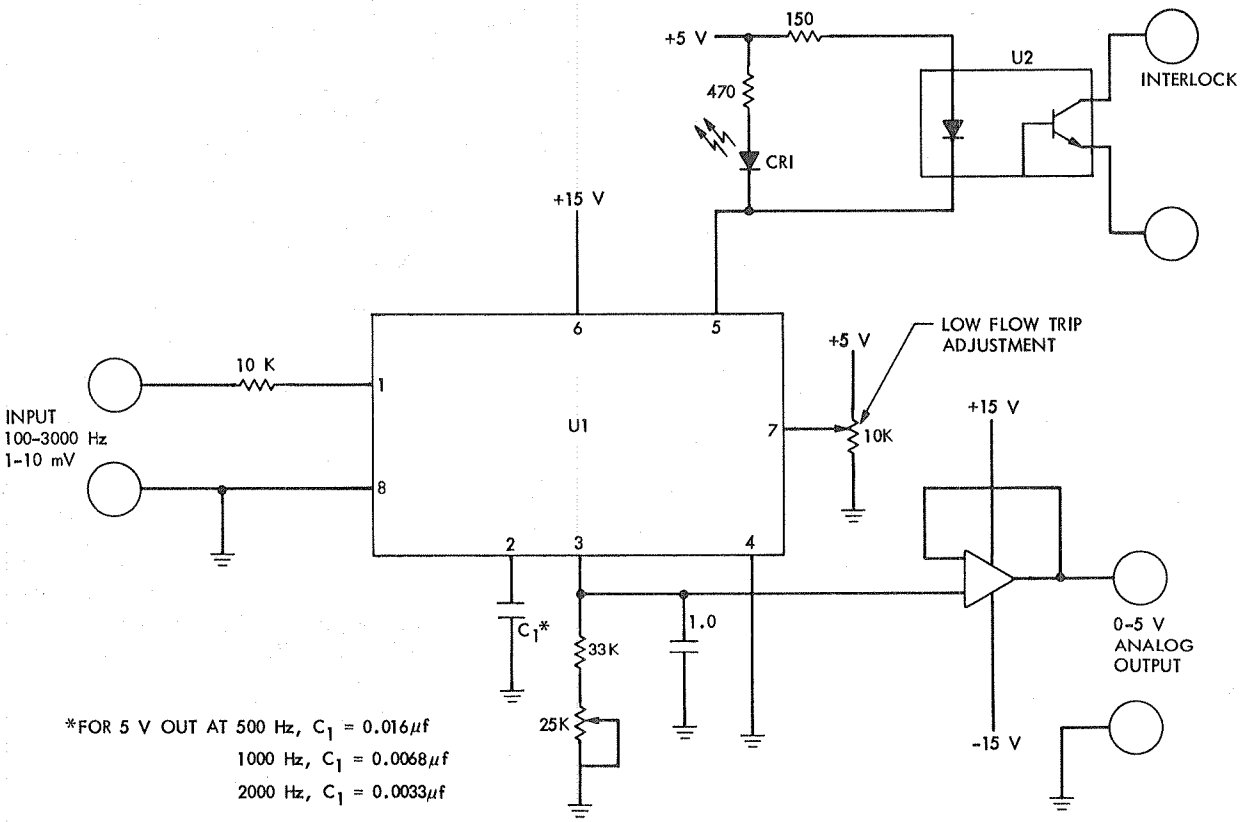

Fig. 7. Flowmeter conditioning circuit

A Note on the R_0-Parameter for Discrete Memoryless Channels

R. J. McEliece
Communications Systems Research Section

We exhibit an explicit class of discrete memoryless channels (q-ary erasure channels) for which we can design practical and explicit coded systems of rate R with R/R_0 as large as desired.

I. Introduction

For discrete memoryless channels, it is widely agreed that R_0 is second only to channel capacity itself as a quantitative measure of the channel's information-transmission capabilities. It has in fact been conjectured that R_0 represents, in some sense, the "practical limit" to reliable communication on such a channel. In this paper we shall show that this cannot be generally true, by exhibiting an explicit class of discrete memoryless channels (q-ary erasure channels) for which one can design inarguably practical and explicit coded systems of rate R, with R/R_0 as large as desired.

II. The q-ary Erasure Channel

This channel has a q-letter input alphabet X and a q + 1-letter output alphabet Y = XU {?}, where "?" is a special erasure symbol. The transition probabilities are

$$\begin{aligned} p(y|x) &= 1-\epsilon \quad \text{if} \quad x=y \\ &= 0 \quad \text{if} \quad x\neq y\neq ? \\ &= \epsilon \quad \text{if} \quad y=?, \end{aligned}$$

where $0 \leqslant \epsilon \leqslant 1$ is the erasure probability. Both capacity and R_0 are achieved with an equiprobable input distribution, and an easy calculation gives

$$C = (1-\epsilon)\log q \quad \text{nats per symbol} \qquad (1)$$

$$R_0 = \log\left(\epsilon + (1-\epsilon)q^{-1}\right)^{-1} \quad \text{nats per symbol.} \qquad (2)$$

If q is a power of two, say $q = 2^b$, we can view this channel as a binary channel (with memory) by taking the input letters to be b-bit binary numbers, and by interpreting the erasure symbol "?" as a b-bit erasure burst. Since each transmitted symbol in the original version of this channel corresponds to b transmitted bits in the new version, we have

$$C = (1-\epsilon)\log 2 \quad \text{nats per bit} \qquad (3)$$

$$R_0 = \frac{1}{b}\log\left(\epsilon + (1-\epsilon)2^{-b}\right)^{-1} \quad \text{nats per bit} \qquad (4)$$

We note that, for fixed ϵ,

$$\lim_{b\to\infty} C = \begin{cases} \infty \text{ nats per symbol} \\ (1-\epsilon)\log 2 \text{ nats per bit} \end{cases}$$

$$\lim_{b\to\infty} R_0 = \begin{cases} \log \epsilon^{-1} \text{ nats per symbol} \\ 0 \quad \text{nats per bit} \end{cases}$$

Thus, by taking the alphabet size (burst length) sufficiently large, we can make the ratio C/R_0 as large as desired.

III. Coding for the q-ary Erasure Channel

We consider first the case $q = 2$, i.e., the binary erasure channel. Linear block codes are especially well suited for this channel (Ref. 1), as we shall now briefly explain. If y is a partially erased codeword from an (n,k) binary block code with parity-check matrix H, to decode y one attempts to express the erased coordinates of y in terms of the unerased coordinates, using elementary row operations on H. The decoding will be successful (i.e., a unique codeword x agreeing with y on its unerased coordinates will be found) if and only if the columns of H corresponding to the erased coordinates of y are linearly independent; but whether successful or not the decoding will require at most r^2 row operations ($r = n - k$ is the code's redundancy) to row-reduce H followed by at most r further row operations to actually compute the values of the erased positions.

Now imagine that we have "built" a "practical" decoder for such a code on a binary erasure channel. We assume the code has rate $k/n = R$, the channel's raw erasure probability is ϵ, and the bit error probability of the decoder is p. We shall now show how to use this code to build an equally practical code for the 2^b-ary erasure channel described in the last section, with the same rate (measured in nats per bit), and with the same decoder bit error probability.

The idea is simply to interleave b copies of the original code. The rate of the interleaved code is the same as the original code, viz., R. The decoding of the interleaved code is actually easier (as measured in computations per decoded bit) than for the original code. This is because the locations of the erasures will be the same for each of the b codewords making up one interleaved block, and so the first step of the decoding, viz., the row-reduction of H, need only be done once. Thus decoding one interleaved block required at most r^2 row operations to row-reduce H followed by at most $b \cdot r$ further row operations to compute the erased components. Since each interleaved block contains bk information bits, the total decoding effort as measured in row operations per decoded bit will be at most $A(r/b + 1)$, where $A = (1 - R)/R$. Thus as the interleaving depth b increases the needed computation per decoded bit slowly decreases to a fixed limit A. We conclude that if the original decoding algorithm was judged to be practical, then the interleaved decoder must also be judged practical. Finally we note that the probability of decoder error is the same for the interleaved and non-interleaved systems, since the interleaved decoder will either decode all b codewords successfully, or none of them.

In summary, given a practical system with R and error probability p for the binary erasure channel, we can construct an equally practical system with the same rate and same error probability for the 2^b-ary erasure channel, for any $b \geqslant 1$. However, as noted in Section II, the R_0-parameter for these channels approach 0 (nats per bit) as b increases. We thus can design a practical system for which R/R_0 is as large as desired.

For example, take $q = 2^{100}$, $\epsilon = 0.01$. Then C = 99 bits/symbol, $R_0 = 6.64$ bits/symbol. The (8,4) Hamming code, interleaved to depth 100, will have a decoded bit error probability 6.8×10^{-4}, will require at most 1.04 row operations (8.32 bit operations) per decoded bit, and has $R/R_0 = 50/6.64 = 7.5$. If we took $q = 2^{1000}$ instead, we would have $R/R_0 = 75$, everything else being the same.

We conclude that there can be no theorem which relates R/R_0 to decoder complexity.

Reference

1. Berlekamp, E. R., "Error-Correcting Codes," *Proceedings of the IEEE*, May 1980, pp. 564–593.

Interleaved Block Codes for the Photon Channel

R. J. McEliece
Communications Systems Research Section

Using a recent idea of J. Massey, we show that interleaved binary block codes combined with pulse position modulation give the best practical coded systems yet devised for optical communication with photon detection.

I. Introduction

In Ref. 1, the use of Reed-Solomon (RS) codes with pulse-position modulation (PPM) was suggested for optical communication using direct photon detection. In Ref. 2, it was shown that PPM is optimal or nearly so in this application, but with no guarantee that RS coding cannot be improved upon. Indeed, in a recent article Massey (Ref. 3) has suggested the use of interleaved binary convolutional codes for this application, and these codes perform almost as well as RS codes. In this article we shall expand on Massey's suggestion and show that interleaved binary block codes can, for a given decoder complexity, perform even better than RS codes. In Fig. 1 we will present performance curves for an explicit code with a bit error probability less than 10^{-6} at a code efficiency of 2.8 nats per photon, using 256-ary PPM. Since channel capacity with this level of PPM is only 5.6 nats per photon, this performance is about as good as could be hoped for with any reasonable decoder complexity.

II. Massey's Equivalence

When M-ary PPM is used, the photon channel becomes, as explained in Ref. 1, an M-ary erasure channel with erasure probability $\epsilon = e^{-\lambda}$, where λ is the expected number of photons received during a time slot when the transmitter is pulsed. How should we code for this channel? In Ref. 1 it was shown that if $M = 2^L$, Reed-Solomon codes over $GF(2^L)$ give good results. More recently Massey (Ref. 3) has suggested that when $M = 2^L$, it might be wise to view the M-ary erasure channel as an array of L parallel, completely correlated, binary erasure channels. It is this latter possibility that we wish to explore here.

Massey's idea is simply that when $M = 2^L$, each input letter to the M-ary erasure channel can be represented by L bits. When this input letter is received correctly, all L bits are received correctly. However, if this input letter is erased, all L bits are erased. For example if $L = 3$, and if $\{0,1,2,3,4,5,6,7\}$ is the transmission alphabet, the sequence 314152653 might be received as 314?5?65?, where "?" denotes a channel erasure. Using the standard octal code 0 = 000, . . . , 7 = 111, this sequence could be viewed as three parallel binary sequences, as follows:

8-ary stream	3 1 4 1 5 2 6 5 3	→	3 1 4 ? 5 ? 6 5 ?
3 parallel binary streams	0 0 1 0 1 0 1 1 0 1 0 0 0 0 1 1 0 1 1 1 0 1 1 0 0 1 1	→	0 0 1 ? 1 ? 1 1 ? 1 0 0 ? 0 ? 1 0 ? 1 1 0 ? 1 ? 0 1 ?
	transmitted		received

Notice that the erasures occuring in the L parallel binary channels occur in exactly the same locations, i.e., if the k-th transmitted bit is erased in any one of the channels, it will be erased in all of them. Thus the 2^L-ary erasure channel is equivalent to L parallel, completely correlated, binary erasure channels as Massey observed. In Ref. 3, Massey suggests that, in view of this equivalence, it might be worthwhile to code for this channel by using an L-fold interleaving of a good code for a single binary erasure channel (BEC). The codes he suggests for this use are in fact short constraint-length convolutional codes with Viterbi decoders. In this paper we will also investigate this interleaving idea, but will consider linear block codes rather than convolutional codes.

III. Linear Block Codes for the BEC

It has been known since the mid-1950's (Ref. 4) that linear block codes are especially well-suited for combatting erasures. Rather than give an abstract explanation of this fact, we will illustrate it by example. We will also consider the implementation of interleaved linear codes on the parallel erasure channels discussed in the last section.

Consider the (8,4) $d = 4$ extended Hamming code with parity-check matrix

$$\begin{matrix} & 0 & 1 & 2 & 3 & 4 & 5 & 6 & 7 \end{matrix} \quad \text{column indices}$$

$$H = \begin{bmatrix} 1 & 1 & 1 & 0 & 1 & 0 & 0 & 0 \\ 1 & 1 & 0 & 1 & 0 & 1 & 0 & 0 \\ 1 & 0 & 1 & 1 & 0 & 0 & 1 & 0 \\ 0 & 1 & 1 & 1 & 0 & 0 & 0 & 1 \end{bmatrix}$$

Suppose we receive the word [1?0???01]. How should we decode it? The idea is to try to express the erased coordinates in terms of the unerased coordinates. In the present case, coordinates 1,3,4,5 have been erased, and to decode we reorder the columns of H so that the columns corresponding to erased coordinates all appear on the left:

$$\begin{matrix} & 1 & 3 & 4 & 5 & 0 & 2 & 6 & 7 \end{matrix}$$

$$H = \begin{bmatrix} 1 & 0 & 1 & 0 & 1 & 1 & 0 & 0 \\ 1 & 1 & 0 & 1 & 1 & 0 & 0 & 0 \\ 0 & 1 & 0 & 0 & 1 & 1 & 1 & 0 \\ 1 & 1 & 0 & 0 & 0 & 1 & 0 & 1 \end{bmatrix}$$

Next, using elementary row operations, we put H into row-reduced echelon form H'. Omitting details, we obtain the result

$$\begin{matrix} & 1 & 3 & 4 & 5 & 0 & 2 & 5 & 7 \end{matrix}$$

$$H' = \begin{bmatrix} 1 & 0 & 0 & 0 & 1 & 0 & 1 & 1 \\ 0 & 1 & 0 & 0 & 1 & 1 & 1 & 0 \\ 0 & 0 & 1 & 0 & 0 & 1 & 1 & 1 \\ 0 & 0 & 0 & 1 & 1 & 1 & 0 & 1 \end{bmatrix}$$

This matrix expresses the erased coordinates as linear combinations of the unerased coordinates, as desired. This is because the definition of a codeword X is the equation $HX^T = 0$, which is equivalent to $H'X^T = 0$, which in our example is equivalent to the four equations:

$$X_1 = X_0 + X_6 + X_7$$

$$X_3 = X_0 + X_2 + X_6$$

$$X_4 = X_2 + X_6 + X_7$$

$$X_5 = X_0 + X_2 + X_7$$

Hence the word [1?0???01] with $X_0 = 1$, $X_2 = 0$, $X_6 = 0$, $X_7 = 1$, must be a garbled version of the codeword [10011001], and the decoding is complete.

Now this particular code is not capable of correcting all patterns of four erasures; e.g., if we had received [1?0??0?1], we would compute

$$\begin{matrix} & 1\,3\,4\,6\,0\,2\,5\,7 \end{matrix} \qquad \begin{matrix} & 1\,3\,4\,6\,0\,2\,5\,7 \end{matrix}$$

$$H = \begin{bmatrix} 1 & 0 & 1 & 0 & 1 & 1 & 0 & 0 \\ 1 & 1 & 0 & 0 & 1 & 0 & 1 & 0 \\ 0 & 1 & 0 & 1 & 1 & 1 & 0 & 0 \\ 1 & 1 & 0 & 0 & 0 & 1 & 0 & 1 \end{bmatrix}, H' = \begin{bmatrix} 1 & 0 & 0 & 1 & 0 & 1 & 1 & 0 \\ 0 & 1 & 0 & 1 & 1 & 1 & 0 & 0 \\ 0 & 0 & 1 & 1 & 1 & 0 & 1 & 0 \\ 0 & 0 & 0 & 0 & 1 & 1 & 1 & 1 \end{bmatrix}$$

In this case H' tells us that the erased coordinates X_1, X_3, X_4 can be expressed in terms of the unerased coordinates X_0, X_2, X_5, X_7 plus the erased position X_6:

$$X_1 = X_6 + X_2 + X_5$$

$$X_3 = X_6 + X_0 + X_2$$

$$X_4 = X_6 + X_0 + X_5$$

Since we do not know the value of X_6, there are in this case *two* possibilities for the transmitted codeword:

$$X_6 = 0\text{: } [10011001]$$

$$X_6 = 1\text{: } [11000011]$$

These are both bona fide codewords, and both agree with the received word on all four unerased positions. In this case our decoder fails, but in any case detects its own failure.

The general situation is this. H will be an $r \times n$ binary matrix, where $r = n - k$ is the code's redundancy. If e positions are erased by the channel, after reordering, the columns H will have the form

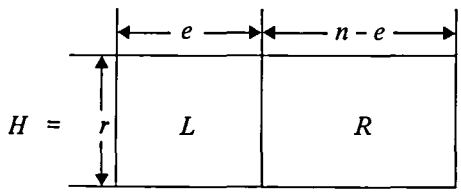

After row-reduction, H' will look like this:

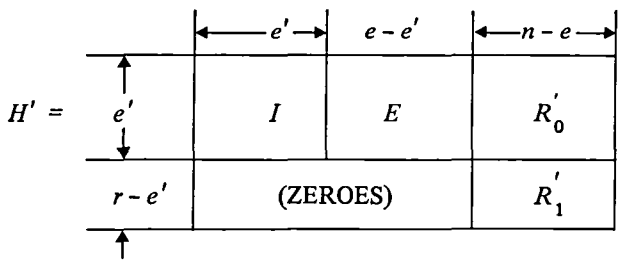

where $e' \leqslant e$, and I is an $e' \times e'$ identity matrix. The given erasure pattern will be correctable if and only if $e' = e$, in which case the top e rows of H' will express the e erased coordinates in terms of the $n - e$ unerased coordinates. (The lower right-hand matrix R_1', expresses parity-checks that must be satisfied by the unerased positions. In the present application this is not useful, but if bit errors as well as erasures are present, R_1' can be used to help locate the errors.) The amount of computation required to row-reduce H is at most r^2 row operations, or $r^2 n$ bit operations. Once H' is known, it requires at most r further row operations, or rn bit operations, to recover the erased coordinates. Since each codeword carries $k = n - r$ information bits, the total computational effort is at most $A(r + 1)$ row operations, or $A(rn + n)$ bit operations per decoded bit, where $A = (1 - R)/R$ and $R = k/n$ is the code's rate.

If we want to use L interleaved copies of this code on the L parallel, completely correlated BECs described in the last section, the decoding effort per bit is considerably reduced. This is because all L garbled codewords will have the same erased positions, and so the reduction from H to H' need only be done once. Thus decoding L codewords requires at most $r^2 + Lr$ row operations or at most $A/L\ r + A$ row operations, or $A/L\ rn + An$ bit operations, per decoded bit. For most choices for the parameters, this is very nearly a savings of a factor of L.

In the next section we will show how these results can be used to design good coding systems for the photon channel.

IV. Performance of Interleaved Block Codes on the Photon Channel

In the last section we discussed the decoding of linear block codes on a BEC, but did not discuss the performance of these codes. For a given choice of n and r, it is in general not easy to find the $r \times n$ parity check matrix H that describes the best possible erasure-correcting linear block code. However, we can give conservative estimates of the performance of linear codes by using the "R_0-coding theorem" (Refs. 4 and 5) which says in this case that for a given choice of r and n, a randomly chosen $r \times n$ parity check matrix H yields a code with probability of decoding error bounded by

$$P_E \leqslant \frac{(1 + \epsilon)^n}{2^r}, \tag{1}$$

where ϵ is the channel's erasure probability. If a code with these parameters is used on the L parallel erasure channels corresponding to the photon channel with 2^L-ary PPM, the erasure probability ϵ is given by Ref. 1 as

$$\epsilon = 2^{-LR/\rho}, \tag{2}$$

where $R = (n - r)/n$ is the code's rate, and ρ is the code's efficiency measured in nats per photon. Combining Eqs. (1) and (2) we have plotted in Fig. 1 (conservative estimates of) the bit error probability of randomly selected (100,50), (200,100), and (300,100) linear codes interleaved to depths $L = 5$ and $L = 8$. Presumably, carefully selected codes with

these parameters would perform somewhat better. The computational effort per decoded bit is, from the remark in the last section, seen to be:

21 row operations (100,50) $L = 5$

14 row operations (100,50) $L = 8$

41 row operations (200,100) $L = 5$

26 row operations (200,100) $L = 8$

121 row operations (300,100) $L = 5$

76 row operations (300,100) $L = 8$.

We note from Fig. 1 that the (300,100) $L = 8$ linear code slightly outperforms the RS code suggested in Ref. 1, and a vector-oriented special purpose decoder for this code would be a considerably simpler device than the corresponding RS decoder.

References

1. McEliece, R. J. and L. R. Welch, "Coding for Optical Channels with Photon Counting," *DSN Progress Report 42-52* (1979), pp. 61-66.
2. McEliece, R. J., Rodemich, E. R., and Rubin, A. L., "The Practical Limits of Photon Communications," *DSN Progress Report 42-55* (1979), pp. 63-67.
3. Massey, J., "Capacity, Cut-Off Rate, and Coding for a Direct-Detection Optical Channel," article in press.
4. Berlekamp, E. R., "Error-Correcting Codes," *Proceedings of the IEEE*, May 1980, pp. 564-593.
5. McEliece, R. J. *The Theory of Information and Coding*, Reading Mass., Addison-Wesley, 1977.

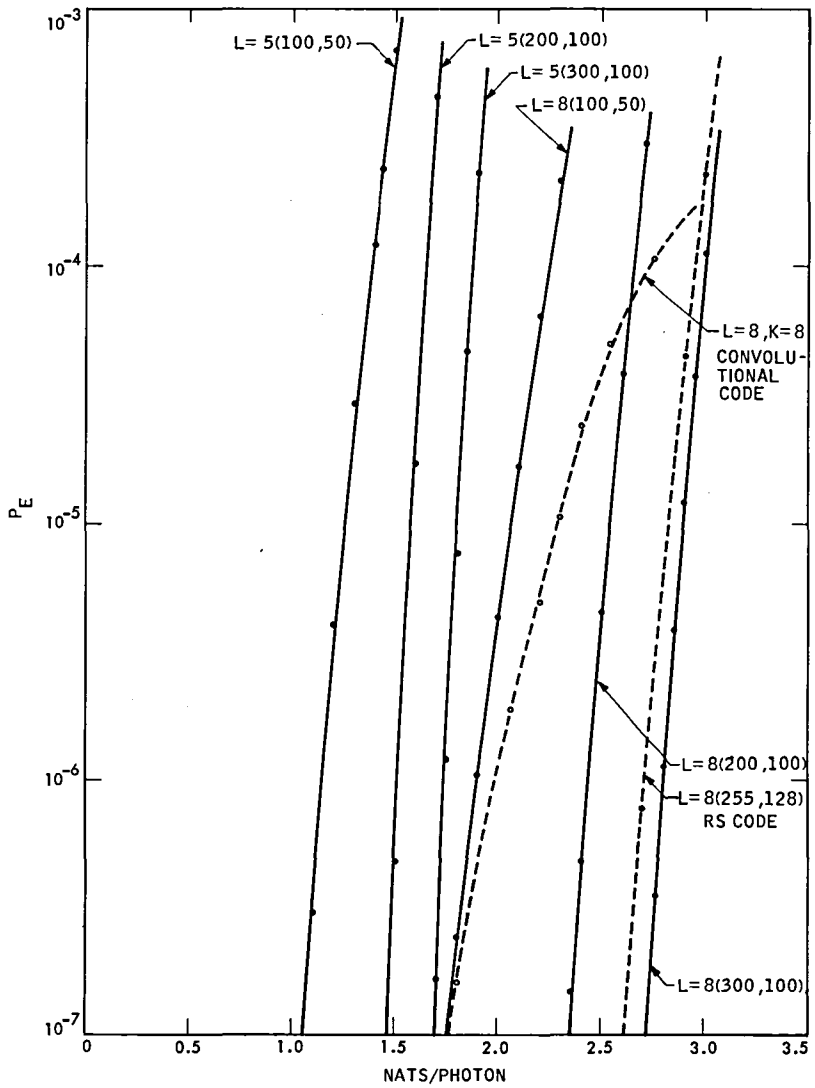

Fig. 1. Code performance curves

RFI Channels

R. J. McEliece
Communications Systems Research Section

We present a class of channel models exhibiting varying burst error severity much like channels encountered in practice. We make an information-theoretic analysis of these channel models, and draw some conclusions that may aid in the design of coded communication systems for realistic noisy channels.

I. Introduction

Most of the published research in information theory deals with memoryless channels, whereas most naturally occurring communication channels exhibit at least some degree of burstiness, in many cases caused by radio frequency interference (RFI). For example, optical communication with direct detection of photons (Ref. 1), spread-spectrum communication in the presence of hostile jamming (Ref. 2), and communication in the presence of friendly radar transmission (Ref. 3) all lead to channel models in which there are periodic bursts of poor data quality. In this article we shall attempt to model these complicated channels with a class of channels we call "RFI channels." The basic idea behind these models, which we will develop in later sections, is that the channel noise severity is required to remain constant over blocks of n transmitted symbols. However, the channel noise severity may change between one block of n symbols and the next.

Although much further work in this area remains to be done, we are able to draw certain conclusions from this class of models that may prove useful in practical situations. Informally, our main conclusion is that the memory length n should be exploited to determine the noise severity within that block – this is a kind of "soft decision" information; once the noise severity has been estimated, the best strategy is to use n-fold coded interleaving to combat the noise.

II. The Channel Models

Consider the following model for a discrete channel ζ with memory. We start with a finite collection of discrete memoryless channels, $\zeta_1, \zeta_2, \cdots \zeta_k$, each with the same input alphabet A, and output alphabet B. When a sequence of letters x_1, $x_2, \cdots$ from A is to be transmitted over ζ, each block of n consecutive letters is sent over one of the auxiliary channels ζ_k, which is selected by an external random variable Z, which takes values in the set $\{1, 2, \cdots, k\}$. If, for example, the ζ_k's are all binary symmetric channels with differing raw bit-error probabilities, the overall channel ζ will be characterized by phased bursts of errors of varying severity.

We consider also another channel $\overline{\zeta}$. This channel is exactly the same as ζ except that it provides to the receiver the index k of the discrete memoryless channel selected by Z.

Our main results are these. First, the capacity of $\overline{\zeta}$ is independent of n, the burst length. We denote this capacity by $\overline{C}$. Second, the capacity of ζ does depend on n, is always less

than $\overline{C}$, and if we denote the capacity of ζ by C_n, we have $\lim_{n\to\infty} C_n = \overline{C}$.

Our results follow fairly easily from calculations with mutual information and entropy. Both channels ζ and $\overline{\zeta}$ can be viewed as discrete memoryless channels with input alphabet A^n. For ζ, the output alphabet is B^n, and for $\overline{\zeta}$, the output alphabet is $B^n \times \{1, 2, \cdots, k\}$. The transition probabilities for ζ are

$$p(\mathrm{y}/\mathrm{x}) = \sum_{k=1}^{n} \alpha_k \prod_{i=1}^{n} p_k(y_i|x_i)$$

where $\mathrm{y} = (y_1, \cdots, y_n)$, $\mathrm{x} = (x_1, \cdots, x_n)$, $p_k(y|x)$ is the transition probability for ζ_k, and α_k is the probability that the channel selected is ζ_k : $\alpha_k = Pr\ \{Z = k\}$. For $\overline{\zeta}$, the transition probabilities are

$$p(\mathrm{y}, k|\mathrm{x}) = \prod_{i=1}^{n} p_k(y_i|x_i)$$

From this memoryless viewpoint, the calculation of the channel capacities is simply a matter of minimizing the appropriate mutual informations. For ζ, the capacity is

$$C_n = \frac{1}{n} \max_{\mathbf{X}} I(\mathbf{X}; \mathbf{Y}) \tag{1}$$

where $\mathbf{X}$ and $\mathbf{Y}$ denote the (n-component) random inputs to and outputs from ζ. For $\overline{\zeta}$, the formula is

$$\overline{C}_n = \frac{1}{n} \max_{\mathbf{X}} I(\mathbf{X}; \mathbf{Y}, Z) \tag{2}$$

(We have indicated a dependence on n, but as indicated above the capacity $\overline{C}_n$ turns out to be independent of the burst length.)

We shall consider $\overline{C}_n$ first, since its calculation is the easier of the two. We have, using standard results about mutual information (Ref. 4),

$$I(\mathbf{X}; \mathbf{Y}, Z) = \sum_{k=1}^{K} \alpha_k I(\mathbf{X}; \mathbf{Y}^{(k)})$$

where $\mathbf{Y}^{(k)}$ denotes the output of the channel ζ_k^n, if $\mathbf{X}$ is the input. Since each ζ_k is memoryless, we have

$$\sum_{k=1}^{K} \alpha_k I(\mathbf{X}; \mathbf{Y}^{(k)}) = \sum_{k=1}^{K} \alpha_k \sum_{i=1}^{n} I(X_i; Y_i^{(k)})$$

$$= \sum_{i=1}^{n} \sum_{k=1}^{K} \alpha_k I(X_i; Y_i^{(k)}) \tag{3}$$

where $\mathbf{X} = (X_1, \cdots, X_n)$ and $\mathbf{Y}^{(k)} = (Y_1^{(k)}, \cdots, Y_n^{(k)})$

To compute $\overline{C}_n$, we are required to maximize this last expression over all random vectors $\mathbf{X} = (X_1, X_2, \cdots, X_n)$. The maximum of the inner sum in Eq. (3), taken over all choices of the random variable X_i, is clearly independent of k, and so from Eq. (2) we have

$$\overline{C}_n = \sup_{\mathbf{X}} \sum_{k=1}^{K} \alpha_k I(\mathbf{X}; \mathbf{Y}^{(k)}) \tag{4}$$

where the supremum in Eq. (4) is taken over all random variables taking values in the input alphabet A. (If it happens that there is a single input distribution X that simultaneously achieves channel capacity on all K channels ζ_k, then

$$\overline{C}_n = \sum_{k=1}^{n} \alpha_k C_k$$

where C_k is the capacity of ζ_k.) Equation (4) thus shows that $\overline{C}_n$ is independent of n, and that it is in fact the capacity of the DMC with transition probabilities $\{\Sigma \alpha_k p_k(y|x)\}$.

We turn now to the computation of C_n. It is an easy exercise to show that

$$I(\mathbf{X}; \mathbf{Y}, Z) - H(Z) \leqslant I(\mathbf{X}; \mathbf{Y}) \leqslant I(\mathbf{X}; \mathbf{Y}, Z) \tag{5}$$

It thus follows that for any random vector $\mathbf{X}$,

$$\frac{1}{n} I(\mathbf{X}; \mathbf{Y}, Z) - \frac{H(Z)}{n} \leqslant \frac{1}{n} I(\mathbf{X}; \mathbf{Y}) \leqslant \frac{1}{n} I(\mathbf{X}; \mathbf{Y}, Z) \tag{6}$$

Since $H(Z)$ is a fixed number $\leqslant \log K$, the left-hand inequality in Eq. (6) shows that

$$\liminf_{n\to\infty} C_n \geqslant \overline{C}_n = \overline{C}$$

and the right-hand inequality shows that $C_n \leq \overline{C}$, and

$$\limsup_{n\to\infty} C_n \leq \overline{C}$$

Together these two inequalities show that $\lim_{n\to\infty} C_n = \overline{C}$, as asserted. (We conjecture, but have not been able to prove, that in fact C_n is a monotonically increasing function of n.)

III. An Example

We illustrate these results with a simple example, with $K = 2$. Channel ζ_1 is a noiseless binary symmetric channel, and channel ζ_2 is a "useless" BSC with raw bit error probability 1/2.

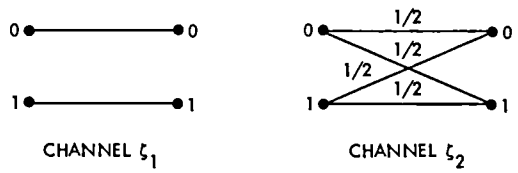

We assume that the channel selector random variable Z is described by $Pr\{Z = 1\} = 1 - \epsilon$, $Pr\{Z = 2\} = \epsilon$. Thus if ϵ is small, the overall channel ζ is characterized by noise-free transmission interrupted by occasional but very severe error bursts.

The capacity of ζ_1 is log 2, and the capacity of ζ_2 is 0; both capacities are achieved by a uniform input distribution, and so by Eq. (4) $\overline{C} = (1 - \epsilon) \log 2$. A straightforward calculation shows that the capacities C_n are given by

$$C_n = (1 - \epsilon_n) \log 2 - \frac{1}{n} \{H(\epsilon_n) + \epsilon_n \log (1 - 2^{-n})\}$$

$$\epsilon_n = (1 - 2^{-n})\, \epsilon,\ H(x) = -x \log x - (1 - x) \log (1 - x)$$

Since $\epsilon_n \to \epsilon$ as $n \to \infty$, it follows from this that $C_n \to \overline{C}$, but of course this also follows from the general results of Section II.

How should these results be interpreted? First, we note that the channel $\overline{\zeta}$ is equivalent to a channel exhibiting erasure bursts, since once it is known that channel ζ_2 was used to transmit a block of n bits, the received versions of these bits should be ignored, since they bear no relationship to the transmitted bits. And it is easy to verify that the capacity of such an erasure-burst channel is indeed $(1 - \epsilon) \log 2$, whatever the burst length.

It is evident that C_n ought to be less than $\overline{C}$, since the receiver using ζ will not know when a received block of length n is bad, whereas the receiver using $\overline{\zeta}$ will, and this extra information cannot possibly hurt performance. But if n is very large, the ζ-users could, for example, include in the n bits in each transmitted packet a certain number of parity checks. To be specific, let us assume in fact that each packet includes $\log_2 n$ parity checks. Then if the packet is transmitted over ζ_1, all of these parity checks will be satisfied upon reception. But if the packet is transmitted over ζ_2, these will be parity checks on random data, and the probability that they will all be satisfied is $2^{-\log_2 n} = n^{-1}$. Thus when n is large, the presence of a useless data packet can be detected with high probability and low overhead. In other words, for large n the channel ζ is virtually identical with $\overline{\zeta}$, and this is what our computations with mutual information predicted.

Thus if n is sufficiently large, a good strategy for communication over ζ is to reserve a certain number of the bits in each transmitter package for parity. This number should be large enough so that the presence of bad data can be detected with high probability, but small enough (relative to n) not to substantially reduce the transmission rate. This strategy will, as previously explained, effectively transform the channel into an erasure-burst channel. Then if n' denotes the number of bits in each packet not reserved for parity, one should code for the channel by interleaving n' copies of a code designed for use on the binary erasure channel (BEC). Since the capacity of the BEC is just as large as that of the erasure-burst channel, presumably there will be no performance loss. Furthermore, the decoding complexity of the n' parallel binary code is much less than n' times the complexity of decoding just one such code; see Ref. 5 for details.

IV. Conclusions

On this basis of the mutual information calculation in Section II, and on the basis of the example in Section III, we draw the following conclusions about RFI channels. First, to communicate reliably over $\overline{\zeta}$, nothing is lost by interleaving, and in addition there may be a considerable advantage in doing so. Second, while there will in general be a penalty in performance if interleaving on ζ is used, if n is large enough, it may be possible to accurately estimate the channel index k affecting a given data packet of length n or by using some kind of generalized parity check. If this can be done, then ζ is effectively transformed into $\overline{\zeta}$ and then interleaving can be used without penalty.

References

1. Massey, J., "Capacity, Cut-Off Rate, and Coding for a Direct-Detection Optical Channel," TDA Progress Report article in this volume (42-60). Jet Propulsion Laboratory, Pasadena, Calif.

2. Viterbi, A. J., "Spread Spectrum Communications – Myths and Realities," *IEEE Communications Magazine*, May 1979, pp. 11-18.

3. Berlekamp, E. R., "Error-Correcting Codes," *Proceedings IEEE*, May 1980, pp. 564-593.

4. McEliece, R. J., *The Theory of Information and Coding*. Addison-Wesley, Reading, Mass., 1977.

5. McEliece, R. J., "Interleaved Block Codes for the Photon Channel," TDA Progress Report article in this volume (42-60). Jet Propulsion Laboratory, Pasadena, Calif.

Temperature Control Simulation for a Microwave Transmitter Cooling System

C. S. Yung
DSN Engineering Section

This article, the first of two, describes and analyzes the thermal performance of a temperature control system for the antenna microwave transmitter (klystron tube). In this article, only the mathematical model is presented along with the details of a computer program which is written for the system simulation and the performance parameterization. Analytical expressions are presented in Appendixes.

I. Introduction

The microwave transmitter is one of the vital subsystems in the Deep Space Network Antenna Tracking System. The transmitter (klystron tube) converts the electrical energy to a microwave signal with a conversion efficiency in the order of 40-60 percent. Due to the inherently large heat generation in the transmitter and the sensitive temperature control requirements, a well-designed cooling system is required. The transmitter cooling design is commonly made, based on past engineering experience taken from the working transmitters. A detailed thermal analysis of an optimized system was not necessary. However, due to the increasing complexity of add-on components in the electrical circuit, for better controls and continuous upgrade of the existing system performance, the need for a new cooling system with an optimum design is found inevitable. In order to support this new cooling system design, this work is initiated to give a detailed thermal analysis and to evaluate the thermal performance of the system. A short computer program was written to analyze the transient cooling process. This article, the first of two, includes the system governing equations needed for a detailed transient thermal analysis and a detailed description of the simulation program. The second phase analysis is intended to evaluate the thermal behavior of the new system under varying operating conditions, with different component selection, location and size on the temperature control requirements.

II. System Description

Figure 1 illustrates one proposed design of the new microwave transmitter cooling system. The numbers assigned to the various points in Fig. 1 represent the fluid stations. The system is comprised of (1) a cross flow air-to-liquid heat exchanger (A), (2) a temperature control valve (B) which controls the amount of fluid flowing out from the heat exchanger (station 1) and the bypass of the returning flow (station 3) to deliver the desired fluid temperature (station 4), (3) a filter (C) which removes contaminants resulted from the corrosion in the system; and (4) a pressurized storage tank (D) which performs as a thermal flywheel or damper for all possible thermal fluctuations in the circuit. The storage tank is charged with nitrogen gas for maintaining the desired pressure. An electric resistance heater is provided inside the storage tank which operates only when the control valve (B) fails to supply a fluid temperature above the temperature setpoint of the tank. A pump (E) pumps the fluid from state 9 to 10 and maintains

the fluid in the loop at the design pressure. A flow meter (F) monitors the system flow rate at station 11. A purity loop (G) purifies the working fluid of the cooling system from state 31 to state 32. A pressure control valve (H) controls the working pressure at the microwave transmitter station 17. A flow bypass valve (I) regulates the proper flow to the microwave transmitter. The microwave transmitter includes two major assemblies, a water load (J) and the klystron assembly itself (K). The changes in fluid states due to the piping pressure drop and heat losses are given different numbers as in the stations 1-2, 4-5, 6-7, 8-9, 10-11, 12-13, 13-14, 13-31, 15-16, 16-17, 16-26, 17-18, 17-21, 19-20, 22-23, 27-28, 32-33, 34-35, 35-3, and 35-36.

III. Thermal Analysis

The following assumptions were made in the mathematical formulation of the system:

(1) The entire system, excluding the storage tank, is assumed at steady state, with the fluid flowing at a constant rate.

(2) The system is located in an environment with uniform ambient temperature and solar radiation.

(3) Axial conduction heat transfer is neglected from one end of a component to another.

(4) Sky and ambient temperatures are assumed approximately the same for simplicity.

(5) The fluid inside the storage tank is assumed to be thoroughly mixed to give a uniform temperature. The fluid temperature leaving the tank is assumed to be the same as the fluid temperature inside the storage tank.

(6) The walls of the tank and the various pipes are assumed isothermal.

(7) The temperature of nitrogen gas inside the storage tank is assumed to be the same as the fluid temperature, with negligible heat transfer effect.

(8) The storage tank is assumed in the form of a cylinder exposed partially to solar radiation. For simulation purposes, the surface area of the storage tank which is exposed to solar radiation is assumed to be a ratio λ of the total tank surface area.

Using the above assumptions, two systems, an insulated system and a noninsulated system, have been analyzed. Appendixes A and B give the details of the heat balance for the insulated and noninsulated systems. The temperature distribution of any piece of piping, whether it is insulated or not, is characterized by the expression in Eq. (A-25).

$$T_f(x) = T_{f,e} + \left[\frac{E_1 - B_1 (T_{f,e} - T_a)}{B_1}\right](1 - e^{-C_1 X}) \quad (1)$$

where B_1 is the overall heat transfer coefficient between the fluid and the ambient air, E_1 is the solar energy absorbed by the pipe, $T_{f,e}$ is the fluid temperature to the pipe entrance, C_1 is the pipe characteristic constant, x is the distance measured from the pipe entrance, and $T_f(x)$ is the fluid temperature at that location.

The general solution for the time history of the storage tank outlet temperature can be expressed as in Appendix B by an equation similar to Eq. (1) as,

$$T_f(t) = T_f(0) + \left[\frac{D_2}{D_1} - T_f(0)\right](1 - e^{-D_1 t}) \quad (2)$$

where $T_f(t)$ is the fluid temperature leaving the tank after a time internal t, and D_1 and D_2 are the storage tank characteristic constants that depend on the mass flow rate, thermal conductances, and the tank inlet fluid temperature as shown in Appendix B. The value D_2/D_1 represents the final equilibrium temperature of the tank with a constant inlet temperature.

In order to determine the time increment for a stable and convergent solution of the transient analysis, the time constant $1/D_1$ is calculated. When time t equals D_1, the temperature difference $(D_2/D_1) - T_f(0)$ would drop by 36.8 percent from its initial value. A new time increment is calculated for each time interval.

The temperature rise due to the pump dissipating work can be determined by using the thermodynamics relationship for the incompressible flow as

$$\Delta T_f = \frac{W_p}{\dot{m}_f C_p} \quad (3)$$

where W_p is the actual pump work in the system and $\dot{m}_f$ and C_p are the fluid mass flow rate and the fluid specific heat, respectively. The heat dissipation in the system can be correlated with the temperature rise of the cooling fluid. The general expression for the fluid outlet temperature $T_{f,ex}$ is

$$T_{f,ex} = \frac{Q + \dot{m}_f C_p T_{f,e}}{\dot{m}_f C_p} \quad (4)$$

where Q is the heat generated by the klystron systems and $T_{f,e}$ is the fluid temperature at the klystron inlet.

Stations 4, 24, 29, and 34 represent the fluid mixing locations. The general expression for the mixed fluid temperature is

$$T_{f,m} = \beta T_{f,1} + (1 - \beta) T_{f,2} \quad (5)$$

where β is the mass ratio of the flow rate in the first stream, whose temperature is $T_{f,1}$, to the total mass flow. $T_{f,2}$ is the fluid temperature of the second stream. The fluid temperature at station 35 represents the return fluid temperature just before the heat exchanger bypass loop. The bypass ratio γ is determined by the temperature control valve and is calculated by iteration at each time step. The final γ value is determined when the system reaches the steady state operating conditions. Due to the insufficient physical information of the heat exchanger, it is assumed that the heat exchanger is of the counter flow type. The fluid temperature leaving the exchanger, $T_{f,ex}$, can be expressed in terms of the entering fluid temperature $T_{f,e}$ as (Ref. 1)

$$T_{f,ex} = T_{f,e} - \frac{(T_{f,e} - T_a)(1 - e^p)}{\left(\frac{\dot{m}_f C_p}{\dot{m}_a C_a}\right) - e^p} \quad (6)$$

where

$$p = UA\left(\frac{1}{\dot{m}_f C_p} - \frac{1}{\dot{m}_a C_a}\right)$$

UA = the product of the overall heat transfer coefficient and the total surface area given in Ref. 2.

C_a = the specific heat of the air

C_p = the specific heat of the fluid

$\dot{m}_a$ = the mass flow rate of the air

$\dot{m}_f$ = the mass flow rate of the fluid

IV. Computer Program Methodology

A computer program entitled Kystron Cooling Project (KCP) is written using the mathematical model developed in Section III and Appendixes A and B. The program includes a main program and five subroutines. The program starts its computation at the heat exchanger outlet (station 1). Initially, the fluid temperature is assumed 10°F above the ambient condition and all fluid is flowing through the heat exchanger (γ equals to zero). The program then proceeds its computation in the sequence as described in Fig. 1. For each of the pipe loss calculations, the subroutine PIPE is called to compute the fluid exit temperature. The storage tank calculation is handled in the TANK subroutine, and the time constant $(1/D_1)$ will be used for the next time increment. In each of the pipe loss calculations, HTCOE and AHTOE subroutines are called to calculate the heat transfer coefficient of the fluid inside the pipe and the heat transfer coefficient to the ambient air, respectively, for different pipe sizes and lengths. The WRTEMP subroutine prints out the fluid condition at each of the stations indicated in Fig. 1. A temperature sensor is built into the program which compares the calculated temperature at station 18 and the design setpoint of the klystron assembly. The difference of the two temperatures will be adjusted by the temperature control valve at station 2. The valve determines the amount of the fluid flow passing through the heat exchanger which mixes with the returning flow (3) to deliver the new adjusted temperature by iterations. When the design condition of the klystron assembly is met for three consecutive times, the system has reached steady state operating condition, and the time required for the first occurrence is considered to be the system response time.

V. Summary

The computer program has not only analyzed the performance of a cooling system, but it also has provided a helpful tool for the designer in setting design requirements. However, in order to evaluate the performance of a system, detailed information of the system is needed. When this study was initiated, several cooling design concepts were considered. Physical dimensions and system control requirements were not available. The second phase of this study will report the performance and design requirements of a finally selected cooling system.

Definition of Terms

A	area
$B_1 - B_6$	thermal conduction
C_a	air specific heat
C_p	fluid specific heat
$C_1 - C_2$	constants
D	diameter
$D_1 - D_2$	constants
$E_1 - E_4$	energy flux
G	heat capacity
$H_1 - H_7$	heat rate
h	convection heat transfer coefficient
I	solar flux
J	constant
K	thermal conductivity
L	pipe length
M	total fluid mass inside the storage tank
$\dot{m}$	mass flow rate
Q	heat rate
T	temperature
t	time
U	effective heat transfer coefficient
V	velocity
x	distance
Y	thickness
α	absorptivity
ρ	density
μ	viscosity
δ	parameter
ϵ	emissivity
β	mass flow ratio
γ	heat exchanger bypass ratio
λ	ratio of the tank surface area exposed to insulation
γ_1	surface area ratio of tank wall and tank insulation

Subscripts

a	ambient air
e	entrance
ex	exit
f	fluid
I	insulation
i	inside
m	mixing fluid
o	outside
ti	tank insulation
tw	tank wall
w	pipe wall
x	location

References

1. Stocker, W. F., *Design of Thermal System*, McGraw-Hill Book Company, New York, 1971.
2. Young, *Standard MWC-Q Technical Data Publication*, Young Radiator Company, Racine, Wisconsin.
3. Suec, J., *Heat Transfer*, Simon and Schuster, New York, 1975.

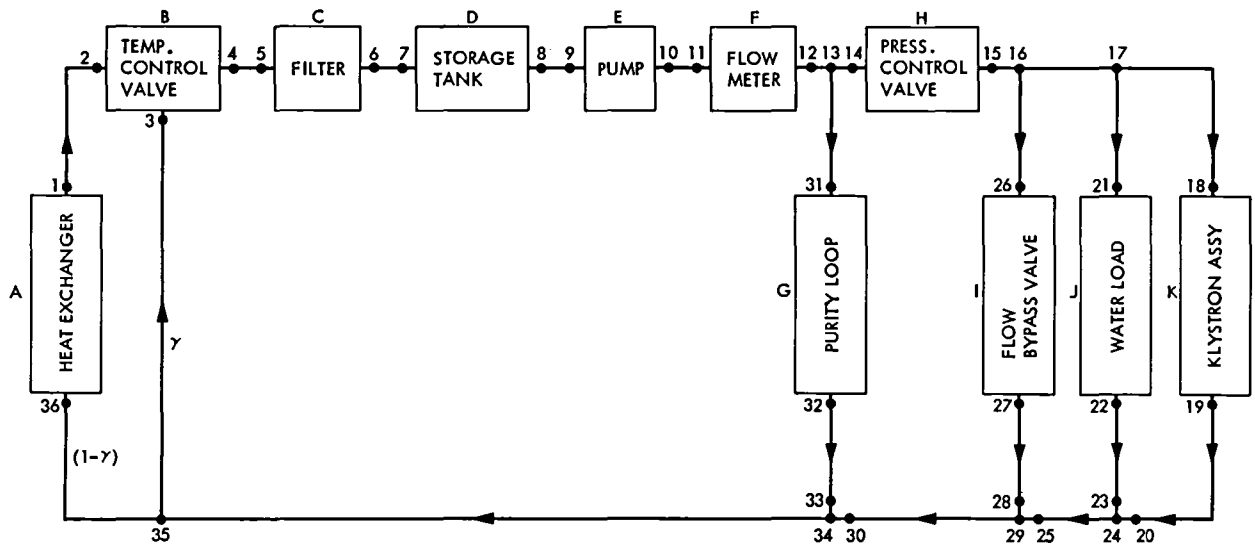

Fig. 1. A candidate cooling loop for the microwave transmitter

Appendix A

Derivation of Temperature Distribution for a Pipe

In this appendix, the derivations of the heat transfer equations for both an insulated and a noninsulated pipe are made. Following the assumptions made in Section III, Fig. A-1 illustrates a segment of an insulated pipe whose length is dx located at a distance x from the inlet fluid section. The differential rates of heat flux are divided as follows:

dQ_1 = total absorbed solar insolation (direct and diffuse) on the outer insulation surface

$$dQ_1 = \alpha_I I D_{I,o}\, dx \tag{A-1}$$

where α_I is the absorptivity of the pipe insulation

dQ_2 = effective heat transfer between the insulation outer surface and the ambient air which combines the convection and radiation parts

$$dQ_2 = U_I (T_{I,o} - T_a)\, \pi D_{I,o}\, dx \tag{A-2}$$

where U_I is the effective heat transfer coefficient

dQ_3 = conduction heat transfer from the insulation layer to the pipe wall

$$dQ_3 = \frac{(T_{I,o} - T_{w,i})\, dx}{\left[\frac{\ln\left(\frac{D_{I,o}}{D_{w,o}}\right)}{2\pi K_I}\right] + \left[\frac{\ln\left(\frac{D_{w,o}}{D_{w,i}}\right)}{2\pi K_w}\right]} \tag{A-3}$$

dQ_4 = convection heat transfer between the interior pipe wall and the fluid flowing through with a heat transfer coefficient h_f

$$dQ_4 = h_f (T_{w,i} - T_f)\, \pi D_{w,i}\, dx \tag{A-4}$$

dQ_5 = sensible heat carried by the fluid from section x to section $(x+dx)$

$$dQ_5 = \dot{m}_f C_p \left(\frac{dT_f}{dx}\right) dx \tag{A-5}$$

Writing the energy balance equations for each of the elementary pipe components at steady state will yield the following equations:

For the insulation surface:

$$dQ_1 - dQ_2 - dQ_3 = 0 \tag{A-6}$$

For the pipe wall:

$$dQ_3 - dQ_4 = 0 \tag{A-7}$$

For the fluid:

$$dQ_4 - dQ_5 = 0 \tag{A-8}$$

The coefficient U_I given in Eq. (A-2), defined as the effective heat transfer coefficient between the insulation outer surface and the ambient air, can be expressed as the summation of a convection heat transfer coefficient h_a and a "linearized" radiation heat transfer one:

$$U_I = h_a + 6\epsilon (T_{I,o}^2 + T_a)(T_{I,o} + T_a) \tag{A-9}$$

The coefficient h_a can be determined by the expression (Ref. 3)

$$h_a = \left(\frac{J K_a}{D_{I,o}}\right)\left(\frac{\rho V_a D_{I,o}}{\mu_a}\right)^n \tag{A-10}$$

where J and n are constants depending upon the Reynolds number as given in Ref. 3 and V_a is the air velocity.

The coefficient h_f given in Eq. (A-4), defined as the convection heat transfer coefficient between the pipe inner surface and the fluid, is obtained from the Nusselt number Nu_D and the diameter $D_{w,i}$ as follows:

$$h_f = \frac{Nu_D K_f}{D_{w,i}} \tag{A-11}$$

The Nusselt number can be determined by applying any one of the following expressions depending on the flow condition:

(a) If Reynolds number Re_D is greater than 7000, the flow is fully developed turbulent (Ref. 3) and the Nusselt number is given by

$$Nu_D = .023\, Re_D^{.8}\, Pr^{.3} \tag{A-12}$$

where Pr is the Prandtl number

(b) if Re is less than 2100, the flow is laminar and the Nusselt number is obtained from

$$Nu_D = 3.66 + \frac{.067\left(\frac{D_{w,i}}{L}\right) Re_D\, Pr}{1 + .04\left[\left(\frac{D_{w,i}}{L}\right) Re_D\, Pr\right]^{2/3}} \tag{A-13}$$

where L is the length of the pipe

If Reynolds number ranges $2100 < Re_D < 7000$, the flow is considered as a transition flow. Since very few experimental data are available in this flow regime, a straight line interpolation for the Nusselt numbers between the laminar regime and the turbulent regime is assumed as a first approximation

$$Nu_D = Nu_D\,(2100) + (Re_D - 2100)\left[\frac{Nu_D\,(7000) - Nu_D\,(2100)}{7000\text{-}2100}\right] \tag{A-14}$$

Equations (A-6) through Eq. (A-8) can be rewritten after substituting all the dQ values and dividing by $(D_{I,o}\, dx)$ as follows:

For the insulation surface

$$E_1 - B_1\,(T_{I,o} - T_a) - B_2\,(T_{I,o} - T_{w,i}) = 0 \tag{A-15}$$

For the pipe wall:

$$B_2\,(T_{I,o} - T_{w,i}) - B_3\,(T_{w,i} - T_f) = 0 \tag{A-16}$$

For the fluid:

$$B_3\,(T_{w,i} - T_f) - G\frac{dT_f}{dx} = 0 \tag{A-17}$$

where

$$\left.\begin{aligned} B_1 &= U_I\,\pi \\ B_2 &= \frac{1}{\left[\frac{\ln\left(\frac{D_{I,o}}{D_{w,o}}\right)}{2\pi K_I}\right] + \left[\frac{\ln\left(\frac{D_{w,o}}{D_{w,i}}\right)}{2\pi K_w}\right](D_{I,o})} \end{aligned}\right\} \tag{A-18}$$

$$\left.\begin{aligned} B_3 &= h_f\pi\left(\frac{D_{w,i}}{D_{I,o}}\right) \\ E_1 &= \alpha_I I \\ G &= \frac{\dot{m}_f\, C_p}{D_{I,o}} \end{aligned}\right\} \tag{A-19}$$

Expressing the temperature $T_{I,o}$ and $T_{w,i}$ in terms of T_a using Eqs. (A-15) and (A-16) yields

$$\left.\begin{aligned} T_{I,o} &= \frac{E_1 + B_1\, T_a + B_2\, T_{w,i}}{B_4} \\ T_{w,i} &= \frac{E_2 + B_3\, T_f}{B_5} \end{aligned}\right\} \tag{A-20}$$

where

$$\left.\begin{aligned} B_4 &= B_1 + B_2 \\ B_5 &= B_3 + B_2 - \left(\frac{B_2^2}{B_4}\right) \\ E_2 &= E_1\left(\frac{B_2}{B_4}\right) + \left(\frac{B_1 B_2}{B_4}\right) T_a \end{aligned}\right\} \tag{A-21}$$

Substituting $T_{w,i}$ in Eq. (A-17), the differential equation for the fluid in the pipe at any position x from the entrance will be

$$\frac{dT_f}{dx} + C_1 T_f = C_2 \tag{A-22}$$

where

$$C_1 = \left(\frac{B_3}{G}\right)\left(1 - \frac{B_3}{B_5}\right)$$

$$C_2 = \frac{B_3 E_2}{G B_5} \tag{A-23}$$

Note that C_1 is positive since $(B_5 - B_3)$ can be proved to be equal to $B_1 B_2 / B_4$.

The general solution of the differential Eq. (A-22) is

$$T_f(x) = \delta e^{C_1 x} + \frac{C_2}{C_1} \tag{A-24}$$

where δ is an arbitrary constant which is determined by the following boundary condition:

At the pipe inlet section ($X = 0$) the fluid temperature $T_{f,e}$ is assumed given. Substituting in Eq. (A-24), the temperature distribution $T_f(x)$ can be reduced to:

$$T_f(x) = T_{f,e} + \left[\frac{E_1 - B_1 (T_{f,e} - T_a)}{B_1}\right](1 - e^{-C_1 x}) \tag{A-25}$$

The quantity $[E_1 - B_1 (T_{f,e} - T_a)]$ represents the net energy exchange between the fluid and the ambient air. B_1 is, therefore, the overall heat transfer coefficient as given by Eq. (A-18), and E_1 is the solar energy absorbed by the system as given in Eq. (A-19).

The second term of Eq. (A-25) $(1 - e^{-C_1 x})$ is considered a dimensionless flow factor. C_1 as given by Eq. (A-23) is a function of the heat transfer coefficients (B's) and the mass flow rate ($\dot{m}_f$).

Equation (A-25) can be applied to a noninsulated pipe, as well with the following changes:

(1) The absorptivity α_w of the pipe wall should be used to replace α_I of the insulation in Eq. (A-1).

(2) The outside diameter $D_{w,o}$ of the pipe should replace $D_{I,o}$ of the insulation.

(3) The outer surface temperature $T_{w,o}$ of the pipe should replace $T_{I,o}$ of the insulation.

(4) The heat conduction term B_2 in Eq. (A-18) should be modified as follows:

$$B_2 = \frac{1}{\left[\frac{\ell n \left(\frac{D_{w,o}}{D_{w,i}}\right)}{2\pi K_w}\right](D_{w,o})}$$

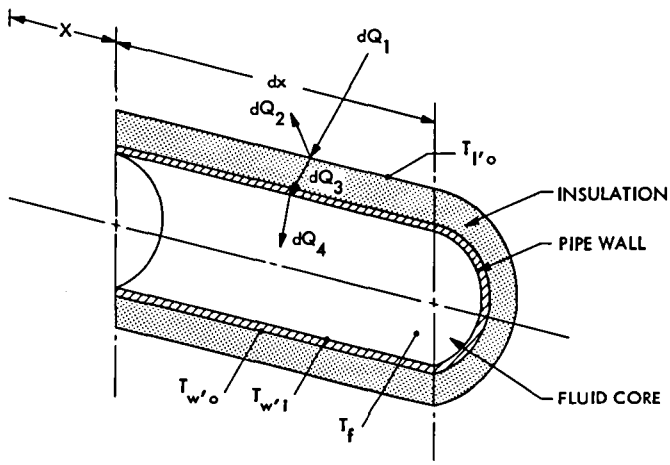

Fig. A-1. Segment of a pipe with thickness dx

Appendix B

Derivation of Temperature Variation for a Storage Tank

In this appendix, the heat transfer equations for an insulated and a noninsulated fluid tank are derived, using the assumptions listed in Section III in the text.

Figure B-1 illustrates a cross section of an insulated storage tank with an insulation thickness Y_I. The heat flux is divided as follows:

H_1 = total absorbed solar radiation (direct and diffuse) on an area with a ratio λ of the outer tank surface area.

$$H_1 = \lambda \alpha_{ti} I A_{ti,o} \tag{B-1}$$

where α_{ti} is the absorptivity of the insulation envelope.

H_2 = effective heat transfer between the insulation outer surface and the ambient air.

$$H_2 = U_{ti} (T_{ti,o} - T_a) A_{ti,o} \tag{B-2}$$

where U_{ti} is the effective heat transfer coefficient which is determined by equations similar to Eqs. (A-9) and (A-10) and $T_{ti,o}$ is the outside tank insulation surface temperature.

H_3 = conduction heat transfer through the insulation layer with thickness Y_{ti}.

$$H_3 = \frac{(T_{ti,o} - T_{tw,i}) A_{tw,o}}{\left(\frac{Y_{ti}}{K_{ti}}\right) + \left(\frac{Y_{tw}}{K_{tw}}\right)} \tag{B-3}$$

H_4 = convection heat transfer from the storage wall to the fluid inside the storage.

$$H_4 = h_{f,T} (T_{tw,i} - T_f) A_{tw,i} \tag{B-4}$$

where $h_{f,T}$ is the convection heat transfer coefficient between the tank wall and the fluid inside the tank.

H_5 = sensible heat gain by the fluid inside the storage tank.

$$H_5 = M C_p \frac{dT_f}{dt} \tag{B-5}$$

where M is the total fluid mass inside the tank

H_6 = extracted sensible heat gain by the fluid passing through the storage tank.

$$H_6 = \dot{m}_f C_p (T_f - T_{f,e}) \tag{B-6}$$

where $\dot{m}_f$ is the steady mass flow rate in and out of the tank, and $T_{f,e}$ is the fluid temperature at the storage tank entrance. $T_{f,e}$ is assumed to be constant in each time step calculation.

H_7 = heat generated by the auxiliary heater located inside the tank. Three energy balance equations are found by grouping Eqs. (B-1) to (B-6) and H_5 as follows:

For the insulation surface

$$H_1 - H_2 - H_3 = 0 \tag{B-7}$$

For the tank wall

$$H_3 - H_4 = 0 \tag{B-8}$$

For the fluid inside the tank

$$H_5 = H_4 + H_6 + H_7 \tag{B-9}$$

After substituting all the values into Eqs. (B-7) to (B-9) and dividing by $(A_{ti,o})$, the energy balance equations become

For the insulation surface

$$E_1 - B_1 (T_{ti,o} - T_a) - B_2 (T_{ti,o} - T_{tw,i}) \tag{B-10}$$

For the tank wall

$$B_2 (T_{ti,o} - T_{tw,i}) - B_3 (T_{tw,i} - T_f) = 0 \tag{B-11}$$

For the fluid inside the tank

$$MC_p \frac{dT_f}{dt} = B_3 (T_{tw,i} - T_f) + G (T_f - T_{f,e}) + \frac{H_7}{A_{ti,o}} \quad \text{(B-12)}$$

where

$$\left.\begin{aligned} B_1 &= U_{ti} \\ B_2 &= \frac{\gamma_1}{\left(\frac{Y_{ti}}{K_{ti}}\right) + \left(\frac{Y_{tw}}{K_{tw}}\right)} \\ B_3 &= h_{f,T}\,\gamma_1 \end{aligned}\right\} \quad \text{(B-13)}$$

$$\left.\begin{aligned} \gamma_1 &= \frac{A_{tw,i}}{A_{ti,o}} \\ E_1 &= \lambda \alpha_{ti} I \\ G &= \frac{\dot{m}_f C_p}{A_{ti,o}} \end{aligned}\right\} \quad \text{(B-14)}$$

Using Eqs. (B-10) and (B-11), temperatures $T_{ti,o}$ and $T_{tw,i}$ can be expressed as

$$\left.\begin{aligned} T_{ti,o} &= \frac{E_1 + B_1 T_a + B_2 T_{tw,i}}{B_4} \\ T_{tw,i} &= \frac{E_2 + B_3 T_f}{B_5} \end{aligned}\right\} \quad \text{(B-15)}$$

where $B_4 = B_1 + B_2$

$$\left.\begin{aligned} B_5 &= B_2 \left(1 - \frac{B_2}{B_4}\right) + B_3 \\ E_2 &= \left(\frac{B_2}{B_4}\right) E_1 + \left(\frac{B_1}{B_4}\right) B_2 T_a \end{aligned}\right\} \quad \text{(B-16)}$$

substituting $T_{tw,i}$ into Eq. (B-12) yields

$$\frac{dT_f}{dt} = D_1 T_f + D_2 \quad \text{(B-17)}$$

where

$$\left.\begin{aligned} B_6 &= B_3 \left(\frac{B_3}{B_5} - 1\right) + G \\ D_1 &= \frac{B_6}{MC_p} \\ E_3 &= \left(\frac{B_3}{B_5}\right) E_2 \\ E_4 &= \frac{H_7}{A_{ti,o}} \\ D_2 &= \frac{E_5 - G T_{f,e} + E_4}{MC_p} \end{aligned}\right\} \quad \text{(B-18)}$$

The final general solution for this differential equation is

$$T_f(t) = \delta e^{-D_1 t} + \frac{D_2}{D_1} \quad \text{(B-19)}$$

where δ is an arbitrary constant determined by the initial condition:

At time equals zero, the fluid temperature inside the tank $T_f(0)$ is given. Substituting in Eq. (B-19) and rearranging terms; the temperature variation $T_f(t)$ is given by

$$T_f(t) = T_f(0) + \left[\frac{D_2}{D_1} - T_f(0)\right] (1 - e^{-D_1 t}) \quad \text{(B-20)}$$

The quantity $[(D_2/D_1) - T_f(0)]$ can be expressed as the amplitude of disturbance which depends on the thermal conductances (B's), the heat fluxes (E's), the flow capacitance (G) and the storage tank inlet temperature ($T_{f,e}$). If the mass flow ($\dot{m}_f$) is equal to zero, the quantity would reduce to become the static disturbant amplitude in the stagnation condition. The factor $(1 - e^{-D_1 t})$ is defined as the time decay factor which describes the time history of the storage tank.

Equation (B-20) can be applied to a noninsulated tank with the following changes:

(1) The outside tank area ($A_{tw,o}$) should be used to replace the outside tank insulation area ($A_{ti,o}$) in all appropriate equations.

(2) The tank wall absorptivity (α_{tw}) should replace the tank insulations absorptivity (α_{ti}) in Eq. (B-1).

(3) The outer tank wall temperature ($T_{tw,o}$) should replace the outer tank insulation's temperature ($T_{ti,o}$) in Eqs. (B-2) and (B-3).

(4) B_2 in Eq. (B-13) should be modified as follows:

$$B_2 = \frac{\lambda}{\left(\frac{Y_{tw}}{K_{tw}}\right)} \qquad \text{(B-21)}$$

(5) The effective heat transfer coefficient U should be recalculated using the outside diameter of the tank instead of the outside diameter of the insulation.

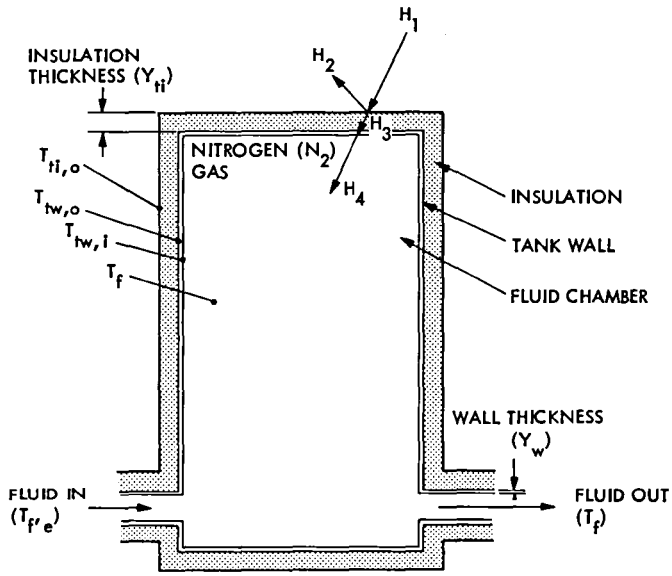

Fig. B-1. Cross section of a storage tank

Implementing the UCSD PASCAL System on the MODCOMP Computer

T. Wolfe
DSN Data Systems Section

This article describes the UCSD PASCAL system developed by the University of California, San Diego, now available on the MODCOMP computer. The system includes a Pascal compiler and many useful utility programs. A BASIC compiler and a FORTRAN 77 compiler are also available. There is currently a large amount of software available written in UCSD PASCAL, including a data base system, word processing systems and a MODULA compiler.

I. Introduction

The UCSD PASCAL* System is a complete interactive software development system consisting of an operating system, compilers (Pascal, BASIC, FORTRAN 77), two text editors (screen editor and line-oriented editor), a linker and many useful utility programs. The system is written and maintained in Pascal. The compiler generates code for an idealized processor known as the "pseudo-machine." The "pseudo-code" (p-code) generated by the compiler is interpreted at runtime by a program (known as the interpreter) which emulates the pseudo-machine. Thus, the operating system, compilers, editors and all user programs are executed using the same interpreter. By writing a new interpreter, the complete programming system may be moved to a new computer.

Because the Pascal and FORTRAN 77 compilers generate the same p-codes (i.e., use the same interpreter), Pascal programs may call FORTRAN subroutines and vice versa. The system also contains an adaptable assembler which is easily modified to produce assembly language for a new computer. Assembly language subroutines thus produced may also be called from either Pascal or FORTRAN. Currently the assembler has not been modified to produce MODCOMP machine code. A system library program may be used to build libraries of useful subroutines and the system linker used to link them to user programs.

Interpreters currently exist for Z80/8080, PDP 11/LSI-11, 6800, 9900 and 6502 computers and are being developed for other computers. Thus, software could be developed on an 8080 micro or any existing system and run on a MODCOMP.

An interpreter for the MODCOMP II and the MODCOMP IV computers has been written in MODCOMP II assembly language. The complete Pascal programming system has been run successfully on a MODCOMP II and MODCOMP IV under both the MAX II/III and MAX IV operating systems. A copy of the system was sent to the Oak Ridge National Labs and was installed and running within an hour.

The interpreter requires approximately 4.5K words of memory and a work area. The minimum memory requirements

*Trademark of the Regents of the University of California.

for the complete system is 16K words plus the interpreter. The maximum is 64K words.

An error was discovered in the MODCOMP teletype handler and several patches for both the MAX II/III and the MAX IV operating systems were recommended by MODCOMP. These patches are documented and available to anyone who wishes to implement the system.

A large portion of the University of Tasmania's Pascal validation suite has been run by JPL, and several errors in the interpreter were discovered and corrected.

II. The Pseudo-Machine

The UCSD PASCAL program development system is an interpreter-based implementation of Pascal. The compiler generates code for a pseudo-machine which is emulated by the interpreter at runtime. The pseudo-machine has a stack architecture with a stack being built from high memory downward (Fig. 1). The interpreter sits in low memory with the heap being built upward from it.

Large programs that normally would not fit into memory may be partitioned into segments, only some of which need be resident in memory at a time. User programs may be partitioned into a maximum of 7 segments, each with up to 127 procedures or functions. During the running of a program each segment is loaded onto the stack as it is needed and then discarded. The first segment to be loaded upon executing the Pascal system is segment zero of the operating system. It contains all the IO functions for the system and user programs and is never discarded from the stack.

The Pascal system has available to it several IO units which may be assigned to MODCOMP logical units. In general it has a console, printer and up to 6 Pascal disk units. (A Pascal disk unit is a MODCOMP disk partition.) Each Pascal disk unit has a directory and may contain up to 77 Pascal files.

A special IO unit (unit 0) is also available to the user. This unit performs a read or write via a simple REX service call. In this manner the user may read or write data not in the Pascal format.

In addition there are three other Pascal IO units which are undefined at this time. They are GRAPHICS, REMIN and REMOUT. These could be defined and an appropriate driver written into the interpreter.

III. Design of the Interpreter

At the start of the project there was no documentation available for the design of any of the existing interpreters. The implementer was also unfamiliar with the MODCOMP computer. The source code (with very poor to nonexistent comments) for an 8080 microcomputer version of the interpreter written by UCSD was available. This source code was used as the design for the MODCOMP interpreter. A mapping of the functions within the 8080 interpreter into MODCOMP II assembly language was the method used to code the interpreter. This method allowed the implementer to learn how the system was designed and to code the interpreter simultaneously. It also allowed the implementor to become familiar with the MODCOMP. The method worked rather well but would have been easier if the source code were properly documented. For example, the carry was used as a flag in various widely separated places in the code. No comments indicated when the carry was set, what it meant or where it was used.

The 8080 interpreter is in reality two separate programs. The first loads the interpreter and initializes the Pascal system and the second is the interpreter. These were combined into one program for the MODCOMP interpreter.

The only interface between the MODCOMP operating system and the Pascal system is REX service calls. This allows the Pascal system to use the flexibility of logical file assignments within the MODCOMP operating system and yet maintain its independence.

The MODCOMP interpreter has three major functional areas. They are:

(1) The BOOTER, which initializes the work space and loads the Pascal operating system. It is executed only once at the beginning of the interpreter.

(2) The BIOS (Basic IO System), which performs all IO operations for the Pascal system.

(3) The p-code interpretive routines which make up the bulk of the interpreter. Program control cycles through these routines as various programs are interpreted.

In order to reduce complexity and the time needed to code the interpreter, the floating point intrinsic routines such as SIN, LN, COS, LOG, FLOAT INTEGER, etc., were taken from the MODCOMP FORTRAN library verbatim. P-code interpretative routines which perform these functions make calls to these routines.

All IO operations in the BIOS are done by IO unit number only. The Pascal operating system maintains all necessary

parameters for reading or writing files by name, all buffering, and directories on all disk units. The BIOS receives only a unit number, number of bytes, a memory address and a disk block number if a disk unit is being accessed.

In the BIOS the unit number is used to index into a jump table and the appropriate IO driver executed. Each type of IO unit has its own driver, depending on its characteristics. For example, each character sent to the printer is saved in a buffer until a carriage return; then the complete line is printed out. All characters sent to the printer are also converted to uppercase because the standard DSN MODCOMP printer cannot handle lowercase characters.

IV. P-Code Conversion

The interpreter would be useless without p-code programs to interpret. The UCSD PASCAL system consists of approximately 20 programs, all in p-code form. These programs were transferred from an 8080 microcomputer to the MODCOMP and converted. Three special programs were needed to convert the byte-sex (see below) of the p-codes to run on the MODCOMP. It should be noted that none of the standard system programs use floating point. This would require a different type of conversion.

The 8080 micro and the MODCOMP use different ordering of bytes in memory (different "byte-sex"). The difference is in the way the two computers store 16-bit integer values in memory and is due mainly to the 8080 being a byte machine and the MODCOMP being a word machine.

The two different ways of ordering bytes in memory are:

(1) Byte ZERO is the byte containing the least significant half of the word. Byte ONE contains the most significant half.

(2) Byte ZERO is the byte containing the most significant half of the word. Byte ONE contains the least significant half.

For example: Storing the hex value 47B8.

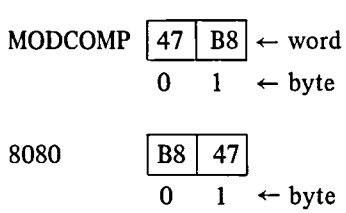

This requires all integer values in the p-codes to have their byte-sex changed when run on the MODCOMP. It was decided to write conversion programs rather than to change the byte-sex at runtime in the interpreter to avoid slowing the runtime execution speed.

As shown in Fig. 2, two programs are necessary to change the byte-sex of a Pascal disk unit to a form usable by the MODCOMP. Each Pascal disk unit contains a directory and files, only some of which may be code files.

The first program (DSKMOD) converts the disk directory and the segment dictionary of all code files. The second program (CODMOD) converts the p-code segments of all code files or any non-code files containing p-codes. For example, the operating system (SYSTEM.PASCAL) is not a code file, although in all other respects it looks like a code file. Library files are also noncode files, but contain code segments.

A third conversion program was also found necessary to convert the op-code data file (OPCODES.II.0) used by the p-code disassembler program. Conversion is not necessary if you never use this program.

It should be noted that these conversion programs are not needed unless the user is transferring a code file from the 8080 micro to the MODCOMP.

A copy program, called appropriately enough "COPY," was written to simplify the transfer of the Pascal system from one MODCOMP computer to another. It copies a MODCOMP disk partition containing a Pascal disk unit (directory and files) to another disk partition or tape. This simple program and the interpreter are all that are needed to install the system on a new MODCOMP computer.

V. System Software Problems

Two system programs were found to have problems. Both were corrected by making small changes in their Pascal source code and recompiling them.

The program PATCH is used to display and modify memory directly. The program displays memory in reverse order for the 8080 micro. Fortunately, the source code for this program contained comments indicating what to change to correct this problem.

The second program with a problem was the system linker (SYSTEM.LINKER). This problem was due to the design of the program. It was designed with the architecture of the 8080 micro in mind. The code was therefore not machine-independent Pascal. Several patches were added to the code, modifying it to work on a word machine. No effort was made to redesign the program.

VI. Conclusion

The UCSD PASCAL programming system is now available on the MODCOMP II and MODCOMP IV computers. It provides a useful program development environment for its users. Using the interactive editors, compilers, linker and libraries, software in Pascal or FORTRAN 77 may be developed quickly. The ability to develop software on a microcomputer and transfer it to a MODCOMP has the large advantage of relieving the overworked MODCOMP computers from software development work.

Follow-on activities should include modifying the assembler to produce MODCOMP machine code and looking into code generation and optimization from the p-code.

References

1. *UCSD PASCAL System II.0 User's Manual*, Institute for Information Systems, University of California, San Diego Campus, March 1979.
2. *UCSD PASCAL System Synchronous Input/Output Subsystem Implementation Guide* (Release Level II.1 Preliminary), University of California, San Diego Campus, 10 April 1979.
3. Bowles, K. L., *Beginner's Guide for the UCSD PASCAL System*, Byte Books, 1980.

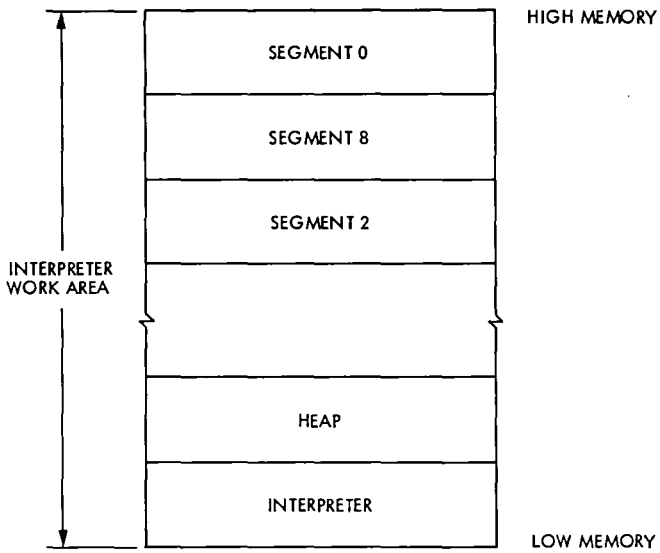

Fig. 1. The general configuration of memory. Segments are loaded into memory as they are needed

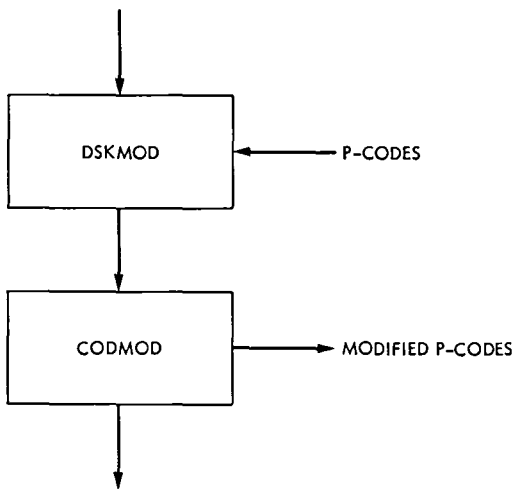

Fig. 2. Flowchart showing the general flow of data and programs necessary to change the byte-sex of a Pascal disk unit containing p-code files

X-Band, Low-Noise, Traveling-Wave Maser

D. L. Trowbridge
Radio Frequency and Microwave Subsystem Section

Four X-band traveling-wave maser (TWM) systems with effective input noise temperatures of 3.5 K and bandwidths varying from 65 to 108 MHz have been supplied to the Deep Space Network. These TWMs are used on the 64-meter antennas at Deep Space Stations 14, 43 and 63 at 8420 MHz to meet the requirements of the Voyager-Saturn encounter. The TWMs use shortened and cooled signal input waveguide to reduce noise and are equipped with superconducting magnets and solid-state pump sources to provide the required stability performance.

I. Introduction

The Voyager encounter with Saturn required increased traveling-wave maser (TWM) sensitivity at X-band. In addition, support of very long baseline interferometry (VLBI) required increased bandwidth at X-band (previous X-band TWMs covered 8395-8445 MHz at the -3 dB points). Three TWM assemblies have been built in response to these requirements and installed at Deep Space Stations (DSS) 14, 43 and 63. A fourth TWM assembly was also built as a spare. The TWMs provide 45 dB net gain with a -3 dB bandwidth varying from 65 to 108 MHz (see Table 1). An effective input noise temperature of 3.5 K and an overall system temperature of 11.0 K were measured during the evaluation of these systems using a low noise horn looking at cold sky. These new X-band TWMs are identified as Block II low-noise TWMs.

II. Design Goals

The following performance design goals were established for the Block II low-noise TWM:

(1) Gain, -43 dB minimum, 46 dB maximum

(2) Bandwidth (-3 dB), > 100 MHz

(3) Gain stability

dB per 10 sec	±0.03
dB per 12 hr	±0.5
dB for tilting	±0.5

Interchangeability with existing Block I TWMs (Ref. 1) was also required.

III. Maser Description

The Block II TWM assembly shown in Fig. 1 is supported by a frame that is similar to the Block I X-band (Ref. 1) and Block IV S-band (Ref. 2) TWMs presently used in the DSN. The Block II TWM assembly is also similar in weight (approximately 80 kg) and size, with the exception of height (the Block II TWM assembly is approximately 10 cm longer). The

difference in height and location of the signal input and output waveguide ports required a new dual TWM mounting stand and waveguide to accommodate both Block I and Block II TWMs interchangeably.

Mounted on the TWM support frames (Fig. 1) is a new pump source assembly similar in design to pump sources used on R&D masers not previously reported. Pump energy is provided by two separate Gunn oscillators at 19 and 24 GHz each with approximately 200 mW output.

The frequency is combined in a manner similar to that used on the Block I X-band TWM described in Ref. 1. The modulation and voltage protection design are similar to that used on Block IV S-band masers (Ref. 2) and an R&D TWM (Ref. 3).

The Block II TWM uses a shortened and cooled signal input waveguide assembly (see Fig. 2) that contributes only 0.3 K to the maser noise temperature; previous Block I TWMs (Ref. 1) used an input waveguide assembly that contributed approximately 3.5 K.

A new half-wavelength stripline comb structure similar to that shown in Fig. 3, is used in the Block II TWMs. The compact size of the structure allows several structures to be used in one superconducting magnet. The Block II TWM uses four structures mounted in one superconducting magnet as shown in Fig. 4. The four structures are connected in series to achieve the required gain-bandwidth product. Steel shims are mounted on the top and bottom of the structure over approximately half of the structure length to spread the magnetic field and obtain the desired stagger-tuned bandpass. The halfwave structure and magnet are shown in Fig. 4 mounted to the refrigerator 4.5 K heat station with the low-noise waveguide in its approximate position. The low-noise input waveguide, halfwave structure, isolator assembly and superconducting magnet will be covered in detail in future reports.

IV. Performance

The gain, bandwidth and noise temperature were measured prior to shipment and are listed in Table 1. The noise temperature was measured using a horn and ambient temperature load (microwave absorber). System noise temperature (including feedhorn, maser, and receiver noise temperature contributions) from the 64-meter stations has been reported as low as 19.5 K. All three 64-meter stations (DSS 14, 43 and 63) are within the expected noise temperature goal of 23 K; the Block II X-band TWMs have met or exceeded the performance goals for Voyager-Saturn encounter. The VLBI 100-MHz bandwidth goal has not been met by all Block II TWMs.

V. Future Development

Future development is planned to produce a repeatable gain-bandwidth product design. A post-amplifier, as part of the maser package, will be added to adjust the package gain to the desired value while achieving wide bandwidth and minimizing follow-on noise contribution (< 0.5 K). Supporting research effort is planned using a X4 scaling of the X-band slow structure at 32 GHz. Study of the fields and modes with the X-band structure are planned to insure proper pump saturation and signal inversion ratios.

Acknowledgement

The X-band maser in this article is the product of the combined effort of the Microwave Electronic Group under the supervision of R. C. Clauss. Thanks are due to D. Sutcliffe for his continuous support in the area of fabrication and procurement.

References

1. Trowbridge, D. L., "X-Band Traveling Wave Maser Amplifier," in *The Deep Space Network Progress Report 42-28*, pp. 69-70, Jet Propulsion Laboratory, Pasadena, Calif., Aug. 15, 1975.

2. Trowbridge, D., and Loreman, J., "S-Band Ultralow Noise Traveling-Wave Maser," in *The Deep Space Network Progress Report 42-53* pp. 148-154, Jet Propulsion Laboratory, Pasadena, Calif., Oct. 15, 1979.

3. Quinn, R., "Low Noise Receivers: Microwave Development," in *The Deep Space Network*, Technical Report 32-1526, Vol. XIV pp. 46-49, Jet Propulsion Laboratory Pasadena, Calif., Apr. 15, 1973.

Table 1. TWM performance

SN	Gain, dB	−3dB bandpass, MHz	Frequency, MHz	Noise temp. within bandpass, K
2001	47	90	8400-8490	3.1 to 3.5
2002	46	108	8396-8504	3.30
2003	44	65	8400-8465	3.1 to 3.7
2004	47	84	8398-8482	4.5 to 4.8[a]

[a]Serial number 2004 demonstrated the same system temperature at DSS 14 (19.5 K) as achieved with SN 2002. The 4.5 to 4.8 K measurements were made during hot and humid weather and may include a source of error caused by an unknown atmospheric contribution which should be calibrated in the future.

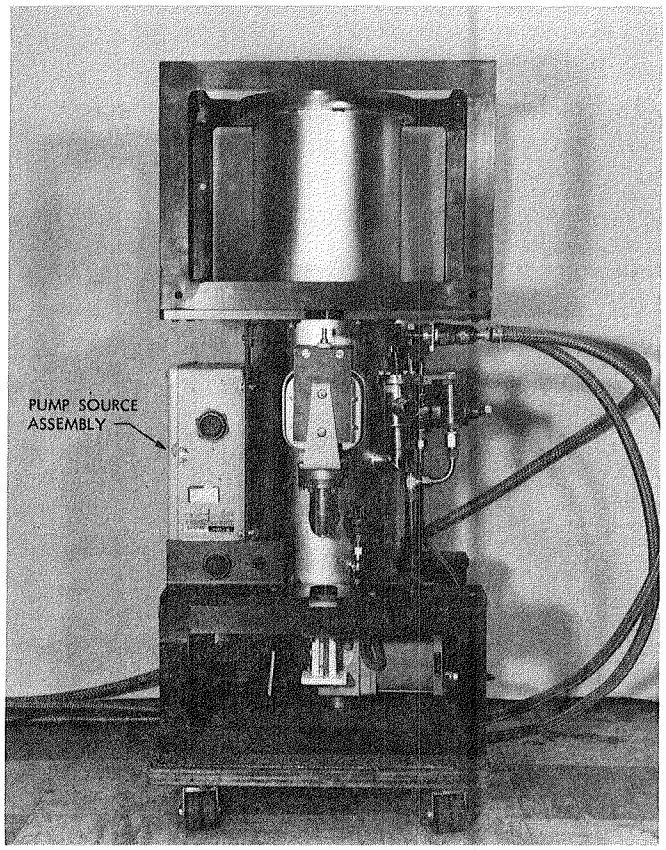

Fig. 1. X-band Block II traveling-wave maser assembly

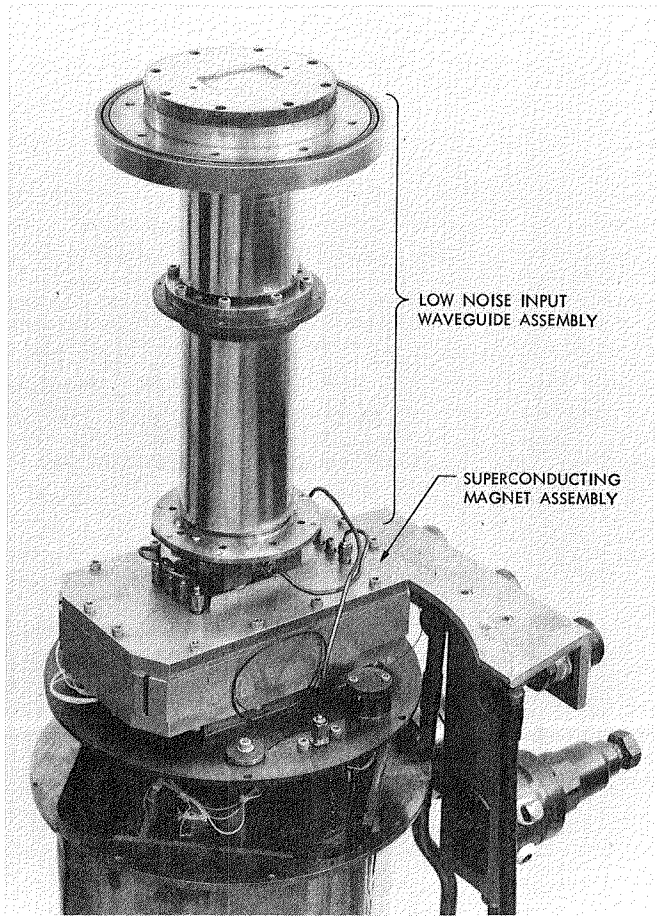

Fig. 2. Low-noise input waveguide, structure assembly and superconducting magnet mounted on helium refrigerator 4.5 K heat station

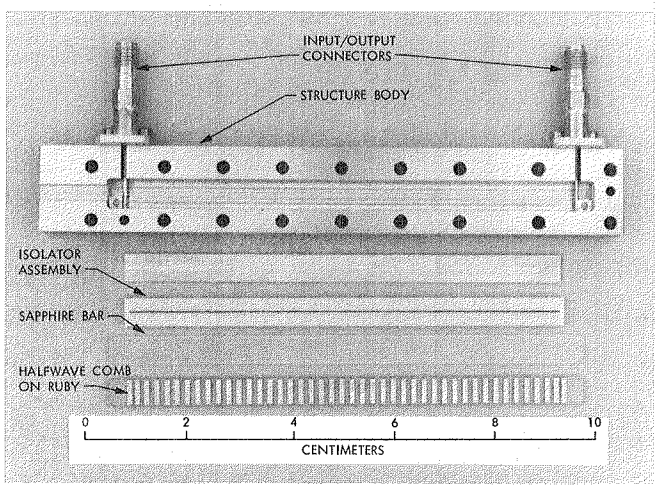

Fig. 3. X-band halfwave stripline comb structure

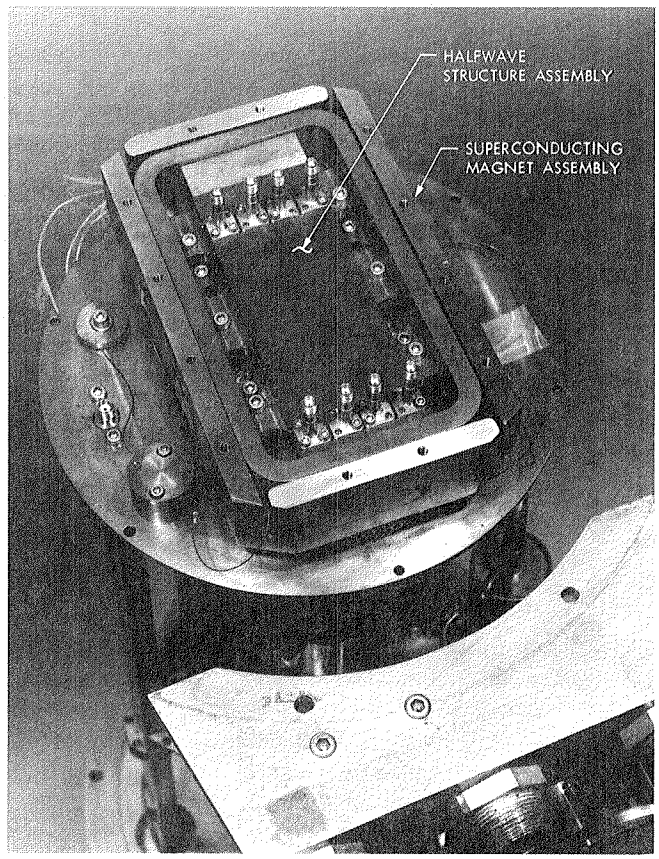

Fig. 4. X-band halfwave structure assembly mounted superconducting magnet

DSS Command Software Update

W. G. Stinnett
DSN Data Systems Section

A new version of the DSS Command Software has been generated for support of the Voyager Saturn encounter. The modifications, additions, and testing results for this version of the software are discussed in this article.

I. Background

The Deep Space Station (DSS) Command Software was initially implemented in late 1976 when new computers were implemented at DSS 12. Modcomp II-25 minicomputers were implemented at the stations throughout the Deep Space Network over a period of time from late 1976 through early 1978. New computers were implemented for the command, telemetry, tracking, and ground communication functions as part of the Mark III Data Subsystem (MDS) implementation project.

Prior to implementation of the new command computers at the DSS, the command data handling function was accomplished in an XDS-920 computer which was shared with the telemetry processing function. This computer system was designated the Telemetry and Command Processor (TCP). With the implementation of the new Modcomp II-25 computers, and the separation of the telemetry and command processing functions, the DSS command computer has been designated the Command Processor Assembly (CPA). The initial implementation of the CPA software was constrained to very much resemble what existed for the TCP. Due to the station-by-station implementation of the CPA, which occurred over approximately one and one-half years, the command data handling characteristics and the interface with flight projects remained the same for the CPA as had existed for the TCP. Therefore, the initial implementation of the software for the CPA included basically the same functional characteristics as the TCP. Support for the following flight projects was provided: Pioneer 6 through 9, Pioneer 10 and 11, Helios 1 and 2, Viking, Pioneer Venus, and Voyager. The software that supported these projects, and was initially implemented in the CPA, was designated Mark III-74. The data processing characteristics were defined and used to support flight project commanding in 1976.

In 1976 and 1977, through negotiations between the Mission Control and Computing Center (MCCC), JPL Flight Project representatives, and DSN personnel, a new end-to-end command data handling system was defined. The command data handling system was termed "store-and-forward". This system took advantage of the increased processing and storage capabilities of the new DSN CPA, and better suited the characteristics of the flight project command generation functions and spacecraft data handling and storage capabilities. In this store-and-forward system, each major element of the system has data handling capabilities for complete sets of spacecraft command information. The flight project command generation software generates files of spacecraft commands to accomplish particular mission objectives. The files are then passed to the

MCCC Command System where they are stored for later transmission to the DSN. Once a Deep Space Station (DSS) has been scheduled, staffed, and initialized for the spacecraft track, the files of command information are transmitted in total to the DSS CPA where they are stored for later radiation to the spacecraft. When the uplink to the spacecraft has been established, the Flight Project Command Operator sends control messages to the DSS CPA to begin radiation of the command information. The files of command information are stored onboard the spacecraft for later automatic execution. This store-and-forward system was implemented in 1978 in the DSS CPA (as well as MCCC and Project Command Generation Software) and was designated Mark III-78.

The Voyager Project was the initial user of the Mark III-78 system. In late 1978, capabilities were developed at the German Mission Operations Center to interface with this new data handling system. The Pioneer and Viking missions continue to use the Mark III-74 data handling system but plans exist to convert the Mark III-78 system at a later date.

II. CPA Software Update Requirements

As with any new significant software package, requirements change with time and anomalies are uncovered during use of the new capabilities. In 1979, it was recognized that modifications and additions would be required for the Mark III-78 CPA software. A new version (OP-G) was scheduled such that it would be available for the Voyager 1, Saturn Encounter.

Effort began in mid 1979 for this new version of CPA software. The scope of the software update involved four areas:

(1) Recode portions of the software to permit recovery of approximately 2000 words of memory. This was necessary to accomplish items (2) through (4).

(2) Correct five Voyager Ground Data System liens.

(3) Provide capability to automatically turn off the CPA local printer during periods of low activity.

(4) Correct anomalies existing in the software.

A. Software Recode

In order to recover the necessary core memory to implement the modifications and additions required, basically two areas were changed in the CPA software. The application software was changed to "fool" the operating system such that more efficient "packing" of the command applications task could be accomplished within the available core memory. Numerous software routines were also modified to become more efficient and thus recover core memory.

B. Voyager Liens

During the time period of use of the Mark III-78 command system, the Voyager Project identified anomalies and new requirements that they desired to be fixed prior to the Saturn encounter. The items were listed as Voyager Ground Data System liens. The liens were (see Progress Report 42-43 for description of CPA data processing capabilities):

(1) Under certain conditions the CPA would report erroneous status of the prime (first) file.

(2) Under certain conditions the CPA would report an erroneous file name for skipped command elements.

(3) Under certain conditions the CPA would generate false expired time alarms.

(4) If the project sent a control message to empty the command queue, and the queue was already empty, CPA software execution would halt.

(5) The Voyager Project desired a modification to change the algorithm for resuming file radiation, i.e., if a resume directive is received by the CPA, the CPA should not resume radiation unless all timing considerations were satisfied.

C. Automatic Turn-Off of Local Printer

Each DSS command subsystem has been implemented with a local character printer for use during software loading and initialization, and as a logging device during operations. These printers have been installed as peripheral devices for all Modcomp II-25 computers implemented in the DSN. These printers have run continuously during program operation regardless of the need for printing. With this continual running, the DSN has experienced a significant failure rate for these printers. In order to alleviate this problem, the Modcomp Operating System has been modified to turn-off these printers when not in use. This version of the operating system was incorporated in the new CPA software version.

D. Anomaly Correction

At the start of implementation of the new version of CPA software, there were thirty-one anomalies open against the CPA software. Some of the anomalies were directly associated with the Voyager liens (see paragraph B above), while others were visible to on-site personnel or by use of the System Performance Test (SPT) software. Much of the effort during this software upgrade involved correction of these anomalies.

III. CPA Software Update—Test Results

The Acceptance Test for this new version of CPA software was successfully completed in late January 1980. As previously stated, this version of the CPA software was implemented with the following scope:

(1) Recode portions of the existing software to permit the recovery of approximately 2000 words of memory.

(2) Correct the five GDS command system liens.

(3) Accommodate the updated Standard Operating System which contains provision for the turning off of the local printer during periods of minimal I/O activity.

(4) Correct DSN anomalies.

Item 1 was accomplished in this upgrade.

Item 2 was accomplished and was successfully testing during the acceptance test. In addition, a test was run in early February with the Voyager Ground Data System personnel which demonstrated clearance of these liens (test between CTA-21 and MCCC).

Item 3 was accomplished and successfully demonstrated during the acceptance test.

Item 4 was accomplished with one anomaly exception. The summary of anomaly status at time of acceptance test completion is given below.

(1) Anomalies corrected and tested 26

(2) Anomalies not repeatable 3

(3) Anomalies closed by document modification 2

(4) Anomalies open were carried as liens on transfer agreement 5

The Software Consent to Ship meeting was held on 31 January 1980. It was agreed that the software was ready to be shipped for the soak period. The software was shipped to Goldstone on 1 February 1980.

During the Voyager Ground Data System tests at Goldstone, prior to going on-line for probationary use, a Class A anomaly was discovered. The anomaly description was:

"During the process of loading command files to the CPA disk, MCCC automatically issues directory recall messages to the CPA. In addition, other directive messages are sent to the CPA during file loading. The loading is not halted during the sending of these directives (i.e., the MCCC does not wait for an acknowledge prior to continuing the load). Under the above conditions, the CPA software is *not* sending the acknowledge messages for the directives."

The software was modified to correct the anomaly. For every block received by the CPA, a check is made to determine if any acknowledge is pending. If any acknowledge is pending, the software will immediately acknowledge (i.e., the delays in the software for acknowledgement will be bypassed).

The acceptance tests were successfully re-run at CTA-21. System Performance Test (SPT) software was modified to test the CPA software for this anomaly. In addition, a test was run with MCCC (and Voyager personnel) to demonstrate correction of the anomaly.

The second Software Consent to Ship meeting was held in early March 1980. It was agreed that the software was ready to be shipped to the Goldstone stations and CTA-21. After successful completion of the soak period at the Goldstone stations, the new version of the CPA software was distributed to all DSN stations. The Voyager Ground Data System Around-the-Net testing was completed in early May 1980 and the software was placed "on-line".

IV. CPA Software—Future Plans

The new version of the CPA software has been on-line for a number of months and has not experienced any problems that will require a software update. However, new requirements are being developed that will require changes to the software. Two versions of the Mark III-78 Command System will be required in the future.

(1) The existing version of the software will require modification to support the Pioneer 10, 11, and 12, Galileo, and the International Solar Polar Missions.

(2) A major modification to the software will be required to support the Mark IV DSN. The Mark IV DSN includes consolidation of STDN and DSN ground tracking stations which will result in requirements on the DSN to track the Highly Elliptical Earth Orbiter Spacecrafts (HEEO). The HEEO spacecrafts will require a significant increase in command bit rate (2000 bps) which will require replacement of the existing Command Modulator Assembly (CMA). This new CMA will require significant changes in the CPA software.

The two future versions of software will require development on an almost concurrent schedule. This will provide an extremely difficult challenge to the DSN implementation organization over the next few years.

RFI Prevention for Colocated Antennas

T. K. Peng
TDA Engineering Office

Current baseline design for the Mark IV-A 1985 Deep Space Network (DSN) calls for colocating the antennas of each Deep Space Communications Complex at one site. This article analyzes potential radio frequency interference (RFI) problems related to colocation and outlines the solutions.

I. Introduction

The Mark IV-A configuration of the Deep Space Network (DSN) is currently being designed for implementation by mid-1985. To reduce life-cycle cost and ensure telemetry and radio metric performance, the present baseline design as of October 1980 requires that all the antennas of each Deep Space Communications Complex (DSCC) be located close to the 64-meter antenna, except for Deep Space Station (DSS) 12 at Goldstone. This study examines the following questions: What are the RFI problems introduced by colocation? What are the solutions and concerns?

Section I defines the baseline network configuration, describes the distinct characteristics of colocated antennas, and identifies potential RFI sources and affected functions.

Section II defines the performance criteria as a design goal for RFI prevention, and describes the analytical model to be used for case-by-case analyses of the RFI sources and effects.

Section III gives the results of analysis for each case and suggests requirements where necessary.

Section IV highlights the conclusions.

Section V summarizes the implementation requirements as suggested and identifies antenna tests necessary to reduce the uncertainties in this analysis. Some of these tests are already underway.

A. Baseline Configuration

The configuration is depicted in Fig. 1. At Goldstone, the following antennas will be colocated:

(1) One 64-meter antenna, transmit and receive, supporting deep-space functions.

(2) Two 34-meter antennas, receive only, supporting deep-space functions or near-earth missions.

(3) One 9-meter antenna, transmit and receive, supporting near-earth missions.

DSS 12, however, will stay where it is and not be colocated.

At Canberra and Madrid, all antennas will be colocated, including the 34-meter transmit-receive antenna.

B. Characteristics of Colocated Antennas

For colocated antennas, the distance between antennas are relatively short (hundreds of meters) and the antennas are

normally within the line of sight of each other. The colocated antennas under study have diverse operating frequency bands, transmitter power levels, and receiver front-ends as shown in Table 1. These antennas also have to point to deep-space missions, near-earth missions, and radio stars, substantially increasing the chance for a transmitting antenna to radiate to the front of a receiving antenna.

C. Potential RFI Sources and Affected DSN Functions

Potential sources of RFI include:

(1) S-band transmitters at the 64-meter and 34-meter antennas.

(2) S-band transmitter at the 9-meter antenna.

(3) Planetary radar transmitters (S- and X-bands) at Goldstone.

(4) Future X-band transmitter at the 34-meter transmit-receive antenna.

(5) Test signal generators.

(6) External sources.

Functions that may be affected include:

(1) Deep space mission X- and S-band receive for telemetry, tracking, and radio science.

(2) Near-earth mission S-band receive.

(3) X- and S-band very long baseline interferometry (VLBI) for navigation and crustal dynamics.

(4) Search for Extraterrestrial Intelligence (SETI).

(5) Radiometer measurements.

(6) Radio astronomy.

II. Performance Criteria and Interference Model

The possible interference between a potential RFI source and an affected function is analyzed according to the performance criteria given below; a description of the mutual interference model follows.

A. Performance Criteria

(1) No significant degradation due to in-band RFI.

(a) Acceptable RFI level for near-earth receive, measured at input to the low-noise amplifier (LNA):

CW[1] type	< -160 dBm (20 dB[2] lower than the carrier level of a typical high-earth orbiter, ISEE-3)
White-noise type	< -185 dBm/Hz (0.5-dB increase in noise temperature)

(b) Acceptable RFI level for deep-space receive, measured at input to the LNA:

CW[1] type	< -192 dBm (20 dB[2] less than the recommended minimum carrier level for 1-Hz loop)
White-noise type	< -202 dBm/Hz (0.1-dB increase in noise temperature)

(2) No receive system saturation due to out-of-band RFI.

(3) Allow antennas to point as close as 10 degrees to each other, from baseline as short as 200 meters.

These criteria would allow daily support of telemetry, tracking, command, and VLBI (to be discussed later) without appreciable restrictions on the pointing of antennas. Radio science and radio astronomy sometimes need a cleaner RF environment that would require some pointing restrictions or schedule coordination.

B. Antenna Mutual Interference Model

The mutual interference geometry is depicted in Fig. 2 where the two antennas are assumed to be within the line of sight of each other. The RFI power measured at the front end of the receiving antenna in Fig. 2 is related to the RFI source power at the transmitting antenna by the following equation:

$$P_R(f, D, \theta_T, \theta_R) = P_T(f) + G_T(f, \theta_T) - L_D(f, D) + G_R(f, \theta_R) - L_F(f) \quad \text{dBm} \quad (1)$$

where

f = frequency of the RFI

D = baseline distance between antennas

P_R = received power at LNA input, dBm

P_T = transmitted power at feedhorn output, dBm

[1]Continuous wave, i.e., sinusoidal signals.

[2]To ensure good carrier acquisition and phase tracking performance in the receiver. For comparison, the CCIR criterion is also −192 dBm based on a 1-Hz loop.

G_T, G_R = relative gains of the transmitting and the receiving antennas at the indicated off-boresight angles in Fig. 2, dBi

L_D = path loss, dB

L_F = attenuation in the downlink filter before the LNA, dB

The transmitted power P_T, can be that of a carrier, a sideband, or a harmonic depending on the frequency of interest. The harmonic power and sideband power can be reduced by using proper filters.

The antenna gain in an off-boresight direction, G_T or G_R, depends on the antenna radiation pattern and the pointing angle. The radiation pattern of a 64-meter antenna measured in S-band at 700-meter range is given in Fig. 3. At present, this is the only near-field data available among all antennas. We have adopted for all cases a model that assumes the curve in Fig. 3 for angles larger than 20 degrees off boresight, a relative amplitude of 10 dBi at 10 degrees, and a linear continuation from 10 to 20 degrees. The radiation pattern beyond 20 degrees is relatively independent of antenna size, frequency, and range because it is generated by forward spillovers that are not intercepted by the antenna subreflector. Within 10 degrees at 200-meter range, the relative amplitude increases rapidly since these angles are very close to, or even inside, the cylindrical projection from the antenna reflector dish. To reduce the uncertainties in the model, some tests are being conducted, and more planned, to obtain radiation patterns for the 34-meter and the 9-meter antennas.

The path loss, L_D, is represented by $(\lambda/4\pi D)^2$ where λ is the wave length and D is the baseline distance.

The filter before the low-noise amplifier with effective attenuation L_F is a design choice to reduce the out-of-band radiation that may cause saturation of the amplifier or the receiver in the in-band frequency region.

III. Case Analyses

Each case of RFI source and effect was examined; most were analyzed using Eq. (1). The findings are summarized below. These findings form the basis for the implementation requirements recommended later in the report.

A. Effects of S-band uplinks on X-band downlinks

It is clear from Table 1 that the fourth harmonics of a certain range of S-band transmit frequencies fall in the pass band of the X-band travelling wave maser (TWM) or other X-band, low-noise amplifiers. The interfering signals must be stopped before leaving the transmitting antenna. To date, the fourth-harmonic filters have been implemented in deep-space transmitters, but they do not exist in near-earth transmitters. With proper filtering, the fourth-harmonic power transmitted from any antenna is expected to be reduced to -120 dBm from experience with deep-space transmitters. If this can be assured, the performance criteria is likely to be met even at 10-degree pointing angles, as shown by the link analysis in Table 2. The uncertainties shown in Table 2 represent our current lack of knowledge of the antenna radiation patterns, not the uncertainties of a stochastic nature. If any pointing angle is larger than 30 degrees instead of 10 degrees, it can be observed from Fig. 3 that there would be an additional 20-dB margin in Table 2, and hence almost no risk in not meeting the performance criteria. If the 9-meter antennas are positioned at the north end of the complexes in the northern hemisphere, and at the south end of the complex in the southern hemisphere, the chances for cross pointing would be greatly reduced. Table 2 has not included the white-noise-type RFI because the noise level in the transmitter is usually much lower than the harmonics level. We expect the noise-type RFI to meet the noise-type criteria when the harmonics meet the CW-type criteria.

The VLBI receive system will be sufficiently protected once the stated performance criteria are met. This is because:

(1) Contribution of RFI to the system temperature would be negligible.

(2) Effect of RFI on quasar or spacecraft signals would be negligible due to interferometry and earth doppler.

(3) RFI interaction with station-generated calibration tones would also be negligible. Each tone is expected to have at least -145-dBm power. With CW-type RFI lower than -192 dBm, the phase error would be less than one millicycle even when the RFI spectrum lies within 5 Hz of the calibration tone, an event with very-low probability.

B. Effects of S-band uplinks on S-band downlinks

S-band uplink interference is out-band since transmitted frequencies are below 2120 MHz and receive frequencies are above 2200 MHz (see Table 1). The question is whether the interference would be strong enough to saturate the receive system and cause nonlinearity in the receive frequency band.

The S-band TWM is known to saturate at the power levels shown in Fig. 4. It is seen that the saturation level at a representative transmitted frequency of 2110 MHz is about -25 dBm. The saturation level for an S-band field effect transistor (FET) with a crustal dynamics frequency range (2220 to 2320 MHz) is estimated to be at -55 dBm at the

same frequency. The result of a link analysis as shown in Table 3 indicates that for receive systems using a TWM at the front end, either a cryogenic filter (currently being developed at JPL) or a regular room-temperature filter can be used to avoid saturation. However, using a room-temperature filter will add about 3 kelvin to the system temperature. For receive systems using a FET at the front end, room-temperature filters would be necessary.

C. Effects of Planetary Radar at Goldstone

The planetary radar operates at 2320 MHz (S-band) and 8495 MHz (X-band). Current ranging code has a fundamental frequency of 200 kHz, with a bandwidth (through the ninth harmonic) of about 2 MHz. Future fundamental frequency could be as high as 2 MHz, with a bandwidth as great as 20 MHz. The carrier and sideband frequencies are too close to the deep-space receive frequency bands to be effectively separated by filtering.

When the X-band radar is transmitting at 400-kW total power with a 2-MHz fundamental frequency and a 128-bit pseudonoise code, a harmonic line at around 8420 MHz could have a strength of about −45 dBm. This calculation assumes that the klystron roll-off and an exciter filter could achieve about 80-dB attenuation at this frequency. Under this assumption, the X-band RFI from the X-band radar is calculated in Table 2. The effect of the S-band radar on the near-earth S-band reception at around 2275 MHz is calculated in Table 3 based on a similar assumption on transmitted power. It is clear from Table 2 that even at very favorable pointing conditions, the X-band reception at nearby deep-space antennas can not meet the performance criteria. Similar calculations have shown that the deep space S-band receive functions can not satisfy the criteria when the S-band radar is operating.

However, Table 3 indicates that the 9-meter station at Goldstone can receive near-earth signals satisfactorily when the S-band radar is operating. This is possible because the performance criteria for near-earth missions are less stringent and because there would be a small hill blocking the line of sight from the 64-meter antenna if the 9-meter antenna is properly located. The effect of the small hill is estimated according to Ref. 2. This hill would also reduce the fourth harmonic RFI from the 9-meter antenna to the 64-meter antenna.

D. Effects of Future X-Band Uplink

The X-band uplink frequency band is separated far enough from the X-band downlink to prevent any interference. This separation is already planned in the microwave and the exciter designs. Furthermore, X-band uplink will not produce any harmonics that would interfere with the K_u-band downlink currently under study at JPL.

E. Effects of Test Equipment Leakage

When test equipment operates at downlink frequencies, any leakage of enough power could interfere with the live downlink. Proper shielding is needed to contain leakage to about −120-dBm CW level and about −135-dBm/Hz noise level in the downlink frequency bands.

F. Effects on Radiometer Measurements

RFI of CW type cannot affect radiometers since radiometers only measure wideband noise power. Noise-type RFI could interfere, but the criteria given above will ensure that any increase of system temperature be lower than 0.1 dB. This is acceptable for current purposes of water-vapor radiometers and noise-adding radiometers.

G. Effects on SETI and Radio Astronomy

The Search for Extraterrestrial Intelligence (SETI) instrument is currently in its conceptual design stage. It is already clear that the extra-wide frequency band of interest to SETI (1 to 25 GHz) requires special measures. The prevention of any transmitted signals in this frequency range (including all transmitters given in Table 1) from either saturating the low-noise amplifier or contaminating the actual signals received from the sky will be necessary. Band-reject filters may therefore be necessary to prevent receiver saturation. Software or other means must be used to separate and delete the transmitted frequencies from the received signal spectrum. Since these frequencies are predictable, it should be possible to identify them as known RFI for deletion. Detailed solutions and alternatives are being studied by the SETI team.

While the performance criteria for RFI prevention would serve to protect the integrity of most of the present radio astronomy observations, they do not guarantee nondegradation of the RF environment at all times. From a radio astronomy standpoint, any degradation, even satisfying a set of more stringent criteria, would still compromise the potential of DSS 14 as a versatile, increasingly sensitive instrument for single-dish radio astronomy observations.

H. External RFI

We must continue to monitor the external RFIs and coordinate with external transmitting sources as we do now, especially at Goldstone. The RFI from satellites or high-flying airplanes will affect the receiving antennas to relatively the same extent whether the antennas are colocated or not. But

more effort may be necessary to coordinate with low-altitude transmitting sources around Goldstone since the DSS 14 site at Goldstone is not protected by hills from the east and the west. On the other hand colocation of antennas could probably make monitoring and coordination easier.

IV. Conclusions

When the requirements in the next section are implemented we expect that the performance and operation of telemetry, tracking, command, and VLBI systems to be essentially unaffected by RFI. The radio science system and the radio astronomy operations may sometimes need a cleaner RF environment that must be assured by antenna pointing precautions and possibly schedule coordinations.

Operational schedule of the planetary radar at Goldstone must be coordinated with the downlink functions in the same frequency band at the nearby 34-meter stations. DSS 12 and DSS 13 will remain unaffected by the radar. The 9-meter antenna at Goldstone could also be relatively unaffected if it is properly located.

The SETI observations will be affected if one of the colocated antennas is used. Band-reject filters will be necessary to prevent receiver saturation. RFI prediction, identification, and rejection schemes will be needed to delete the intracomplex RFI. Alternative solutions are being studied by the SETI team.

V. Recommendations

A. Recommended Implementation Requirements

(1) Implementation of filters.

(a) Fourth-harmonic filters for GSTDN transmitters.

(b) Exciter filters for Goldstone radar.

(c) Downlink filters at 34-meter and 9-meter antennas.

(2) Location of 9-meter antennas to minimize RFI.

(3) Transmitting and receiving antennas not to point within 10 degrees of each other, with more restrictions on special occasions.

(4) Schedule restriction on Goldstone radar and colocated 34-meter antennas.

(5) Deletion of dual-frequency uplink capability at 9-meter antennas to eliminate intermodulation products.

(6) Control of test-signal leakage.

(7) SETI to have filters to prevent saturation and software to identify and reject known RFI.

(8) Predictions, to trace and predict the intracomplex RFI from the transmitters, based on antenna pointing predictions. These predictions would be necessary for scheduling SETI observations or those radio astronomy and radio science experiments, that are more sensitive than the performance criteria given in Section II.

(9) Continued frequency coordination to prevent external RFI.

B. Recommended Tests

(1) Near-field (about 200-meter range) antenna radiation patterns for 64-meter and 34-meter antennas, at S-band and X-band.

(2) Mutual interference between antennas at current conjoint site as a function of pointing angles, at S- and X-band.

(3) Radiation patterns of the 9-meter antenna (S-band and fourth harmonic) and the power level of its fourth-harmonic radiation.

(4) Planetary radar sideband power and terrain effect measurement.

The first two tests are on-going at the conjoint stations in Australia. The last two tests are still being planned.

Acknowledgement

The author wishes to thank his colleagues at JPL for providing the technical data needed for this study. He particularly thanks D. Bathker, N. Ham, and D. Hersey for many lengthy discussions without which this analysis could not have been accomplished.

References

1. Bathker, D. A., *Predicted and Measured Power Density Description of a Large Ground Microwave System*, Technical Memorandum 33-433. Jet Propulsion Laboratory, Pasadena, Calif., April 1971.
2. International Telephone and Telegraph, *Reference Data for Radio Engineers*, Chapter 28, H. W. Sams & Co., 1968.

Table 1. RF characteristics of receive systems and transmitters

Receive system	Frequency range, MHz	System temperature, K, and front-end amplifier
Deep-space receive		
Spacecraft S-band	2290 to 2300	20, TWM[a]
Spacecraft X-band	8400 to 8440	20, TWM
VLBI		
S-band	2265 to 2305	20, TWM
X-band	8400 to 8500	20, TWM
Crustal dynamics		
S-band	2220 to 2320	150, FET[b]
X-band	8200 to 8600	160, FET
Near-earth missions		
S-band	2200 to 2290[c]	150, FET or PARAMP
SETI wideband	1 GHz to 25 GHz	15 to 35[d]

Transmitter	Frequency range, MHz	Maximum power, kW
Deep-space transmit		
S-band, 20 kW (64 m, 34 m)	2110 to 2120	20
S-band, 100 kW (64 m)	2110 to 2120	100
Goldstone planetary radar		
S-band	2320[e]	400
X-band	8495[e]	400
X-band, 20 kW (34 m)	7145 to 7190	20
Near-earth missions		
S-band, 20 kW (9 m)	2025 to 2110[c]	20

[a] Travelling-wave maser.

[b] Field effect transistor.

[c] Future high earth-orbiter missions (starting from AMPTE) will use 2225 to 2275-MHz range for downlink and 2050 to 2095-MHz range for uplink.

[d] Design for the wide-band, low-noise amplifier is still being studied.

[e] Ranging sidebands (up to 9th) will extend to ±20 MHz.

Table 2. X-band RFI link analysis

Parameter	Fourth harmonics effect on 64 m and 34 m		Planetary radar effects on 34 m	
	Assumption	Effect, dB	Assumption	Effect, dB (8420 MHz)
P_T	20 kW, filtered	−120 dBm CW	400 kW, filtered	−45 dBm CW
G_T	10 deg	+10 ±5	90 deg	−15 ±5
L_D	200 m	−97 ±3	200 m	−97 ±3
G_R	10 deg	+10 ±5	90 deg	−15 ±5
L_f	None	0	None	0
P_R		−197 ±13 dBm		−172 ±13 dBm
Criteria		−192 dBm CW		−192 dBm CW

Table 3. S-band RFI link analysis

Parameter	Planetary radar effect on 9-m		Saturation due to out-band RFI	
	Assumption	Effect, dB (2275 MHz)	Assumption	Effect, dB (2110 MHz)
P_T	400 kW, filtered	−45 dBm, CW	20 kW	73 dBm, CW
G_T	90 deg	−15 ±5	10 deg	+10 ±5
L_D	640 m	−96 ±3	200 m	−86 ±3
G_R	10 deg	+10 ±5	10 deg	+10 ±5
L_f	None	0	Cryogenic or room temp.[a]	−45 or −75
Hill		−40 ±10	None	0
P_R		−186 ±23 dBm		−38 ±13 dBm cryogenic or −68 ±13 dBm room temp.
Criteria		−160 dBm CW		−25 dBm CW (TWM) or −55 dBm CW (FET or PARAMP)

[a]3-kelvin noise penalty.

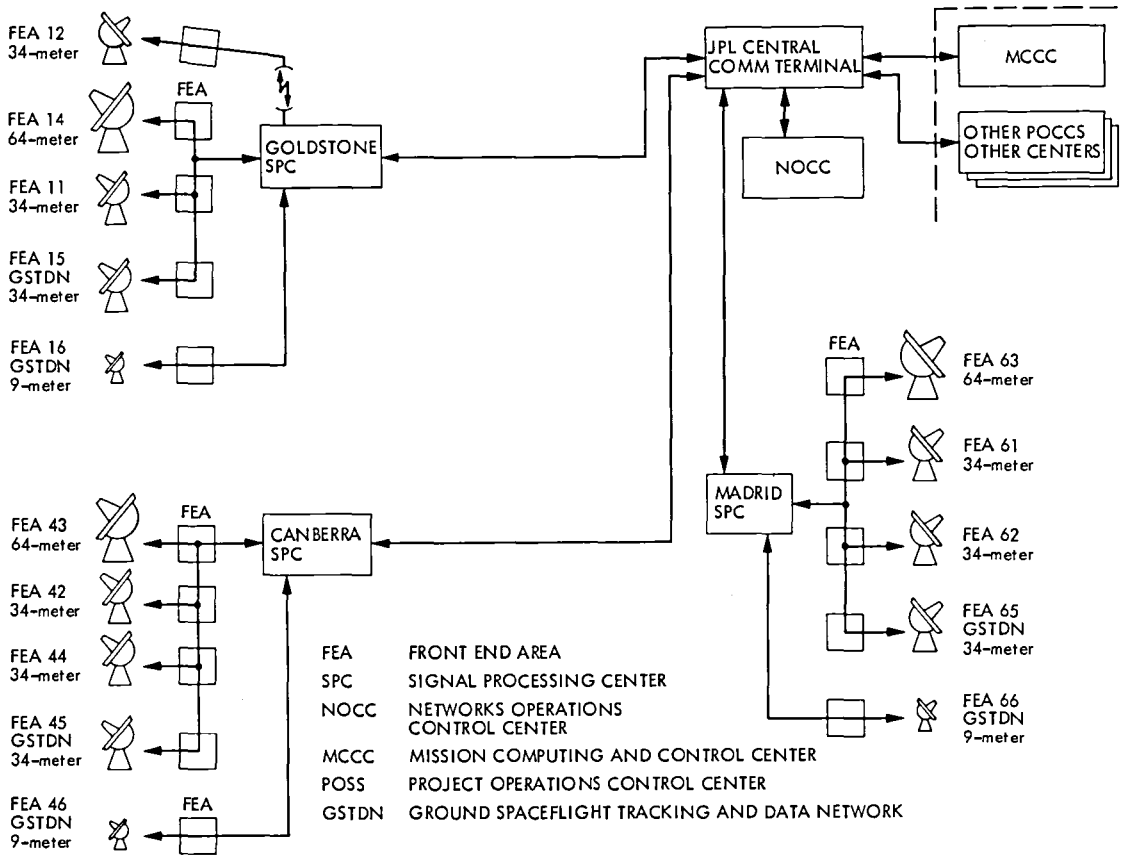

Fig. 1. Mark IV-A 1985 DSN baseline configuration

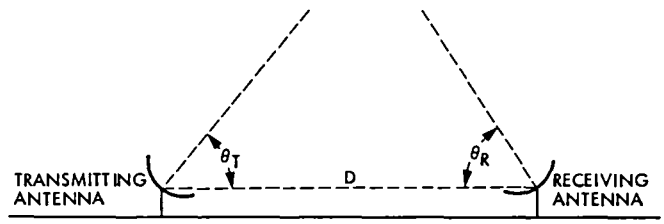

Fig. 2. Antenna mutual interference geometry

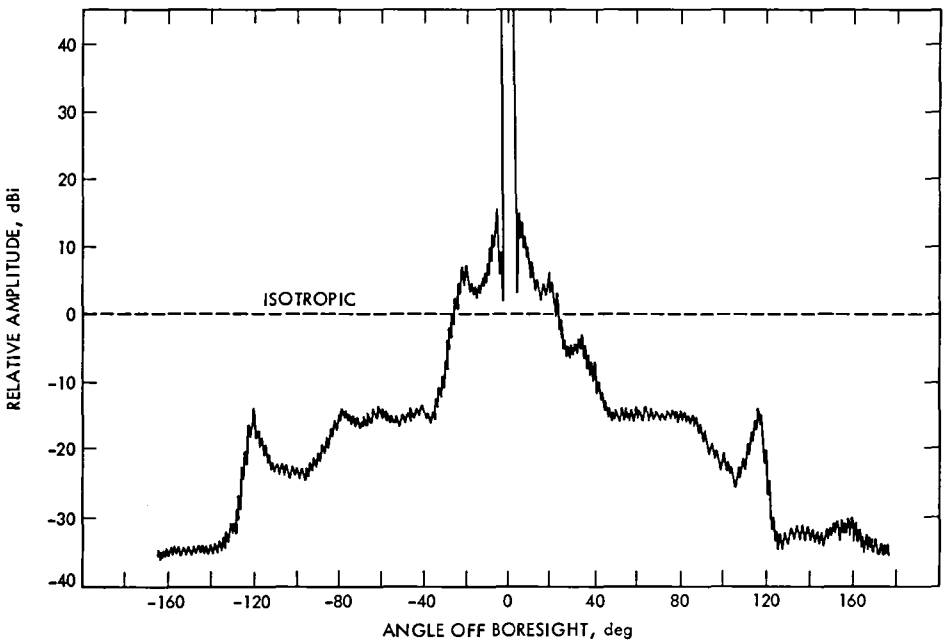

Fig. 3. Measured azimuth pattern of the 64-m advanced antenna system at Goldstone, Calif.; 2115 MHz, range = 700 m (from Ref. 1)

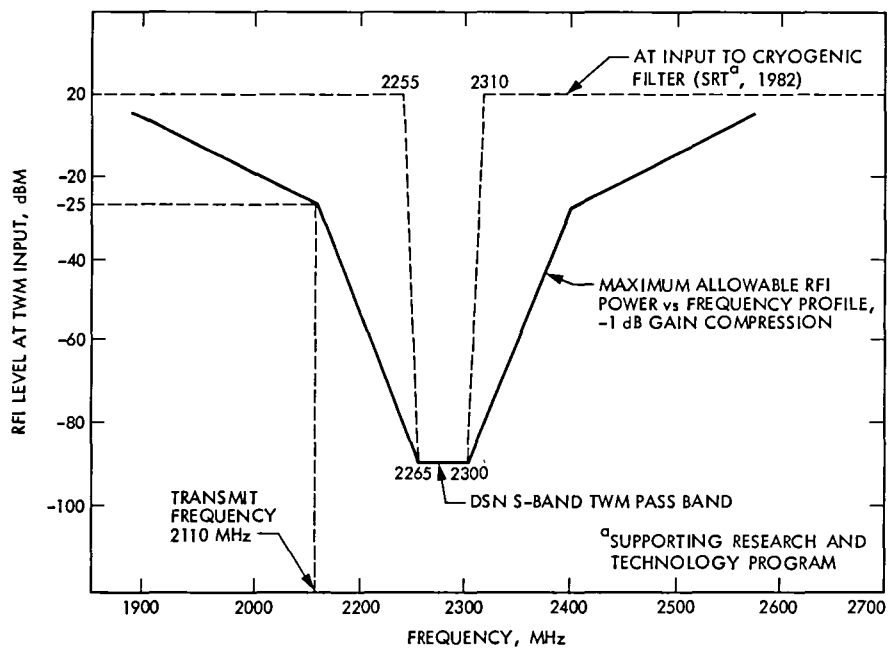

Fig. 4. S-band TWM saturation power level vs frequency

Prototype Real-Time Baseband Signal Combiner

L. D. Howard
Radio Frequency and Microwave Subsystems Section

This article describes the design and performance of a prototype real-time baseband signal combiner, used to enhance the received Voyager 2 spacecraft signals during the Jupiter flyby.

I. Introduction

Signal enhancement obtained by arraying the 64-meter and 34-meter antennas at each Deep Space Communications Complex (DSCC) is an operational requirement for both Voyager Saturn flybys. Arraying is performed by a Real-Time Telemetry Combiner (RTC) Subsystem located at each 64-meter site. This subsystem resynchronizes and sums the baseband signals from each antenna site. The output signal-to-noise ratio (SNR) is given by $SNR_{RTC} = \Sigma\, SNR_{inputs}$ as shown graphically in Fig. 1.

This article describes the prototype Voyager RTC which is based on the theoretical work by R. Winkelstein (Ref. 1) and a successful research and development combiner demonstrated by H. Wilck (Ref. 2).

The RTC design characteristics are:

(1) Combine baseband signals for the 64- and 34-meter antennas without degrading the optimal combined signal-to-noise ratio (SNR) by more than 0.2 dB.

(2) Operate in an unattended mode.

(3) Control and monitor functions performed remotely from a Data System terminal or locally via dumb terminal.

(4) Identical hardware for both 34- and 64-meter signals, so that external delay mechanisms could be eliminated and hardware would be interchangeable.

(5) Capable of open-loop tracking when signal is too weak to provide useful correlation feedback.

(6) Provide for automatic signal acquisition, tracking, lost signal detection, and reacquisition.

(7) Provide self-test, calibration, and diagnostics.

(8) Provide for compensating relative delays of 2 to 115 microseconds.

(9) Bandwidth to be equal to or greater than 10 mega-samples per second.

(10) Alignment tolerance plus or minus 30 nanoseconds cumulative tolerance over entire track.

Signal power degradation due to signal misalignment in the delay channels requires an alignment accuracy of 1.5 percent of a subcarrier cycle to keep source degradation less than 0.1 dB. With a maximum subcarrier rate of 500 kHz this becomes a ±30 ns alignment tolerance. Because of the requirement that the RTC track open loop, without alignment error feedback from the correlators, the ±30 ns tolerance must be cumulative over the entire track.

II. Implementation

Signals from the 64-meter and 34-meter station receiver outputs pass through identical hardware delay paths in the RTC (Fig. 2). Baseband signals enter the RTC through low-pass filters (LPF) whose purpose is to prevent aliasing in the subsequent sample data process. Then an automatic gain control (AGC) normalizes the filtered inputs to a fixed power level within the range of the 8-bit analog-to-digital converters (ADC). This LPF-AGC-ADC path is implemented as a single RF printed circuit board for each input channel.

The ADC, and an 8-bit first-in first-out memory (FIFO) are driven by a separate 10-MHz phase programmable input clock for each channel. The input and output clocks are phase programmable synthesizers operating at 10 MHz. The necessary central processing unit (CPU) controlled variable delay to resynchronize the input signals is obtained by cycle (phase) slipping the input clocks relative to the common output clock. The synthesizer has 0.1 degree programmable phase resolution at 10 MHz, which corresponds to a delay line resolution of 27.8 picoseconds (far better than required).

At the output of the FIFO delay lines both signals have been resynchronized. The analog signals are then reconstructed by 8-bit digital-to-analog converters (DAC). Low-pass filters (LPF) remove the DAC clocking noise, and finally an analog summing amplifier produces the RTC combined output.

The RTC is driven by a microprocessor controller consisting of two boards, a central processing unit module and an extended memory module (XMEM). The design is an outgrowth of the system described in Ref. 3.

III. RTC Firmware

The operating program for the RTC resides as approximately 40K bytes of resident EPROM on the CPU and XMEM modules. The program is written in Intel's PL/M language. The function of the program is to provide both normal operational and diagnostic-maintenance capabilities for the RTC system.

A. Normal Operation

Normal operation consists of two phases; an initialization phase, and a tracking phase.

1. **Initialization.** Upon initialization, the RTC runs through a number of internal self-checks. It verifies the functioning of the station clock, checksum verifies the EPROM, initializes interfaces, parity checks the random access memory (RAM), and tests the delay line functioning and the operation of the synthesizers. If any problems are encountered, the RTC enters the diagnostic mode; otherwise operator inputs consist of a set of pointing predicts (for calculated delay and open-loop operation) and signal characteristics (for correlator closed loop operation).

2. **Tracking.** During normal tracking the delay lines are updated at 1-second intervals for either closed-loop or open-loop operation. These updates are triggered by CPU interrupts generated by a programmable real-time clock on the CPU module. In addition to the real-time clock interrupt, six other levels of interrupt are utilized during normal operation. Three interrupts support communications, star ports A and B and the RS232C interface; and three interrupts support real-time failure diagnosis, RAM parity, and delay line problems for FIFOs.

Because all seven interrupts function asynchronously and at their own rates, common routines are re-entrant, and interrupts are disabled and re-enabled around critical calculations.

B. Diagnostics/Maintenance Operation

The RTC program provides detailed on-line and off-line diagnostic, and maintenance features.

1. **On-line diagnostics.** During normal tracking the RTC is able to detect and locate hardware problems to the module replacement level to permit rapid and effective spares substitution.

2. **Off-line maintenance.** Although the maintenance depots have automatic test equipment (ATE) for board troubleshooting it is primarily geared to small- and medium-scale integrated circuit technology. In theory the ATE could be used on LSI boards such as in the RTC, but in practice, the amount of programming effort required could easily exceed the development effort of the original machine. Experience has shown that resident maintenance software is at present the most effective method of providing an on-site repair capability; therefore an extensive set of maintenance routines is also part of the RTC firmware. These routines allow bit level control of the RTC hardware, as well as automated testing of FIFO and correlator performance, and permit troubleshooting of the hardware in place.

IV. RTC Testing

The RTC is designed to perform signal combining with an output SNR within 0.2 dB of theoretical as given in Fig. 1. Detailed prototype testing was done at the Compatibility Test Area (CTA-21) with field verification tests at DSS 14 (Ref. 4). Signal-to-noise ratio estimates measures from the Symbol Synchronizer Assembly (SSA) were found to be insufficiently precise to provide the 0.1 dB necessary for RTC performance

verification. Instead, telemetry symbol error rates (SER) from known data were used, and the SNR was derived by inverting the relation SER = 1/2 (1 -Erf $\sqrt{\text{SNR}}$). These measurements are sufficiently precise to permit 0.1-dB performance verification. Precalibration procedures before arraying (Fig. 3) use two completely redundant telemetry strings. They are provided a common simulated spacecraft test signal and their output SER and SNRs are compared. This serves to calibrate the indicated SNR with actual SNR (as determined from SER). This is important since SERs are unavailable for actual spacecraft tracks. The DSS 14 precal also determines which telemetry string is performing better. This difference is usually very small (<0.2 dB) The best telemetry string is then used for the prime data source.

The normal tracking configuration appears in Fig. 4. The 64-meter antenna telemetry string acts as backup for the RTC string. The 34-meter string is used to provide SSA SNR data only, since no useful telemetry is available at 34-meter signal levels.

V. Voyager 2 Jupiter Encounter RTC Performance

Figures 5 and 6 display the results of measurements made during the Voyager 2 Jupiter Encounter (July 1979). Figure 5 displays SSA SNR 10-minute averages for DSS 14, DSS 12, and the RTC. Note that DSS 12 SNRs are offset by 3 dB from DSS 14 and the RTC SNRs for plot compactness. Figure 6 displays SNR differences (DSS 14 – DSS 12, RTC – DSS 14) and RTC theoretical gain. These values derived from the measurements in Fig. 5, but are displayed in a format where RTC performance is independent of output SNR. RTC theoretical gain is what would be given from Fig. 1. It is important to emphasize that Figs. 5 and 6 represent actual measurements taken under field conditions during a planetary flyby. Because this data was taken under encounter conditions, there are numerous factors which were beyond experimental control; an explanation of these factors is necessary to understand the data presented.

A. Symbol Rate Normalization

Data was taken at several symbol rates. If the telemetry chain were perfect, the SNR change between symbol rate R_{sy1} and rate R_{sy2} would be given by

$$\frac{SNR_1}{SNR_2} = \frac{R_{sy2}}{R_{sy1}} ;$$

i.e., SNR dB 67.2 kbps -2.34 dB = SNR dB 115.2 kbps

Using this relation, all data was normalized to Voyager high rate of 230400 symbols per second (115.2 kbps, coded). Symbol rate SNR dependence of the telemetry showed that only the next lower rate 134400 symbols per second (67.2 kbps, coded) was usable. Even so, significant jumps (0.5 dB) are apparent at bit rate changes (telemetry string performance degrades at higher rate). This system problem was identified and solved after installation of the prototype RTC.

B. SNR Measurements

The basic measurement was a 10-minute average of SSA SNR estimates. These values are derived from an analog power measurement (Ref. 5). Calibration curves exist, but these curves were found to be in error in the SNR range of interest for DSS 12. In fact, DSS 12 was running so close to SSA threshold that it was very difficult to keep the SSA in lock; which accounts for the sparsity of DSS 12 data points. No acceptable SSA SNR calibration procedures existed during prototype testing at symbol SNR less than -2 dB, since for single stations these signal levels are normally too low to be of any use. It is a problem unique to measurement performance when arraying to require accurate SNR measurements down to, and occasionally below, previously accepted lock thresholds. This problem has been partially solved by recalibrating the SSA so that a symbol SNR measurement as low as -5 dB is considered accurate.

VI. Conclusion

The prototype RTC has performed to design expectations, resulting in a commitment to design operational systems to support the Voyager Saturn Encounter. An advanced research effort is underway to address solutions to operational system problems associated with real-time arraying, the results of which will be reported in future Progress Reports.

References

1. Winkelstein, R. A., "Analysis of the Signal Combiner for Multiple Antenna Arraying," in *The DSN Progress Report 42-25*, pp. 102-118, Jet Propulsion Laboratory, Pasadena, Calif.

2. Wilck, H., "A Signal Combiner for Antenna Arraying," in *The DSN Progress Report 42-25*, pp. 111-117, Jet Propulsion Laboratory, Pasadena, Calif.

3. Parham, O. B., "Microcomputer Central Processing Unit Module," in *The DSN Progress Report 42-41*, pp. 172-175, Jet Propulsion Laboratory, Pasadena, Calif.

4. Simon, N. K., and Hoyes, C., "Preliminary Telemetry Operations Experience with the Real-Time Combiner: 1 November 1978 to 1 November 1979," in *The DSN Progress Report 42-55*, pp. 90-96, Jet Propulsion Laboratory, Pasadena, Calif.

5. Lesh, J. R., "Accuracy of the Signal-to-Noise Ratio Estimator," Technical Report 32-1526, Vol X, pp. 217-232, Jet Propulsion Laboratory, Pasadena, Calif.

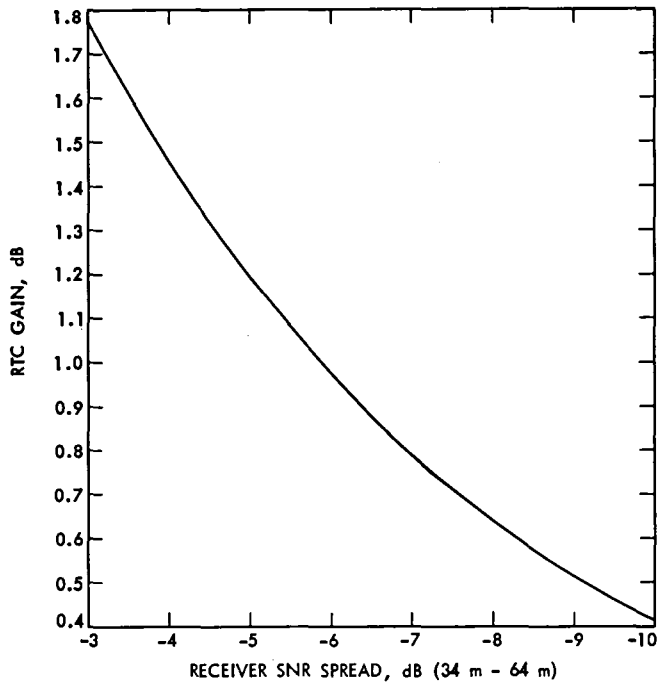

Fig. 1. RTC SNR improvement vs 34-m/64-m spread

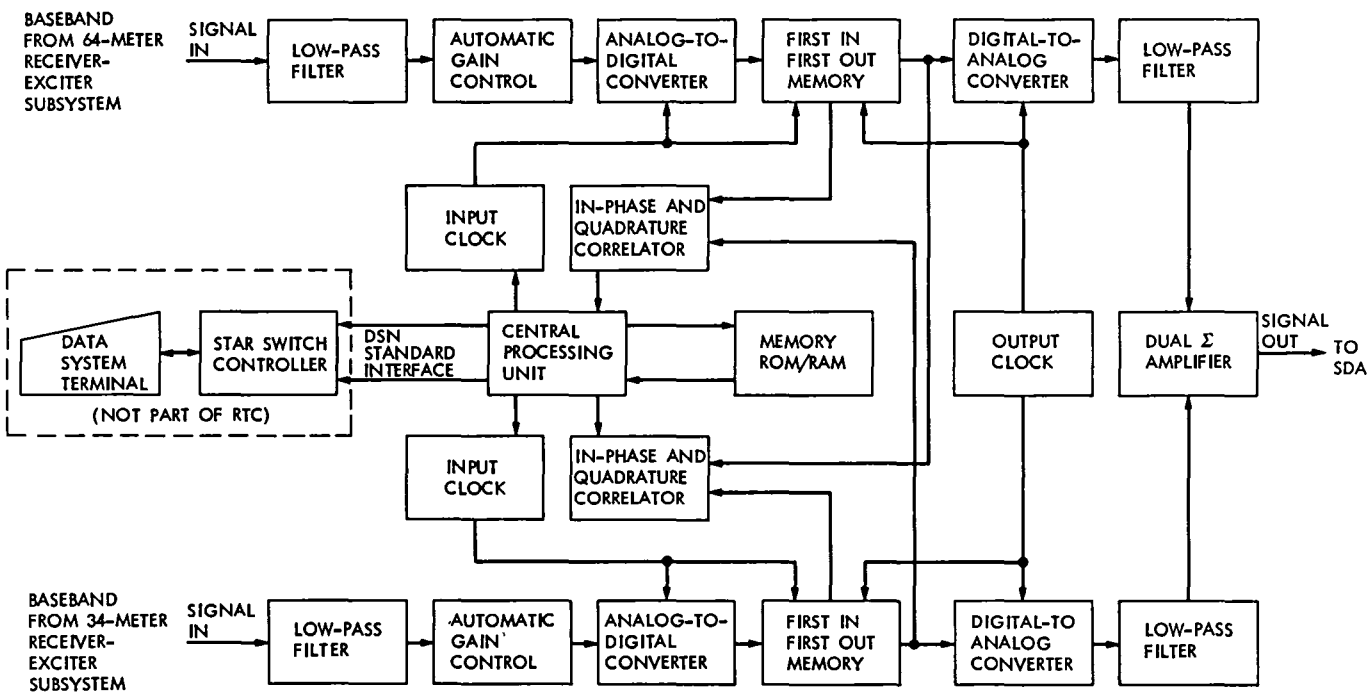

Fig. 2. RTC assembly block diagram

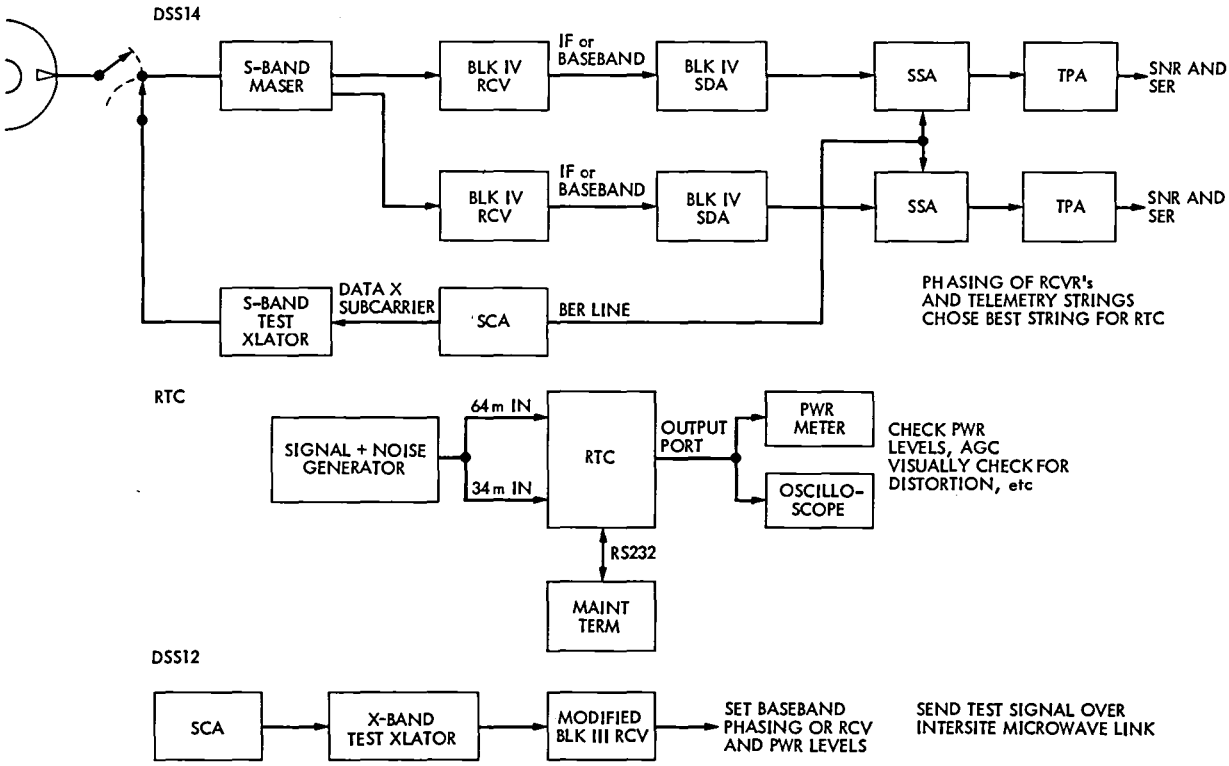

Fig. 3. Precalibration configuration

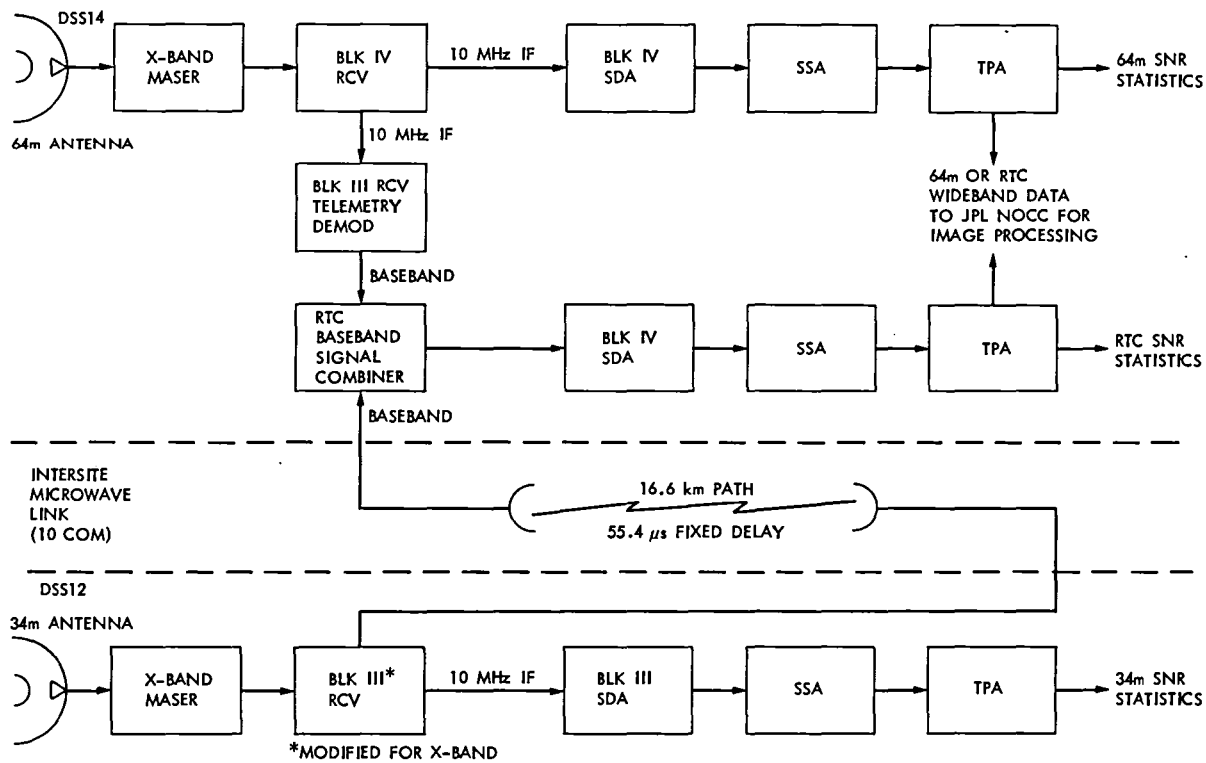

Fig. 4. Normal tracking configuration

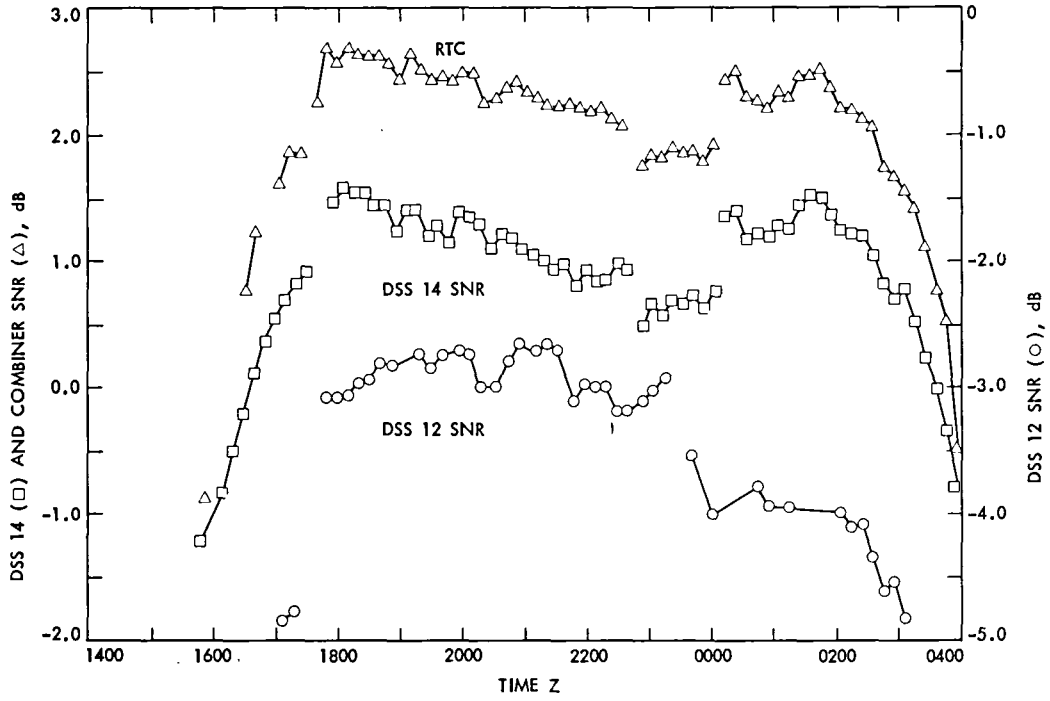

Fig. 5. RTC performance at J11, DOY 186/187, Pass 687 (SSA SNR 10-minute averages)

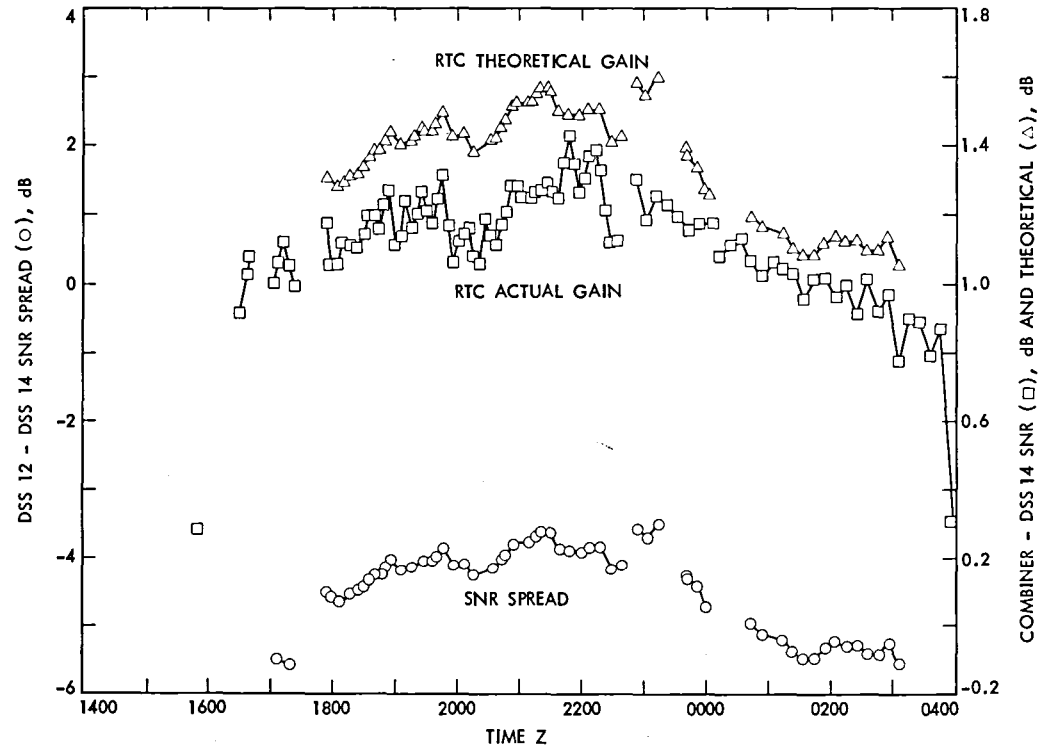

Fig. 6. RTC performance at J11, DOY 186/187, Pass 687 (SNR differences and RTC theoretical gain)

The Microprocessor-Based Synthesizer Controller

M. R. Wick
Radio Frequency and Microwave Subsystems Section

Implementation and performance of the new microprocessor-based controller and Dana Digiphase Synthesizer (DCO) is presented. Since the previous report, six Synthesizer Controllers have been installed in the DSN exciter in the 64-meter and 34-meter subnets to support uplink tuning required for the Voyager-Saturn Encounter.*

I. Introduction

The previous report describes the prototype Synthesizer Controller design features in control and monitor of a Dana Model 7010-S-241 Frequency Synthesizer. Subsequently, six production controllers have been installed in the 64-meter and 34-meter subnet (six stations) exciter to support the Voyager Project Saturn Encounter beginning in November 1980.

II. Implementation

The initial installation is a backup to the existing POCA and is under control of the Metric Data Assembly (MDA), as shown in Fig. 1. The need for an uplink tuning capability was given a greater emphasis because of the limited frequency tracking range of the Voyager 2 spacecraft receiver. The MDA was upgraded to incorporate a tuning capability including control of the existing Programmed Oscillator Control Assembly (POCA). The existing number of POCAs in the network, however, was insufficient to meet the needs, and additional controllers had to be built. The new Synthesizer Controller was developed to supplement the POCA and provide improved performance such as that needed for uplink tuning: namely, additional ramp storage (100 ramps) and precision phase control during ramping (needed in doppler data processing).

In the presently implemented configuration with the MDA, frequency profile parameters (f,t) pairs, are received via the MDA and converted to the format required for the POCA (or new Synthesizer Controller). The POCA requires rate and time pairs $(f_i t_i)$ to produce a sequence of linear ramps and the Synthesizer Controller is designed to accept up to 100 ramps defined by frequency time pairs in the form $(\Delta f_i, \Delta t_i)$. Frequency and time increments are input to the Synthesizer Controller along with a beginning or start frequency f_0. The Controller calculates the rate(s) $\dot{f}_i$ to an accuracy of 10^{-22} Hz/s to minimize the errors related to rate truncation. The additional rate resolution (10^{-22} Hz/s) exceeds that of the existing POCA resolution capability (10^{-5} Hz/s). The additional resolution was implemented in the design to minimize the ramp end-point frequency error due to truncation. This extended resolution was initially troublesome under control from the MDA because of the difference between the POCA and Synthesizer Controller. The MDA data interface for reporting the actual tuning rates provides for a maximum

*The combined capability of the Synthesizer Controller and Synthesizer is often referred to as a Digital Controlled Oscillator (DCO).

resolution of 10^{-5} Hz/s. The additional precision of the Synthesizer Controller was not being read out because of previously defined data format constraints. This additional precision resulted in a pseudo residual ramp error in the doppler data reduction process, and it was determined necessary to artificially limit the new Controller rate resolution.

This system deficiency will be corrected in a proposed firmware design change planned for implementing after Voyager 1 Saturn encounter. It will provide an additional (optional) capability to limit the resolution to 10^{-5} Hz/s. The proposed design change will permit an optional selection of the ramp resolution 10^{-5} Hz/s and retain the full resolution (10^{-22} Hz/s) for future use. In this revision to the firmware, the ramp rate is first calculated from the Δf_i, Δt_i frequency increment and time increment pairs to a precision of 10^{-22} Hz/s and then rounded to 10^{-5} Hz/s. The target frequency change ($\Delta f_i'$) is then calculated to agree as determined from

$$\Delta \dot{f}_i' = f_i'(\Delta t_i)$$

The process is required to preserve the phase control accuracy of the ramp control algorithm. The difference between the commanded Δf_i and actual $\Delta f_i'$ is sufficiently small to be ignored for an eight hour tracking period. Figure 2 illustrates the effect of this roundoff procedure for a typical ramp.

III. Performance

Test data in tests conducted during the production of the six Controllers verified the design objective for phase control accuracy of 10^{-12} cycles in eight hours during ramping. Tests conducted require a phase error between a theoretical calculated value and the actual phase of no greater than ±1 cycle. Tests included (1) a ramp over a period of eight hours using a ramp rate which covers the synthesizer tuning range (40-51 MHz) and (2) a ramp sequence using the maximum rate (±100 kHz/s) over the tuning range.

References

1. Donnelly, H., Wick, M. R., et al., "The Microprocessor-Based Synthesizer Controller," in the *DSN Progress Report 42-54*, Jet Propulsion Laboratory, Pasadena, Calif., Dec. 15, 1979.
2. "Dana Model 7010-S-179 Digiphase Frequency Synthesizer," Dana Publication 980428-S-179, July 1971.

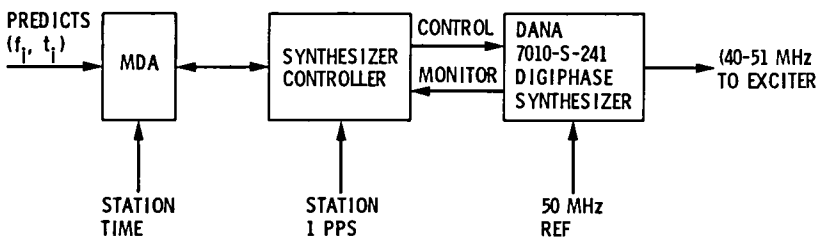

Fig. 1. Functional diagram, uplink tuning

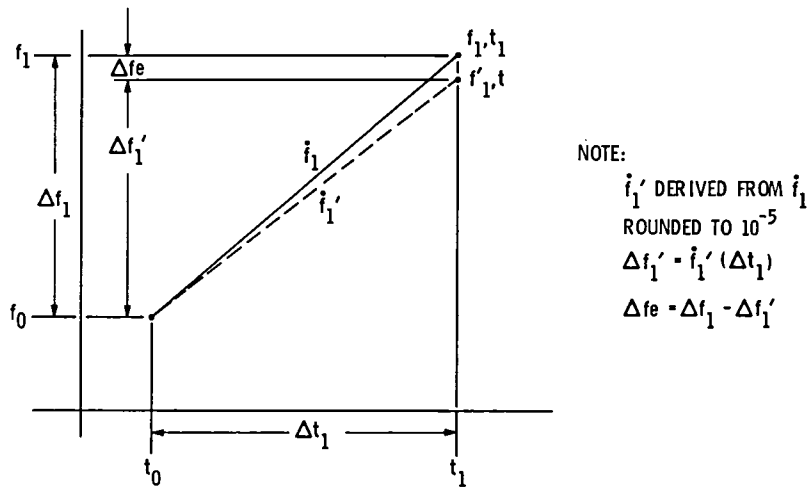

Fig. 2. Ramp resolution (10^{-5} Hz/s vs 10^{-22} Hz/s)

Block IV Receiver Tracking Loop Performance in the Presence of a CW RFI

M. K. Sue
Telecommunications Systems Section

This article is a part of a continuing effort to develop models to characterize the behavior of the Deep Space Network (DSN) Receiving System in the presence of a radio frequency interference (RFI). A model that allows one to predict the tracking performance of the Block IV receiver in the presence of a CW RFI is discussed. Experimental and analytical results are provided for a typical DSN operational mode. A curve of protection criteria that extends the current CCIR recommendation is also presented.

I. Introduction

Communications systems such as the Deep Space Network (DSN) often are operated in a radio frequency interference (RFI) environment. The high sensitivity required to achieve planetary communications makes the DSN highly sensitive to RFI. To prevent RFI from causing detrimental effects on the DSN Receiving Systems, it is necessary to first determine their RFI susceptibility characteristics. This study is a part of a continuing effort to develop models to characterize the RFI susceptibility of various parts of the DSN Receiving System. When a very strong RFI signal is present at the DSN Receiving System input, it can saturate the maser and various parts of the receiver, producing harmonics, gain compression, and other nonlinearities. These characteristics have been studied in Ref. 1. In this article, we are dealing with CW RFIs that are close in frequency to the carrier frequency. Due to the high sensitivity of the carrier tracking loop, this type of RFI will degrade the carrier loop performance much before saturation effects become noticeable. It is the purpose of this study to develop an analytical model that will allow us to predict the tracking performance of the Block IV receiver when operated in the presence of a CW RFI in the receiver passband. It is hoped that this model together with the saturation models presented in Ref. 1 can provide information necessary for RFI protection and coordination.

II. Effects of a CW RFI on a Phase Locked Loop

The effects of a CW RFI on a phase locked loop have been studied and documented by various authors (Refs. 2 through 7). The analysis on which the model to be developed is based is, however, from Refs. 2, 3, and 8. For the purpose of self-containment, necessary steps are repeated here. Basically when an RFI is present at the input of a phase locked loop with a fixed frequency offset from the desired signal, it creates a constant phase offset (static phase error) and a beat note that phase modulates the voltage-controlled oscillator (VCO) output. The beat frequency is the RFI offset frequency. Specifically, if we assume that the loop is initially locked to a desired signal with root-mean-square (rms) amplitude A and frequency $\omega_c/2\pi$, and that a CW RFI, with rms amplitude B and offset frequency $\Delta\omega/2\pi$, is present at the input, then the input to the loop is

$$x(t) = \sqrt{2}A \sin(\omega_c t) + \sqrt{2}B \sin(\omega_c + \Delta\omega)t \quad (1)$$

Equation (1) can be rewritten as

$$x(t) = A(t) \sin(\omega_c t + \delta(t)) \quad (2)$$

where:

$$A(t) = \sqrt{2}A\,(1 + R^2 + 2R \cos \Delta\omega t)^{1/2} \quad (3)$$

$$\delta(t) = \tan^{-1}(R \sin(\Delta\omega t)/(1 + R \cos(\Delta\omega t))) \quad (4)$$

and $R = B/A$ is the interference-to-signal ratio (ISR).

Assuming that the phase locked loop remains in lock with the desired signal with a phase error $\phi(t)$, then the VCO output is

$$r(t) = \sqrt{2} \cos(\omega_c t - \phi(t)) \quad (5)$$

The phase detector output, i.e., the error signal, is then

$$\ell(t) = x(t) \cdot r(t)$$

$$= \frac{\sqrt{2}}{2} A(t) \sin(\delta(t) - \phi(t)) \quad (6)$$

where the double frequency term has been ignored.

The phase error, $\phi(t)$, is related to the error signal, $\ell(t)$, by Eq. (7)

$$\phi(t) = -K \frac{F(p)}{p} \ell(t) \quad (7)$$

where $p = d/dt$ is the Heaviside operator, K is the open loop gain and $F(s)$ is the loop filter transfer function. For the DSN Block IV receiver, the loop filter is a lead-lag filter having this form:

$$F(s) = \frac{1 + \tau_2 s}{1 + \tau_1 s} \quad (8)$$

where τ_1 and τ_2 are time constants.

Instead of solving the set of nonlinear differential equations (Eqs. 6 and 7) for $\phi(t)$, Bruno and Blanchard adopted a trial solution,

$$\phi(t) = \lambda + m \sin(\Delta\omega t + \nu) \quad (9)$$

which yields the following set of constraint equations (Ref. 4),

$$\sin(\lambda) = \frac{-m^2 \delta \cos\psi}{2J_0(m)} \quad (10)$$

$$\sin(\lambda - \nu) = \frac{-m^2 \delta \cos\psi}{2RJ_1(m)} \quad (11)$$

$$R^2 = \left[\frac{m\delta \sin\psi + 2J_1(m)\cos\lambda}{J_0(m) - J_2(m)}\right]^2 + \left[\frac{m^2 \delta \cos\psi}{2J_1(m)}\right]^2 \quad (12)$$

where ψ is the phase angle of $F(j\Delta\omega)$, J_0, J_1, and J_2 are Bessel functions of the first kind, and δ is given by this equation,

$$\delta = \frac{\Delta\omega}{AK|F(j\Delta\omega)|} \quad (13)$$

The term λ in the above equations is the static phase error (SPE) and m is the modulation index or phase jitter.

Equations (9) through (12) represent the model of a phase locked loop operated in the presence of a CW RFI. This model assumes a noiseless condition that is approximately true when the loop is operated at strong signals. At weak signal levels where the noise effect dominates, this model is expected to fail. It is noted that λ in the above equations is restricted to the range of $-\pi/2$ to $\pi/2$ with $|\lambda| = \pi/2$ representing the limiting condition beyond which the loop can no longer lock to the desired signal.

To evaluate the RFI effect on the loop, Eqs. (10), (11), and (12) must be solved simultaneously for λ, m, and ν for a given R and $\Delta\omega$. This involves solving a set of nonlinear equations, which is not a trivial job. For small values of m, i.e., $m << \sqrt{2}$, Levitt (Ref. 4) is able to reduce Eqs. (10), (11), and (12) to an explicit form

$$m^2 \cong R^2/(\delta^2 + 2\delta \sin \psi + 1) \tag{14}$$

$$\sin \lambda \cong \frac{-m^2\delta \cos \psi}{2} \tag{15}$$

$$\sin (\lambda - \nu) \cong \frac{-m\delta \cos \psi}{R} \tag{16}$$

The explicit form makes it much easier to evaluate the RFI effect and is applicable to the Block IV phase locked loop in most cases.

III. The Effects of a Band Pass Limiter

The phase locked loop model presented in the above paragraph does not account for the effects of a band pass limiter (BPL). Since the Block IV receiver has a limiter in the 100-kHz module, the phase locked loop model must be modified to account for the limiter effects before it can be applied to the Block IV receiver. There are two parameters in the model needing modification. In the absence of a band pass limiter, the product AK in Eq. (13) is a constant for a given loop and a given input signal level, independent of the RFI power level. With a band pass limiter, AK must be replaced by $\alpha_L K$ to account for the limiter suppression effects, where K now is the strong signal open loop gain and α_L is the limiter suppression factor that is a function of both the signal-to-noise ratio and ISR. In addition, due to the suppression of the signal by RFI and vice versa, the interference-to-signal ratio that the loop sees, called the effective ISR, is not the same as that at the limiter input. This is the second parameter that needs to be modified.

The response of a BPL to two CW signals in noise was studied by J. J. Jones (Ref. 8). Again, only necessary steps are repeated here for clarity. If we assume that the input to an ideal BPL consists of two CW signals in additive narrowband gaussian noise and let $W(t)$ denote the input signal, then

$$W(t) = W_1(t) + W_2(t) + n(t) \tag{17}$$

where $W_1(t) = \sqrt{2}\,A \sin(\omega_c t)$ is the signal, $W_2(t) = \sqrt{2}\,B \sin((\omega_c + \Delta\omega)t)$ is the RFI with offset frequency $\Delta\omega/2\pi$, and $n(t)$ is the additive narrowband gaussian noise with total noise power N. The power in the signal is then $S_1 = A^2$ and the power in the RFI is $S_2 = B^2$. The interference-to-signal ratio at the limiter input is $R = B/A = (S_2/S_1)^{1/2}$.

The output of the BPL consists of both discrete and continuous components due to signal, RFI, and noise. If we let $Z(t)$ denote the output of the limiter near the carrier frequency, then the correlation function of $Z(t)$ is

$$R_z(\tau) = \sum_{i=-\infty}^{\infty} \sum_{\ell=-\infty}^{\infty} \sum_{k=|i|,|i|+2\cdots}^{\infty} 2\,\frac{b^2{}_{K|\ell||\ell-|i+1||}}{\left(\frac{K+|i|}{2}\right)!\left(\frac{K-|i|}{2}\right)!}\rho^K(\tau) \tag{18}$$

where $\rho(\tau)$ is the correlation function of the base band components of $n(t)$, normalized to unit power.

The output power for the signal and interference in the fundamental frequency band are:

$$(S_1)_0 = \frac{2}{\pi^2}\left(\frac{S_1}{N}\right)\left[\sum_{i=0}^{\infty}\frac{\left(-\frac{S_1}{N}\right)^i}{i!(i+1)!} \times \Gamma(i+1/2)\,{}_2F_1\left(-i, -i-1; 1; \frac{S_2}{S_1}\right)\right]^2 \tag{19}$$

$$(S_2)_0 = \frac{2}{\pi^2}\left(\frac{S_2}{N}\right)\left[\sum_{i=0}^{\infty}\frac{\left(-\frac{S_1}{N}\right)^i}{(i!)^2} \times \Gamma(i+1/2)\,{}_2F_1\left(-i, -i; 2; \frac{S_2}{S_1}\right)\right]^2 \tag{20}$$

where $\Gamma(\cdot)$ is the gamma function and ${}_2F_1(a, b, c, d)$ is the Gauss hypergeometric function.

Assuming that signal components at high-frequency bands can be ignored, we can define a quantity called effective ISR as:

$$R_e = \left[\frac{(S_2)_0}{(S_1)_0}\right]^{1/2} \tag{21}$$

The limiter suppression factor α_L is given by

$$\alpha_L = \left[\frac{(S_1)_0}{8/\pi^2}\right]^{1/2} = \frac{\pi\,(S_1)_0^{1/2}}{2\sqrt{2}} \tag{22}$$

Using Eqs. (21) and (22) and substituting R_e for R and K for AK in Eqs. (10) and (13), we now have a model that can

predict the performance of the Block IV receiver in the presence of RFI. The equations defining this model are:

$$\sin(\lambda) = \frac{-m^2 \delta \cos\psi}{2J_0(m)} \tag{23}$$

$$\sin(\lambda - \nu) = \frac{-m^2 \delta \cos\psi}{2R_e J_1(m)} \tag{24}$$

$$R_e^2 = \left[\frac{m\delta \sin\psi + 2J_1(m)\cos\lambda}{J_0(m) - J_2(m)}\right]^2 + \left[\frac{m^2 \delta \cos\psi}{2J_1(m)}\right]^2 \tag{25}$$

$$\delta = \frac{\Delta\omega}{\alpha_L K |F(j\Delta\omega)|} \tag{26}$$

where ψ as before, is the phase angle of the loop filter, and K is the strong signal open loop gain.

IV. Numerical Results

The analytical model developed in the previous paragraphs has been applied to the DSN Block IV receiver for two tracking modes. These two modes are: (a) wide, Bn = 2 kHz, 2 BLO = 10 Hz, S-band (wide/2 kHz/10 Hz), and (b) wide, Bn = 2 kHz, 2 BLO = 30 Hz, X-band (wide/2 kHz/30 Hz), where Bn is the predetection noise bandwidth and 2 BLO is the two sided threshold loop bandwidth. Three sets of curves have been generated for each of these two modes. They are:

(1) Receiver drop lock level as a function of RFI offset frequency (ΔF) with margin (M) as a parameter, where margin is defined as the ratio of signal to noise in 2 BLO.

(2) Static phase error (λ) vs ISR with ΔF as a parameter.

(3) Rms phase jitter ($m/\sqrt{2}$) vs ISR with ΔF as a parameter.

These curves are shown in Figs. 1 through 6. It is noted that as the signal or the RFI becomes too large, computation of $(S_1)_0$ or $(S_2)_0$ breaks down. It is thus necessary to employ asymptotic approximation when this happens (Ref. 8). This explains why the curves in Figs. 1 and 2 are not completely smooth.

V. Experimental Verification

Experimental verification of this model was performed in the Telecommunications Development Laboratory (TDL) using the Engineering Model Block IV receiver. The test set up is shown in Fig. 7. The RFI source was located in a screen room to minimize leakage that might affect the performance of the receiver or the calibration of the ISR. A doppler jitter program was used to measure the static phase error and rms phase jitter.

Experimental results are shown in Figs. 8 through 12. Figures 8 through 9 show the measured drop lock level as a function of RFI offset frequency. Experimental data agree very well with analytical results for strong signal conditions. At weak signal level (M = 10 dB), agreement is slightly poor. This is reasonable owing to the fact that the noise effects have been neglected in the development of the phase lock loop model. Figure 10 shows the measured static phase error as a function of ISR for some selected frequencies. The reason that these particular frequencies were chosen is because of the fact that the highest sampling rate of the Doppler Phase Jitter Program used in this test is 5 ms. These frequencies were chosen such that λ and m could be sampled correctly. Experimental data of the static phase error agrees very well with analytical data.

Figure 12 shows the measured phase jitter as a function of ISR. The measured values differ from theory by approximately a factor of two when ΔF is less than 100 Hz and ISR is less than 0 dB. When ΔF is larger than 100 Hz, or when ISR is larger than 0 dB, good agreement between experiment and theory is observed.

VI. Computer Simulation

A computer simulation program has been implemented on a Modcomp computer to further verify the analytical results. This program performs a block-by-block simulation of the operation of a phase locked loop preceded by a band pass filter. This loop is equivalent to the tracking loop of the Block IV receiver. Limited simulation results have been obtained and they show good agreement with experimental data (Figs. 13 through 15).

VII. CW RFI Protection Ratio

Whether one can perform RFI management effectively often depends on one's ability to accurately estimate the maximum acceptable interference power level, or the so called protection criterion. Current CCIR recommendation (Ref. 9)

provides worst-case protection criteria based only on interference that may fall in the loop bandwidth. Based on the experimental and analytical results of this study, we have determined protection criteria as a function of frequency for the Block IV receiver under the influence of the type of RFI discussed in this article. A simplified straight-line approximation of the protection criteria as a function of RFI frequency offset is shown in Fig. 16. This protection is based on a maximum acceptable tracking loop degradation of 10 deg of static phase error or peak phase jitter, whichever is larger. This criterion is consistent with the current CCIR recommendation on protection for deep-space communications, which calls for a maximum acceptable degradation of 10 deg of phase modulation (Ref. 9). The maximum allowable absolute RFI power level in Fig. 16 is based on a 10-dB carrier margin, 10-Hz threshold loop bandwidth, and a −215.0-dBW/Hz noise spectral density. This noise spectral density corresponds to the nominal value expected for X-band operations. While the S-band and K_u-band noise spectral densities are different from that of the X-band, the difference is small enough (1.6 dB, Ref. 9) that Fig. 16 may be considered adequate for all three frequency bands.

Based on Fig. 16, the maximum allowable power level for an in-band interference is −210 dBW. This value confirms the current CCIR recommendation of −220.0 dBW for a 1-Hz bandwidth, which corresponds to −210 dBW for a 10-Hz bandwidth.

It is noted that the protection criteria presented here are for receiver tracking only. Effects on telemetry, ranging, doppler, etc., have not yet been considered. Protection criteria for the receiving system as a whole would have to include all these effects. This will be examined in the future. Meanwhile, it is recommended that Fig. 16 be used for analysis of specific RFI coordination problems encountered by the DSN.

VIII. Conclusion

An analytical model that models the response of a phase locked loop preceded by a band pass limiter has been presented. This model can be used to predict the performance of the Block IV receiver carrier tracking loop in the presence of a CW RFI. Sets of curves have been generated for the static phase error, phase jitter, and out-of-lock values for the Block IV receiver using the often used tracking modes. Experimental verification and some computer simulation have been performed to verify the analytical results. Simulation and experimental results show good agreement with theoretical prediction for the static phase error and out-of-lock values. Predicted phase jitter is consistently lower than the experimental and simulated results by a factor of one-half for small ISR when the offset frequency is small. For large ISR, good agreement is observed. The analytical model assumes a noiseless condition, which is valid only when the loop is operated at strong signal levels. Experimental data indicate, however, that even at the minimum operating signal level of 10-dB carrier margin, reasonably good prediction can still be obtained.

Based on both analytical and experimental results, a protection criteria curve has been developed to protect the Block IV receiver tracking loop against CW RFI. This curve extends the current CCIR recommendation to allow calculation of out-of-band interference.

Acknowledgment

The author would like to thank H. de la Rambelje of the Telecommunications Systems Section for his computer simulation, J. F. Weese, also of the Telecommunications Systems Section, for his support in TDL, and M. A. Koerner for his invaluable technical discussions.

References

1. Hersey, D. R., and Sue, M. K., "Maximum CW RFI Power Levels for Linear Operation of the DSN Block IV Receiver at S-Band Frequencies," *DSN Progress Report 42-56, January and February 1980.* Jet Propulsion Laboratory, Pasadena, Calif.
2. Bruno, F., "Tracking Performance and Loss of Lock of a Carrier Loop Due to the Presence of a Spoofed Spread Spectrum Signal," in *Proceedings of the 1973 Symposium on SSC.* Hazeltine Corp.
3. Blanchard, A., "Interference in Phase-Locked Loops," *IEEE*, AES-10, No. 5, September 1974.
4. Levitt, B. K., "Carrier Tracking Loop Performance in the Presence of Strong CW Interference," *DSN Progress Report 42-51, March and April 1979.* Jet Propulsion Laboratory, Pasadena, Calif.
5. Britt, C. L., and Palmer, D. F., "Effects of CW Interference on Narrow-Band Second-Order Phase-Lock Loops," *IEEE*, AES-3, No. 1, January 1967.
6. Kliger, I. E., and Olenberger, C. F., "Phase-Lock Loop Jump Phenomenon in the Presence of Two Signals," *IEEE*, AES-12, No. 1, January 1976.
7. Olenberger, C. F., "Effects of Automatic Gain Control on Phase-Locked Loop Behavior in the Presence of Interference," *IEEE*, AES-12.
8. Jones, J. J., "Hard-Limiting of Two Signals in Random Noise," *IEEE Transactions on Information Theory*, IT-9, January 1963.
9. *Recommendations and Reports of the CCIR, 1978*, Vol. II, Report 685 and Recommendation 365-3. International Radio Consultative Committee, XIVth Plenary Assembly.

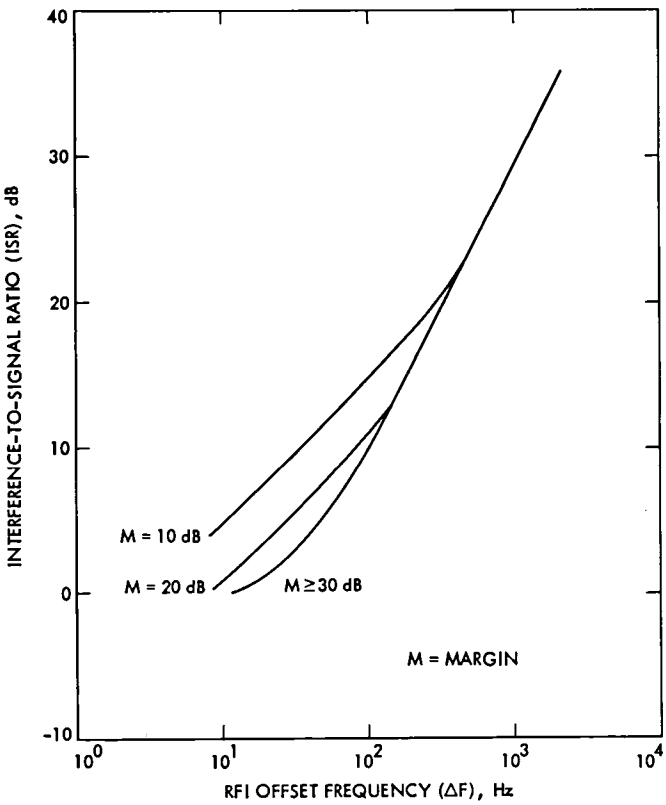

Fig. 1. Block IV receiver droplock levels vs RFI offset frequency with margin as a parameter (wide/2 kHz/10 Hz)

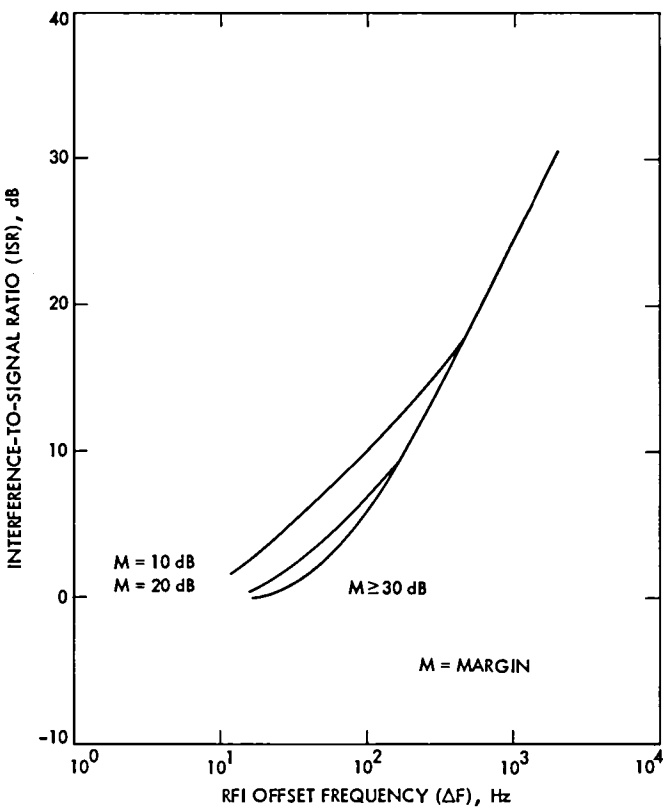

Fig. 2. Block IV receiver droplock levels vs RFI offset frequency with margin as a parameter (wide/2 kHz/30 Hz)

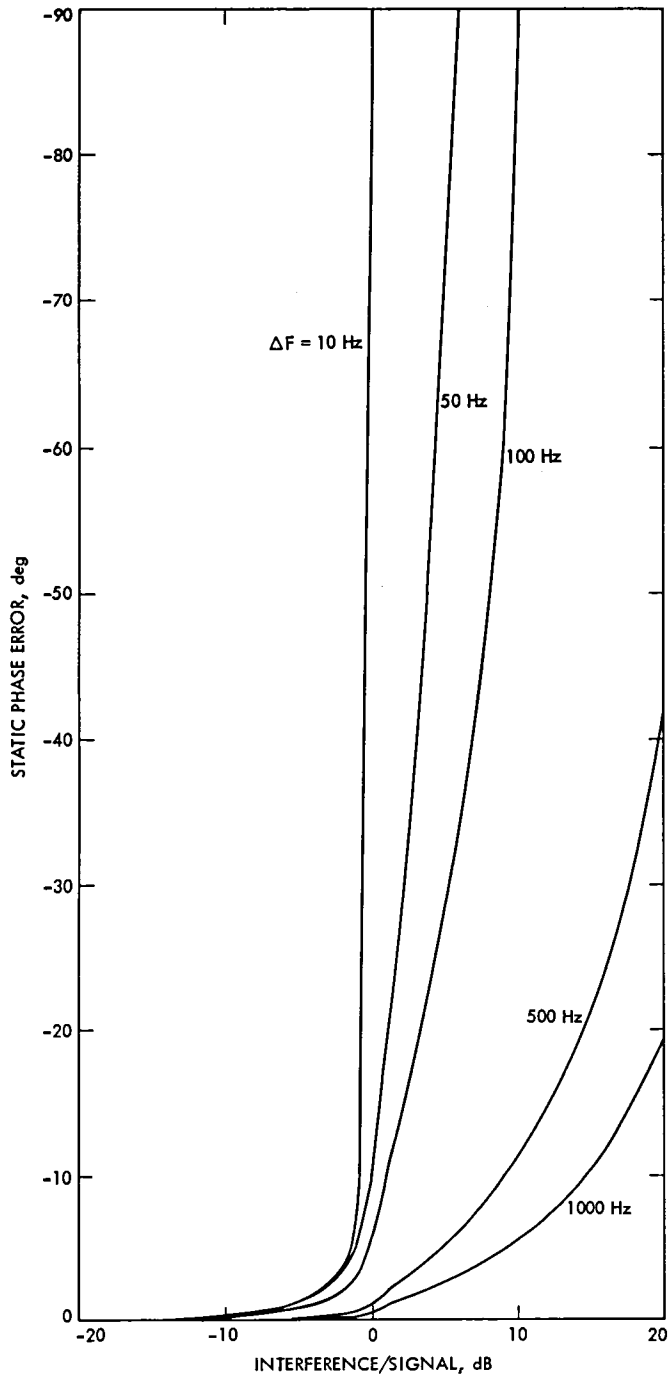

Fig. 3. SPE vs ISR with ΔF as a parameter (strong signal, 2 *BLO* = 10 Hz wide mode)

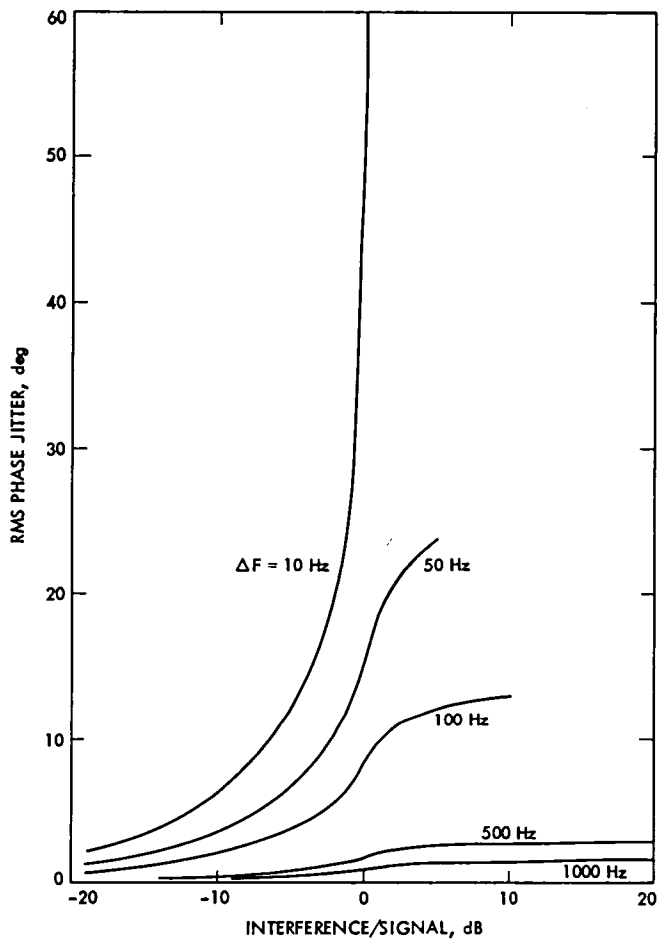

Fig. 4. Rms phase jitter vs ISR with ΔF as a parameter (strong signal, 2 *BLO* = 10 Hz, wide mode)

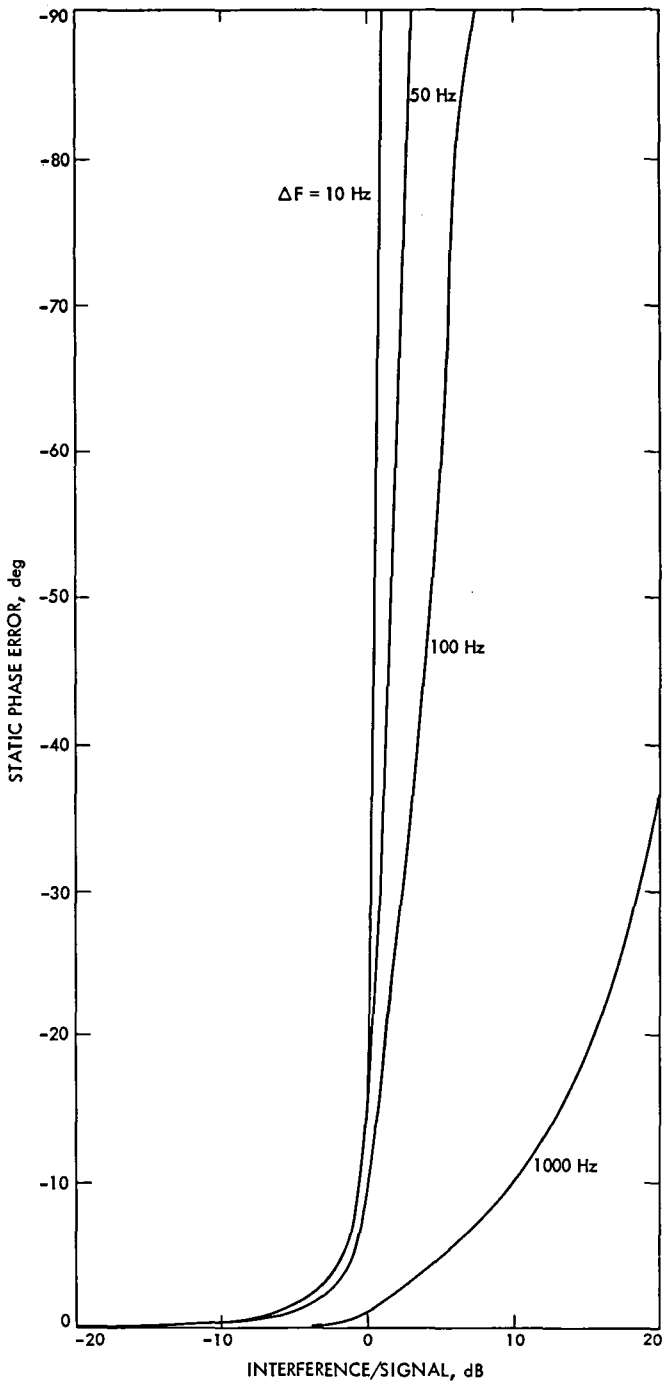

Fig. 5. SPE vs ISR with ΔF as a parameter (strong signal, 2 *BLO* = 30 Hz, wide mode)

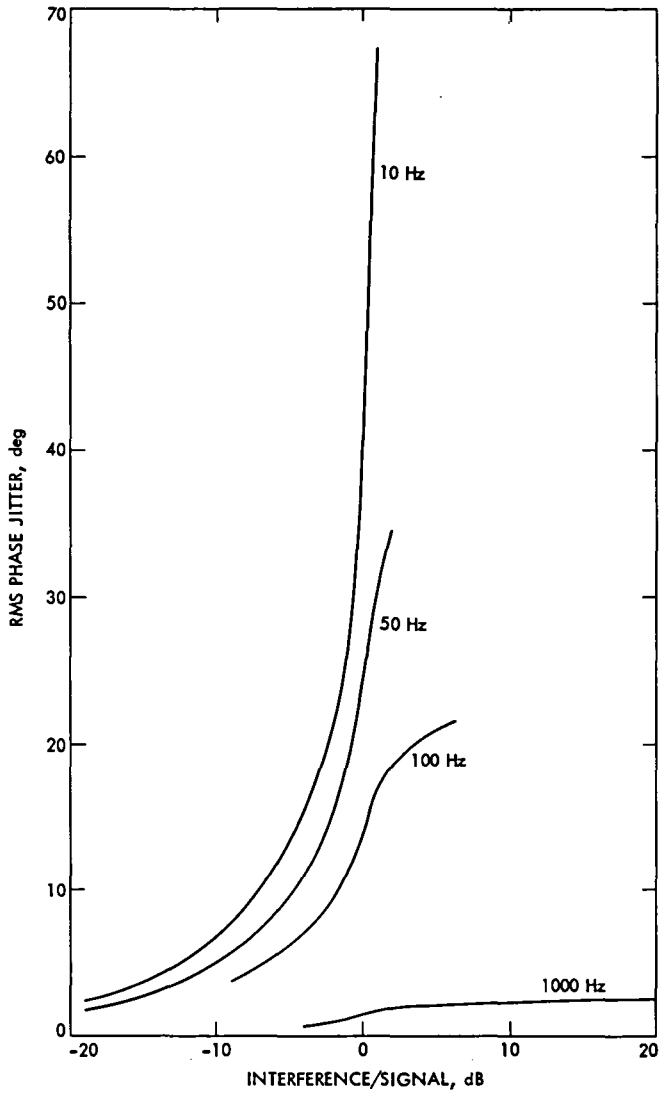

Fig. 6. Rms phase jitter vs ISR with ΔF as a parameter (strong signal, 2 *BLO* = 30 Hz, wide mode)

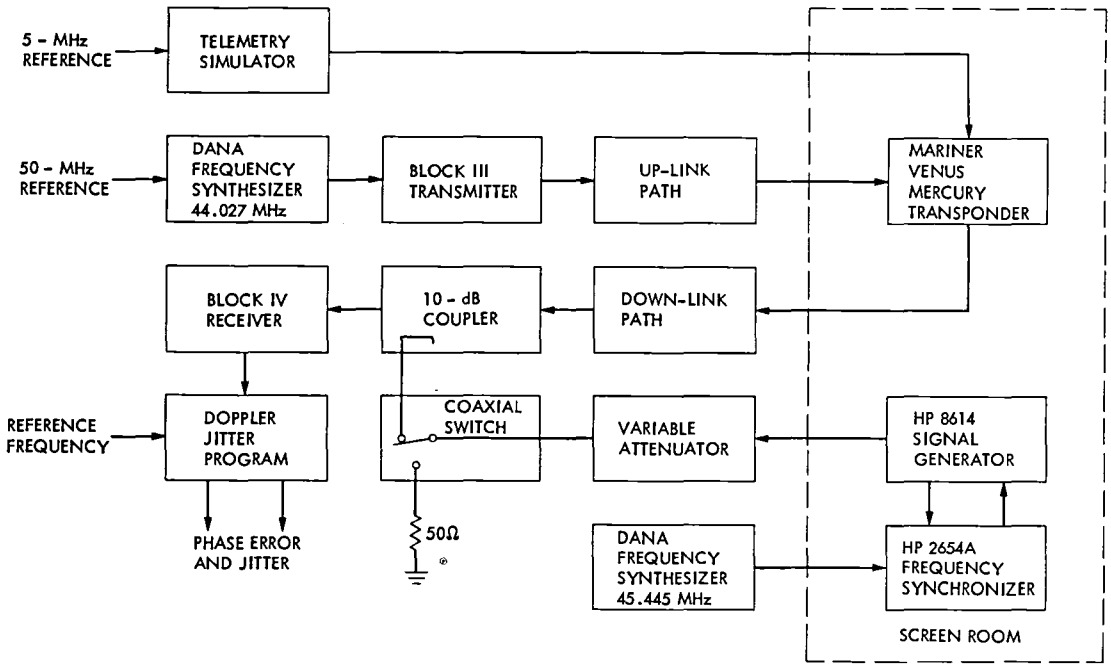

Fig. 7. TDL RFI test setup

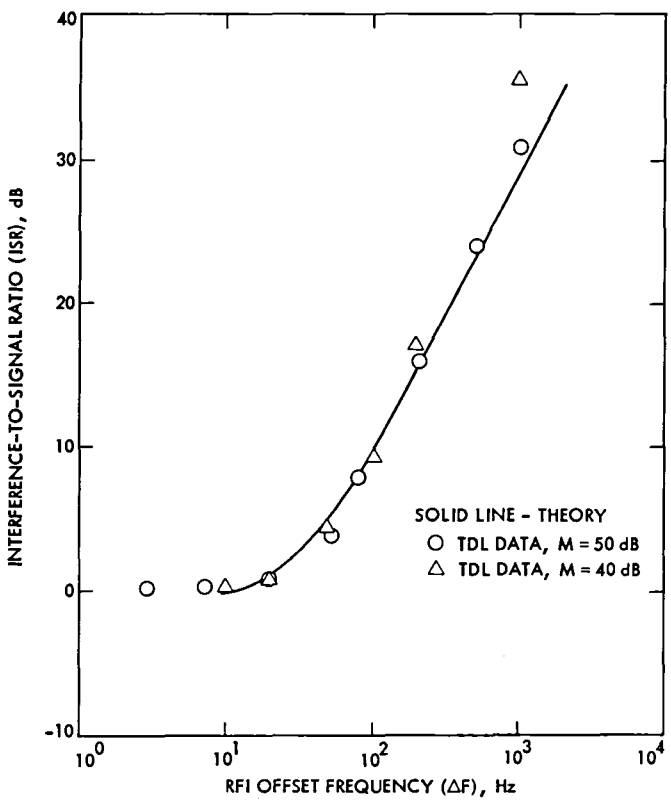

Fig. 8. Block IV receiver droplock level: comparison of analytical and experimental results (strong signal, 2 *BLO* = 10 Hz, wide mode).

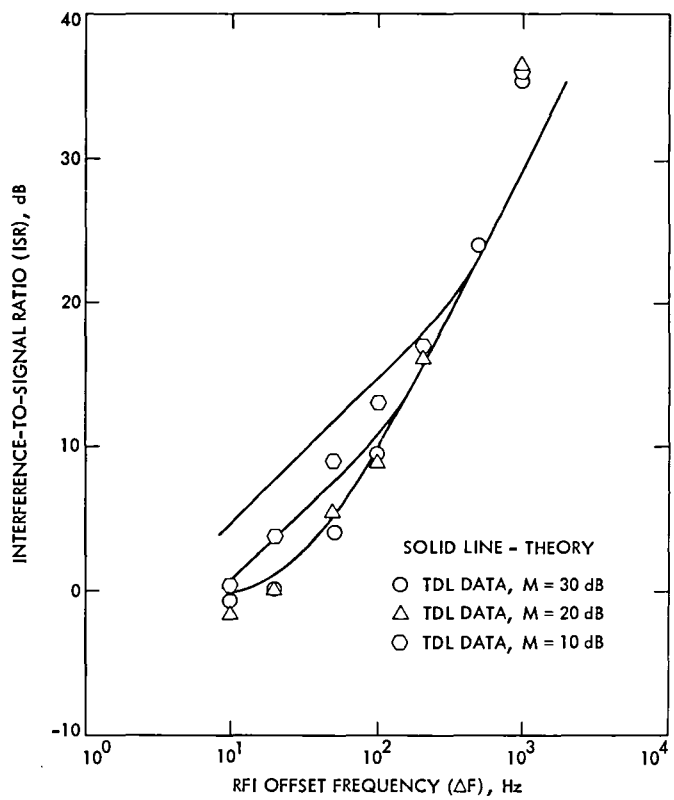

Fig. 9. Block IV receiver droplock level: comparison of analytical and experimental results (moderate to weak signals, 2 *BLO* = 10Hz, wide mode)

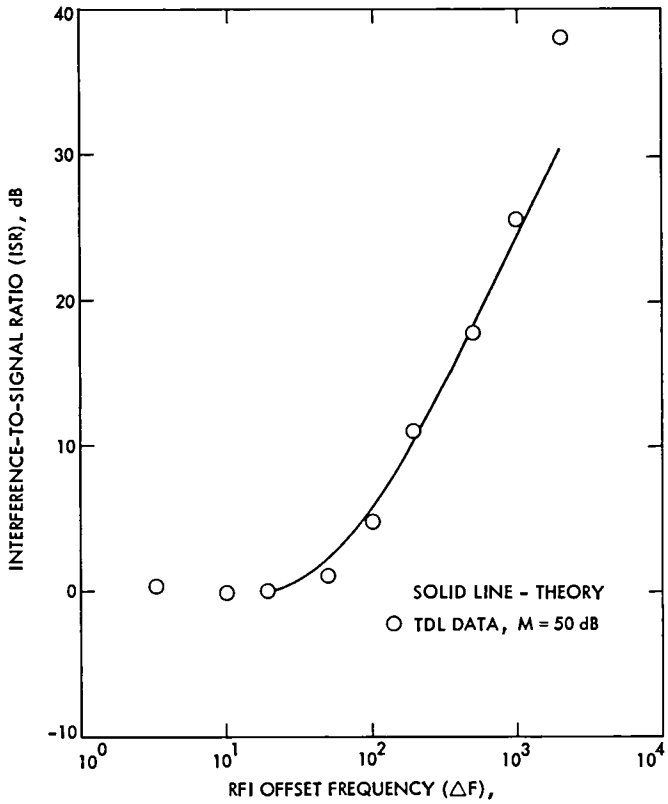

Fig. 10. Block IV receiver droplock level: comparison of analytical and experimental results (strong signal, 2 *BLO* = 30 Hz, wide mode)

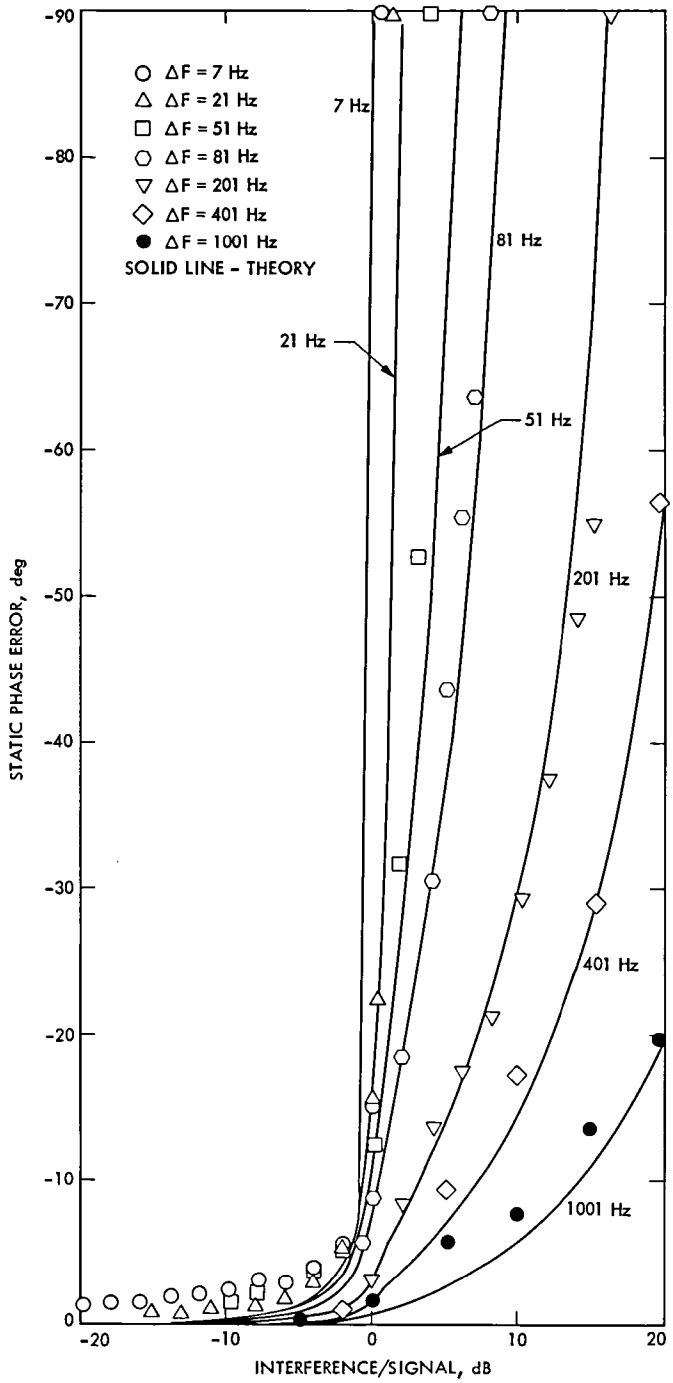

Fig. 11. SPE vs ISR: comparison of analytical and experimental results (strong signal, 2 *BLO* = 10 Hz, wide mode)

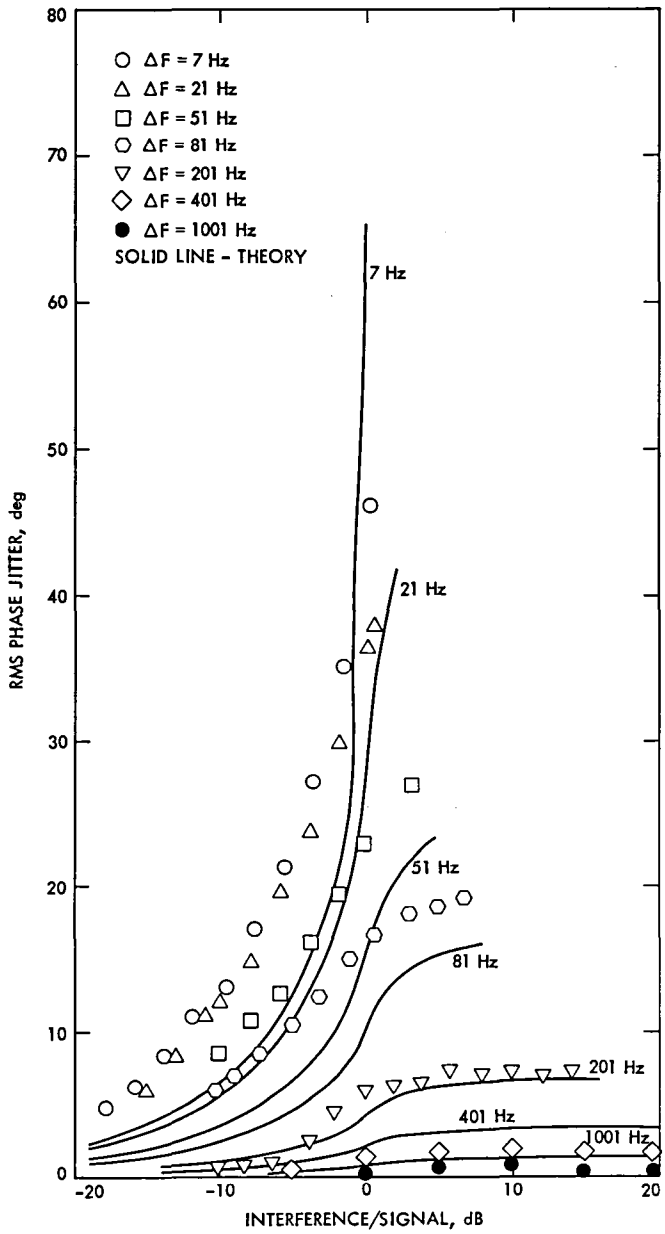

Fig. 12. Rms phase jitter vs ISR: comparison of analytical and experimental results (strong signal, 2 *BLO* = 10 Hz, wide mode)

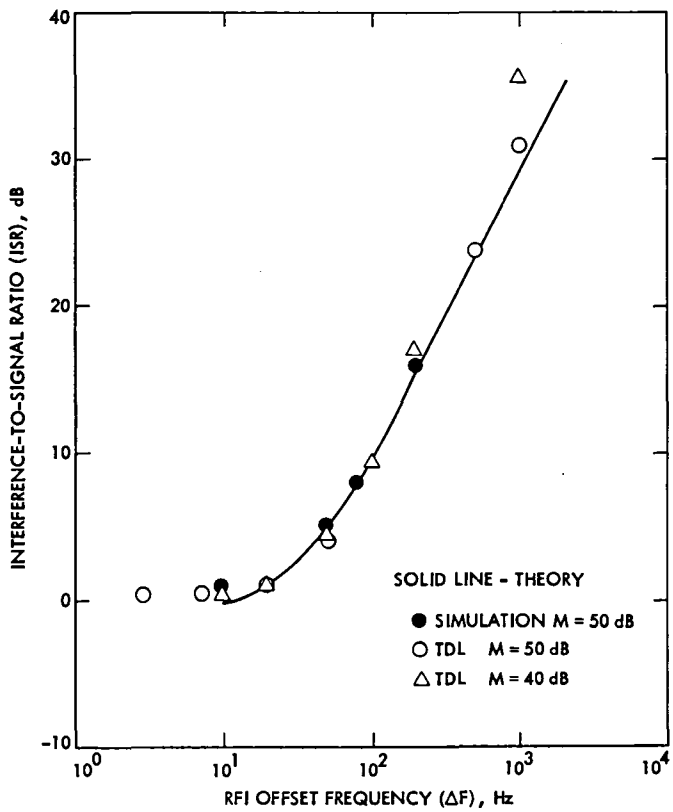

Fig. 13. Comparison of analytical, experimental, and simulated data for the Block IV receiver droplock level (wide/2 kHz/10 Hz)

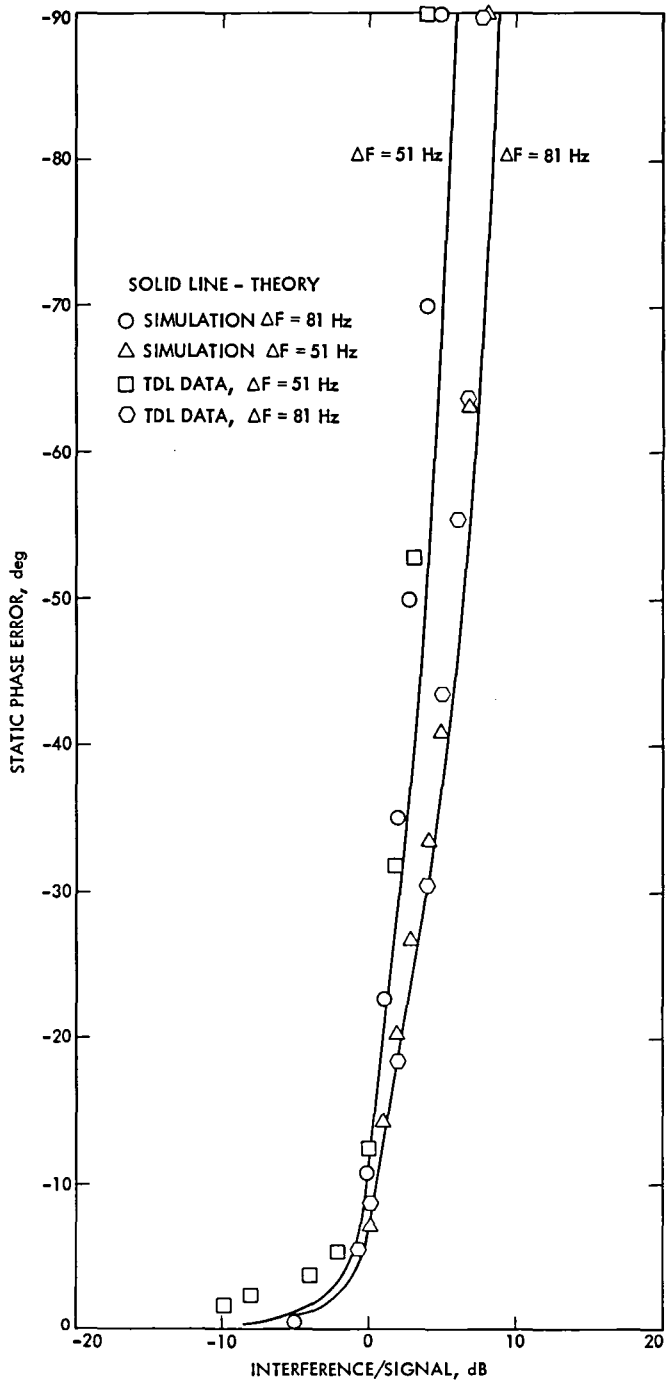

Fig. 14. Comparison of analytical, experimental, and simulated data for the Block IV receiver static phase error (wide/2 kHz/10 Hz)

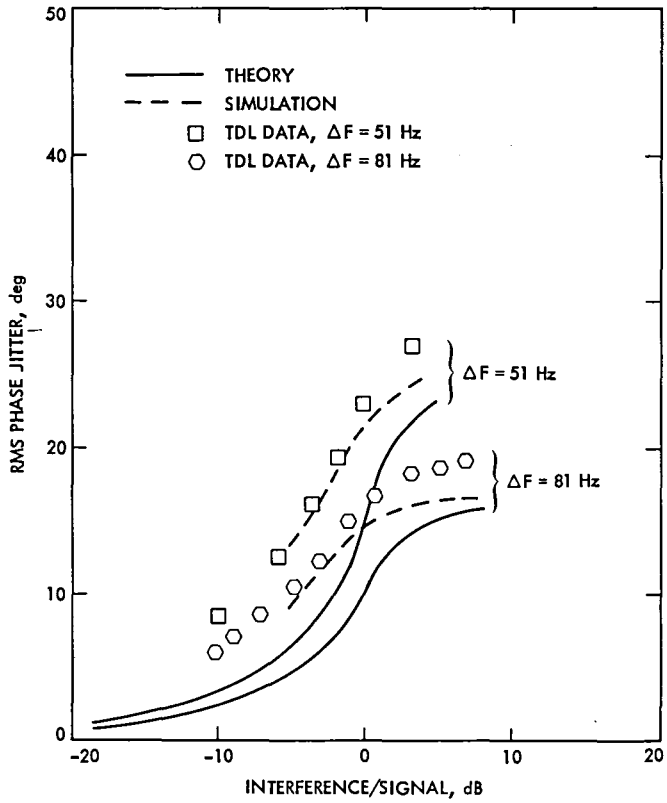

Fig. 15. Comparison of analytical, experimental, and simulated data for the Block IV receiver rms phase jitter (wide/2 kHz/10 Hz)

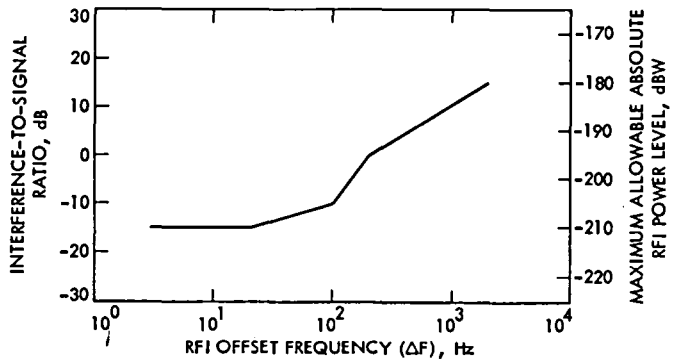

Fig. 16. Recommended protection criteria for CW RFI for Block IV receiver (absolute power level based on 10-dB carrier margin and −205 dBW noise power in a 10-Hz bandwidth)

Radio Frequency Performance of DSS 14 64-Meter Antenna at X-Band Using an Improved Subreflector

A. J. Freiley
Radio Frequency and Microwave Subsystems Section

In February and March 1980, the DSS 14 64-meter antenna X-band gain was determined using the R&D XKR feedcone. Tests prior to, and following the installation of an improved subreflector, proved the new unit largely (if not totally) restored initial performance levels at that station. The X-band peak gain with the new subreflector is +71.8 dBi (area efficiency of 47.3 percent); an increase of +0.47 dB due to the new unit installation. The tests further showed a significant shift in the axial focus required (function of elevation angle) which, if not implemented operationally, will cause a serious degradation.

An historical summary of all documented X-band gain measurements at DSS 14, covering the period 1968 to 1980, is included and reviewed. This summary traces the initial performance through various major configuration changes such as the installation of the X-band dual hybrid mode horn within the operational XRO feedcone. Finally, based on the summary and recent data, a peak X-band antenna gain of +72.1 dBi (area efficiency of 50.8 percent) is projected for the operational feedcone. Recommendations for further work are given.

I. Introduction

The X-band radio frequency performance of the NASA/JPL Deep Space Network 64-meter antenna at DSS 14 was measured in February and March 1980 at 8420 MHz (3.56-cm wavelength) to evaluate the expected improved antenna gain performance due to the installation of a new subreflector with improved surface tolerance. The replacement of the subreflector was part of total Voyager Enhancement Task to realize 2 dB of vital X-band gain and noise temperature improvements in the ground station performance for the Voyager Saturn encounter, and beyond.

To more fully appreciate the results presented here, an historical summary of DSS 14 64-meter antenna X-band gain measurements spanning the years 1968 to 1980 is presented with emphasis on the measurements of February and March 1973. In February and March 1973, DSS 14 was fitted with (1) a major structural brace to improve the gravity-induced, large-scale structural deviations of the main reflecting surface (dependent on elevation angle), and (2) a modified subreflector with welded seams to improve noise burst problems associated with diplexed high-power microwave transmission. The distorted subreflector and reset main reflector (necessitated by the structural brace installation) unexpectedly

resulted in a 0.46-dB loss of peak X-band gain, however, the incremental gain loss with elevation angle due to the gravity-induced surface tolerance deviation was improved. That is, the structural brace appeared successful in "flattening" the gain function with elevation angle, compared with the initial performance. The detailed results are reported in Ref. 1.

The February and March 1980 X-band antenna performance was measured by observing selected radio sources (3C274 and DR21) before and after the installation of the new subreflector. These radio source calibrators are generally well suited for the calibration of large ground-based reflector antennas and were selected to maintain consistency with previous measurements. The gain-stabilized noise-adding radiometer (NAR) was employed to measure the system noise temperature (Ref. 2), and to a large degree is responsible for the precision of the measurements reported here. The problematic absolute accuracy of this work is most likely ±0.5 to 0.6 dB (3σ) primarily due to radio source flux uncertainty, but the gain differences reported herein are considered highly accurate (±0.04 dB, 3σ) as well as exhibiting high precision in the order of hundredths of a decibel.

II. Microwave Receiving System

The receiving system used to perform the measurements reported herein incorporated the X- and K-Band Radar (XKR) feedcone followed by an R&D receiver. The microwave feed features a single hybrid mode corrugated conical feed horn with 22 dB of gain, selectable right and left circular polarization (RCP/LCP), and a low-noise traveling wave maser (TWM). The functional block diagram of the receiving system is given in Fig. 1. The receiving bandwidth was limited to ±5 MHz by the IF filter just preceding the broadband square law detector (Ref. 3). This system offered a total system operating noise temperature at zenith of 20 kelvins. Of this 20 kelvins, the TWM contributed 8 kelvins and the R&D receiver follow-up contributed 0.2 to 0.4 kelvin.

III. Antenna Modification

As part of the Voyager Enhancement Task, two major activities were scheduled during March 1980 that required evaluation. The first was to replace the original welded subreflector with an improved surface tolerance model. The root-mean-square (rms) surface tolerance of the new hyperboloid was reported to be 0.25 mm (0.010 inch); similar to the original tricone subreflector (1970) at 0.30 mm (0.012 inch) rms (Ref. 4). The second activity was to optically measure and reset the surface of the main reflector. RF gain measurements were to be performed before and after each activity to document the improvement of each step. If the improved subreflector realized an increase in antenna gain of 0.25 dB or better, the reset of the main reflector surface would then be deemed too risky in terms of possible mishap, and the loss of Voyager operational antenna tracking time would be deferred.

IV. Technique

The radiometric techniques used to evaluate the improvement in antenna gain were the same as was described in Ref. 5 with the addition of a system linearity test. The boresight optimization was achieved by using the conical scan technique. The antenna focal length changes were measured using the technique of stepping the subreflector in the axial or Z direction while measuring the loss in antenna gain at each step to determine the optimum setting. The actual gain or efficiency measurements employed the on-off sequence of system temperature measurements that yields the increase in system noise contributed by the radio source calibrator as measured with the NAR. The calibration of the NAR used the ambient calibration load as a temperature reference.

To achieve the accuracies and precisions necessary to determine the small changes in overall antenna performance, the Receiving System must have the linearity to accommodate all expected noise levels. The linearity of the receiver is a vital part of that capability. As part of a precal of each observing session, a system linearity test measured the input-output noise characteristics of the Receiving System. Excess noise was injected at the TWM input and measured as an increase in normal operating system temperature. By examining the increase at each of two noise levels produced by the normal zenith looking system and the calibration ambient load, a measure of the system linearity is achieved. The results of this test are discussed in Section VI.

V. Radio Source Calibrators

The standard radio sources, 3C274 and DR21, were selected as prime calibrators for this series of observations. The source availability during the allotted scheduled time for the measurements and maintenance of consistent calibrations (both before and after the antenna modification as well as antenna calibration measurements previously reported) were considered in source selection (Refs. 1 and 5).

The assumed flux density and other source parameters are given in Table 1. The assumed flux density S, is the result of radio source ratio measurements reported in Ref. 6. The source temperature, T_s, is the standard value on which the system efficiency is based and is determined from the flux density at the frequency of interest for a 100-percent efficient antenna by the relationship.

$$T_s = \frac{S A_p}{2k}$$

where A_p is the physical area of the antenna and k is Boltzmann's constant (1.380622×10^{-23} W/H_z - K). The typical corrected peak antenna temperatures, ΔT_a are also listed for reference in any future work. The source resolution correction, C_r, was applied to the measured antenna temperature, ΔT_a, to correct for the systematic error resulting from partial resolution of the radio source by the antenna beam. These sources are considered to exhibit strong, time-stable flux levels, and are well suited for use as gain standards for large ground-based antennas.

VI. Radiometric Observation

Observing sessions were conducted during February and March 1980 to determine the X-band performance of the 64-meter antenna. Special considerations were given to the areas of antenna pointing, optimum focus with elevation angle, receiver linearity, system temperature, as well as the overall antenna gain. The gain improvement realized from the new subreflector was sufficient to defer the measurement and reset of the main reflector surface. Therefore, only two extensive observing sessions, one prior to (February 1980) and one following (March 1980) the subreflector installation, were all that was allotted to achieve the performance verification.

A. Antenna Pointing

The antenna pointing system performed well during the observing sessions: no difficulties were encountered. A comparison of offsets prior to and following the subreflector replacement indicated no notable change as measured by the conical scan boresight technique. The scan radius used to boresight the antenna ranged from 0.015 to 0.020 degrees with a scan period of about 60 seconds. The beamwidth of the antenna at X-band was 0.038 degrees (137 arc seconds) and no change attributed to the subreflector replacement was measured.

B. Axial Focus

The subreflector axial focus positions as a function of elevation angle were measured to determine any shift in the optimum focus curve. The standard technique as described in Ref. 5 was used for this measurement. The measurements of the optimum axial focus position as a function of elevation angle are presented in Fig. 2 and show a significant shift between the before and after measurements. The optimum axial focus curve indicates a nominal 1.3-centimeter (0.5-inch) shift. At the high elevations, the difference is in the order of 1.0 centimeter (0.4 inch), and at the low elevation it is in the order of 1.5 centimeters (0.6 inch). Comparison of the axial focus for the before case and for the previous measurements reported in Ref. 5 show good agreement given the limited amount of data and the time between measurements. This minor difference is considered to be of little significance. However, the 1.3-centimeter (0.5-inch) shift detected by this series of measurements suggest a significant change that could and would affect the optimum antenna gain performance as a function of elevation angle. If ignored, this important offset could cause as much as 0.45-dB reduction in peak antenna gain. Apparently, the "match" between the main reflector (paraboloid) focal point and the subreflector (hyperboloid) focal point has been dramatically affected. It is not known if this might be a "best RF fit" (in a rms sense) due to a previously distorted subreflector, or merely an offset bias, due perhaps to different backup attachment details on the subreflector.

C. System Temperature

The total operating system noise temperature is a cornerstone of the large antenna gain measurements, and its accuracy and stability is of major importance. The operational XRO feedcone was to be the prime system used for this series of antenna measurements. During the February to March 1980 period, this system experienced gain stability problems of a few tenths of a dB (in the radiometric precision sense). In all cases, however, the XRO system was within specification for spacecraft tracking wherein slight gain instabilities are unimportant. Subsequent improvements in cabling details improved the XRO system, but not within the time frame for the antenna measurements. Therefore, the more stable XKR feed system was employed with its R&D receiver. The zenith operating system noise temperature was 20 kelvins including the TWM contribution of 8 kelvins and the R&D receiver follow-up contribution of 0.2 to 0.4 kelvin.

D. System Linearity

To measure Receive System linearity performance, the manual Y-factor instrumentation was used. The noise power contributed to the system from the noise diode can be measured at two points on the characteristic noise power input-output curve. The system is switched first to the ambient calibration load at about 300 kelvins, then the noise power from noise diode is injected and the amplitude of the noise power is measured. Then the system is switched to the feedhorn with the noise diode off. The noise power level falls to about 20 kelvins. Again, the noise power contributed by noise diode is injected into the system and its amplitude is again determined. The discrepancy between the two indicated noise diode temperatures is a measure of the system ability to linearly handle system noise temperatures in the range of 300

to 400 kelvins. For this XKR receiving system, the noise diode contributed 101 kelvins to the normal operating temperature. (i.e., 400-kelvin maximum levels must be transferred through all receiver stages, without clipping or saturating.)

This requires the system to have a linear response over a 13-dB range from 20 to 400 kelvins (zenith T_{op} = 20 kelvins: calibration load plus noise diode T_{op} = 400 kelvins). For typical DSN Receiving Systems with TWM gain set at 45 dB and the Block IV DSN receiver, the measurement of noise diode temperature at the high power levels is typically 10 to 20 percent lower than the same measurement at the zenith operating temperature. This demonstrates system saturation or clipping at the higher levels. To insure quality measurements with such a system, the gain of the TWM is reduced 3 to 6 dB to achieve linear operation. The R&D receiver used for 1980 measurements required no more than a 3-dB reduction in maser gain to achieve a linear receiver characteristic. However, this 3-dB gain reduction does cause the receiver follow-up temperature to double, but offered no difficulty in accomplishing the needed measurements.

E. System Gain

The intent of replacing the subreflector was to restore the previous (January 1973) performance as reported by the measurements reported in Ref. 1. In those measurements the system efficiency decrease was reported to be from 51.3 to 46.1 percent, based on an accepted flux density for 3C123 of 9.4 Jansky. Since the first JPL X-band measurements in 1968 (Ref. 7), 9.4 Jansky was the best available estimate of flux density. Later measurements and open literature reports of 3C123 flux density proved the 9.4 Jansky to be in error, and established the level at 10.05 Jansky (Ref. 6). Applying the revised flux density for the January and May 1973 measurements, performance levels were in actuality 48.0 and 43.1 percent, respectively. This translates to a gain loss of 0.46 dB due to the subreflector and concurrent main reflector work.

The recent measurements in February to March 1980 are presented in Fig. 3. The system efficiency shown as a function of elevation angle includes the atmospheric loss nominally incurred. Prior to the subreflector replacement, the peak system efficiency was 42.5 percent at 42.7-degrees elevation. Following the change, the peak system efficiency was 47.3 percent at 43.9-degrees elevation. The gain improvement attributed to the improved subreflector was 4.8 percent increase in system efficiency which corresponds to 0.47-dB increase in the overall antenna gain. This reliable result was quite sufficient to defer the planned main reflector surface reset since it is clear the welded subreflector was primarily responsible for the gain degradation in 1973. The gain deficiency of the DSS 14 64-meter antenna has been largely (perhaps totally) corrected and the gain performance has been reestablished at the 71.8-dBi level for XKR R&D feedsystem.

Comparison of the 1980 and 1973 results shows remarkable repeatability and similarity. The high-level performance measurements prior to the 1973 modifications and after the 1980 subreflector installation agree to within 0.7 percent and the lower level performance of the intervening years agree to within 0.6 percent. The elevation angle at which the peak performance occurs agrees to within 2 degrees in all cases. The agreement of these measurements taken 7 years apart indicate the antenna system has experienced very little or no "aging" or loss of performance with time during that period and is in contrast to the conclusions reached in Ref. 5.

A complete summary of DSS 14 64-meter antenna X-band performance measurements is given in Table 2. The measurements are classified by date and the feedcone system used for the measurements. The entries for March 1980 using the XRO dual hybrid mode horn feedcone are not measured values but have been predicted based on the November 1979 measurements and February to March 1980 measured performance increase. The significant figures of the values presented here do not necessarily denote the absolute accuracy of the measurement but are presented to provide resolution into the order and repeatability of the measurements.

VII. Conclusions

The performance of the DSS 14 64-meter antenna at X-band was measured using the XKR feedcone. The performance level anticipated with the 1973 antenna upgrade has finally been achieved. The antenna efficiency as measured with the XKR feed has increased from 42.5 to 47.3 percent, which nets an increase of 0.47 dB. With this increase, the overall gain of the 64-meter antenna with the XKR feed is 71.8 dBi. The gain of the antenna using the operational XRO feed with the recently installed dual hybrid mode feed will also exhibit a similar gain change of 0.47 dB above that reported in Ref. 5. This performance should be 50.8 percent efficient, which corresponds to a peak antenna gain at 72.1 dBi. A natural follow-on activity should pursue the measurements of antenna gain using the XRO with the new feed, confirm that performance level, and check the critical Z-axis focus characteristics.

Comparison of the measurements of antenna efficiency reported here and that of Ref. 1 (both using the XKR feed) shows good agreement both in peak performance and in the pointing angles at which that performance occurs. However, the measurement using the XRO feed shows distinct differences in the shape of the efficiency curve with elevation

(Ref. 5). The peak performance occurred at about the 52-degree elevation and was consistent prior to and following the installation of the new feed. This compares to the 42-degree elevation angle peak of this current set of measurements, which agrees more closely with the mechanical analysis of the 64-meter antenna (Ref. 8) and the 1973 measurements. Resolution of this discrepancy would improve the communication link predictions and analysis for spacecraft tracking, and would enable improved confidence in engineering predictions for possible future performance enhancement of the 64-meter antenna system, as well as other important DSN antenna projects.

The optimum axial focus has changed significantly with the installation of the improved subreflector. The optimum focus curve has shifted axially approximately −1.3 centimeters (−0.5 inch); physically the optimum subreflector focus is now closer to the feed. In anticipation of the requirement for automatic subreflector focusing for spacecraft tracking, a complete measurement of optimum axial focus for the XRO feed should be undertaken and analyzed. Also, periodic optical alignment of the main reflector panels of all 64-meter antennas is recommended to maintain the network performance at or above this high level.

To enhance the accuracy of antenna gain measurements, improvements in the following areas are needed and recommended: (1) the noise instrumentation, both Y factor and NAR, should be upgraded; (2) the system linearity, mainly within the receivers (especially the DSN Block IV Receivers) needs improvement. The DSN Block IV Receiver typically exhibits 10 to 20 percent nonlinearity at a 300 to 400 kelvin noise level into the maser input. The linearity problems outlined are present with the standard 40-MHz bandwidth TWM. With the new Block IIA 100-MHz bandwidth units, the linearity problems will become more acute. Last, but by no means least, the absolute flux density of the X-band radio source calibrators should be established to a level comparable to the S-band calibrators reported in Ref. 9.

Finally, the influence of the structural brace on the vital X-band efficiency with its elevation angle dependency is emphasized. The other 64-meter stations (DSSs 43 and 63), although fitted with dual hybrid mode feeds, good subreflectors, and other common features, do not have the structural brace installed as yet. This feature should be finally implemented at those stations to realize the full potential of the 64-meter network.

References

1. Freiley, A.J., *Radio Frequency Performance of DSS-14 64m Antenna at 3.56 and 1.96cm Wavelength*, Technical Report 32-1526, Vol. XIX, pp. 110-115, Jet Propulsion Laboratory, Pasadena, California.

2. Batelaan, P.D. Goldstein, R.M., Stelzried, C.T., "A Noise-Adding Radiometer for Use in the DSN", *Space Program Summary, 37-65*, Vol. II, pp. 66-69, Jet Propulsion Laboratory, Pasadena, California.

3. Reid, M.S., Gardner, R.A., Stelzried, C.T., *A New Broadband Square Law Detector*, Technical Report 32-1599, Jet Propulsion Laboratory, Pasadena, California, September 1, 1975.

4. Lobb, V.B., private communications, September, 1980.

5. Freiley, A.J., "Radio Frequency Performance of DSS-14 64m Antenna At X-band using a Dual Hybrid Mode Feed", *DSN Progress Report 42-53*, pp. 132-140, Jet Propulsion Laboratory, Pasadena, California, July and August 1979.

6. Turegano, J.A., Klein, M.J., "Calibration Radio Sources for Radio Astronomy: Precision Flux Density Measurements at 8420 MHz", *Astron. Astrophys.*, Vol. 86, pp. 46-49.

7. Bathker, D.A., *Radio Frequency Performance of a 210-ft Ground Antenna: X-Band*, Technical Report 32-1417, Jet Propulsion Laboratory, Pasadena, California, December 15, 1969.

8. Lobb, V.B., and Katow, M.S., "64-Meter-Diameter Antenna with New Braces: Installation Description and Computed Performance for Gravity Loads," *Deep Space Network Progress Report*, Technical Report 32-1526, Vol. XVII, pp. 93-99, Jet Propulsion Laboratory, Pasadena, California, Oct. 15, 1973.

9. Freiley, A.J., Batelaan, P.D., and Bathker, D.A., *Absolute Flux Density Calibrations of Radio Sources: 2.3 GHz*, Technical Memorandum 33-806, Jet Propulsion Laboratory, Pasadena, California, December 1, 1977.

Table 1. Radio source calibrations for 64-meter antenna

Source	Flux density[a] 8420 MHz S, Jansky	Source temperature (100% efficient antenna) T_s, kelvin	Typical measured antenna temperature ΔT_a, kelvin	Source resolution correction C_r	Source position (1950.0)	
					Right ascension, hr-min-s	Declination, deg-min-s
3C274	46.0	53.6	25.4	1.085	12 28 17.3	12 39 48
DR21	21.4	25.0	11.8	1.030	20 37 14.2	42 09 07

[a]Flux density values from Ref. 6.

Table 2. Historical summary of X-band performance measurements of DSS 14 64-meter antenna

Measurement date	Feedcone designation	Peak antenna efficiency η, %	Elevation angle, deg	Antenna gain G, dBi	Gain increase ΔG, dB
Feb. 1968[a,b]	XCE	48.6	≈47	71.91	–
Jan. 1973[b,c]	XKR	48.0	≈42	71.85	Ref.
May 1973[b,c]	XKR	43.1	≈42	71.38	−0.46
July 1979[d]	XRO	42.0	52	71.27	Ref.
Nov. 1979[d]	XRO	45.6	52	71.63	+0.36
Feb. 1980	XKR	42.5	43	71.32	Ref.
Mar. 1980	XKR	47.3	44	71.78	+0.47
Mar. 1980[e]	XRO	50.8	≈52	72.10	–

[a]Ref. 7, single feedcone configuration; all others are tricone configuration.

[b]1968 and 1973 measurements have been corrected by the ratio of the original assumed source flux density to the improved value.

[c]Ref. 1.

[d]Ref. 5.

[e]Predicted XRO performance based on the November 1979 measured performance and the February to March, 1980 measured performance increase.

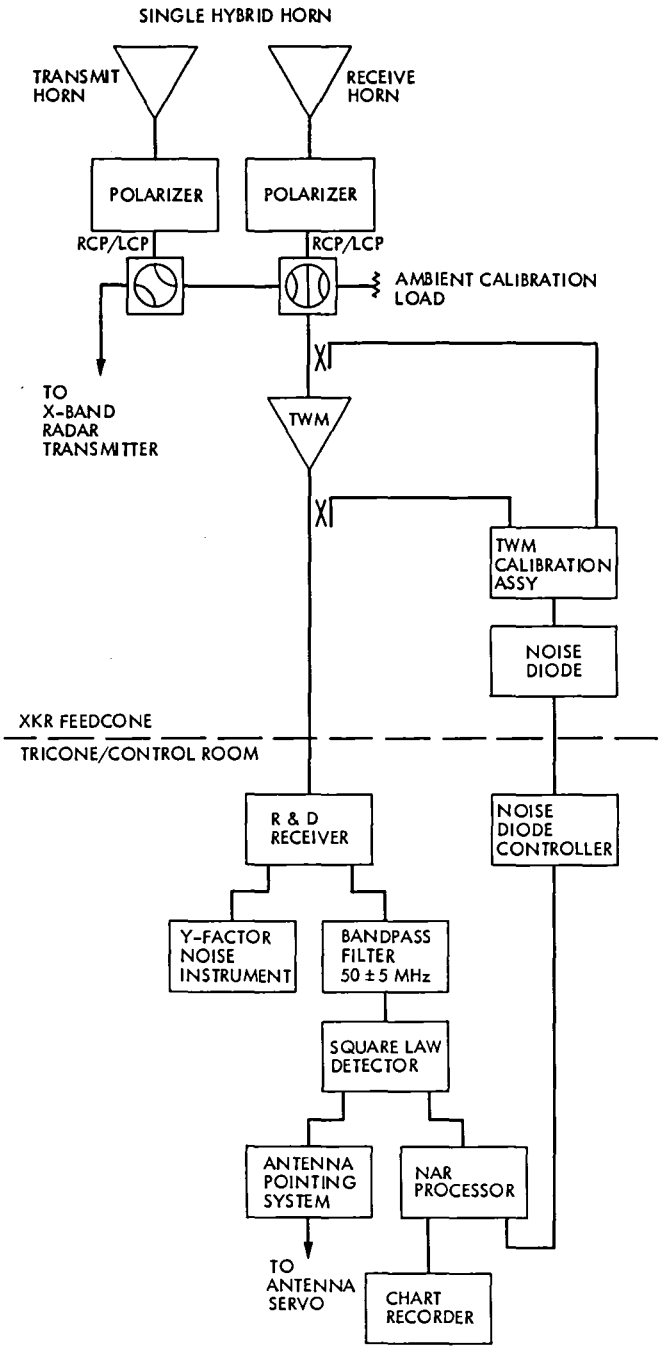

Fig. 1. The XKR X-band receiving system functional block diagram

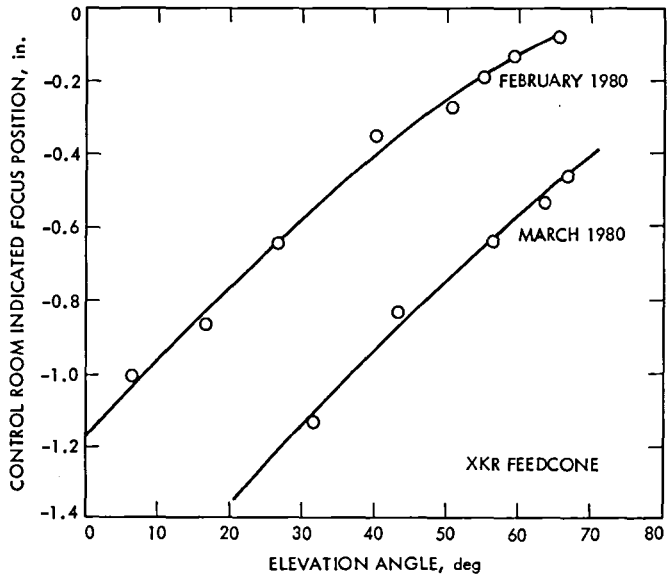

Fig. 2. DSS 14 64-meter antenna X-band optimum axial focus position as a function of elevation angle

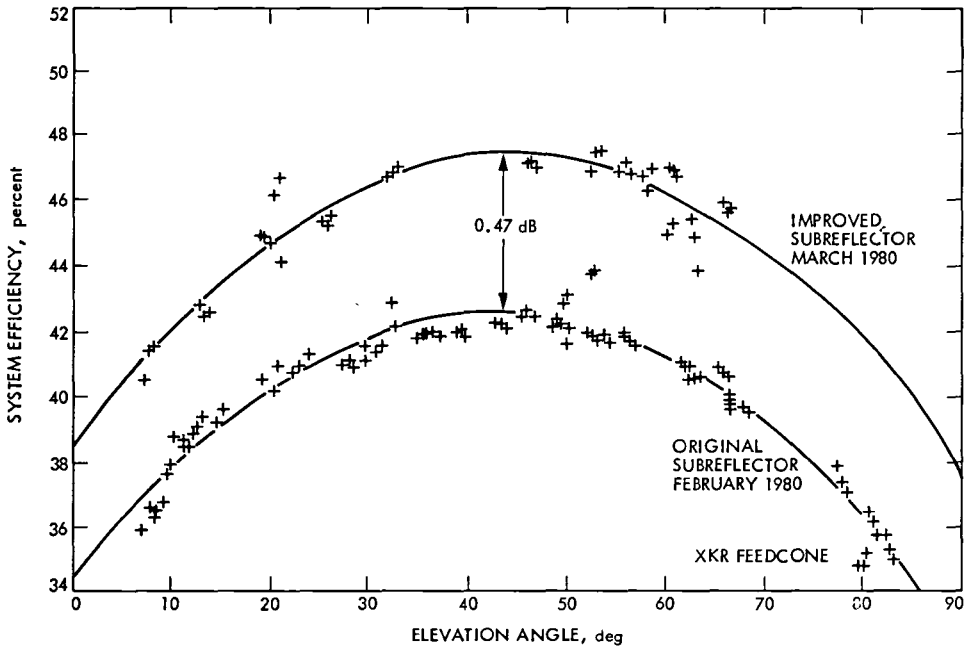

Fig. 3. DSS 14 overall antenna system efficiency at X band (8.42 GHz) with an improved subreflector

Goldstone Radio Spectrum Protection

B. A. Gaudian
Goldstone Operations Section

R. B. Cushman
Bendix Field Engineering Corporation

Goldstone is located amidst several military installations where equipment used in the test and training activities is a source of potential electromagnetic interference to the Goldstone tracking receivers. Coordination of the military and NASA Goldstone activities in the Mojave Desert Area is an effective method to protect the Goldstone radio spectrum while maintaining compatible operations for the military and Goldstone.

I. Introduction

One of the prime reasons for selecting Goldstone as the site for the NASA DSN and STDN spacecraft communications stations was its remote location, which provides protection for the sensitive receivers from local interference. The RF environment has changed significantly since Goldstone began operations in 1958. There has been and will continue to be an expansion of the civilian and military use of the radio spectrum for communication, navigation, detection, guidance, and electronic countermeasures (ECM). Each additional system may present a potential electromagnetic interference threat to the DSN/STDN stations.

The present electromagnetic interference (EMI) environment exists because Goldstone is located within one of the largest military training areas in the United States, designated the R2508 Complex. Goldstone's location within the complex is illustrated by Fig. 1. On the northern and eastern boundaries of Goldstone is Fort Irwin (R-2502). Fort Irwin has recently been selected as the Army National Training Center (NTC) and when fully operational the U.S. Army will evaluate techniques and tactics and conduct training in a realistic warfare scenario. On the western border of Goldstone is the Naval Weapons Center (R2524). The Naval Weapons Center is engaged in testing and evaluating new weapon systems including electronic warfare (EW) systems. To the south and west are several gunnery ranges used to conduct both airborne and ground forces training.

Because of the potential for EMI occurrences within the R-2508 Complex, a NASA/DOD Memorandum of Understanding (MOU) was published on 18 December 1978 to provide a means of coordinating activities for minimizing the impact of potential conflicts. The MOU states that the Department of Defense and the National Aeronautics and Space Administration will jointly establish a Mojave Coordinating Group (MCG) for operational coordination, scheduling, and problem resolution. The primary functions of the MCG are to coordinate major DOD events, classify NASA tracking events, analyze compatibility of events, coordinate facility modifications, and develop procedures. No real-time coordination functions are performed by the MCG as a group. All real-time

coordination is conducted between individual members of the group as the need arises. The MCG, as chartered by the MOU, sets the rules.

II. Functions of the MCG

The MCG is a professional military and civilian technical management group interested in protecting a vital national resource, the radio spectrum. To efficiently protect the radio spectrum and the individual interests of each member of the group requires advance coordination of each major DOD/NASA event. As soon as a major activity is conceived it is the responsibility of the sponsor of the activity to arrange for a project briefing for the MCG. Each member of the MCG must examine the details of the activity and determine the impact, if any, to the organization he is representing.

The specific functions of the MCG are: to coordinate major DOD events, to classify NASA tracking events for specific protection, to analyze compatibility of events, to coordinate facility modifications, and to develop procedures.

A. Coordination of Major DOD Events

At every MCG meeting a representative of the Western Area Frequency Coordinator presents a DOD Operations Schedule. The schedule lists future R-2508 DOD operations by program, sponsor, location, and date. If there are any conflicts of interests, the affected parties may either discuss the problem at the meeting or by personal contact at a later date.

In addition, the military representatives provide a preview of major military exercises in the Mojave Desert far in advance of the actual occurrence. Details of the exercise are expanded as operational plans develop. Goldstone is primarily concerned with the nature of the systems to be deployed, frequencies, air activities, and troop deployment. It is the responsibility of the Goldstone Radio Spectrum Coordinator to protect not only the radio frequency environment but also to protect the physical environment of the Goldstone Complex.

B. Classification of NASA Goldstone Tracking Events

Classification of NASA Goldstone tracking events means sorting the satellite and spacecraft tracking events in terms of their relative importance to mission success. There are 3 classes of NASA Goldstone events.

Class 1 Critical Events are so important in terms of science-mission success or personnel safety that uninterrupted tracking and data acquisition must be guaranteed. The following are Class 1 events:

(1) Initial acquisition through spacecraft stabilization.

(2) Primary mission events, including planetary encounters, orbit insertions, probe entries, landings, and selected orbital/surface operations.

(3) Shuttle flights requiring acquisition/recovery by the Goldstone STDN.

(4) Spacecraft emergencies when designated by the NASA Associate Administrator for Space Tracking and Data Systems.

Class 2 Sensitive Events are highly important in terms of science-mission objectives. The following are Class 2 events:

(1) Trajectory correction maneuvers.

(2) Spacecraft attitude maneuvers

(3) Spacecraft/satellite emergencies

(4) Station calibrations for Class 1 events

(5) Solar conjunctions

(6) Precision navigation tracking cycles

(7) Other selected events:

  (a) Planetary operations

  (b) Radio astronomy planetary radar

  (c) Far-encounter operations

  (d) Readiness tests

  (e) Spacecraft calibrations

Class 3 Routine Events are those events which do not meet the Class 1 or Class 2 criteria, but require normal spectrum protection. When possible, Class 3 events are scheduled to avoid activities having known EMI sources.

The classification of Goldstone NASA DSN/STDN events is normally performed by the Goldstone Radio Spectrum Coordinator in conjunction with information from the Jet Propulsion Laboratory flight project offices. The Goldstone Radio Spectrum Coordinator continually reviews the schedule of events and updates it for submission to the MCG. Each month a teletype message is transmitted to all interested organizations, listing the Class 1 and Class 2 events, the times that Goldstone requires spectrum protection, and the specific spectrum protection required.

C. Analyzing Compatibility of Events

If there is any question of compatibility, the Electromagnetic Compatibility Analysis Center (ECAC), located in Annapolis, Maryland, will be requested to produce a computer

profile of the system planned for the Mojave Desert Area. ECAC has access to many commercial and military equipment specifications, including some classified systems. ECAC also has on file the susceptibility characteristics of the DSN and STDN antenna and receiver systems. The ECAC analysis will compare the frequency, power, and the spectral characteristics to existing systems and submit a written report of their findings to the MCG or to the MCG requestor. Based upon ECAC's findings a determination will be made concerning the compatibility of the equipment with established operations. Prior coordination will be required when specific equipment or events present interference potential.

D. Coordinating Facility Modifications

Facility modifications may seem to have no relationship to the radio spectrum and little potential impact on activities other than those of the involved facility. Actually, however, facility modifications may create not only an EMI problem but also a safety problem. It is the responsibility of the sponsor to present a modification briefing to the MCG for examination by the members.

Examples of modifications that could impact Mojave operations are DSN high-power radiation power increases, installation of the Goddard Mobile Laser (MOBLAS), relocation of the Cuddeback air/ground gunnery range, and construction of new facilities.

E. Development of Procedures

The MCG depends upon the Central Coordinating Facility (CCF), which is knowledgeable of all operations in the R-2508 complex, to recognize problems and conflicts as they arise. It is necessary for the CCF to adopt standard operating procedures that have been recommended by the MCG.

In addition to the CCF procedures, each facility in the R-2508 complex has its own local operating procedures. The MCG as a group produces procedures to control, coordinate and isolate radio spectrum problems in the Mojave Desert Area.

III. Real-Time Coordination

Real-time coordination mainly involves those events requiring attention prior to the bimonthly MCG meetings. These events could be special weapons tests, aircraft/EW activities in the R-2508 complex and surrounding airspace, Goldstone high-power radiation requirements, and NASA spacecraft emergencies and personnel emergencies, or they could include assistance in identifying the source of any external radio frequency interference thought to have caused an unexpected data interruption or signal degradation.

A prerequisite to real-time coordination is the availability of adequate means for communication. A two-digit hotline provides a dedicated, point-to-point telephone link between sponsors, ranges, and operational areas in the R-2508 complex (See Fig. 2). NASA/DOD teletype circuits are also used to coordinate on a day-to-day basis. Future plans call for the addition of at least one Autovon line to Goldstone for contacting the many military agencies outside the R-2508 complex.

A. Event Notification

Although most NASA spacecraft events are scheduled well in advance, most of the routine military operations conducted in the area are not. However, the need for adequate advance notification of scheduled events is constantly stressed, as time is required to analyze the impact of the activity on the DSN/STDN missions.

B. EMI Avoidance

The majority of military activities involving EW emitters or airborne telemetry are coordinated to minimize the potential for EMI. However, one of the difficulties is that in many of the activities there are uncertainties such as the actual frequency bands to be used, the power of the radiation, and the time period or the area in which the activity will take place. When an activity is thought to pose an EMI threat, efforts are made to provide sufficient distance or frequency separation to avoid interference.

C. Contingencies

In the event NASA has a spacecraft emergency, all military activities that have the potential to cause EMI to Goldstone will be requested to terminate the emitters at the earliest possible time.

IV. Spectrum Protection Requirements

The stringency of the type of spectrum protection required for an event depends upon its classification according to the provisions of paragraph II.A. Spectrum protection for the three classes of Goldstone tracking events is provided as described below.

Class 1 Critical Event

(1) No airborne EW within line of sight of Goldstone.

(2) No airborne Tactical Air Navigation System (TACAN) transmissions on Channels 116 through 126 within 50 nautical miles of Goldstone.

(3) No operation that would have a theoretical possibility of EMI impact on Goldstone.

(4) Specific spectrum protection for the STDN for shuttle missions will be coordinated through the Western Area Frequency Coordinator (WAFC) until standardized protection is established.

Class 2 Sensitive Event

(1) No airborne noise jamming 1800-2700 MHz and 7900-9000 MHz within line of sight of Goldstone.

(2) No airborne repeat jamming 2150-2350 MHz and 8350-8550 MHz within line of sight of Goldstone.

(3) No airborne TACAN transmissions on Channels 116 through 126 within 50 nautical miles of Goldstone.

(4) No airborne EW to be conducted using EA-6B, EF-111 or EF-16 aircraft within line of sight of Goldstone.

(5) Specific spectrum protection for the STDN for launch pass coverage will be handled in near real-time with the WAFC, due to instability of the launch dates/times.

Class 3 Routine Events

(1) NASA and DOD activities to be scheduled and coordinated for compatibility.

(2) Predictions of EMI potential provided to the flight projects.

V. Conclusion

Protection of the Goldstone radio spectrum is very essential to the safeguarding of data communications capabilities between spacecraft and the Goldstone tracking antennas. This spectrum protection is being successfully accomplished through the mutual coordination and cooperation of the DOD and NASA Goldstone representatives in spite of the high density of potential military sources of electromagnetic interference. The maintenance of operational compatibility between both agencies is essential and continued coordination and cooperation are considered to be the key elements in maintaining this compatibility.

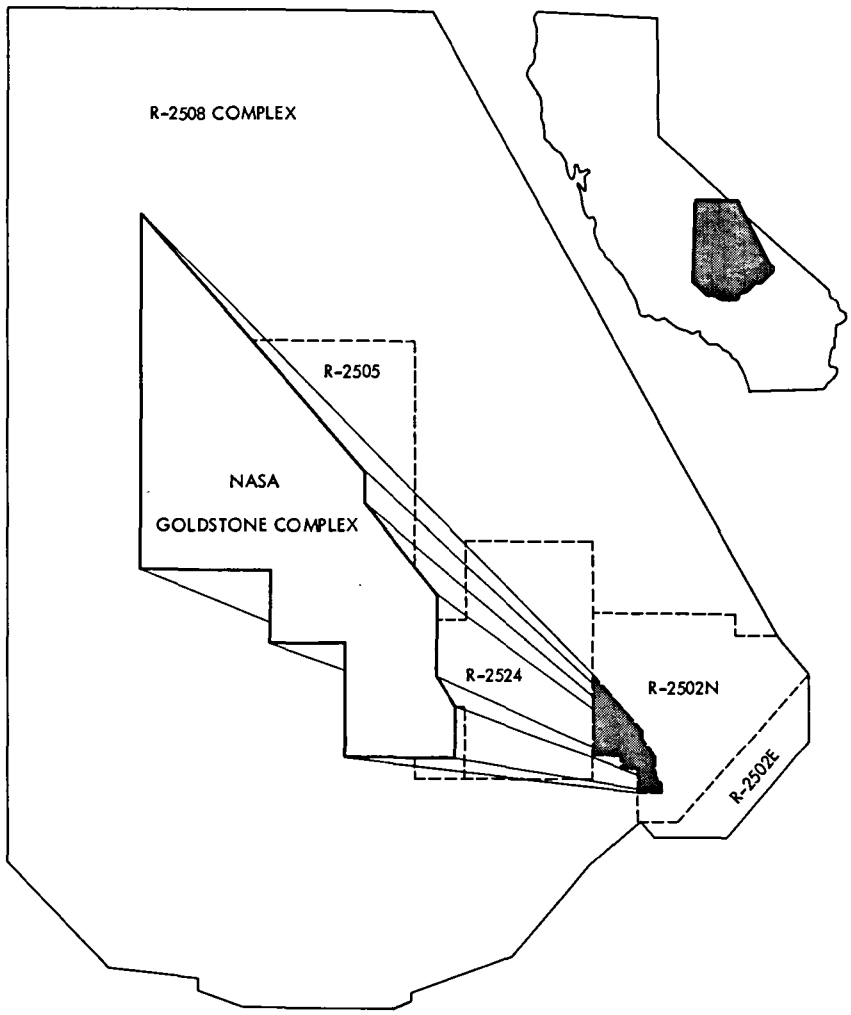

FORT IRWIN (NATIONAL TRAINING CENTER) - R-2502E & R-2502N
U.S. NAVAL WEAPONS CENTER - R-2505 & R-2524

Fig. 1. NASA Goldstone location within the R-2508 Complex

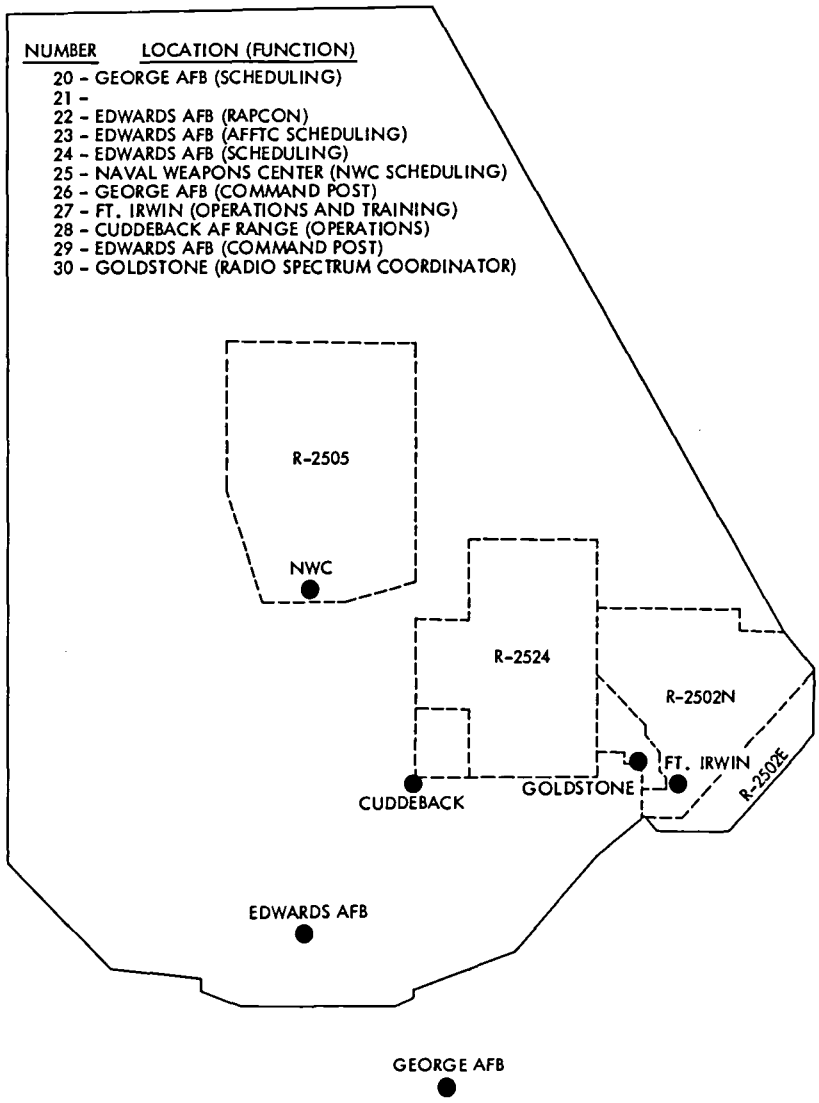

Fig. 2. R-2508 Complex two-digit hotline

An Estimating Rule for Deep Space Station Control Room Equipment Energy Costs

H. C. Younger
Deep Space Network Support Section

The cost of electricity to power equipment in control rooms of Deep Space Stations is about $1/yr/W. This rule can be used to estimate power costs for new equipment under development, helping to reduce life-cycle costs and energy consumption by justifying design alternatives that are more costly, but more efficient.

I. Introduction

With costs of energy steadily increasing, the Deep Space Network has become more conscious of the energy costs associated with electronic equipment. Specifications for new equipment generally require that development personnel consider energy conservation in the equipment design, and this consideration is being evaluated at design reviews.

There has thus arisen a need for a simple rule to estimate energy costs associated with new equipment for the Deep Space Stations. Many such rules exist in other fields. For example, building construction costs are estimated in dollars per square foot, with published values appropriate to geographical areas. Costs of photovoltaic cells are estimated in dollars per peak watt. A similar rule has been developed for estimating the cost of electricity required to operate equipment installed in the control rooms of Deep Space Stations.

II. Electricity Costs

There are two principal components in the cost of electricity for Deep Space Station (DSS) control room equipment. One is the direct cost of the electricity, whether purchased commercially or generated at the station. The other is associated with the heat produced by the equipment. Each station has an air conditioning system. This is designed to maintain the control room equipment within a controlled temperature range as well as to maintain the control room itself within an appropriate range for human comfort. Because of the large amount of heat generated by the equipment in a station, this is essentially a cooling load for the vast majority of outside climatic conditions. New control room equipment will add to the heat load on the air conditioning equipment, and the increased cooling load will produce an additional increment of electricity cost.

The cost of electricity at the Goldstone stations is approximately $0.063/kWh. This is chiefly commercial power. At the Madrid stations, the 1979 cost of power for local diesel generation equipment was $0.067/kWh. Figures for the Australian stations are believed to be about the same. A value of $0.065/kWh is used for the computations in this article.

Most DSS control room equipment is operated continuously, and this is assumed to be the case for new equipment to which the rule is to be applied. A load of one watt consumes 8.76 kWh in one year (8760 hours). With current electrical

costs at $0.065/kWh, this is an annual cost of $0.57/yr/W for direct electrical usage.

The heat produced by equipment dissipating 8.76 kWh is 29,898 Btu. This is the amount of heat that must be removed from a DSS control room by its cooling system in a year for each watt of electrical power dissipated in equipment. Assuming an average cooling system energy efficiency rating (EER) of 7 Btu/Wh, the electricity required for cooling is 4271 Wh/yr. At $0.065/kWh, this is a cooling cost of $0.28/yr/W.

Adding the direct and cooling costs of electricity, the total cost of electricity for DSS control room equipment is approximately $0.85/yr/W at the present time. Electricity costs at the stations have been rising at a rate of about 15%/yr for the past few years, and the pattern is unlikely to change soon. At this rate, DSS control room equipment energy cost will be $1/yr/W in 1981. This value is easy to remember, and it is recommended as an estimating rule for energy costs in new equipment implementations.

III. Conclusion

The existence of a simple estimating rule makes it practical to trade off energy costs for capital costs in new equipment design. For example, DSS electronic equipment is typically powered by a commercial power supply which converts 110-volt, 60-Hz primary power to one or more DC voltages used by the equipment components. A conventional regulated power supply has a typical efficiency of 40 percent, while a switching regulated power supply has a typical efficiency of 75 percent. A conventional power supply delivering 100 watts to its load will require 250 watts of primary power, while the switching power supply under the same load will require only 133 watts. This difference of 117 watts will cost approximately $117/yr for additional energy. This is usually enough to pay for the added power supply cost in a matter of months.

NASA–JPL–Coml., L.A., Calif.

End of Document